



UNIONE EUROPEA
Fondo Sociale Europeo
Fondo Europeo di Sviluppo Regionale



Università di Napoli
"Federico II"



Università di Camerino



Consiglio Nazionale
delle Ricerche

PHD DEGREE IN QUANTUM TECHNOLOGIES

XXXVII CYCLE

A new setup for single Strontium atoms in Optical Tweezers

PHD THESIS

Author

Luca GUARIENTO

Supervisor

Dr. Jacopo CATANI

Cosupervisor

Prof. Leonardo FALLANI

Academic discipline FIS/03

ACADEMIC YEARS 2021/2024

Luca GUARIENTO

A NEW SETUP FOR SINGLE
STRONTIUM ATOMS IN OPTICAL
TWEEZERS

PhD Thesis

PhD degree in Quantum Technologies

February 2025

Contents

List of Figures	vii
List of Tables	ix
1 Introduction	1
1.1 Quantum simulation	2
1.2 State-of-the-art tweezer array experiments	3
1.3 General overview of the experiment	3
1.3.1 Experimental apparatus	4
1.3.2 Strontium atoms	4
Relevant transitions	5
2 Atom-Light Interaction	9
2.1 Fundamentals of atom-light interaction	9
2.2 Laser cooling with Doppler and Zeeman effects	11
2.3 Zeeman slower, 2D MOT and 3D MOT	13
2.3.1 Transverse cooling	13
2.3.2 Zeeman slower	15
2.3.3 Magneto-Optical Trap	16
2.4 Off-resonant atom-light interaction, optical trapping and cooling	18
2.4.1 Atomic polarizability	19
2.4.2 Harmonic oscillator approximation	21
2.4.3 Atom cooling in tweezers	22
3 Optical Tweezers and Rydberg atoms	25
3.1 Optical Tweezers	25
3.1.1 Optical setup	25
3.1.2 Arrays of optical tweezers	29
Acousto-optic deflectors	29
Spatial light modulators	32
3.1.3 Defect-free array of single atoms	33
Loading multiple atoms from the red MOT	34

	Light-assisted collisions	35
	Reordering	36
3.2	Rydberg atoms	38
3.2.1	Two different excitation schemes	39
3.2.2	Rydberg excitation coupling strength	40
3.2.3	Rydberg blockade	44
3.3	Quantum simulation and computation	45
3.3.1	Quantum simulation of spin models	46
3.3.2	Optimization protocols and quantum annealing	48
3.3.3	Quantum gates for quantum computing	49
4	Site-resolved single-atom imaging	51
4.1	Imaging using the blue transition	51
4.2	Imaging using the red transition	53
4.3	Atomic fluorescence collection	55
4.3.1	Dipole radiation	55
4.3.2	Imaging system and cameras	55
	EMCCD cameras	57
	qCMOS cameras	57
4.3.3	Point-like source PSF	58
4.3.4	Binary thresholding	59
	Fidelity	59
	Survival rate	61
4.4	Alternative imaging schemes	61
4.4.1	Fast imaging with an ultra-low noise camera	62
	Comments on the imaging technique	68
4.4.2	Five-level imaging scheme	69
5	Experimental apparatus	77
5.1	Overview of the experimental apparatus	77
5.2	Vacuum system	80
5.2.1	Strontium atomic source	81
5.2.2	Pumping chamber and glass cell	83
5.2.3	Outgassing in UHV systems and limit pressure	85
5.2.4	Assembling and bakeout	86
	Vacuum failure	87
	Second assembly and bakeout	90
5.2.5	Tips and tricks for the vacuum system	91
5.3	Main Magnetic field coils	92
5.3.1	Motivation and requirements	93
	B field for magneto-optical traps	93
	Excitation to the clock state	94
5.3.2	High field coils	96
	Water cooling circuit	100
	Electric circuit	102
5.4	Stray fields compensation coils	104
5.4.1	Supportive structure	105
5.5	Microscope objective	106

5.5.1	5-axes control	107
5.5.2	Alignment procedure	107
5.6	Laser systems	109
5.6.1	Blue laser	109
5.6.2	Red laser	111
	Frequency locking to ULE cavity	111
5.6.3	Tweezers laser	115
5.6.4	UV laser	115
5.7	Control system	116
6	Production of a two-stage Magneto-Optical Trap	119
6.1	Blue and red optical setups	119
6.2	Blue MOT, imaging and characterization	122
6.2.1	Number of atoms and temperature	123
6.3	Red MOT	126
6.3.1	Multi-frequency MOT	127
	Red transition spectroscopy and shielding-enhanced blue MOT	132
6.3.2	Single-frequency MOT	134
7	Loading atoms in an array of optical tweezers	137
7.1	Alignment of the optical tweezers	137
7.2	Overlap the red MOT and the tweezer array	140
7.3	Fluorescence imaging of atoms in tweezers	141
7.4	Cooling and light-assisted collisions	143
7.5	Towards single atoms in optical tweezers	145
	Conclusions and outlook	149
	Bibliography	151

List of Figures

1.1	Relevant energy levels for ^{88}Sr .	5
2.1	Schematic representation of the transverse cooling and Zeeman slower mechanism	14
2.2	Schematic representation of the MOT technique	17
2.3	In-tweezer cooling schemes	23
3.1	Airy disk profile	27
3.2	Working principle of an AOD to generate a tweezer pattern	30
3.3	Setup for the generation of optical tweezer arrays	31
3.4	Sketch of the light-assisted collision mechanism	36
3.5	Sketch of the reordering sequence of a 2D array	37
3.6	Two possible excitation schemes to Rydberg states.	40
3.7	Simulation of two-photon Rydberg Rabi oscillation	43
3.8	Optimization of two-photon Rydberg transition parameters	44
3.9	Sketch of the Rydberg blockade mechanism	45
4.1	Blue imaging scheme	52
4.2	Red imaging scheme	54
4.3	Fluorescence detection minimal setup	56
4.4	Simulated count histogram for binary thresholding	60
4.5	Amplification and detection with an image intensifier	63
4.6	Scattered photon map in a fast imaging sequence	66
4.7	Survival and fidelity for the fast imaging scheme simulation	68
4.8	Survival and recapture probability for TOF fluorescence imaging	70
4.9	Dressing the 3P_1 state for imaging	71
4.10	Optimization of repumpers beam for the dressed imaging scheme	73
4.11	Optimization of 688 nm beam for the dressed imaging scheme	74
4.12	Optimization of 689 nm beam for the dressed imaging scheme	75
5.1	Side view of the main optical table	78
5.2	Vacuum system mounted on a translation stage	79

5.3	3D render of the vacuum system	80
5.4	Atomic source CAD design	81
5.5	Optical setup for the atomic beam preparation	82
5.6	Vacuum lifetime and reordering time	87
5.7	Melted brazing of the viewport that caused the vacuum failure	89
5.8	Burnt getter material deposited inside the vacuum chamber	90
5.9	Residual Gas Analyserpartial pressure measurement	91
5.10	CAD design of the water-cooled coils	97
5.11	Simulation of the expected magnetic field profile	98
5.12	Linear dependence of the magnetic field on the driving current	99
5.13	Measured spatial magnetic field profile compared to the simulation	100
5.14	Measured anti-Helmholtz quadrupole field	101
5.15	Circuit for the fast switch-off of the coils	103
5.16	Sketch of the H-bridge circuit to control the high-field coils	104
5.17	CAD drawing of the compensaton coils assembly	106
5.18	Front view of the microscope objective	108
5.19	Optomechanic setup for the 461 nm laser	110
5.20	Optomechanic setup for the 689 nm laser	112
5.21	Frequency offset PDH lock	113
5.22	Frequency noise spectrum of the locked red laser	114
6.1	Sketch of the blue and red 3D MOT optics	120
6.2	Sketch of the blue and red 3D MOT optics on the upper lying breadboards	121
6.3	Example of absorption imaging fit of a blue MOT	124
6.4	TOF average cloud size measurement	125
6.5	2D MOT power and frequency optimization	126
6.6	3D MOT power and frequency optimization	127
6.7	RF signal modulation for multifrequency red MOT	128
6.8	Multifrequency laser beam spectrum	129
6.9	Current transient between blue and red MOT	131
6.10	Broadband red MOT loading time	132
6.11	Shielding effect on the blue MOT	133
6.12	Single-frequency red MOT temperature	134
6.13	SF red MOT peak density as a function of laser power and frequency .	135
6.14	Absorption image of the blue, red BB and red SF MOT	136
7.1	Tweezers setup used for the characterization	138
7.2	Array of 5x5 tweezers	139
7.3	Imaging setup used for the characterization and experimental sequence	142
7.4	Fluorescence imaging of multiple atoms in an array of optical tweezers, towards the detection of single atoms	143
7.5	Sisyphus cooling frequency optimization	144
7.6	LAC frequency optimization	145
7.7	Measured count histogram for single-atom fluorescence	146
7.8	Towards single atom averaged fluorescence	147

List of Tables

2.1	Summary of polarizabilities at $\lambda_L = 813.4$ nm, considering a linear polarization along \hat{x} , and zero magnetic field. Taken from Ref. [69].	20
3.1	Scaling of relevant Rydberg atoms properties.	38
3.2	Quantum defects for the 3S_1 and 3D_1 Rydberg series in Strontium. The values are taken from Ref. [103].	41
4.1	Initial parameters for the optimization of the scattering rate in the dressed-state imaging scheme.	72
4.2	Optimized parameters for the scattering rate in the dressed-state imaging scheme.	74
5.1	Optimized power, beam size and polarization for Zeeman slower and 2D MOT beams.	83
5.2	Common classification of vacuum regimes.	84
5.3	B field homogeneity for a separation of $500 \mu\text{m}$ from the field center.	97
5.4	B field amplitude and gradients comparing the simulations and measurements.	100
5.5	Main properties of the set of compensation coils.	105
5.6	Specifications of the high-NA microscope objectives.	107
6.1	Optimal parameters for the blue MOT	128

List of Abbreviations

MOT	M agneto O ptical T rap
AOD	A cousto O ptic D eflector
EMCCD	E lectron M ultiplying C harge C oupled D evice
qCMOS	q uantitative C omplementary M etal O xide S emiconductor
UHV	U ltra H igh V acuum
NA	N umerical A perture
PSF	P oint S pread F unction
LAC	L ight- A ssisted C ollisions
ROI	R egion- O f I nterest
IGBT	I nsulated- G ate B ipolar T ransistor

Physical Constants

Speed of Light	$c = 2.997\,924\,58 \times 10^8 \text{ m s}^{-1}$
Boltzmann constant	$k_{\text{B}} = 1.380\,649 \times 10^{-23} \text{ J K}^{-1}$
Planck constant	$h = 6.626\,070\,15 \times 10^{-34} \text{ J s}$
Reduced Planck constant	$\hbar = 1.054\,571\,817 \times 10^{-34} \text{ J s}$
Bohr magneton	$\mu_{\text{B}} = 9.274\,010\,065\,7(29) \times 10^{-24} \text{ J T}^{-1}$
^{88}Sr mass	$M = 1.459\,707\,05(13) \times 10^{-25} \text{ kg}$
Vacuum permittivity	$\epsilon_0 = 8.854\,187\,818\,8(14) \text{ F/m}$
Electron mass	$m_e = 9.109\,383\,713\,9(28) \times 10^{-31} \text{ kg}$
Proton mass	$m_p = 1.672\,621\,925\,95(52) \times 10^{-27} \text{ kg}$
Nuclear magneton	$\mu_{\text{N}} = 5.050\,783\,739\,3(16) \times 10^{-27} \text{ J T}^{-1}$
Bohr radius	$a_0 = 5.291\,772\,105\,44(82) \times 10^{-11} \text{ m}$

List of Symbols

t	time	s
k	wave number	m^{-1}
M	mass	kg
p	momentum	kg m s^{-1}
I	intensity	W/m^2 (kg/s^3)
B	magnetic field	T
F	force	N
E	energy	J
P	power	W
T	temperature	K
U	trap depth	J
w_0	tweezer waist	m
z_R	Rayleigh distance	m
f	lens focal length	m
R	interatomic distance	m
λ	wavelength	m
Γ	linewidth	rad/s
τ	lifetime	s
Δ	detuning	rad/s
ω	angular frequency	rad/s
α	polarizability	Fm^2
θ	angle	rad
Ω	Rabi frequency	rad/s

Chapter 1

Introduction

Single neutral atoms trapped in arrays of tightly focused optical dipole traps, called *optical tweezers*, have become a widespread technology to approach different research fields, ranging from quantum simulation and computation to quantum metrology. This thesis is the result of the work of my three-year PhD, carried out within the Strontium Rydberg Lab group at the University of Florence. I present here the realization of an experimental platform based on individually trapped strontium atoms that will be employed for quantum simulation experiments. In the first chapter, we present an historical overview of the quantum simulation, the experimental state-of-the-art and the main characteristics of strontium atoms. In Chapter 2, atom-light interaction, laser cooling and trapping are discussed, while in Chapter 3 we introduce two crucial elements of the platform, which are optical tweezers and excitations to Rydberg states. In Chapter 4 we present an overview of a few different techniques for imaging single atoms in optical tweezers. The experimental apparatus and laser systems are described in Chapter 5. Finally, the realization of a two-stage Magneto-Optical Trap (MOT) and single-atom trapping are reported in Chapters 6 and 7, respectively.

My primary contribution to the experimental setup construction, described in Chapter 5, involved the assembly of the vacuum system and its bakeout, the design of the optical setups for the main laser systems and the design and implementation of a pair of water-cooled coils. After setting-up the experiment, I contributed in realizing a two-stage Magneto-Optical Trap, whose details are reported in Chapter 6, and trapping the atoms in optical tweezers, to which Chapter 7 is dedicated. I also had the opportunity, during the three years, to spend four months in the SrMic group led by Prof. Florian Schreck at the University of Amsterdam, which is also developing an experimental platform based on strontium atoms in optical tweezers. During this period, I had the time to familiarize with a different experimental setup and environment, after which I focused on developing two alternative imaging schemes that could possibly reduce the time required for single-atom detection sequences.

These concepts developed with valuable support from the SrMic team members are presented in the second part of Chapter 4, which is focused on single-atom detection.

1.1 Quantum simulation

A quantum simulator is a controllable quantum system that is designed to model and study a Hamiltonian, or a class of Hamiltonians, describing complex physical systems, which are difficult to study in their original context, in a controlled experimental setup. These platforms allow for simulating many-body physics problems, which can be often very difficult to solve exactly and efficiently with classical computational methods, in a synthetic system. Difficulties arise in particular when systems composed of many interacting quantum objects are considered. In such scenario, an exact prediction of the evolution of the system based on microscopical properties is almost impossible. Since the dimensionality of the Hilbert space describing a many-body system scales exponentially as a function of the number of quantum objects, a simulation of the evolution of the system is out of reach for a classical computation. The problem can be tackled using a quantum simulator, where the Hamiltonian of the desired quantum system is mapped onto another quantum system characterized by a high degree of controllability of its parameters that mimics the behavior of the original. This concept, first proposed by R. Feynman [1], leverages one quantum system to simulate another. The power of this approach lies in the precise control over the experimental parameters of the simulator, enabling a detailed study of quantum phenomena that are otherwise not observable in real-world systems.

Over the past decades, several atom-based quantum simulation platforms have emerged [2, 3]. Among them, ultracold atoms in optical lattices [4, 5] and trapped ions [6, 7] have been particularly successful. Ultracold atoms, capable of reaching quantum degeneracy, have enabled the study of many-body systems governed by Bose-Einstein and Fermi-Dirac statistics. Milestone experiments with ultracold atoms in optical lattices include observing the superfluid-to-Mott-insulator transition [8], Anderson localization [9], and fermionic superfluid pairing [10]. However, the long experimental cycles and limited control over individual particles in traditional optical lattice experiments represent relevant limitations of the platform. In contrast, trapped ion platforms provide a higher control over individual particles and offer faster experimental cycles, making them ideal for quantum state manipulation and spin-model simulations [11, 12]. Anyway, scalability is a challenge in this platform due to the Coulomb interaction between ions, restricting the system to tens of particles. In recent years, neutral atoms in optical tweezers have emerged as a platform, offering the scalability of optical lattices and the individual control found in trapped ions. These optical tweezers, created by tightly focusing laser beams, can trap individual atoms in micron-size optical potentials. This system combines rapid experimental cycles and high quantum control with the scalability of neutral atom platforms, leveraging the exceptional versatility of tailored and controllable optical potentials [13, 14, 15]. Atom arrays assembled in defect-free configurations, with arbitrary geometries and zero configurational entropy, can be assembled using atom-sorting techniques. These arrays provide the flexibility to simulate a variety of quantum systems and single-atom imaging can be performed with high-fidelity. The optical tweezer technique, invented by Arthur Ashkin in the 1970s [16] for which he was awarded the Nobel prize in 2018,

was developed to optically trap neutral particles using the dipole force of the light. Initially, this technique was applied to trap many different objects besides atoms, including small dielectric spheres and biological particles such as viruses and living cells [17]. Optical tweezers were then employed to trap neutral atoms in the first implementation of an *optical dipole trap* [18]. In parallel, new laser cooling and manipulation techniques were being developed, leading to the groundbreaking results mentioned above. When the current technology found a hard limit in the poor individual atom addressability achievable with standard optical lattice techniques, experiments with optical tweezers were proposed again to obtain single atom addressability [19, 20, 21, 22]. In parallel, a new approach to optical lattice physics, combining the use of microscope objectives with tailored optical potentials in the so-called *quantum gas microscopes* techniques, also allowed for excellent single-atom addressability [23, 24, 25, 26, 27]. Although single atoms can be identified, the trapping potential is produced by optical lattices, which have a fixed geometry and are not easily reconfigurable in comparison to optical tweezer arrays. Many experiments were proposed to leverage the high degree of control provided by optical tweezers. Since the individual neutral atoms are isolated in the tweezer array, a long-range interaction (on a length scale of a few μm) is necessary to address many-body Hamiltonians. The use of strong, long range Rydberg interaction between highly excited atoms was proposed as a good candidate to implement quantum simulation and quantum computing protocols [28, 29], and was then successfully applied to single atoms in optical tweezers [30, 31, 32].

1.2 State-of-the-art tweezer array experiments

While the first experiments with optical tweezers were performed using few rubidium atoms [30, 31, 32], the technology quickly advanced to allow for quantum simulation with hundreds of single atoms [33, 34, 35, 36]. Experiments with caesium atoms were also successfully demonstrated [37], also setting the current record with the groundbreaking number of 6100 qubits [38]. On the other hand, alkaline-earth atoms were implemented in the platform more recently [39, 40, 41], and relevant results have already been shown, such as high fidelity and survival imaging schemes both with strontium and ytterbium [41, 42, 43, 40, 44]. Different schemes for high-fidelity qubits have been explored, encoding the qubit basis in nuclear spin states [42, 44] or in the ground and clock states [45, 46, 47]. Moreover, optical clocks in strontium tweezer arrays have been demonstrated [48, 49]. Finally, a benefit of using alkaline-earth atoms is that they can be optically trapped even when they are excited to Rydberg state due to the presence of a second valence electron [50], as opposed to alkali species, which only have one core electron.

1.3 General overview of the experiment

In this section we give a brief overview of the experimental setup, introducing the main components as detailed in Chapter 5. Then, we present some of the properties of strontium atoms, focusing on the bosonic isotope ^{88}Sr that we employ in our experiment.

1.3.1 Experimental apparatus

The experiment was constructed over a period of three years, starting with an almost empty laboratory where the laser sources were installed and the vacuum system was assembled. The vacuum system is composed by a commercial atomic source, a pumping chamber hosting the ultra-high-vacuum (UHV) pumps and glass cell where the experiment takes place. The whole apparatus is approximately only 1 m long (Sec. 5.2). It is mounted on a translation stage that allows us to remove it from the bulk part of the experiment where the glass cell is surrounded by an assembly of magnetic field coils of different sizes, consisting of a pair of water-cooled. A pair of water-cooled high-field coils are assembled together with three pairs of compensation coils that allow for a fine control of the magnetic field in the position of the atoms (Sec. 5.3). The high-field coils generate a high gradient which is required to trap the atoms in the Magneto-Optical Trap. All the optics for the MOT are mounted directly on the optical table, while the optical tweezers and detection optics are mounted on a large breadboard which is placed on top of the optical table (Sec. 5.6 and 6.1). Most of the laser sources and their respective setups are assembled on a dedicated optical table. The experimental cycle is controlled with the “Labscript suite”, an open source environment based on Python (Sec. 5.7).

1.3.2 Strontium atoms

Strontium is an alkaline-earth atom that has four different stable isotopes, three of them bosonic (^{88}Sr , ^{86}Sr , ^{84}Sr) and one fermionic (^{87}Sr). As for all of the alkaline-earth (like) atoms, the two valence electrons are in an s-orbital and the ground state, in which the two electrons’ spin are anti-parallel, is a 1S_0 state. Strontium atoms can be excited bringing one of these two electrons in an excited state, where the spins can remain anti-parallel or become parallel. The first kind of excited states are called “singlet” states, while the latter are called “triplet” states. The results presented in this thesis are obtained using bosonic ^{88}Sr strontium, whose relevant internal states structure and transitions are reported in Fig. 1.1.

The first excited singlet state (1P_1) is used to perform a first magneto-optical-trap (MOT) in which the atoms are trapped and cooled down to a few mK temperature (see Sec. 6.2). This transition can also be used for very fast imaging given the large linewidth $\Gamma = 2\pi \times 30$ MHz. The transitions towards triplet states, also called intercombination transitions, are a distinctive feature of alkaline-earth atoms. The additional complexity and richness of the atom’s internal structure, compared to one-electron alkali-like atoms, can be exploited as a useful tool. In particular, the 3P_J states are connected through narrow and ultra-narrow linewidth transitions to the ground state and are commonly used levels in the manipulation of this kind of atoms. The $^1S_0 \rightarrow ^3P_1$ transition ($2\pi \times 7.5$ kHz linewidth) can be used to perform a second MOT stage, producing a colder cloud of atoms, besides offering the possibility of in-trap cooling, as described in Sec. 2.4. The 3P_0 state is instead a long-lived metastable state that is commonly referred to as the clock state as it is employed in metrology experiments and optical atomic clocks being an extremely precise oscillator that can be used for frequency and time reference. Its long lifetime and stability is also appealing as an additional ground state to excite the atoms to upper-lying states or, together with the ground state itself, as a qubit basis in quantum computing field. The 3P_2

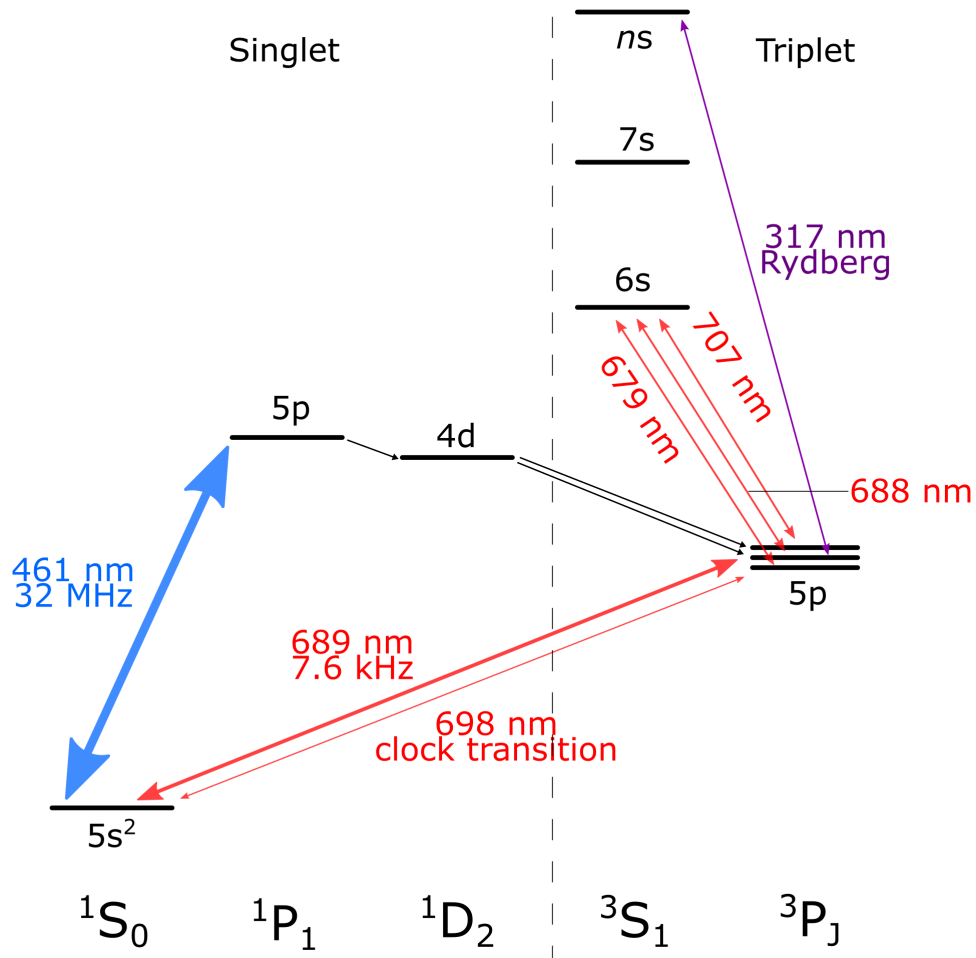


FIGURE 1.1: Simplified energy levels scheme for ^{88}Sr . All the energy levels relevant for this thesis are reported, separating the singlet and triplet states.

state is also a metastable state that can be used in excitation schemes. Unlike the 3P_0 state, the 3P_2 state has a nonzero magnetic moment that makes it sensitive to magnetic fields. For this reason, it is favorable to use the 3P_0 state for optical clock operations.

Relevant transitions

Here we report the main properties of some of the transitions relevant for ^{88}Sr , as these data are often used throughout the thesis.

Blue transition

$5s^2\ ^1S_0 \leftrightarrow 5s5p\ ^1P_1$, $\lambda = 460.9\ \text{nm}$, $\Gamma = 2\pi \times 30\ \text{MHz}$ ($\tau = 5.3\ \text{ns}$) [51].

This broad transition, which couples the ground state to the singlet $5s5p\ ^1P_1$ state, allows initial manipulation of the hot atomic beam. It is employed for slowing the flux of atoms, trapping them in the first stage of the MOT and imaging. The transition is not strictly closed, as the 1P_1 state has a weak decay channel into the $5s4d\ ^1D_2$

state, which then decays into the $5s5p\ ^3P_{1,2}$ states. As explained in Sec. 6.2, this is a limitation for the blue MOT.

Red transition

$5s^2\ ^1S_0 \leftrightarrow 5s5p\ ^3P_1$, $\lambda = 689.4\text{ nm}$, $\Gamma = 2\pi \times 7.5\text{ kHz}$ ($\tau = 21\ \mu\text{s}$) [52].

This is a narrow intercombination line connecting the ground state with the triplet $5s5p\ ^3P_1$ state. Given the narrow linewidth, compared to the blue transition, this transition does not scatter photons fast enough to trap a hot flux of atoms directly in a red MOT. However, it can be artificially broadened with proper techniques to increase the capture range of the MOT, and used for a second-stage MOT, which allows for a colder and denser cloud of atoms, as explained in Sections 2.1 and 6.3. This transition is also used for in-tweezer cooling (see Subs. 2.4.3), and it can be employed in imaging schemes (see Sec. 4.2).

Repumper transitions

$5s5p\ ^3P_0 \leftrightarrow 5s6s\ ^3S_1$, $\lambda = 679.1\text{ nm}$, $\Gamma = 2\pi \times 1.4\text{ MHz}$ ($\tau = 112\text{ ns}$) [52].

$5s5p\ ^3P_1 \leftrightarrow 5s6s\ ^3S_1$, $\lambda = 687.8\text{ nm}$, $\Gamma = 2\pi \times 4.3\text{ MHz}$ ($\tau = 37\text{ ns}$) [52].

$5s5p\ ^3P_2 \leftrightarrow 5s6s\ ^3S_1$, $\lambda = 707.0\text{ nm}$, $\Gamma = 2\pi \times 6.7\text{ MHz}$ ($\tau = 24\text{ ns}$) [52].

These dipole-allowed transitions connect the states in the 3P_J manifold to the $5s6s\ ^3S_1$ state. They are important to avoid dark states when the blue transition is used for MOT and imaging. The atoms decay via the weak channel and populate, in the end, the $^3P_{0,1}$ states. Atoms in the 3P_1 state decay back to the ground state in a few μs , but the 3P_0 population is in a dark state. To remove the atoms from this dark state, we can use a laser addressing the 679 nm, but the atoms pumped in the 3S_1 state will decay in all the 3P_J states. Therefore, a second repump laser at 707 nm is still necessary to remove the atoms from the 3P_2 metastable state. Similar schemes can be used to incoherently pump optically the atoms in one of the 3P_J states, switching on two lasers to remove the atoms from two of the three states.

Clock transition

$5s^2\ ^1S_0 \leftrightarrow 5s5p\ ^3P_0$, $\lambda = 698.4\text{ nm}$, $\Gamma \rightarrow 0$ ($\tau \rightarrow \infty$) (see Sec. 5.3).

The clock transition has exactly zero linewidth in the bosonic isotopes of strontium, all having nuclear spin $I = 0$, as it is doubly forbidden by selection rules. The mechanism for opening up the channel, using a strong magnetic field ($B \sim 1000\text{ G}$), to coherently populate the 3P_0 state is explained in Sec. 5.3. Under this condition, $\Gamma(B) \propto B^2$ and $\Omega(B) \propto B\sqrt{I}$, where $\Omega(B)$ is the Rabi frequency of the clock transition and I is the intensity of the driving laser beam. The clock state can be used as intermediate metastable state to excite the atoms to Rydberg states. In the fermionic isotope ^{87}Sr the nuclear spin is $I = 9/2$, which allows for natural hyperfine mixing of the electronic states. This mixing results in the clock transition exhibiting a small but nonzero linewidth.

Rydberg excitation lines

$5s5p\ ^3P_0 \leftrightarrow 5sns\ ^3S_1$, $\lambda \sim 317\text{ nm}$ (see Sec. 3.2).

$5s5p\ ^3P_1 \leftrightarrow 5sns\ ^3S_1$, $\lambda \sim 319\text{ nm}$ (see Sec. 3.2).

This transition is key for all the quantum simulation and computation applications that will be implemented with this platform. As explained in Sec. 3.2, the exact wavelength of the transition depends on the target Rydberg state, labeled by the principal quantum number n . In strontium, two schemes for the excitation are possible, either with a two-step transition using the clock state 3P_0 as metastable intermediate state, or with a two-photon transition leveraging the 3P_1 intermediate state, as detailed in Sec. 3.2.

Chapter 2

Atom-Light Interaction

In this chapter I will review the physical framework to understand atom-light interaction, the cooling and trapping processes, and the effects of temperature and external magnetic fields. This theoretical discussion focuses on modeling some of the fundamental processes and properties of the experimental sequence in terms of experimentally accessible quantities.

2.1 Fundamentals of atom-light interaction

The common concept behind all the laser cooling techniques, such as optical molasses, magneto-optical trapping and Zeeman slowing, is the momentum conservation in the atom-photon interaction during absorption and emission processes. Standard laser cooling techniques involve reducing the atom's kinetic energy through repeated cycles of photon absorption and re-emission. The kinetic energy of an atom of mass M is [53, 54]

$$E = \frac{\hbar^2 K^2}{2M}, \quad (2.1)$$

where $\hbar K$ is the particle's momentum. A photon, on the other hand, carries a momentum given by $p = \frac{h}{\lambda} = \hbar k$, where λ is the photon wavelength and $k \equiv \frac{2\pi}{\lambda}$ is defined as the wave number. Given the total momentum conservation of the atom-photon system, if the atom absorbs a photon exactly counter-propagating, the atom will decrease its momentum by $\hbar k$. After a time that is determined by the lifetime of the excited state of the atom, a photon with approximately the same energy and wave number, will be spontaneously emitted. The k-vector of the spontaneously emitted photon has a random direction, and averaging over many absorption-spontaneous emission cycles the momentum transferred by the emitted photon to the atom averages to zero. If the atom is illuminated with a laser beam opposed to its motion direction, it will

absorb and spontaneously emit photons for many cycles, the net effect being a reduction of the momentum in the motion direction. This process strongly depends on the properties of the atom and light.

We can define the scattering rate as the rate at which an atom interacts with photons. The scattering rate is defined by considering a two-level system in a near-resonant regime, neglecting all the other electronic levels:

$$R_{sc} = \frac{\Gamma}{2} \frac{s}{1 + s + 4\Delta^2/\Gamma^2} \quad (2.2)$$

where the laser beam is detuned by a quantity Δ from the atomic resonant frequency of the transition with linewidth Γ . The saturation parameter s of the transition is defined as $s \equiv I/I_{sat}$, I being the intensity of the laser beam and I_{sat} the saturation intensity of the transition

$$I_{sat} = \frac{2\pi^2\hbar\Gamma c}{3\lambda^3} \quad (2.3)$$

where c is the speed of light in vacuum. The scattering rate is crucial in all the cooling mechanisms described below: optical molasses, magneto optical trapping and Zeeman slowing. By properly engineering the spatial and temporal dependence of the scattering rate it's possible to cool down the atoms. By second Newton's Law

$$\mathbf{F} = \frac{d\mathbf{p}_{atom}(t)}{dt} = M \frac{d\mathbf{v}(t)}{dt} = \frac{d\mathbf{p}_{photons}(t)}{dt} \quad (2.4)$$

where the last equation assumes the momentum conservation. If the photon flux is constant, i.e. the laser beam in CW with constant power,

$$\frac{d\mathbf{p}_{photons}}{dt} = \frac{N}{\Delta t} \hbar\mathbf{k} = R_{sc}\hbar\mathbf{k}, \quad (2.5)$$

where N is the number of photons absorbed by the atom in a time interval Δt . Plugging this in the previous equation, the atom's momentum derivative becomes:

$$\frac{d\mathbf{p}_{atom}(t)}{dt} = R_{sc}\hbar\mathbf{k} \quad (2.6)$$

Finally, the differential equation describing the position of the atom $x(t)$ is the following, considering a one-dimensional motion for simplicity, where the laser beam is counterpropagating to the atom's motion:

$$\frac{d^2x(t)}{dt^2} = -\frac{1}{M} R_{sc}(x, t)\hbar k, \quad (2.7)$$

where the spatial and time dependence of the scattering rate is made explicit. The deceleration of the atom is proportional to the scattering rate, which has a maximum value of $R_{sc} = \Gamma/2$ for $\Delta = 0$ and $s \gg 1$. This physical hard limit shows why transitions with large Γ are used to cool down atoms with high initial velocity.

2.2 Laser cooling with Doppler and Zeeman effects

As mentioned before, Eq. 2.2 contains all the information required to understand the most common cooling techniques. A very complete description of these processes can be found in Ref. [55, 56]. Actually, the scattering rate depends on several physical constants such as Γ and tunable parameters such as the laser beam intensity, that appears in the definition of the saturation parameter s , and the detuning Δ . The latter in particular can be simply tuned by changing the frequency of the laser with respect to the electronic transition, resulting in a global change of the scattering rate. Another approach to actively modify Δ is to exploit the dependence of the effective detuning on the atom's velocity via the Doppler effect and on the magnetic field, in case of magnetically sensitive sublevels, via the Zeeman effect. These two effects can allow for tuning the scattering rate for different classes of atoms, hence performing a selective cooling. The Doppler effect appears when considering the moving frame of the atom, for which the laser light appears shifted in frequency depending on the atom velocity in the lab frame. Like in the Doppler effect that we experience daily for acoustic waves, the atom in a moving frame will perceive the peaks and valleys of the electromagnetic wave as compressed as it moves towards the light source, leading to a higher frequency. In contrast, as the atom moves away from the source, the wave peaks and valleys are stretched out, resulting in a lower frequency. This compression or stretching of the wave alters the spacing between successive peaks (or valleys), which the observer perceives as a shift in frequency. In terms of the resonant angular frequency ω_0 , the laser angular frequency ω_L , laser wave vector \mathbf{k}_L and atom velocity \mathbf{v} , the resonant angular frequency is [55]:

$$\omega' = \omega_L - \mathbf{k}_L \cdot \mathbf{v}. \quad (2.8)$$

If we express the detuning of the laser beam in the lab frame as

$$\Delta_l = \omega_L - \omega_0, \quad (2.9)$$

we can relate it to the detuning in the atom's frame:

$$\Delta_a = \omega' - \omega_0 = (\omega_L - \mathbf{k}_L \cdot \mathbf{v}) - \omega_0 = \Delta_l - \mathbf{k}_L \cdot \mathbf{v}. \quad (2.10)$$

As the atom perceives a detuning which is altered by the relative motion of the atom and photon, we have to replace Δ_a in Eq. 2.2 to get the effective scattering rate. This means that if the atom and the photons are counter-propagating, then $\mathbf{k}_L \cdot \mathbf{v} < 0$ and $\Delta_l < \Delta_a$. The resonant condition $\Delta_a = 0$ will occur when the detuning in the lab frame compensates exactly for the Doppler shift, that is $\Delta_l = \mathbf{k}_L \cdot \mathbf{v}$. If the atom is moving towards the source this term is negative and the laser has to be set to a frequency lower than resonance (red detuning), while if the atom is moving away from the source the laser will need to be at higher frequency to be seen as resonant. Note that this equation is in the nonrelativistic limit, which is valid in general in ultracold-atoms experiments as the fastest atoms will move at most at hundreds of meters per second.

The Zeeman effect can shift the atomic transition frequency via an interaction between an external magnetic field and the atom's magnetic moment. The interacting

Zeeman Hamiltonian for a magnetic field \mathbf{B} is

$$\hat{H}_Z = \frac{\mu_B}{\hbar} (g_S \hat{\mathbf{S}} + g_L \hat{\mathbf{L}} + g_I \hat{\mathbf{I}}) \cdot \mathbf{B}, \quad (2.11)$$

where $\hat{\mathbf{S}}$, $\hat{\mathbf{L}}$ and $\hat{\mathbf{I}}$ indicate the electron spin, electron orbital and nuclear spin angular momentum respectively, and g are the corresponding ‘‘g-factors’’¹. Considering a \mathbf{B} field along the z -axis, solving the dot product gives a scalar equation

$$\hat{H}_Z^{(z)} = \frac{\mu_B}{\hbar} (g_S \hat{S}_z + g_L \hat{L}_z + g_I \hat{I}_z) B_z = \frac{\mu_B}{\hbar} (g_J \hat{J}_z + g_I \hat{I}_z) B_z. \quad (2.12)$$

In the latter equivalence, the addition of angular momentum $J_z = L_z + S_z$ was taken into account in the application of the projection theorem, introducing the Landé factor g_J . In the case of bosonic strontium isotopes, the nuclear magnetic moment is zero, so we can drop the $g_I \hat{I}_z$ term and consider just the effect of J angular momentum. This assumption is not valid in ^{87}Sr , for which $I=9/2$, or in general for atoms with hyperfine structure. Assuming a small perturbation of the magnetic field to the atomic Hamiltonian, including the fine structure, the zero-field eigenstates $|J, m_J\rangle$ of the operators \hat{J}_z and $\hat{\mathbf{J}}^2$ are considered. The first-order perturbation theory corrections are obtained by calculating the expectation values of the Zeeman Hamiltonian in this basis, which means calculating the matrix elements of this form $\langle J, m_J | \hat{H}_Z^{(z)} | J, m_J \rangle$ [57]. Since in the chosen basis $\hat{J}_z |J, m_J\rangle = \hbar m_J |J, m_J\rangle$, the Zeeman Hamiltonian with $I=0$ is diagonal, and the corrections for each m_J state is

$$\Delta E_{m_J} = m_J g_J \mu_B B_z \quad (2.13)$$

where the Landé g-factor can be calculated via angular momentum algebra, considering $g_S = 2$ and $g_L = 1$:

$$g_J \approx 1 + \frac{J(J+1) + S(S+1) - L(L+1)}{2J(J+1)}. \quad (2.14)$$

The result above is obtained by defining the B-field direction as the quantization axis. The detuning of a transition between two states with m_J and m'_J in the presence of a magnetic field \mathbf{B} is

$$\Delta = \left(\frac{m'_J g'_J \mu_B B_z}{\hbar} - \frac{m_J g_J \mu_B B_z}{\hbar} \right) \quad (2.15)$$

The detuning introduced by the Doppler and Zeeman effects, whose values are given by from Eqs. 2.10 and 2.15, can be plugged into Eq. 2.2 to calculate the modified scattering rate. The result in Eq. 2.15 can be extended to the case of ^{87}Sr , which has a hyperfine structure and the contribution of the nuclear spin cannot be neglected. This case is not of interest to us, since all the results and calculations carried out in this thesis are focused on the bosonic ^{88}Sr . We refer the reader to Ref. [58] for a detailed discussion.

¹There are alternative definitions of the nuclear g-factor g_I , where the dependence on the nuclear magneton μ_N is explicit. Indeed, the nuclear magneton is smaller than the Bohr magneton by a factor $m_e/m_p \sim 5 \times 10^{-4}$, where m_e and m_p are the electron and proton masses.

2.3 Zeeman slower, 2D MOT and 3D MOT

In this section, we will discuss three types of cooling techniques used in the experiment, Zeeman slowing (ZS), transverse cooling (TC) and magneto-optical trapping (MOT). These techniques are based on tailoring and engineering the scattering rate experienced by the atoms, which allows us to cool a thermal atomic flux with an initial velocity of around 450 m/s, ultimately trapping the atoms in a MOT at a temperature of a few μK . As I will describe in Sec. 5.2, in our system the source of ^{88}Sr atoms is an oven that works at 420 $^\circ\text{C}$, which produces a flux of thermal atoms with average velocity around 450 m/s. The atoms are slowed down with the Zeeman slower technique and deflected in a modified TC section. Finally, the atoms are trapped in a 3D MOT that finalizes the cooling and confines the atoms. We can use the results from Sec. 2.2 to describe how the averaged force given by photon scattering leads to selective atom cooling. As we will see, the only difference between the three techniques is the spatial and temporal dependence of the detuning Δ , and therefore of the scattering rate.

2.3.1 Transverse cooling

The easiest case to study is the TC, which consists of a 2D version of optical molasses. There is no magnetic field involved, and the equations will only include the Doppler shifted values for laser detuning. A sketch of the TC configuration is shown in Fig. 2.1(a). We consider an atomic flux streaming towards positive y axis, while two orthogonal counter-propagating laser beams are oriented along the x axis. Typically, a root-mean-square (rms) angular divergence can be defined for an atomic beam. The purpose of TC is to reduce the angular divergence of the beam along one direction orthogonal to the average beam direction. We can consider an atom which is moving at an angle θ compared to the average direction of the atomic beam. In the atoms frame, the radiation pressure force in this configuration, considering the Eqs. 2.2, 2.7 and 2.10, becomes

$$F_x = \frac{\Gamma}{2} \hbar k_L \left[-\frac{s}{1 + s + 4 \frac{(\Delta_l + k_L v \sin(\theta))^2}{\Gamma^2}} + \frac{s}{1 + s + 4 \frac{(\Delta_l - k_L v \sin(\theta))^2}{\Gamma^2}} \right] \quad (2.16)$$

where k_L is the wave number of the laser, Γ is the transition linewidth, Δ_l is the laser detuning in the lab frame and s the saturation parameter. The angle θ is considered to be positive when the atom moves to the right with respect to the y axis in Fig. 2.1(a), and this gives the sign of the dot product on the denominator. The transverse cooling method affects only the velocity components orthogonal to the average beam propagation $v \sin(\theta)$. If $\theta > 0$, and the atom is moving to the right, then the term in the denominator is $k_L v \sin(\theta) > 0$. It is possible to select a negative detuning in the lab frame $\Delta_l < 0$ in such a way that the term in the first denominator $(\Delta_l + k_L v \sin(\theta))^2$ is zeroed, while in the equivalent term in the second denominator $(\Delta_l - k_L v \sin(\theta))^2 > 0$ as detuning and Doppler shift sum up. This imbalance makes the first term in the force expression larger than the second, favoring on average a force that pushes the atom from right to left and therefore bringing it back towards $\theta = 0$. With analogue reasoning, atoms with $\theta < 0$ will more likely scatter photons from the left beam. A

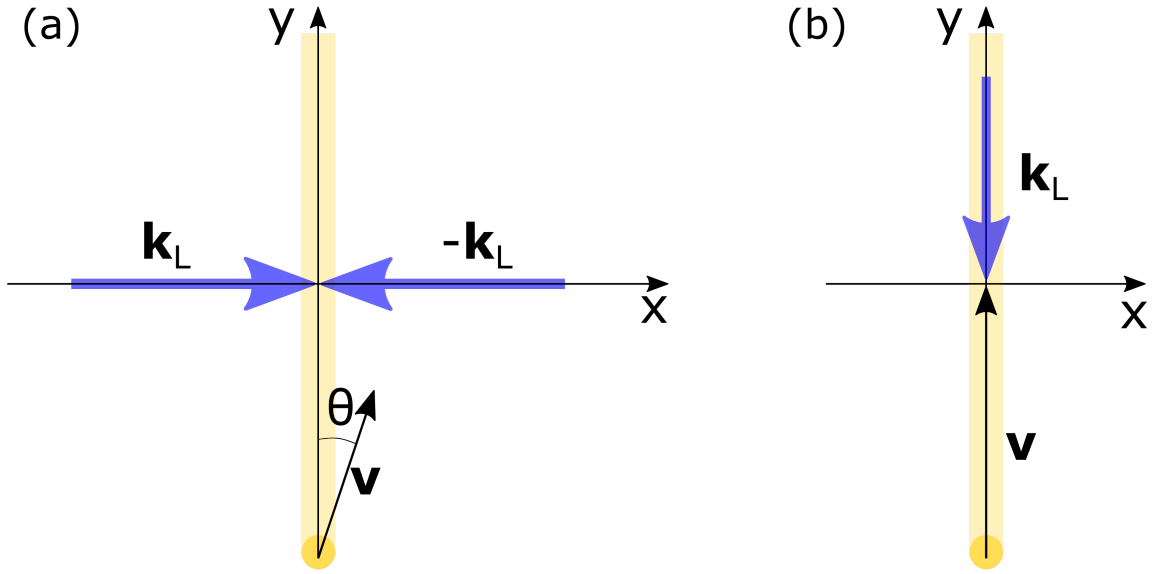


FIGURE 2.1: (a) Schematic representation of the transverse cooling mechanism. An atomic beam along the y axis is represented by the light yellow line, assuming a propagation towards positive y . Two light blue arrows represent the pair of counter-propagating laser beams used for transverse cooling. The velocity distribution includes atoms that travel at an angle θ with respect to the propagation axis, indicated by the dashed line. The goal of TC is to shrink the angular distribution around $\theta = 0$. (b) Sketch of the Zeeman Slower configuration, where the atoms are slowed down by scattering photons of a counterpropagating laser beam. The radiation pressure is selective for classes of velocities that become resonant with the radiation in different positions along the motion axis.

similar approach is used in our setup to deflect the mean trajectory of the atomic beam by an angle $\theta_d = 20^\circ$. This step of the atomic sample preparation is described in Sec. 5.2.1 as "2D MOT" and consists of two beams orthogonal to the motion of the atomic beam, retroreflected by in-vacuum optics. The beams are only partially reflected thus obtaining an imbalanced TC scheme, that allows for deflecting the average motion direction by a finite angle θ_d . We can adapt Eq. 2.16 using two different saturation parameters s to account for the power imbalance. Imposing $\theta = \theta_d = 20^\circ$, the force will have a maximum value when its derivative with respect to the velocity is 0, which occurs when $(\Delta_l + k_L v \sin(\theta))^2$ is zeroed. By changing the detuning Δ_l we can select a different central velocity v whose propagation direction will be deflected by θ_d . After optimizing the experimental parameters for our experiment, we set $\Delta_l = -2\pi \times 22$ MHz (see Tab. 6.1), which corresponds to an average velocity of $v = 29.6$ m/s. Atoms faster than this will be deflected by a smaller angle, while slower atoms will be deflected more.

2.3.2 Zeeman slower

The second cooling technique, experimentally demonstrated for the first time in Ref. [59], is the Zeeman slower. This is widely used in most of the ultracold atoms experiments and combines the Doppler and Zeeman effects to slow, and therefore "cool" an atomic beam from hundreds of m/s initial velocity down to a few tens of m/s². The reference frame is reported in Fig. 2.1(b) the atomic beam propagates along the y axis towards positive values, while a counter-propagating laser beam points towards negative values. Combining Eqs. 2.2, 2.7, 2.10 and 2.15, the radiation pressure force becomes

$$F_y = -\frac{\Gamma}{2} \hbar k_L \frac{s}{1 + s + 4 \left(\Delta_L + \left(\frac{m'_J g'_J \mu_B B_y}{\hbar} - \frac{m_J g_J \mu_B B_y}{\hbar} \right) + k_L v \right)^2 / \Gamma^2}, \quad (2.17)$$

where this time the magnetic field is considered to be oriented along the y axis and the laser beam and atoms are exactly counter propagating ($-\mathbf{k}_L \cdot \mathbf{v} = k_L v$). The saturation parameter s is considered to be constant as the laser beam intensity will not vary much along the propagation axis if the beam is well collimated. In a real Zeeman slower design the magnetic field is varied along the y axis, to compensate for the reduction of Doppler shift as the velocity of the atoms reduces. A common choice is to impose a constant deceleration along the flight path, meaning that the scattering rate has to be constant, i.e. the detuning in the atom frame is constant:

$$\Delta_a = \Delta_l + B_y(y) \left(\frac{m'_J g'_J \mu_B}{\hbar} - \frac{m_J g_J \mu_B}{\hbar} \right) + k_L v(y) = \text{const} \quad (2.18)$$

We already know that the highest scattering rate is for zero detuning, so we can impose that the detuning in the atom frame is zero. By imposing $\text{const} = 0$, the equation above can be rewritten as

$$-\Delta_l = B_y(y) \left(\frac{m'_J g'_J \mu_B}{\hbar} - \frac{m_J g_J \mu_B}{\hbar} \right) + k_L v(y). \quad (2.19)$$

The kinematic motion equation of an object with constant acceleration a gives a velocity $v(y)$ that varies spatially like this

$$v(y) = \sqrt{v_0^2 + 2ay} \quad (2.20)$$

Where v_0 is the initial velocity. Substituting $v(y)$ into Eq. 2.19 and solving for $B_y(y)$ gives us the spatial profile of the magnetic field that satisfies the constant scattering rate condition:

$$B_y(y) = -\frac{\Delta_l}{\xi_y} - \frac{k_L}{\xi_y} \sqrt{v_0^2 + 2ay} \quad (2.21)$$

where the constants are collected into $\xi_y \equiv \left(\frac{m'_J g'_J \mu_B}{\hbar} - \frac{m_J g_J \mu_B}{\hbar} \right)$. Recalling Eq. 2.7, the maximum deceleration achievable for a transition with linewidth Γ is $a_{max} = -\frac{\Gamma \hbar k}{2M}$,

²The Zeeman Slower allows for an effective reduction of the average kinetic energy per atom. The velocity distribution after this stage, although it is not a thermal distribution can be associated with an ensemble temperature.

which suggests that it's convenient to use broad atomic transitions for this technique. Eq. 2.21 can be used to design a real Zeeman slower, which is typically realized with an electromagnet consisting of a series of concentric coils with increasing number of windings along the slower axis. The deceleration and initial and final velocities set the extension of the coils along the y axis, which is typically a few tens of cm long. For example, a_{max} for the blue transition with $\Gamma = 2\pi \times 30$ MHz (see Subs. 1.3.2) is roughly 10^6 m/s², which requires an extension of $L=10$ cm to slow down the atoms from an initial velocity of 450 m/s to 0 m/s. The commercial atomic source that we employ in the experiment (see Sec. 5.2 for a full description) exploits a set of permanent magnets just ~ 5 cm long to generate the Zeeman slower magnetic field. This is a compromise solution and the exact magnetic field profile is unknown, as the atomic source that we employ is patented. The maximum velocity class that can be slowed down to a few tens of m/s in a Zeeman slower where the interaction region is 5 cm long is roughly 320 m/s, even considering the maximum deceleration which is achieved with $s \gg 1$. This means that the design of the commercial source is a compromise between compactness and slowing efficiency. Moreover, the assumption of constant saturation parameter s falls as the company recommends using a slightly focused Zeeman slower laser beam for optimal results, as explained in Sec. 5.2.1. As we can see in Eq. 2.17, this is also varying the radiation pressure force, making it stronger where the intensity is higher, i.e. where the laser beam is more focused.

2.3.3 Magneto-Optical Trap

The last cooling technique to describe is the MOT, experimentally demonstrated in Ref. [60] for the first time. This technique also relies on a combination of Zeeman and Doppler shift to have a radiation pressure force that on average not only cools the atoms, but also confines them. Typically a 3D MOT configuration is employed, with three pairs of counter-propagating beams along orthogonal axes to provide cooling in all the three directions. We could use this configuration of laser beams, with red detuned frequency to compensate for the Doppler shift, to cool down the atoms in a 3D optical molasses, similarly to the TC scheme described above. The addition of a quadrupole magnetic field centered in the crossing of the three pairs of beams can also provide trapping of the atoms. The motion of the atoms can be decomposed along the cartesian axes solving each scalar equation independently. The quadrupole field in the anti-Helmholtz configuration commonly defines the field of two identical round coaxial coils in which the current flows in opposite direction. This takes the form:

$$\mathbf{B} = b[x, y, -2z] \quad (2.22)$$

where b is the gradient, and the component along the coils axis z has opposite sign and twice the magnitude due to Maxwell's law $\nabla \cdot \mathbf{B} = 0$. Apart from the differences in sign and amplitude, the three axes can be studied independently in the same way. Referring to Fig. 2.2 we consider the z -axis radiation pressure force, which has two contributions from the two counter-propagating beams. The equation of the force in

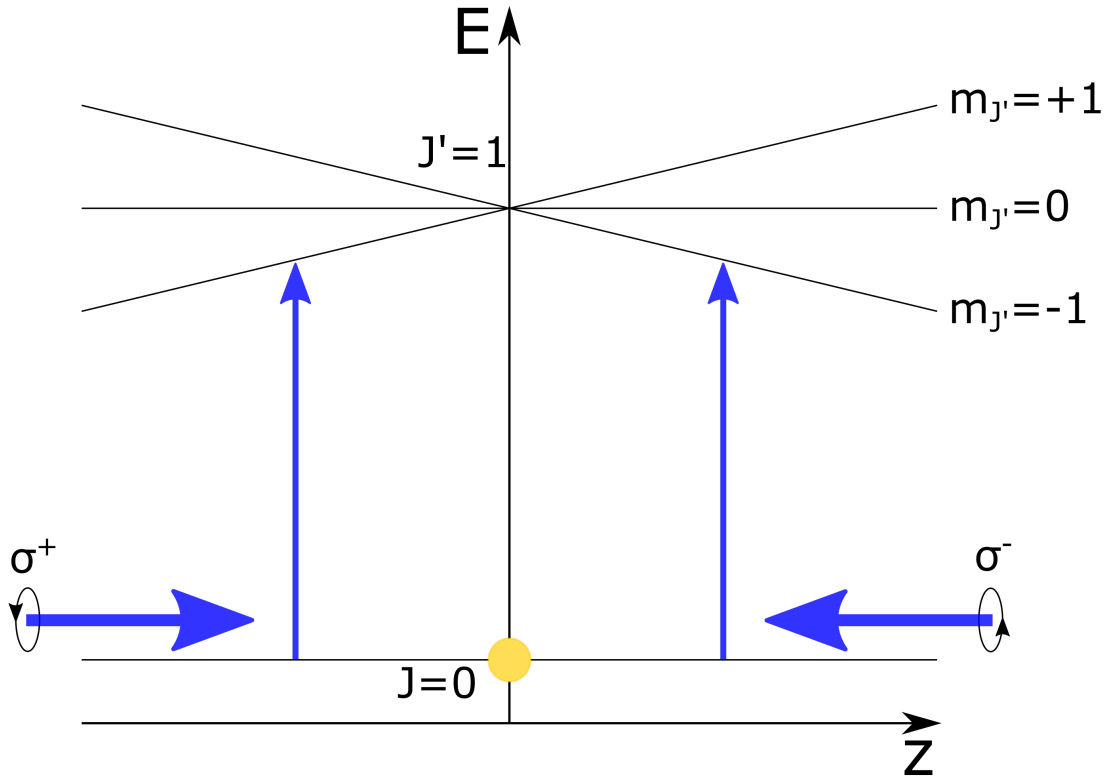


FIGURE 2.2: Schematic representation of the MOT cooling and trapping technique. An atom moving along the z axis, represented as the yellow circle, is shined by two counter-propagating beams. In both the MOT stages in our experiment the lower lying state is the ground state with $J=0$, while the upper state has $J'=1$. The Zeeman shift splits linearly the three m_J substates. By using a red detuned laser light the scattering rate becomes spatially-dependent, producing a restoring force towards the center of the quadrupole field.

this case takes the form

$$F_z(t) = \frac{\Gamma}{2} \hbar k_L \left[\frac{s}{1 + s + 4 \left(\Delta_l + \left(\frac{m'_J g'_J \mu_B}{\hbar} - \frac{m_J g_J \mu_B}{\hbar} \right) bz + k_L v \right)^2 / \Gamma^2} + \frac{s}{1 + s + 4 \left(\Delta_l - \left(\frac{m'_J g'_J \mu_B}{\hbar} - \frac{m_J g_J \mu_B}{\hbar} \right) bz - k_L v \right)^2 / \Gamma^2} \right] \quad (2.23)$$

and it can be approximated under the assumptions of small velocities ($k_L v \ll \Gamma$) and small displacements ($g_{J'} M_{J'} \mu_B bz / \hbar \ll \Gamma$). The first term of the series expansion is [61]:

$$F_z(v, z) = 8 \hbar k_L \frac{I}{I_s} \frac{\delta_L / \Gamma}{[1 + 2NI/I_s + 4\delta_L^2/\Gamma^2]^2} \left(k_L v + \frac{g_{J'} M_{J'} \mu_B bz}{\hbar} \right) \quad (2.24)$$

$$= -\alpha v - \kappa z$$

where in the last equivalence the constant values were collected in the factors α and κ defined as

$$\alpha = -8\hbar k_L^2 \left(\frac{I}{I_s} \right) \frac{\delta_L/\Gamma}{[1 + (2\delta_L/\Gamma)^2]}, \kappa = \alpha \frac{g_{J'} M_{J'} \mu_B b}{\hbar k_L}. \quad (2.25)$$

Eq. 2.24 describes a damped oscillator, whose motion equation is the following:

$$\frac{d^2 z}{dt^2} + \gamma \frac{dz}{dt} + \omega_{\text{trap}}^2 z = 0 \quad (2.26)$$

where $\gamma = \alpha/M$ and $\omega_{\text{trap}} = \sqrt{\kappa/M}$, with M being the mass of the atom. The 3D MOT parameters can be tuned to maximize different quantities, like the atom number, the density, the capture velocity range or the damped harmonic oscillator parameters. The atom, via a continuous absorption and re-emission of photons, is actually undergoing a random walk that limits its minimum kinetic energy and, therefore, the minimum energy that the atom can have. The minimum temperature that an ensemble of atoms can get with this physical process is known as the Doppler temperature [55]:

$$k_B T_D = \frac{\hbar \Gamma}{4} \frac{1 + \left(\frac{2\Delta}{\Gamma} \right)^2}{\frac{2|\Delta|}{\Gamma}} \quad (2.27)$$

$$T_D^{\text{min}} = \frac{\hbar \Gamma}{2k_B}$$

where Γ is the transition linewidth, inverse of the atomic level's lifetime τ , Δ is the detuning with respect to the transition, \hbar is the reduced Planck's constant and k_B is the Boltzmann's constant. The Doppler temperature is lower bounded by the linewidth of the transition: the blue transition with $\Gamma = 2\pi \times 30$ MHz has a Doppler temperature of $T_D^{\text{min}} \simeq 720$ μK , while the red transition with $\Gamma = 2\pi \times 7.5$ kHz has a Doppler temperature of $T_D^{\text{min}} \simeq 180$ nK. While the broad blue transition allows for an efficient capture of atoms with a few m/s velocity, the achievable temperature is too high to load the atoms in optical tweezers. Therefore, a narrow linewidth transition, which would scatter photons too slowly to cool down the atoms coming from the Zeeman slower and 2D MOT (see Sec. 5.2), can be used as a second MOT stage to cool the atoms down to ~ 1 μK temperature, as detailed in Sec. 6.3.

2.4 Off-resonant atom-light interaction, optical trapping and cooling

In this section we will address some fundamental concepts of atom-light interaction in a far off-resonant regime, opposed to the near-resonant one discussed in the previous section. This paves the way for the description of the *optical tweezers* trapping potential and of some important parameters that are involved. The potential generated by the interaction of an atom with an oscillating light field in a far off-resonant regime is commonly referred to as optical dipole potential, light shift, or AC Stark shift [62, 63, 64]. Optical trapping of sodium atoms with a single strongly focused Gaussian laser beam tuned several hundred GHz below the D_1 resonance transition was demonstrated for the first time in Ref. [65]. The potential describing an optical

dipole trap generated by a focused laser beam can be calculated using the expression [66]

$$U(r, z) = -\frac{1}{2\epsilon_0 c} I(r, z) \alpha(\lambda_L), \quad (2.28)$$

where ϵ_0 is the vacuum permittivity, c is the speed of light, $I(r, z)$ is the intensity of the Gaussian beam at variable distance r from the beam axis and z along the propagation axis, and $\alpha(\lambda_L)$ is the polarizability of the atomic state at the trapping wavelength λ_L . The Gaussian laser beam spatial dependence has the form

$$I(r, z) = \frac{2P_L}{\pi w^2(z)} e^{-2r^2/w^2(z)} \quad (2.29)$$

where P_L and $w(z)$ indicate the power and $1/e^2$ radius of the trapping beam. Substituting Eq. 2.29 in Eq. 2.28 we obtain

$$U(r, z) = -\frac{P_L}{\epsilon_0 c \pi w^2(z)} \alpha(\lambda_L) e^{-2r^2/w^2(z)}. \quad (2.30)$$

The beam size $w(z)$ along the propagation axis has its minimum value w_0 in $z=0$, referred to as the beam waist, and then it increases on a lengthscale defined as Rayleigh length z_R :

$$w(z) = w_0 \sqrt{1 + \left(\frac{z}{z_R}\right)^2}, \quad z_R = \frac{\pi w_0^2}{\lambda_L}. \quad (2.31)$$

2.4.1 Atomic polarizability

The optical dipole trap can both confine or repel an atom, depending on the atom internal state energy levels and the corresponding sign of the polarizability. In general, it produces an energy *light shift* that is maximum in absolute value where the intensity of the beam is maximum. If the shift decreases the energy of the state, the atom will feel a confining potential, whereas if the shift increases the energy, the atom will be anti-trapped. Calculating the polarizability $\alpha(\lambda_L)$ of an atomic level for an off-resonant laser beam at wavelength λ_L can be fairly complicated, as in many relevant cases the two-level system approximation is not valid. When the trapping light at λ_L is far off-detuned from all the optical transitions from the target level, the contribution of each of them has to be taken into account. Eq. 2.32 can be used to calculate the polarizability of an electronic state i as a function of the angular frequency of the laser $\omega_L = 2\pi c/\lambda_L$:

$$\alpha_i(\omega_L) = 6\pi\epsilon_0 c^3 \sum_k \frac{A_{ik}}{\omega_{ik}^2 (\omega_{ik}^2 - \omega_L^2)} \quad (2.32)$$

where A_{ik} indicates the reduced dipole matrix elements from the target state i to all the involved states k and ω_{ik} is the transition frequency between the levels. The derivation of Eq. 2.32 can be found in Ref. [67]. In general, all the fine structure and, if present, hyperfine structure energy levels, will have polarization-dependent polarizabilities. Magnetic fields can also play a role, as they can affect the energy of the states with nonzero magnetic moments. A detailed analysis and calculation of atomic polarizabilities can be found in Refs. [68, 69, 70]. In particular, Ref. [70]

TABLE 2.1: Summary of polarizabilities at $\lambda_L = 813.4$ nm, considering a linear polarization along \hat{x} , and zero magnetic field. Taken from Ref. [69].

State	$ m_j^x $	Polarizability [au]
$5s^2 \ ^1S_0$	0	286
$5s5p \ ^3P_0$	0	286
$5s5p \ ^3P_1$	0	195.1
	1	353.9
$5s5p \ ^3P_2$	0	464.3
	1	391.6
	2	173.8
$5s4d \ ^1D_2$	0	256.8
	1	522.2
	2	1318
$5s5p \ ^1P_1$	0	708.4
	1	737.8
$5s6s \ ^3S_1$	0	-494.1
	1	-481.9

focuses on a method to calculate polarizabilities including fine and hyperfine structure and Zeeman effect for Strontium atoms. Note that quite often the polarizability values are reported in atomic units (au). These units can be converted to SI units (Fm^2) via the conversion factor $4\pi\epsilon_0 a_0^3$, where a_0 is the Bohr radius.

A fundamental concept regarding atomic state polarizability is the so-called *magic trapping* condition, which consists in finding a wavelength λ_{magic} for which the polarizability of two electronic levels is the same. In general, the wavelengths are non-magic because the two levels will couple to different set of states, but it's possible to calculate and experimentally implement optical dipole traps for which the magic condition is fulfilled. The consequence of using a magic trap is that the light shift will be the same on both energy levels, independently on the laser intensity, making the transition between those two levels unshifted by the trapping light. This is not the case in any non-magic trap, for which the differential light shift between the two levels depends on the laser power. Power and pointing stability fluctuations can be a source of decoherence when driving a transition between the two levels, a reason why magic traps are commonly used in precise measurement systems such as optical atomic clocks addressing narrow clock transitions.

Strontium has a magic wavelength for the clock transition at $\lambda_{\text{magic}} = 813.4$ nm. Among the magic wavelengths that enable the excitation of the 1S_0 to the 3P_0 state with no light shift, this is the most convenient choice as it is in the IR range and Ti:Sapph lasers providing several W of optical power are available.

Polarizability values for some relevant atomic levels at $\lambda_L = 813.4$ nm calculated in Ref. [69] are reported in Tab. 2.1.

2.4.2 Harmonic oscillator approximation

Two important quantities in experiments with optical dipole traps, and more specifically with optical tweezers, are the trap depth and the trap frequency. The trap depth is defined as the maximum value of the dipole potential in Eq. 2.30, which occurs at $r = 0$ and $z = 0$:

$$U_0 = \frac{P_L}{\epsilon_0 c \pi w_0^2} \alpha(\lambda_L), \quad (2.33)$$

which is often reported in frequency units or temperature units dividing it by h or k_B , respectively. Substituting typical values for ground-state atoms in our optical tweezers traps at 813.4 nm, $P_L = 5$ mW, $w_0 = 1$ μm and $\alpha(\lambda_L) = 286$ au from Tab. 2.1:

$$U_0(^1S_0)/h = 4.3 \text{ MHz}, \quad U_0(^1S_0)/k_B = 205 \text{ } \mu\text{K}. \quad (2.34)$$

The trap depth gives an upper bound to the energy (or temperature) of the atoms that can be trapped in the dipole microtrap. We will consider a regime in which the trap depth is much larger (typically a couple of orders of magnitude) than the atoms temperature. Under this assumption, the Gaussian intensity profile can be expanded for small displacements around the trap center to calculate the trap frequencies in the radial and axial directions. A Taylor expansion to the second order of the radial coordinate r dependence of the exponential in Eq. 2.30 for $z=0$ gives

$$e^{-2r^2/w_0^2} \approx 1 - \frac{2r^2}{w_0^2} \quad (2.35)$$

which leads to a small-oscillation approximation of the dipole potential:

$$U_{HO}(r, 0) = -\frac{P_L}{\epsilon_0 c \pi w_0^2} \alpha(\lambda_L) \left(1 - \frac{2r^2}{w_0^2}\right) = U_0 + \frac{2P_L \alpha(\lambda_L) r^2}{\epsilon_0 c \pi w_0^4} \quad (2.36)$$

where the subscript HO indicates the harmonic oscillator approximation and the expression of the trap depth U_0 was used in the second equality. In this approximation the dipole potential assumes the form of a constant, the trap depth, plus a term quadratic in the radial coordinate r . A harmonic oscillator frequency can be defined by imposing:

$$\frac{1}{2} M \omega_{HO,r}^2 r^2 = \frac{2P_L \alpha(\lambda_L) r^2}{\epsilon_0 c \pi w_0^4} \quad (2.37)$$

where M is again the mass of the atom. Resolving for the radial trap frequency $\omega_{HO,r}$ we obtain:

$$\omega_{HO,r} = \sqrt{\frac{4P_L \alpha(\lambda_L)}{M \epsilon_0 c \pi w_0^4}}. \quad (2.38)$$

To get the axial trap frequency, we expand $U(r, z)|_{r=0}$ in Taylor series up to the second order in z :

$$\begin{aligned} U(r, z)|_{r=0} &= -\frac{P_L}{\epsilon_0 c \pi w_0^2 (1 + (z/z_R)^2)} \alpha(\lambda_L) \approx \\ &\approx -\frac{P_L}{\epsilon_0 c \pi w_0^2} \alpha(\lambda_L) \left(1 - (z/z_R)^2\right) = U_0 + \frac{P_L \alpha(\lambda_L)}{\epsilon_0 c \pi w_0^2 z_R^2} z^2. \end{aligned} \quad (2.39)$$

Also in this case we have a constant term given by the trap depth plus a term quadratic in the axial coordinate z . By imposing the equivalence of this term with a harmonic oscillator term along z , like in Eq. 2.37, we get

$$\frac{1}{2}M\omega_{HO,z}^2 z^2 = \frac{P_L \alpha(\lambda_L)}{\epsilon_0 c \pi w_0^2 z_R^2} z^2 \quad (2.40)$$

and solving for the angular frequency $\omega_{HO,z}$:

$$\omega_{HO,z} = \sqrt{\frac{2P_L \alpha(\lambda_L)}{M \epsilon_0 c \pi w_0^2 z_R^2}}. \quad (2.41)$$

Typical values for the trapping frequencies of an atom in the ground state can be calculated using the polarizability of the 1S_0 state from Tab. 2.1, $P_L = 5$ mW, the mass of ^{88}Sr atom M , $w_0 = 1$ μm and $z_R = 3.9$ μm calculated from Eq. 2.31:

$$\omega_{HO,r} = 2\pi \times 44.1 \text{ kHz}, \quad \omega_{HO,z} = 2\pi \times 8.1 \text{ kHz}. \quad (2.42)$$

It is important to note that both the trap depth and trap frequencies depend on the power and waist of the optical tweezer. The trap depth is directly proportional to the laser power, $U_0 \propto P_L$, and inversely proportional to the square of the waist, $U_0 \propto w_0^{-2}$. Similarly, the trap frequencies are proportional to the square root of the laser power, $\omega_{HO,r}, \omega_{HO,z} \propto \sqrt{P_L}$, and also inversely proportional to the square of the waist, $\omega_{HO,r}, \omega_{HO,z} \propto w_0^{-2}$ (for the axial trap depth, the Rayleigh distance z_R can be substituted in Eq. 2.41 to make this dependence clear). By using a micrometer-sized optical dipole trap, it's possible to achieve deep trap depths with only a few mW of power per tweezer, which is crucial for scaling the system to include hundreds of identical optical tweezers. Additionally, generating trap frequencies in the tens of kHz allows the vibrational states within the trap to be resolved in the excitation of the atoms on narrow transitions such as $^1S_0 \rightarrow ^3P_1$. This technique can be used, for example, to perform sideband-resolved cooling within the trap.

2.4.3 Atom cooling in tweezers

We conclude this section by describing two techniques to cool strontium atoms in a tweezer using the narrow red $^1S_0 \rightarrow ^3P_1$ transition. Cooling the atom to the motional in-trap ground state is fundamental for reducing the uncertainty on the atom's position, which is fundamental for the Rydberg interaction, as well as helping in keeping the atom trapped during some of the fluorescence imaging protocols, which heat up the atom via photon scattering.

The first cooling method, known as *sideband cooling*, has been demonstrated for a variety of ultracold atoms platforms, including optical tweezers [71, 72, 73, 74, 75]. It can be performed in a magic trap, in which the ground U_g and excited U_e state potentials are equal, as shown in Fig. 2.3(a). In the harmonic-oscillator approximation, which is valid in the limit of low temperatures, the motion of the atom is quantized, and the motional energy states, also called vibrational levels, are equally spaced. The ground and excited vibrational states are separated by $\hbar\omega_{HO,g}$ and $\hbar\omega_{HO,e}$, respectively. If the laser addressing the $g \rightarrow e$ transition is detuned by $\Delta = -\omega_{HO,g}$, the

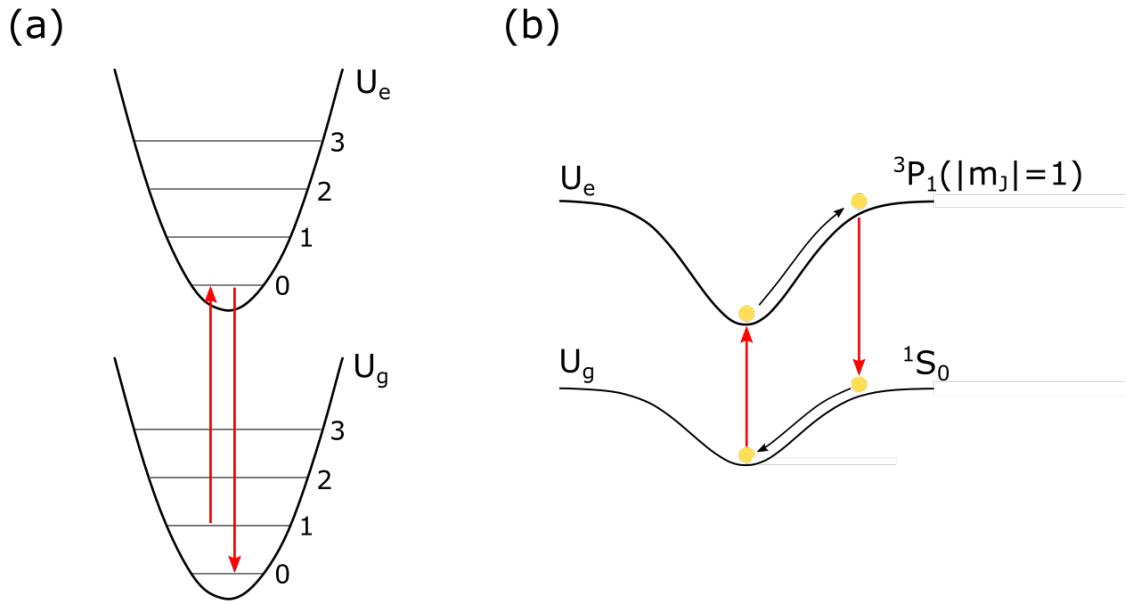


FIGURE 2.3: (a) Sketch of the resolved-sideband cooling process, with the dipole potential in deep optical tweezers for the ground (U_g) and excited (U_e) states in magic trapping condition in harmonic-oscillator approximation. The first vibrational levels are reported for both the potentials, separated in energy by the trap frequency $\omega_g = \omega_e$. A red-sideband selective excitation, together with a spontaneous emission to the ground state, produces on average a reduction of the occupied vibrational state, and therefore of the energy of the atom. (b) Sketch of the Sisyphus cooling process for a non-magic dipole trap. The difference in trap depth implies a position-dependent resonant frequency, which can be used in a cycle of absorption+spontaneous emission to decrease the atom's kinetic energy in the trap.

atom can be excited from the state $|g, n\rangle$ to the state $|e, n-1\rangle$, where the second label in the ket indicates the vibrational state. When the trap frequency is large enough compared to the spontaneous decay linewidth ($\omega_{HO,g} \gg \Gamma$), red sideband excitation becomes possible, and the atom will most likely decay back to the ground state potential, ending up in the $|g, n-1\rangle$ state. As a result, an absorption and spontaneous emission cycle produces, on average, a net reduction of one vibrational quantum.

However, the process takes place in the Lamb-Dicke regime, where the root-mean-square displacement of the atom in the harmonic potential is much smaller than the wavelength of the cooling laser, which can be expressed in terms of a Lamb-Dicke parameter:

$$\eta = k \sqrt{\frac{\hbar}{2M\omega_{HO,g}}}, \quad (2.43)$$

where k is the cooling light wave number, and the Lamb-Dicke regime stands when $\eta \ll 1$. In this regime, the probability of changing the vibrational state during a transition is strongly suppressed. Even though the excitation probability is reduced, $\eta \ll 1$ is favorable for not heating the atoms due to photon recoil energy. This also affects red sideband excitations, making them less likely, though still possible with

a small probability. While most absorption and emission cycles will not change the vibrational state, averaging over many cycles leads to a gradual reduction of the vibrational level. Only a few of these cycles will reduce n , but over time, this mechanism can effectively cool the atom by driving it towards lower vibrational states. Considering the trap frequencies typical for our tweezers, reported in Eq. 2.42, the Lamb-Dicke parameter is $\eta \sim 0.3$ for the radial directions and $\eta \sim 0.8$ for the axial direction. We are in a moderate Lamb-Dicke regime where the transitions that change vibrational states are suppressed but not zero, enabling the sideband cooling mechanism.

The second cooling method, reported in a sketch in Fig. 2.3(b), is the so-called *Sisyphus cooling*, which was demonstrated for strontium atoms in optical tweezers [39, 76, 77] and optical lattices [78, 79]. This method can be applied to non-magic optical tweezers, and works in both scenarios where the excited state is either more tightly trapped than the ground state ($U_e > U_g$) or less tightly trapped ($U_e < U_g$). In the first case, we have *attractive* Sisyphus cooling, while in the second case, we have *repulsive* Sisyphus cooling. From Tab. 2.1, the polarizability of the $^3P_1(m_J = 0)$ state is smaller than that of the ground state, whereas the polarizability of the $^3P_1(|m_J| = 1)$ states is larger, allowing both cases to be addressed. Let's consider the latter case, for which we have attractive Sisyphus cooling. The situation depicted in Fig. 2.3(b) is now a semi-classical representation of the atom motion as the atom oscillates around the trap center. If the cooling laser beam is tuned to match the resonance condition at the bottom of the trap, then the atom will start oscillating in the upper trap at frequency ω_e climbing the potential hills. On a timescale set by the excited-state lifetime, the atom will eventually decay back to the ground state, emitting a photon that matches the energy gap in a position that most likely will be different from the center of the trap. Since the energy of the spontaneously emitted photon is larger than the energy of the absorbed one, due to the larger confinement of the excited state, in a full cycle the atom loses kinetic energy and is therefore cooled down. A similar mechanism can work for repulsive Sisyphus cooling, where the resonant energy gap is smaller when the atom is excited far away from the trap bottom. In this case the atom climbs the energy potential hill when it oscillates in the ground state potential, and loses energy in the photon exchange cycle. Whereas attractive Sisyphus cooling in optical tweezers with strontium was first demonstrated a few years ago [39], the repulsive Sisyphus cooling was achieved only recently in Ref. [77]. Remarkably, non-magic trapping results in non-orthogonal harmonic oscillator levels of $|e\rangle$ and $|g\rangle$ in both the radial and axial directions, enabling a single cooling beam to remove energy from all directions [76, 80].

In our experiment the 813.4 nm optical tweezers produce a non-magic trap for the $^1S_0 \rightarrow ^3P_1$ transition, and we will implement attractive Sisyphus cooling with a circularly-polarized light to address the $|m_J| = 1$ states.

Chapter 3

Optical Tweezers and Rydberg atoms

In this chapter we will go deeper into the peculiarity of the experimental platform, further exploring the optical tweezers technology and introducing the fundamental concepts underlying Rydberg atoms. The final section of the chapter is left for an overview of the applications and physical systems that can be investigated with Rydberg atoms in optical tweezers, ranging from the quantum simulation of spin models to the implementation of quantum gates operations for quantum computing. Within this broad range of applications, we will also outline the specific topics that will be explored in our experiment.

3.1 Optical Tweezers

So far we have seen how a micron-sized optical dipole potential can be used to trap neutral atoms. In this section we will describe the optical setup used to generate a single optical tweezer and how to scale up the system to 1D and 2D arrays.

3.1.1 Optical setup

An optical tweezer is obtained by tightly focusing a laser beam through a simple lens or a microscope objective. Given its microscopic length scale, the optical setup needs a precise design to minimize aberrations that could distort the micro trap. In Sec. 2.4 we assumed an ideal case with perfect Gaussian laser beam profile, and aberrations would complicate the description of the system in a nontrivial way, also limiting the control on experimental parameters. Aberration-corrected microscope objectives are used to focus the laser beam. These objectives usually give better performances than achromatic lenses and they can be optimized for multiple wavelengths, which is fundamental to use the microscope not only to project the optical tweezers, but also

to collect the imaging light and produce a site-resolved image of the trapped atoms. Describing the laser beam as a Gaussian profile is valid under the *paraxial approximation*, where we assume that the amplitude $A(\mathbf{r})$ of the electromagnetic wave travelling along the z -direction varies slowly along z within the distance of a wavelength λ [81]

$$\frac{\partial A}{\partial z} \ll kA, \quad (3.1)$$

where $k = 2\pi/\lambda$ is the wave number. The full expression of the electric field travelling along the z -axis in paraxial approximation, is given by [81]:

$$A(r, z) = A_0 \frac{w_0}{w(z)} \exp\left(-\frac{r^2}{w^2(z)}\right) \exp\left(-ikz - ik\frac{r^2}{2R(z)} + i\zeta(z)\right), \quad (3.2)$$

where A_0 is the amplitude peak value, w_0 is the beam waist and $w(z)$ the $1/e^2$ radius along the propagation direction z . The radial direction is indicated by r , k is the wave number, $R(z)$ is the curvature radius of the wavefront, $\zeta(z)$ is the Gouy phase¹ and ω is the angular frequency. The Gaussian beam intensity in Eq. 2.29 is proportional to the square modulus of the complex electric field, $I(r, z) \propto |A(r, z)|^2$.

The Gaussian beam shape can be modified by placing a telescope on the beam path giving a magnification M . This modifies the wavefront, affecting the characteristic length scales describing the Gaussian beam. It can be demonstrated [82] that the waist w_0 , the Rayleigh length z_R and the position of the focal plane z_0 are modified like

$$\begin{aligned} w'_0 &= Mw_0 \\ z'_R &= M^2 z_R \\ z'_0 &= M^2 z_0 \end{aligned} \quad (3.3)$$

where the primed values indicate the modified values after the telescope. The scaling for the focal plane position allows for determining how moving the first lens of a telescope by a quantity z_0 with respect to the ideal $4f$ configuration affects the focal plane of the second lens, shifting it by a quantity z'_0 . This is valid under the assumption that $z_0, z'_0 \ll f_1, f_2$, where $f_{1,2}$ indicate the focal lengths of the telescope lenses. The scaling for the focal plane position assumes an optical system with two lenses (or one lens and one objective) with focal lengths f_1 and f_2 . In an ideal $4f$ optical system the two lenses are spaced by $f_1 + f_2$ and the two focal planes matched by the optical system are at distances f_1 and f_2 from the two lenses. By moving the first lens the M -scaling is important in the design of the optical setup for the tweezer generation described in Subs. 3.1.2 as well as in the detection setup described in Subs. 4.3.2. However, the paraxial approximation starts to fail when we consider tightly focused laser beams like the optical tweezers, for which the intensity profile varies on the order of z_R which is a just a few μm , comparable with the wavelength of the laser beam. In Ref. [82] the validity limits of the paraxial approximation are investigated, introducing higher-order effects that lead to aberrations. We refer to Ref [82] for a detailed description of different optical aberration effects.

Even if we consider an ideal optical system with no aberrations, a focused laser

¹The Gouy phase is defined as $\zeta(z) = \arctan\left(\frac{z}{z_R}\right)$

beam will have a finite waist which is limited by the diffraction limit. On the other hand, the smallest spot size that an imaging system can resolve is also limited by the diffraction induced by finite-sized optical elements. The image that an imaging

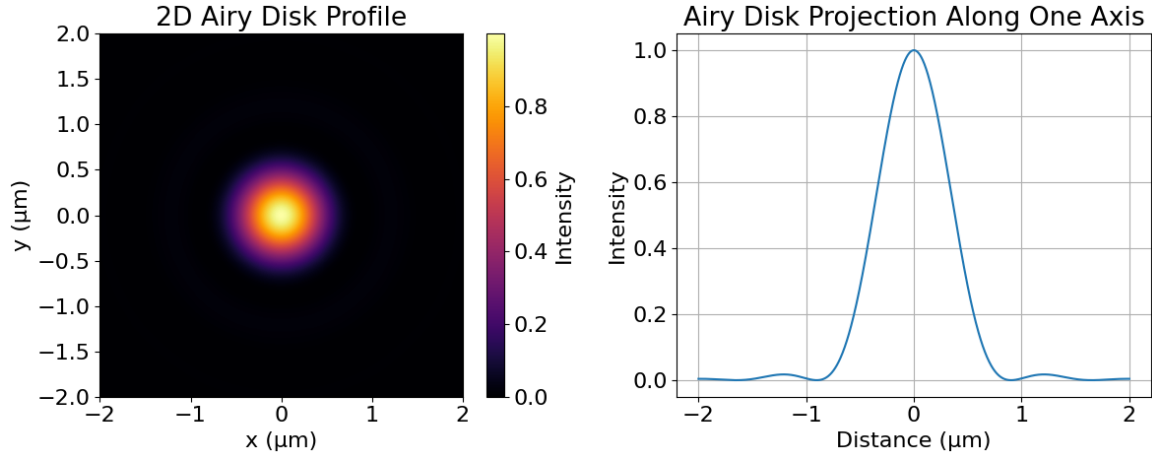


FIGURE 3.1: Airy disk profile describing the PSF of an imaging system in 2D and 1D section. The intensity profile is characterized by a central peak surrounded by concentric fringes arising from the diffraction due to the finite aperture of the microscope objective. The PSF has a first minimum at a distance r_0 which defines a characteristic length scale of the imaging system.

system produces when the object is a point source is called the *point spread function* (PSF). The PSF of a perfect imaging system (no geometrical aberrations) with circular aperture with finite diameter D is a diffraction pattern called the *Airy disk*. The intensity profile of the Airy disk, shown in Fig. 3.1, is given by [83]

$$I(\theta) = I_0 \left(\frac{2J_1(ka \sin(\theta))}{ka \sin(\theta)} \right)^2 \quad (3.4)$$

where $J_1(x)$ is the first-order Bessel function, k is the wave number, a is the spot size and $\theta = \arctan(w_0/z_R)$ is the Gaussian beam divergence in the paraxial approximation. The minimum spot size is conventionally defined as the distance between the central peak and the first minimum, which occurs at

$$ka \sin(\theta) \approx 1.22\pi. \quad (3.5)$$

Introducing the definition of the *numerical aperture* (NA) of the imaging system and solving for a we find a definition of the diffraction limit spot size a_0 :

$$\text{NA} = n \sin(\theta_{max}) \quad \rightarrow \quad a_0 = \frac{0.61\lambda}{\text{NA}} \quad (3.6)$$

where $\theta_{max} = \arctan\left(\frac{D}{2f}\right)$ denotes the maximum aperture of the lens or objective, n is the refractive index of the medium and the vacuum value $n = 1$ was considered for a_0 calculation. Eq. 3.6 sets the theoretical lower bound diffraction limit for an imaging system with given NA and λ . Real systems can get close to the diffraction

limit although imperfections might produce a larger PSF. For a measured PSF, the distance between the Airy disk central peak and the first minimum r_0 defines the best resolution achievable in the real imaging system for a point source. If r_0 equals the diffraction limit a_0 , the system is said to be *diffraction limited*. This generally happens only at specific wavelengths for which the imaging system has been designed. The commercial microscope objective used in our experiment, described in Sec. 5.5, is designed to be diffraction limited for two relevant wavelengths, at 813 nm and 461 nm. These two wavelengths correspond to the laser beam used for projecting the optical tweezers and the laser beam used for the fluorescence imaging. It is desirable to have the smallest PSF in both the cases, to produce the tightest optical tweezer possible to have both large trap depths and trapping frequencies, and to have the highest resolution possible in the detection process. The diffraction limit spots for 461 nm (NA=0.56) and 813 nm (NA=0.55) for our objective (see Tab. 5.6) are:

$$a_0(461 \text{ nm}) = 502 \text{ nm}, \quad a_0(813 \text{ nm}) = 902 \text{ nm}. \quad (3.7)$$

The size of the PSF indeed determines a length scale beyond which two point sources can be distinguished. This is relevant regarding the detection of single atoms to understand what is the minimum distance they must be separated to be distinguishable. Even though an atom is essentially a point source, since its characteristic size is set by the quantum harmonic-oscillator size which is typically smaller than the wavelength that it emits², the fluorescence will appear extended as the PSF characteristic of the imaging system. The so-called Rayleigh criterion states that two PSFs are distinguishable if the separation between their centers Δr is larger than r_0 :

$$\Delta r > r_0. \quad (3.8)$$

This topic will be further discussed in Chapter 4.

An interesting discussion in Ref. [69] reports the numerical study of the optimal ratio between the Gaussian beam waist w_i and the microscope objective's back focal plane aperture R . The trap depth, axial and radial trap frequencies are studied as a function of this parameter. Intuitively, if w_i is smaller than the aperture R , the effective NA of the objective is reduced to the size of the laser beam, thus producing a larger tweezer in the focal plane. On the other hand, when w_i overcomes R a fraction of the laser power is lost as the Gaussian profile is cut by the objective's aperture. A numerical simulation carried out in Ref. [69] shows that the best compromise, considering a constant power of the input beam, is to have $w_i/R \approx 1$.

In this section, we discussed the key concepts and tools required for creating optical tweezers. A high-NA objective is required both to focus the tweezer on a micron scale to get sufficiently deep traps, and to obtain a small PSF. It is beneficial to use a laser beam that satisfies the $w/R = 1$ criterion to optimize the trapping efficiency. However, imperfections in other components of the optical system can introduce aberrations, resulting in a tweezer profile larger than the diffraction limit. Particular care is required in the optical design to minimize aberrations and ensure the tweezers approach the diffraction limit as much as possible.

² $r_{RMS} = \sqrt{\frac{\hbar}{2M\omega_r}} \simeq 36 \text{ nm}$ for typical tweezers parameters.

In the next section we will see how to produce an array of optical tweezers exploiting two types of optomechanical devices, acousto-optic deflectors (AODs) and spatial light modulators (SLMs). The design of the optical setup will be outlined, focusing on the key parameters necessary to implement and harness the capabilities of these devices.

3.1.2 Arrays of optical tweezers

The possibility of scaling up the system, producing not only a single optical tweezer but an array of them, opens the way towards many interesting experimental applications. We will here describe the working principle of AODs and SLMs and how they can be used to modify the input laser beam such that the microscope objective projects an array of optical tweezers instead of a single tweezer. In the following subsection we will describe how multiple atoms can be loaded from the red MOT to the tweezers and how to induce a loss mechanism to end up with single atoms in tweezers. Finally, the reordering procedure to obtain a defect-free array will be outlined.

Acousto-optic deflectors

Acousto-optic deflectors (AODs) exploit the interaction between light and acoustic waves in crystalline materials to deflect a laser beam at an output angle determined by the acoustic wave frequency [84]. An AOD essentially consists of two components: a piezoelectric transducer and a crystal. When an RF signal is applied to the transducer through an RF matching circuit, it converts the electrical signal into a sound wave that propagates through the crystal. This sound wave forms a diffraction grating that allows the laser beam to be diffracted. These devices are similar to acousto-optic modulators, or AOMs, but they are typically designed to have a larger bandwidth with almost flat efficiency, such that many different beams can be deflected at the same time. An exhaustive characterization of AODs for the generation of optical tweezers is reported in chapter 4 of Ref. [85]. Another difference from AOMs is that the crystal in AOD devices is mounted at an angle such that the beam deflected for a frequency at the center of the bandwidth propagates straight, whereas the zeroth order comes out at a separated angle. The diffraction angle compared to zero-order beam, for a laser beam with wavelength λ , is [84]:

$$\theta_D = \frac{\lambda f}{v_s} \quad (3.9)$$

where f is the RF frequency and v_s the speed of sound in the medium. Our AOD devices are manufactured by AA Opto-Electronics (DTSX-400-810 for $\lambda = 813.4$ nm) and have a measured bandwidth of ± 20 MHz around the central frequency $f_0 = 101$ MHz. The angular separation between the zeroth order and the first order at the central frequency can be calculated with Eq. 3.9 to be $\theta_0 = 0.13$ rad = 7.2° .

A single AOD can generate a 1D line consisting of tens of deflected beams if the spectrum of the RF driving the AOD is made up of multiple frequency components. To transform the angular separation into spatially separated laser beams, it's sufficient to place a lens at its focal distance from the center of the AOD. This arrangement ensures that each deflected beam, exiting the AOD at a different angle, will then

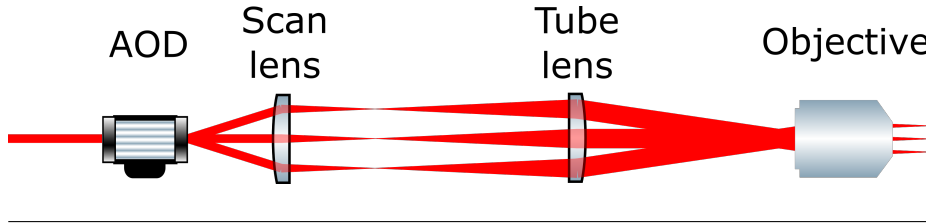


FIGURE 3.2: An AOD can produce a line of multiple diffracted beams. A lens, often referred to as scan lens, is placed at focal distance from the AOD plane to map the angular separation of the beams into an array of beam that propagate parallel to each other and are focused at the focal distance from the scan lens. A second lens (tube lens) is placed in a $4f$ configuration with respect to the scan lens. These two lenses form a telescope, which can change the waist and angular separation of the array of beams according to the magnification M of the telescope. The beams after the tube lens have a beam size magnified by a factor $M = f_{tube}/f_{scan}$, where f_{tube} and f_{scan} are the focal lengths of the two lenses, while the angular separation is de-magnified by the same factor. A microscope objective, similarly to the scan lens, converts the collimated beams, entering the objective at different angles, into an array of focused beams that propagate parallel to each other.

travel in a straight line parallel to each other. Moreover, each beam is focused at the lens focal plane, which is conjugated with the AOD plane. This setup creates a 1D array of focused beams that travel parallel to one another, forming a spatial pattern in the lens focal plane, as shown in Fig. 3.2. As discussed in Subs. 3.1.1, it is advantageous to use an aberration-corrected optical element, such as a microscope objective, to focus the laser beams and create optical tweezers, rather than a simple lens. Additionally, telescopes can be employed to adjust the beam size to match the back focal plane of the objective. In our setup, a lens placed after the AOD, known as the *scan lens*, converts angular separation into spatial separation. This scan lens forms a telescope with the *tube lens*, which reconverts the beam array into angularly separated collimated beams. These beams are then focused by the objective into an array of optical tweezers, all propagating in parallel and focusing in the objective's focal plane, as shown in Fig. 3.2.

The 1D array of optical tweezers generated by an AOD can be easily expanded into a 2D array by adding a second AOD oriented at a 90° angle relative to the first. By labeling the laser beam propagation direction as z , the first AOD axis as x , and the second AOD axis as y , it is straightforward to apply the same approach described earlier to introduce deflection along both x and y axes. Since each deflector has a finite axial size (a few centimeters), even when placed close together, their deflection planes will not overlap, causing a mismatch when positioning the scan lens at the focal distance from one of the devices. To resolve this, a 1:1 relay telescope in a $4f$ configuration is sufficient to match the deflection planes of the two AODs, thus defining a unique plane to be matched with the scan lens position.

While we have already discussed the optimal size of the input beam waist w_i , we can now define the spatial displacement of two optical tweezers corresponding to RF frequency tones f_1 and f_2 fed through the AOD. The two beams are deflected out of the AOD at angles θ_1 and θ_2 , respectively, and we consider the effect of the scan lens and tube lens telescope. A telescope with magnification $M = f_{tube}/f_{scan}$ de-magnifies

the angular separation by a factor $1/M$. The distance between two tweezers focused by the objective is then [86]:

$$d_{\text{tweez}} = 2f_{\text{obj}} \cdot \tan\left(\frac{\theta_1 - \theta_2}{2M}\right) = 2f_{\text{obj}} \cdot \tan\left(\frac{(f_1 - f_2)\lambda}{2v_s} \cdot \frac{1}{M}\right) \quad (3.10)$$

where f_{obj} is the effective focal length of the microscope objective. If more than one telescope is present on the optical path, it's sufficient to calculate the global magnification factor M and substitute it in Eq. 3.10. A sketch of the final setup for

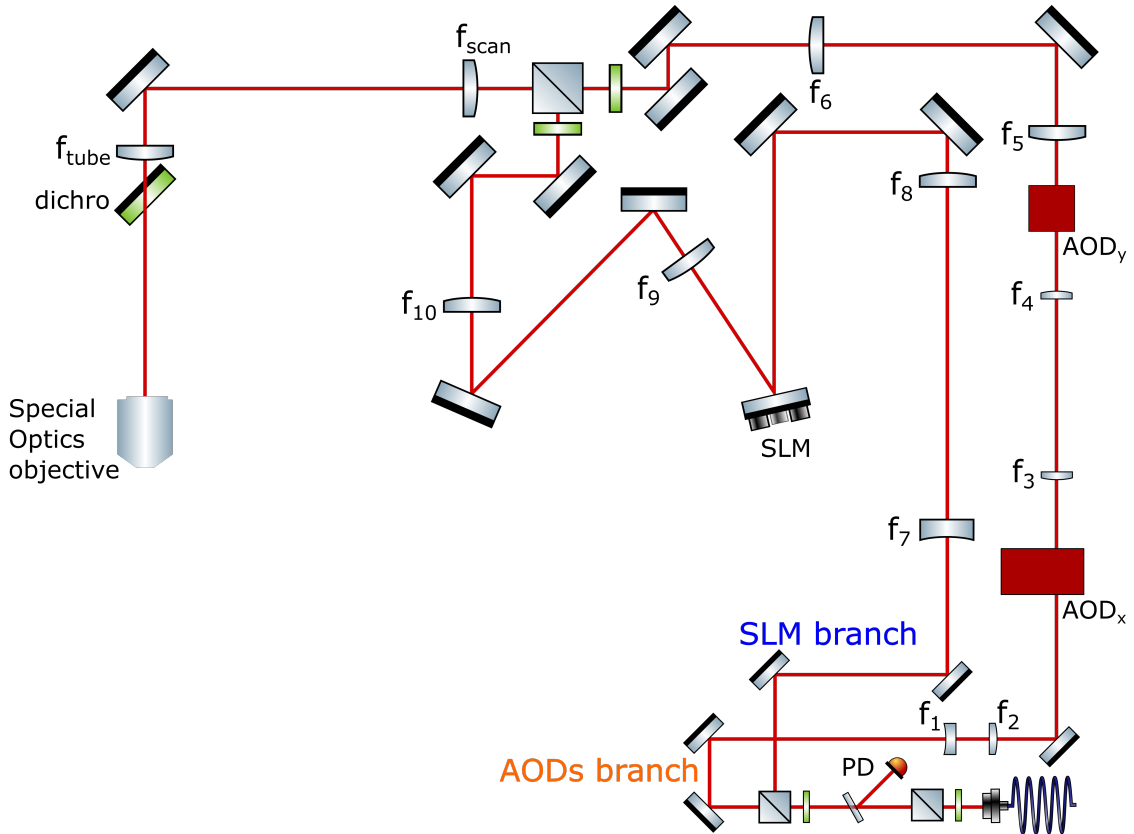


FIGURE 3.3: Sketch of the optical setup for the generation of optical tweezer arrays employing AODs and SLM. Two separate paths are created to use the two devices separately and then recombined.

the generation of optical tweezer arrays is shown in Fig. 3.3. Both the AODs and SLM setups are represented: the AODs setup is highlighted in orange while the SLM part, discussed in the next paragraph, is highlighted in light blue. The two paths are combined with two waveplates and a PBS in a section of the beam path where the beam is collimated to minimize possible distortions, and they share a common telescope before the objective. The waist of the laser beam at the fiber's output is $w = 1.1$ mm. A waveplate and a PBS translate polarization fluctuations into power fluctuations, which are monitored by a photodiode (PD), whose signal can be used in a feedback loop to stabilize the power output of the fiber. On the AODs path, a

telescope expands the waist by a factor of 1.5 ($f_1 = -100$ mm, $f_2 = 150$ mm), and the beam is then deflected along x and y directions via the two orthogonal AODs. A 1:1 relay telescope ($f_3 = f_4 = 100$ mm) allows to match the planes of the AODs. Since this path has to be recombined with the SLM path and we need room for two adjustment mirrors and a dichroic mirror before the objective, we decided to introduce a second relay telescope before the scan and tube lenses. This relay telescope magnifies the waist by a factor of 4 ($f_5 = 75$ mm and $f_6 = 300$ mm), while the scan and tube lenses give another factor of 2 ($f_{\text{scan}} = 150$ mm and $f_{\text{tube}} = 400$ mm).

With this configuration we obtain a beam waist at the objective's back focal plane of $w_i = 13.2$ mm, almost the same size as the radius of the aperture $R=13.5$ mm. The maximum extension of the tweezer array, by considering two frequencies at the edge of the RF bandwidth in Eq. 3.10, is $d_{\text{tweezer}} \sim 150\mu\text{m}$.

Spatial light modulators

The second type of devices that are commonly used to modulate an incoming Gaussian beam to produce, in the focal plane of the objective, a spatial modulation of the beam, are the spatial light modulators (SLMs). Among the variety of devices, we will focus on the reflective liquid crystal SLMs. A liquid crystal chip is embedded between a glass plate and a reflective silicon substrate layer. On top of the silicon substrate, an array of electrodes is arranged, defining the pixel unit of the display. By controlling independently the electric potential of each electrode, the liquid crystal molecules can be reoriented. The tilt of the molecules depends on the strength of the electric field, making each pixel of the display tunable. The physical consequence is a local variation of the refractive index of the liquid crystal, that can be used to modulate the phase of an incoming laser beam. The device imprints a phase mask on the beam such that, by placing a lens at focal distance from the SLM, it converts a phase modulation in the SLM plane into a spatial modulation in its focal plane (Fourier plane). In other words, the lens performs a Fourier transform of the phase mask in the conjugated plane [33, 34, 87, 38]. The incoming beam has to be linearly H-polarized and incidence angle has to be as small as possible to produce a reliable phase modulation on the whole beam. A detailed and exhaustive description of how to use a SLM to produce an array of optical tweezers can be found in Ref. [88].

In our optical setup, reported in Fig. 3.3, the laser beam on the SLM path is magnified with a telescope ($f_7 = -100$ mm and $f_8 = 500$ mm) to match the vertical side of the SLM display (15.36 mm \times 9.6 mm). This configuration sets a balance between maximizing the area of the display used for generating the tweezer pattern and minimizing power loss by avoiding clipping of the beam along the shorter axis. The phase modulated light is conjugated to the back focal plane of the objective by means of two telescopes ($f_9 = 200$ mm and $f_{10} = 300$ mm) that magnify the size of the phase-modulated image to approximately 28 mm at the back focal plane of the objective. Before the objective a dichroic mirror transmits the tweezer light and is used to separate the blue light fluorescence collected from the objective and reflected on a different path.

The SLM phase mask is calculated via the weighted Gerchberg-Saxton algorithm [88, 89, 90]. This is a refined version of the Gerchberg-Saxton algorithm, which calculates the phase mask to reproduce a target intensity pattern in the Fourier image plane by iteratively looking at the projected field and the target pattern and how much

they differ. Initially, all the pixel are assigned with random phases ϕ_0 from 0 to 2π . The phase is multiplied by the amplitude of the Gaussian beam incident on the display A_0 . The initial light field is

$$E_{\text{in}}^0 = A_{\text{in}}^0 e^{i\phi_0}, \quad (3.11)$$

and the effect on the Fourier plane is estimated by applying a Fast Fourier Transform (FFT) to the input light pattern, which gives

$$E_{\text{out}}^0 = \text{FFT}(E_{\text{in}}^0) = A_{\text{out}}^0 e^{i\varphi_0}. \quad (3.12)$$

where A_{out}^0 is the amplitude of the output light field and φ_0 the phase of the first iteration. The amplitude is now constrained to the target value $A_T = \sqrt{I_T}$ where I_T is the target intensity, which replaces the calculated value A_{out}^0 :

$$G_{\text{out}}^0 = A_T e^{i\varphi_0}. \quad (3.13)$$

Going back to the SLM plane via Inverse Fast Fourier Transform (IFFT) gives:

$$G_{\text{in}}^0 = \text{IFFT}(G_{\text{out}}^0) = A_{\text{in}}^1 e^{i\phi_1}, \quad (3.14)$$

where A_{in}^1 and ϕ_1 are the resulting amplitude and phase. Now the second amplitude constraint is applied, by replacing the correct input amplitude A_0 and keeping the phase for the next iteration:

$$E_{\text{in}}^1 = A_{\text{in}}^0 e^{i\phi_1}. \quad (3.15)$$

The iteration proceeds until either a maximum number of iterations is reached or the difference between the calculated amplitude in the Fourier plane A_{out}^n and the target A_T is below a certain threshold. All the amplitudes and phases here are to be intended as an array of values for each pixel of the SLM. In the weighted GS algorithm, the first amplitude constraint in the Fourier plane is weighted by a factor w :

$$w = e^{G(I_T - I_{\text{out}})} \quad (3.16)$$

where I_T and I_{out} denote the intensity of the target image and the reconstructed image, respectively, and G a gain factor that can be optimized to speed up the convergence of the algorithm. Instead of simply replacing A_{out} with the target amplitude $A_T = \sqrt{I_T}$, the weight w is multiplied by the target amplitude: $A_{\text{out}} = w \cdot A_T$. The weights are updated at every iteration with the new I_{out} values and the iteration is stopped after a maximum number of cycles or when the difference with the target image is below a certain threshold.

3.1.3 Defect-free array of single atoms

One of the key features of optical tweezer experiments is the possibility to create arrays of individual atoms, one in each tweezer, organized in a defect-free pattern. This is achieved by first loading multiple atoms in each tweezer from the red MOT, and then inducing *light-assisted collisions* (or LAC), that are particularly efficient in tightly focused dipole traps, to remove atoms from the tweezers ending up with either

one or zero atoms. At this point, a defect-free array can be built via rearrangement of the filled traps.

Loading multiple atoms from the red MOT

The preparation of a cold cloud of atoms via a single-frequency MOT on the narrow $^1S_0 \rightarrow ^3P_1$ will be described in Subs. 6.3.2. From this cold and dense cloud of atoms we can load atoms in optical tweezers. The procedure to overlap the red MOT and the optical tweezer array is described in Chapter 7.

Trapping atoms in the optical tweezers requires the trap depth to be deep enough to capture one or multiple atoms. Moreover, since we want to initially load all the tweezers, we want to have a high density to have at least one atom in the trapping volume of each tweezer. This last requirement can be expressed in terms of the red MOT parameters, such as the temperature and density, and the tweezer trap depth and dimensions. Following the calculations in section 2.4 in Ref. [69], we can consider a semiclassical model described by the Hamiltonian $H(r, z, p) = \frac{p^2}{2m} + U(r, z)$, where $U(r, z)$ is the tweezer potential introduced in Eq. 2.30. Although, in theory, any atom with negative total energy can be trapped, it is more practical to impose a more stringent condition by counting only those atoms whose kinetic energy is less than a fraction κ of the trap depth, that is, less than κU_0 . Accounting for this cutoff parameter we can calculate the maximum momentum p_{\max} that an atom can have and the corresponding maximum radial $r_{\max}(p)$ and axial $z_{\max}(p)$ displacement inside the tweezer:

$$\begin{aligned} p_{\max} &= \sqrt{2mU_0\kappa} \\ r_{\max}(p, z) &= w_0 \sqrt{\frac{1}{2} (1 + z^2/z_R^2) \ln \left(\frac{1 + z_{\max}^2(p)/z_R^2}{1 + z^2/z_R^2} \right)} \\ z_{\max}(p) &= z_R \sqrt{\frac{p_{\max}^2}{\kappa p^2 + (1 - \kappa)p_{\max}^2} - 1} \end{aligned} \quad (3.17)$$

where w_0, z_R are the waist and Rayleigh distance already defined. We can also assume that the atoms in the MOT have a thermal distribution and the tweezer capture volume is small compared to the size of the MOT (typical lengthscale for a tweezer is $\approx 1 \mu\text{m}$ compared to the red MOT diameter of $\approx 200 \mu\text{m}$), allowing us to consider the atomic density $n(T_M) \approx n$ to be constant to the peak value that we measure experimentally. The number of atoms that are within the cut-off phase space when instantaneously turning on the tweezer is

$$N^{\text{inst}} = \frac{8\pi^2 n(T_M)}{(2\pi m k_B T_M)^{3/2}} \int_0^{p_{\max}} dp p^2 \exp\left(\frac{-p^2}{2m k_B T_M}\right) \int_0^{z_{\max}(p)} dz r_{\max}^2(p, z) \quad (3.18)$$

which is not solvable analytically but can be treated numerically if we consider typical tweezer and red MOT parameters. We will assume these parameters to be $U_0 = k_B \times 200 \mu\text{K}$, $w_0 = 1 \mu\text{m}$, $z_R = 3.9 \mu\text{m}$, $\kappa = 0.5$, $T_M = 10 \mu\text{K}$ and $n = 8 \times 10^{10} \text{ cm}^{-3}$. Eq. 3.18 gives then $N^{\text{inst}} \sim 0.34$. We refer the reader to [69] for further insights on the calculation. This estimate implies that roughly one out of every three tweezers is filled as soon as the array is activated. However, the presence of a deep dipole potential modifies the local density by a Boltzmann factor depending on the tweezer potential,

$n_{\text{tweezer}} = n \cdot e^{\frac{U(r,z)}{k_B T_t}}$ [91], where T_t is the temperature of the atoms in the tweezer. This exponential factor can hugely increase the local density, thus increasing the number of atoms that are instantaneously within the tweezer capture volume. This effect is balanced by the red MOT light, which still interacts with the atoms falling in the tweezer potential, producing an effective thermalization process. Moreover, the high density increases the probability of light-assisted collisions that induce pairwise losses, as detailed in the next Subsection. While a detailed dynamic model of multi-atom loading goes beyond the scope of this basic estimation, we can reasonably assume that all tweezers will likely be filled in a short amount of time.

The result of this balance is a Poisson distribution of the loaded number of atoms [19], whose mean value is difficult to measure experimentally via fluorescence imaging. This is due to both the detection camera technology, that allows for a precise discrimination of zero and one/many atoms but doesn't allow to clear out multiple occupations, and the fluorescence imaging itself, that might induce collisional losses that affect the number of atoms during the measurement. Based on more refined estimations, the typical mean number of atoms initially loaded in each optical tweezer is $N \sim 5$ [70, 69, 92]. We will now discuss how to engineer atom-atom collisions to produce losses and reduce the tweezers occupation to binary, with either zero or one atom per tweezer.

Light-assisted collisions

The ultimate goal that we want to achieve is to prepare an array of tweezers with just one atom per tweezer. Ideally we would like to develop a mechanism that induces one-by-one atom losses to reduce the initial occupation down to one. This kind of process is rather complicated and a few techniques were developed, up to now, to implement it in platforms using alkali atoms [93, 94, 95]. Another common approach is to induce pairwise losses [39, 96, 97] via light-assisted collisions that for strontium can be operated on the $^1S_0 \rightarrow ^3P_1$ transition. The laser beam is tuned to account for the light shift induced by the tweezer light on the two levels, and induces a photo-association process to a molecular state, as depicted in Fig. 3.4. A pair of atoms in the electronic excited molecular state gain enough kinetic energy to be expelled from the tweezers as soon as they decay back to the ground state.

Through this mechanism of pairwise losses, also called parity projection (PP), the initial number of atoms loaded in every tweezer is diminished by 2 for each collision. Therefore after a few interactions the traps that were initially loaded with an even number of atoms will become empty, while the traps that were loaded with an odd number of atoms will end up with a single atom. The loss process ends with the binary occupation as no more pairwise collisions can happen. Given the initial Poissonian occupation of the tweezers, it can be demonstrated that the number of even and odd occupations approximately equals for \bar{N} larger than 5, so we expect on average to have 50 % of the tweezers empty and the remaining 50 % with one atom. This characteristic can serve as a signature for experimentally detecting the pairwise loss process taking place.

A process that induces only one-by-one losses would be preferable as both even and odd initial occupations could be reduced to single-atom occupation. Anyway, engineering such process via light-assisted collisions is rather complex because the

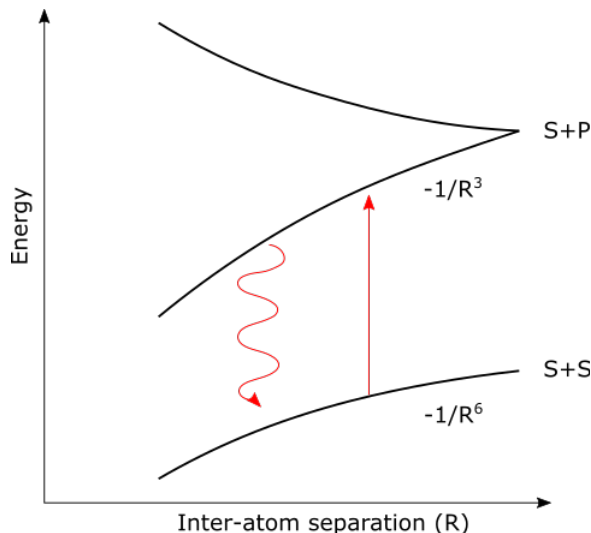


FIGURE 3.4: The molecular potential of two atoms in S angular momentum state (1S_0) scales as R^{-6} as the inter-atomic distance R changes. When the red light eventually excites one of the two atoms to the 3P_1 state (straight arrow), the molecular potential scales as a dipole-dipole potential (R^{-3}). As the atoms get closer in this steeper potential, the pair gains energy in the relative-motion frame until a less energetic photon is re-emitted (wavy arrow) on a timescale set by the P-state lifetime. The total energy gained by the pair of atoms is enough to expel both from the trap. The S+P molecular potential can be either attractive or repulsive, based on the spin configuration of the two atoms.

atoms should acquire enough energy to expel just one atom from the trap, and this requires a fine tuning of the laser parameters on the molecular potential. Moreover, as soon as just one atom remains in the tweezer, it has to be shielded from the light-assisted collision to freeze those tweezers that have already reached single occupancy.

Reordering

After the PP process, the array of optical tweezers will be randomly populated by single atoms. Even employing more elaborated schemes to have a higher fraction ($> 80\%$) of occupied sites [95, 98, 99], the array will still present some defects. In order to prepare a defect-free array deterministically, the atoms can be rearranged with a movable optical tweezer, superimposed to the static array, that picks the atom from one site and moves it to a target site. While the SLM is typically too slow to perform a dynamic sorting, since it has a refresh rate on the order of tens of milliseconds, a pair of orthogonal AODs can be used dynamically by feeding a time dependent RF signal. By Eq. 3.9 we know that the AODs deflect the beam at an angle proportional to the driving RF frequency and that the angle is converted into a spatial displacement in the focal plane of the objective. To generate a movable tweezer it's enough to drive the AODs with a time-dependent waveform generated by an arbitrary waveform generator (AWG) containing a sweep of frequency tones. We use a Spectrum M4i.6631-x8 AWG to generate the static frequencies as well as the sweeps for the reordering. This card, which is implemented in the main PC of

the experiment, can control two channels independently with a 400 MHz bandwidth, sampling rate of 1.25 GS/s, a 16 bit resolution and 2 GS on-board memory to store pre-calculated waveforms that are ready-to-use. Each channel's waveform is attenuated and filtered with a low-pass filter at 150 MHz and a high-pass filter at 5 MHz to remove harmonics and DC signals, then it's amplified with a Mini Circuits ZHL-5W-1+ 5 W RF amplifier and finally connected to the AOD. The attenuators before the amplifier allow us to use the full range of the AWG signal, thus avoiding any risk of breaking the amplifier or the AOD which requires a 2 W signal.

The optimal sequence for reordering the atoms is calculated based on the initial occupation of the array, which is detected via a fluorescence image. Many groups have developed their own algorithm to calculate the optimal sequence to move the atoms from the initial positions to a set of target positions [22, 21, 100], thus creating a defect-free subset. We are currently working on ours. A sketch of the reordering sequence is shown in Fig. 3.5

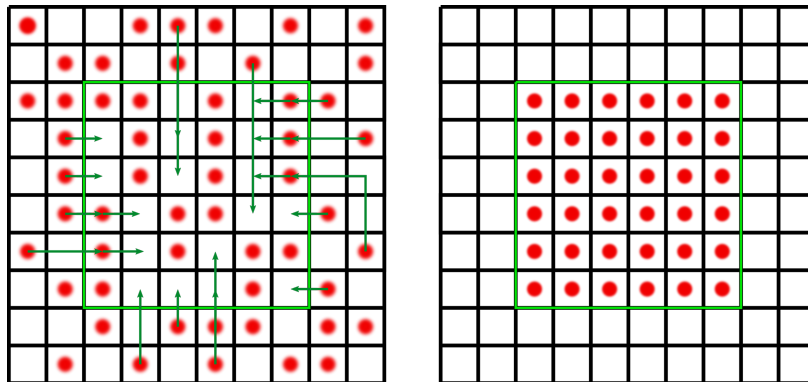


FIGURE 3.5: Sketch of the reordering sequence of a 2D array. The atoms location is detected via fluorescence imaging. Then, a sequence of moves picks the atoms from an initial position and moves them to a target position. The algorithm that calculates the sequence of moves has to take into account constraints such as emptying a trap before moving another atom there. An optimized sequence might calculate the shortest paths dividing the array in subsets, thus reducing by far the number of possible paths to analyse.

Since this method relies on one-by-one sorting, the time required for the moves increases significantly as the size of the array increases. A typical move requires roughly 1 ms to efficiently transport the atom without significant losses. In an array with several hundreds of sites, the time required for the reordering is not negligible with respect to the vacuum lifetime. This led some groups to develop cryogenic setups, where the vacuum lifetime is significantly enhanced, as mentioned later on in Subs. 5.2.3, leaving enough time to sort thousands of atoms [101]. Another approach consists in using the SLM not only to generate the initial pattern, but also to dynamically reorganize all the atoms in parallel. Although the low refresh rate of the device (our Meadowlark Optics E-1920x1200 refreshes at 60 Hz) can produce flickering in the image pattern, thus heating or losing the atoms, a fast purely SLM-based rearrangement has been demonstrated in Ref. [102]. In particular, a modified Gerchberg-Saxton algorithm was implemented on a Meadowlark XY series with 2 kHz refresh rate obtaining a loading probability of 0.98 for up to 30-atoms arrays.

TABLE 3.1: Scaling of relevant Rydberg atoms properties.

Property	n -scaling
Binding energy E_n	n^{-2}
Level spacing $E_{n+1} - E_n$	n^{-3}
Radiative lifetime τ	n^3
Orbital radius $\langle r \rangle$	n^2
Dipole moment $\langle np er nd \rangle$	n^2
Scalar polarizability	n^7
Dipole-dipole coefficient C_3	n^4
van der Waals coefficient C_6	n^{11}

3.2 Rydberg atoms

In this section, we will explain how to implement long-range interactions into the system via excitation to Rydberg states. We will present two potential excitation schemes for Strontium atoms and provide an overview of our approach, along with the expected coupling strength estimate. Lastly, we will discuss the possibility of generating entangled states between neighboring atoms as a result of Rydberg excitation.

Rydberg states are typically defined as electronic states characterized by a high principal quantum number n . An atom in a Rydberg state behaves as a highly excited Hydrogen-like atom, having a valence electron orbiting around the positively charged nucleus. The screening effect of all the other electrons can be accounted for as a quantum defect $\delta_{n,l,j}$ which is function of the principal quantum number n , the orbital and total angular momenta l and j , and the binding energy is very well described by [103]

$$E_{n,l,j} = E_\infty - \frac{Ry}{(n - \delta_{n,l,j})^2}, \quad (3.19)$$

where E_∞ is the ionization energy, considering the ground-state energy as zero-energy level, and Ry is the Rydberg constant corrected by the reduced mass, which reads:

$$Ry = \left(\frac{m_e}{M + m_e} \right) \left(\frac{m_e e^4}{8\epsilon_0^2 h^2} \right), \quad (3.20)$$

where M is the atom mass, m_e is the electron mass, e is the unitary electric charge, h is the Planck's constant and ϵ_0 is the vacuum permittivity. The binding energy scales then as n^{-2} , which implies that the energy difference between two Rydberg states Δ_n scales as n^{-3} . The n -scaling of many properties of Rydberg atoms were experimentally investigated in Ref. [103] and are reviewed in Refs. [104, 105]. The n -scaling of a few important properties are reported in Tab. 3.1.

In general, Rydberg atoms have extreme properties due to the enormous wave-function that can extend on a hundreds of nanometers scale. Remarkably, they can have a lifetime of tens of μ s: the decay rate towards a specific lower-energy state scales as [103]

$$\Gamma \propto \frac{|\mu|^2 \omega^3}{3\pi\epsilon_0 \hbar c^3} \quad (3.21)$$

where μ is the transition dipole moment and ω is the emission frequency. The spontaneous decay towards neighboring Rydberg states is suppressed because ω is small, whereas the decay towards the ground state is suppressed because of a small μ due to a very small overlap between the wavefunctions.

Another interesting property of Rydberg atoms is the scaling of interaction coefficients, both for the dipole-dipole interaction between two different Rydberg states ($C_3 \sim n^4$) and for the van der Waals interaction between two atoms in the same Rydberg state ($C_6 \sim n^{11}$).

For two atoms separated by a distance $R \gg \langle r \rangle$ (with $\langle r \rangle$ representing the typical size of the electronic wavefunction), the interaction is mainly driven by the dipole-dipole Hamiltonian [13]:

$$\hat{V}_{dd} \sim \hat{d}_1 \hat{d}_2 / (4\pi\epsilon_0 R^3), \quad (3.22)$$

where \hat{d}_i is the electric dipole moment scaling as n^2 .

The simplest case is that of two atoms excited to the same Rydberg state $|nS\rangle$. In this case, there is no first-order energy correction in perturbation theory, as the average electric dipole moment of an atom in a $|nS\rangle$ state is zero. However, a second-order energy correction arises due to the coupling between the pair of atoms in the $|nS, nS\rangle$ state and other states with opposite parity, such as $|nP, nP\rangle$ states, which are detuned by an energy Δ . This coupling results in an induced dipole-dipole interaction, giving rise to a van der Waals correction of the energy of the initial $|nS, nS\rangle$ state that scales as [106]:

$$V^2/\Delta \propto \frac{C_6}{R^6}. \quad (3.23)$$

Hence, we find that $C_6 \sim d^4/\Delta \sim n^{11}$, which can lead to coupling strengths on the order of MHz on a few μm scale between high- n Rydberg states [107, 108, 45]. In the complementary case, where the two atoms are excited to Rydberg states of different parity, such as $|nS\rangle$ and $|nP\rangle$, the dipole-dipole Hamiltonian contributes to the energy correction in first-order perturbation theory. Here, the interaction scales as

$$V \propto \frac{C_3}{R^3}, \quad (3.24)$$

and therefore the interaction coefficient scales as $C_3 \sim d^2 \sim n^4$.

The possibility of inducing strong long-range interactions is of utmost importance for experiments with single atoms in optical tweezers, as otherwise individual ground-state neutral atoms would be non-interacting. Moreover, the interaction strength can be tuned both by changing the target Rydberg state (changing n means changing the coupling strength) and tuning the distance between the atoms by changing the pattern of the traps. We will now describe two possible ways of exciting atoms to Rydberg states in the specific case of Strontium atoms.

3.2.1 Two different excitation schemes

Rydberg states usually have enough energy that a direct single photon excitation would require deep ultraviolet lasers, which are not very practical to work with. Two-step or two-photon excitations are often used instead. A possibility is to use one of the triplet states in the 3P_J manifold as intermediate state. Referring to Fig. 1.1,

the metastable clock 3P_0 state can be used in place of the ground state, pumping the atoms first to this intermediate state and then addressing a Rydberg state with a single-photon transition (see Fig. 3.6(a)). Alternatively, a two-photon excitation with the first photon coupling off resonantly to the 3P_1 intermediate state can be exploited to populate the Rydberg state as coherently as a single photon excitation (see Fig. 3.6(b)). These two schemes are not the only ones, as other excitation schemes involving both triplet and singlet states were proposed [109, 110, 111]

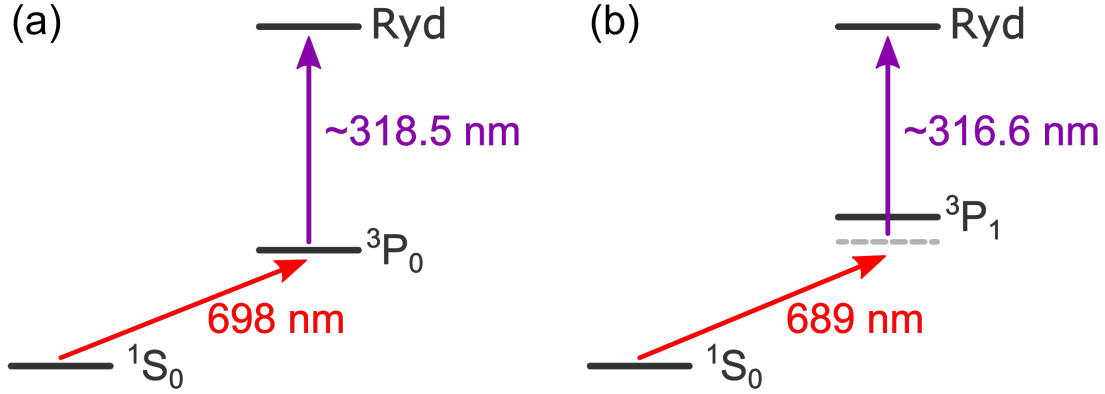


FIGURE 3.6: (a) Sketch of a two-steps excitation to a Rydberg state employing the clock 3P_0 state as an intermediate metastable state. The Rydberg state is then coherently populated with a single UV photon whose wavelength is roughly 318.5 nm. The exact value depends on the energy of the specific Rydberg state to address. (b) Sketch of a two-photon excitation to a Rydberg state. The two photons are detuned by the intermediate 3P_1 state to coherently populate the Rydberg state. The UV photon wavelength is roughly 316.6 nm but the exact value depends on the energy of the specific Rydberg state to address.

Regarding the two-steps excitation, the 3P_0 state has dipole allowed transitions towards states in the $5sns$ 3S_1 and $5snd$ 3D_1 series. The energy of Rydberg levels is determined by Eq. 3.19, where we introduced the quantum defect $\delta_{n,l,j}$. For a specific series with fixed l and j , like the 3S_1 and 3D_1 series, the quantum defect can be expressed in terms of a series expansion in n :

$$\delta_n = \delta^{(0)} + \frac{\delta^{(2)}}{(n - \delta^{(0)})^2} + \frac{\delta^{(4)}}{(n - \delta^{(0)})^4} + \dots, \quad (3.25)$$

where the constant values $\delta^{(k)}$ are determined by fitting to spectroscopic data [112, 113]. The first terms obtained in Ref. [112] are reported in Tab. 3.2.

3.2.2 Rydberg excitation coupling strength

In this subsection we will derive an estimated value of the Rabi frequency achievable in the two schemes with our current laser parameters. For simplicity, we can start with the two-step excitation (Fig. 3.6(b)), where the Rabi coupling of the 3P_0 state to the Rydberg state can be calculated directly. The Rabi frequency for a dipole-allowed

TABLE 3.2: Quantum defects for the 3S_1 and 3D_1 Rydberg series in Strontium. The values are taken from Ref. [103].

	$\delta^{(0)}$	$\delta^{(2)}$	$\delta^{(4)}$
3S_1	3.371(2)	0.5(2)	-10(20)
3D_1	2.658(6)	3(2)	-8800(7000)

transition from the state $|g m_{J_g}\rangle$ to the state $|r m_{J_r}\rangle$ is given by

$$\Omega(I, \hat{\epsilon}) = \frac{1}{\hbar} \sqrt{\frac{2I}{c\epsilon_0}} \langle r m_{J_r} | \hat{\epsilon} \cdot \vec{d} | g m_{J_g} \rangle \quad (3.26)$$

where I is the laser intensity, $\hat{\epsilon}$ is the laser polarization and \vec{d} is the dipole operator. The equation can be expanded via the Wigner-Eckart theorem [57], which introduces a reduced dipole matrix element (RDME) and a sum over the Clebsch-Gordan coefficients, which is further simplified in the case of interest for us with $J_g=0$ and $J_r=1$ [69]. Under these assumptions and considering the peak intensity of the Gaussian laser beam defined in Eq. 2.29, we obtain:

$$\Omega = \frac{1}{\hbar} \frac{2}{w_0} \sqrt{\frac{P}{3\pi c\epsilon_0}} \langle r || d || g \rangle \quad (3.27)$$

with w_0 and P indicating the waist and power of the laser beam and $\langle r || d || g \rangle$ the RDME. The RDME scaling for the Rydberg series is very well approximated by the following equation [103]:

$$\langle r || d || g \rangle \propto (n)^{-3/2} \quad (3.28)$$

where n denotes the quantum-defect-corrected principal quantum number. This gives a good approximation of all the RDMEs for Rydberg transitions as soon as one particular value is determined, either by computing it or by measuring its value for a specific n . This scaling is essentially a consequence of the wavefunction n -scaling for Rydberg states, as the RDME is mainly determined by the small overlap between the 3P_0 wavefunction, which is concentrated around the nucleus, and the Rydberg state wavefunction, which instead spreads over hundreds of nm. In Ref. [69] the Rabi frequency for $n=61$ was measured and, knowing the laser beam parameters w and P , the extracted RDME value is $\langle 5s61s^3S_1 || d || 5s5p^3P_0 \rangle = 4.6 \times 10^{-3} ea_0$, where e is the elementary charge and a_0 the Bohr radius, thus giving the following scaling law:

$$\langle 5sns^3S_1 || d || 5s5p^3P_0 \rangle = 2.0 \times (n)^{-3/2} ea_0. \quad (3.29)$$

If we now consider the beam parameters for the UV laser setup that we designed, we can calculate an estimate of the achievable Rabi frequency. For a beam power of $P = 250$ mW focused on an elliptical light sheet with $w_{0,x} = 20 \mu\text{m}$ and $w_{0,z} = 500 \mu\text{m}$, which allows us to focus the beam for higher intensity but still addressing the whole tweezer array with a global beam, the expected Rabi frequency from the clock to the

Rydberg state is:

$$\Omega_{Ryd,698}(n = 60) = \frac{2}{\hbar} \frac{1}{\sqrt{w_{0,x}w_{0,z}}} \sqrt{\frac{P}{3\pi c \epsilon_0}} \langle r || d || g \rangle = 2\pi \times 3.5 \text{ MHz}. \quad (3.30)$$

The coupling can occur at a MHz rate once the atom is loaded to the clock state. The Rabi coupling of the ground state to the clock state in bosonic strontium is given by Eq. 5.8. If we consider a beam shaped with the same elliptic shape ($w_{0,x} = 20 \mu\text{m}$ and $w_{0,z} = 500 \mu\text{m}$), $B = 900 \text{ G}$ and $P_{\text{clock}} = 100 \text{ mW}$, we get a Rabi frequency $\Omega_{\text{clock}} = 2\pi \times 8 \text{ kHz}$.

Moving now to the two-photon excitation scheme (Fig. 3.6(a)), the overall Rabi coupling is given by

$$\Omega_{\text{Ryd},689} = \frac{\Omega_{689}\Omega_{317}}{2\Delta}, \quad (3.31)$$

where $\Omega_{\text{Ryd},689}$ represents the Rabi frequency of the two-photon process, Ω_{689} and Ω_{317} the single-photon Rabi frequencies for the individual processes, and Δ stands for the detuning from the intermediate state. Ω_{689} and Ω_{317} can be estimated independently, where the laser beam shape considered is once again an ellipse with $w_{0,x} = 20 \mu\text{m}$ and $w_{0,z} = 500 \mu\text{m}$ for both beams. The expression for the UV photon Rabi frequency can also be derived from Eq. 3.27, and since we assume the same beam parameters used to calculate the Rabi frequency from the clock to the Rydberg state, we will have again $\Omega_{317} = 2\pi \times 3.5 \text{ MHz}$. Although now we are considering the 3P_1 state instead of the 3P_0 , we used the same RDME since we assume the corrections to be small, as the dominant contribution is given by the spatial extension of the Rydberg wavefunction. The Rabi frequency of the red photon transition can be obtained by inverting an alternative definition of the saturation parameter s :

$$s = 2 \frac{|\Omega_{689}|^2}{\Gamma_{^3P_1}^2} \quad \rightarrow \quad \Omega_{689} = \sqrt{\frac{s}{2}} \Gamma_{^3P_1}. \quad (3.32)$$

With the peak intensity of the 689 nm laser beam, for which the maximum power available is $P_{689} = 500 \text{ mW}$ and the saturation intensity is $I_s = 3 \mu\text{W}/\text{cm}^2$, we get $\Omega_{689} = 2\pi \times 1.7 \text{ MHz}$, where the beam shape considered is once again the elliptical shape $w_{0,x} = 20 \mu\text{m}$ and $w_{0,z} = 500 \mu\text{m}$. This high intensity results in significant saturation of the transition, broadening the line to $\Gamma_{^3P_1,\text{sat}} = \sqrt{s+1} \cdot \Gamma_{^3P_1} = 2\pi \times 2.4 \text{ MHz}$. If the two-photon transition is driven with a detuning comparable to this saturated linewidth, the intermediate state becomes substantially populated, affecting the fidelity of coherent Rabi oscillations. Instead, if the detuning is too large, the achievable Rabi frequency becomes very small.

To optimize the balance between two-photon Rabi frequency and fidelity, we simulated the population dynamics of a three-level system using the Optical Bloch Equations (OBE) [58]. The time evolution of the populations in the ground state (1S_0), intermediate state (3P_1), and Rydberg state is shown in Fig. 3.7. A sine function is fitted to the populations of the ground and Rydberg states to extract the Rabi frequency and the coupling fidelity, which corresponds to the amplitude of the sine function. By varying the Rabi frequency of the first photon Ω_{689} , and the detuning Δ , we generated the heatmaps shown in Fig. 3.8. The left plot represents the two-photon Rabi frequency, while the right one shows the coupling fidelity. The fidelity is strongly

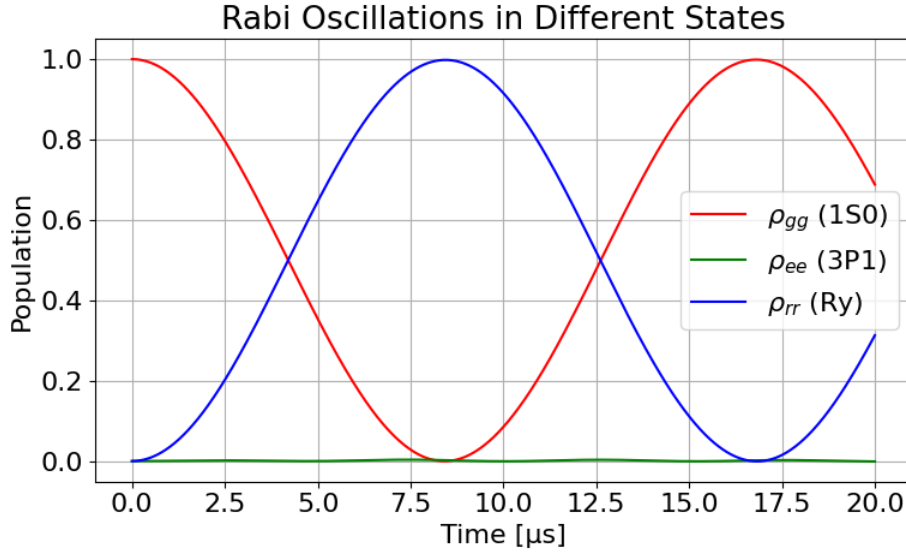


FIGURE 3.7: Rabi oscillation between the ground and Rydberg state in the two-photon excitation scheme for $\Omega_{689} = 2\pi \times 1.7$ MHz, $\Omega_{317} = 2\pi \times 3.5$ MHz, $\Delta = 2\pi \times 50$ MHz. If the detuning of the first photon from the intermediate state 3P_1 is large enough (see text) the transition is driven coherently and the 3P_1 state population remains negligible.

dependent on Δ but nearly independent on Ω_{689} . To achieve a fidelity larger than 99.8%, the detuning must be set to $|\Delta| > 2\pi \times 40$ MHz. However, increasing the detuning reduces the Rabi frequency, while a higher Ω_{689} increases it. For $\Omega_{689} = 2\pi \times 1.7$ MHz and $\Delta = 2\pi \times 40$ MHz, the two-photon Rabi frequency is $\Omega_{\text{Ryd},689} = 2\pi \times 74$ kHz, with 99.8% fidelity. To achieve a fidelity of 99.9%, the detuning must be increased to 50 MHz, resulting in a Rabi frequency of $\Omega_{\text{Ryd},689} = 2\pi \times 59$ kHz. Further increasing the red photon Rabi frequency would require either more laser power or reducing the beam size to increase the intensity. The first option is currently not feasible, as we are already considering the maximum available laser power. Reducing the beam size below $w_{0,x} = 20$ μm would make alignment with the tweezer array extremely challenging and require high pointing stability to keep the Gaussian beam well-centered on the array.

In conclusion, while two-photon Rabi coupling is easier to access experimentally, since we don't need an ultranarrow laser source (like the clock laser) and we can directly employ the same laser that is already used for the red MOT, it demands careful control to ensure coherent driving. The highest achievable Rabi frequency is on the order of tens of kHz, which is approximately 50 times smaller than the coupling possible with a two-step scheme. The latter is more complex, as two separate single-photon transitions have to be addressed, but allow for faster and coherent drive of the Rydberg transition. The two-photon sequence will be soon implemented in the lab, as we already have the necessary laser systems. Then, the two-step method might be explored later when the clock laser will be purchased too.

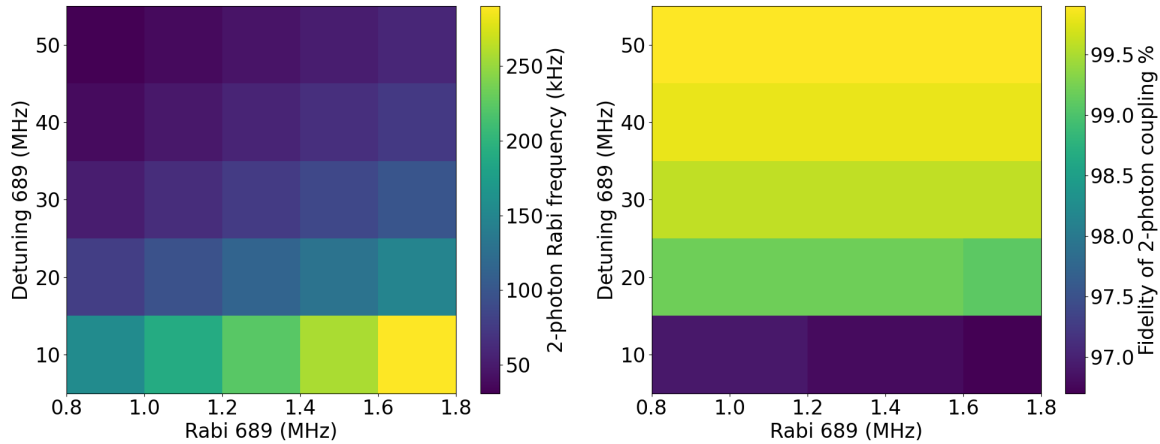


FIGURE 3.8: Two-photon Rabi frequency (left) and fidelity of the two-photon Rabi oscillation (right) as a function of Ω_{689} and Δ .

3.2.3 Rydberg blockade

An interesting effect arising from Rydberg excitation is the so-called *Rydberg blockade*. This phenomenon occurs when two atoms close to each other experience the strong van der Waals interaction described above. The interaction prevents both atoms from being simultaneously excited to the Rydberg state. Essentially, if one atom is excited to a Rydberg state, the strong interaction shifts out of resonance the transition for the nearby atoms. This effect creates a *blockade radius* R_b within which only one atom can be excited to the Rydberg state. Although the van der Waals interaction is not a step function but decays with the distance as R^{-6} , a threshold can be set to the interaction radius for which the strength of the van der Waals interaction equals the Rabi coupling:

$$\frac{C_6}{R^6} = \hbar\Omega_{Ry} \quad (3.33)$$

which can be solved for R to find the blockade radius:

$$R_b = \left(\frac{C_6}{\hbar\Omega_{Ry}} \right)^{\frac{1}{6}}. \quad (3.34)$$

The blockade radius can be tuned by choosing a Rydberg state with a different n , which modifies the C_6 coefficient. The blockade mechanism is central to many quantum simulation and computation schemes, as it enables the creation of entangled states. Indeed, if two atoms initially in the ground state $|gg\rangle$ are excited by a global beam, the doubly excited state $|rr\rangle$ will be unaccessible because of the blockade mechanism, and the system will evolve in a collective entangled state

$$|\psi_+\rangle = \frac{(|gr\rangle + |rg\rangle)}{\sqrt{2}} \quad (3.35)$$

with an enhanced coupling $\sqrt{2}\Omega$ [13]. It is straightforward to extend this effect to multiple atoms: if instead of just a pair of atoms, we have N atoms within the radius of the blockade, the blockade will allow just one atom to be excited and the remaining

$N - 1$ will remain in the ground state. A sketch of such configuration in a 2D square array is shown in Fig. 3.9. Similarly to the two atoms case, the system will evolve

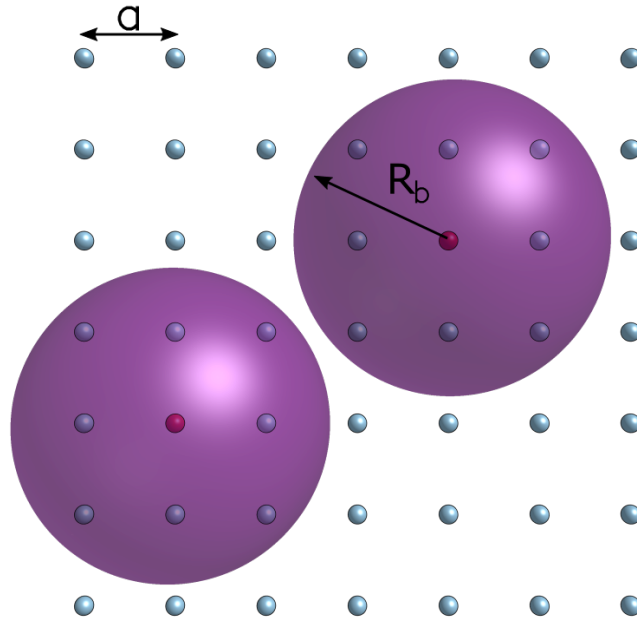


FIGURE 3.9: Sketch of the Rydberg blockade mechanism in a 2D square array. The blockade radius extends beyond nearest-neighbors and next nearest-neighbors (on the square diagonal). Once an atom is in the Rydberg state, the excitation of all the others within R_b will be prevented by the strong long-range interaction, thus generating a multi-particle entangled state.

from the N -atoms ground state $|g \dots g\rangle$ into a multiparticle entangled state:

$$|\psi_N\rangle = \sum_{i=1}^N \frac{|g \dots g r_i g \dots g\rangle}{\sqrt{N}} \quad (3.36)$$

with a collective Rabi frequency $\sqrt{N}\Omega$. In a packed array of atoms in optical tweezers, this collective effect can introduce long-range correlations extending to several sites. Moreover, since both the blockade radius and the interatomic distance are adjustable, with the latter being controlled by varying the trap distance in the tweezer array, the number of atoms affected by the blockade mechanism can be highly tunable.

3.3 Quantum simulation and computation

In the previous sections, we have outlined the technical framework of Rydberg atoms in defect-free arrays of optical tweezers. This platform demonstrates high flexibility, allowing for the creation of multi-dimensional arrays of single atoms with arbitrary geometries and tunable inter-atomic spacing. Moreover, it enables fast, long-range interactions via Rydberg excitation, providing a powerful tunable tool for manipulating atomic states over large distances. In this section, we will explore in detail the quantum simulation applications that leverage these capabilities, highlighting how this

platform is perfectly suited to investigate phenomena in quantum spin models, quantum phase transitions, quantum annealing and optimization problems. Additionally, we will briefly discuss other potential research directions, such as the implementation of quantum gates, which represents the building block towards the implementation of digital quantum computing protocols. We will not focus here on other interesting research lines that have already been implemented with this platform, such as quantum metrology (see Refs. [48, 49] for experimental applications to optical clocks).

3.3.1 Quantum simulation of spin models

A promising research line that we aim to investigate with this platform is the study of spin systems. Rydberg atoms in optical tweezers have already been shown to be very well suited for simulating the behavior of different spin Hamiltonians in both one and two dimensions, as discussed in Refs. [13, 15, 114, 115]. The first experimental realizations of Ising spin models were demonstrated in Refs. [116, 117, 118, 119], where van der Waals interactions between identical Rydberg states were engineered to investigate the generation of anti-ferromagnetic (AFM) ordering and the properties of the quantum phase transition between ferromagnetic (FM) and AFM ordering. Subsequent studies used anisotropic dipole-dipole interactions between different Rydberg states to explore systems driven by an XY-spin Hamiltonian [120, 121]. More recently, 2D arrays with hundreds of atoms implementing Ising Hamiltonians have also been achieved [33, 34]. Interestingly, the tweezer array can be initialized in a so-called frustrated geometry, like a triangular or Kagome lattice, to study the evolution of the system under frustration [122].

The Hamiltonian for an ensemble of atoms, where the ground state $|g\rangle$ is coherently coupled to a Rydberg state $|r\rangle$ by a global laser field with Rabi frequency Ω and detuning δ , can be mapped directly onto a spin-1/2 quantum Ising model, with the two states in the spin basis identified as $|\downarrow\rangle = |g\rangle$ and $|\uparrow\rangle = |r\rangle$. The resulting Hamiltonian is [13, 15]:

$$H = \frac{\hbar\Omega}{2} \sum_i \sigma_x^i - \hbar\delta \sum_i n_i + \sum_{i<j} V_{ij} n_i n_j, \quad V_{ij} = \frac{C_6}{R_{ij}^6}, \quad (3.37)$$

where \hbar is the reduced Planck's constant, n_i is the operator counting the number of Rydberg excitations at site i , and σ_x^i is the Pauli matrix at the site i . By explicitly writing the number of Rydberg excitations as $n_i = (\sigma_z^i + 1)/2$, which is valid as each site is occupied by just one atom that can be either in the ground ($n_i=0$) or Rydberg ($n_i=1$) state, this Hamiltonian can be related to the Ising Hamiltonian [123]. The first term represents the interaction of the spin with a transverse magnetic field $B_\perp \propto \Omega$, while the second term mimics the interaction with a longitudinal field $B_\parallel \propto -\delta$. The Ising coupling $J_{ij} = V_{ij}$ decays with the distance between atoms R_{ij} as $1/R_{ij}^6$. Since we are considering a uniform global Rabi coupling, which can be achieved through two approaches in Strontium as described in Subs. 3.2.1, Ω and δ are not site-dependent. However, the Hamiltonian can be engineered to include site-dependent Rabi frequencies and detunings by addressing individual tweezer array sites with an additional laser, for instance by overlapping the tweezer array with an addressing array generated by a separate SLM path or crossed AODs.

Let's consider a 1D chain or a 2D square array driven by the Hamiltonian in Eq. 3.37. If we take into account just nearest-neighbour interactions between Rydberg occupations in sites i and $i + 1$, $V_{i,i+1} = V$, the effect of the van der Waals interaction will favour antiferromagnetic ordering since $V > 0$. However, in the limit of $\Omega, \delta \gg V$, the spins will align along the direction of the effective magnetic field, which dominates the energy of the system. In the real system, the van der Waals interaction strength depends on the distance between the sites and decays rapidly with increasing distance. We can use the notion of blockade radius R_b defined in Subs. 3.2.3 to set a threshold: for large distances, the Rabi coupling dominates the energy scale and the interaction only gives a marginal contribution, while for small distances, the interaction can overcome the Rabi frequency, significantly affecting the spin population of the ensemble. The blockade radius is defined as the threshold distance for which the Rabi coupling and van der Waals interaction are equal, meaning that the energy contributions of the first and third terms in Eq. 3.37 are equal.

If the blockade radius extends to multiple sites of the array, the approximation of only nearest-neighbour interaction is no longer valid. In particular, the interaction can be the dominant energy scale for nearest-neighbours, but become negligible for next nearest-neighbours: $V_{i,i+1} \gg \Omega, \delta \gg V_{i,i+2}$, thus resulting in antiferromagnetic (AFM) ordering. By tuning the interaction range and/or the distance between the sites of the tweezer array, the blockade radius can extend to multiple array spacings a . For $R_b = 2a$, the energy scales hierarchy is $V_{i,i+1} \gg V_{i,i+2} \gg \Omega, \delta \gg V_{i,i+3}$, resulting in a ground state of the ensemble of atoms with one Rydberg excitation followed by two ground state atoms (showing Z_3 symmetry [124]).

Typically, during an experiment, the interaction term is constant, while Ω and δ can be adjusted to investigate different regimes. A common approach is to initialize the system in a trivial state, such as the paramagnet, and suddenly change one of the experimental parameters, a procedure often called *quenching*, to observe the evolution of the system under the Ising-like Hamiltonian. The single-site resolution allows for measuring both the total magnetization of the system, which is defined as the fraction of Rydberg excitations ($|\uparrow\rangle$) over the total number of atoms, and the spin-spin correlation function, which is the probability of finding a Rydberg excitation in site j if one is already present in site i .

We can now extend this system to the XY model by considering atoms excited to different Rydberg states that are dipole-coupled, such as $|nS\rangle$ and $|nP\rangle$, typically separated by a few GHz. These two states can again serve as spin basis: $|\downarrow\rangle = |nS\rangle$ and $|\uparrow\rangle = |nP\rangle$. The dipole-dipole interaction induces a coherent exchange of the internal states of the atoms, and the interaction potential scales as C_3/R^3 , where C_3 is the interaction coefficient, and R is the distance between the atoms. The corresponding XY spin Hamiltonian, where a microwave field coupling $|nS\rangle$ and $|nP\rangle$ states is used to drive the effective external magnetic field, is expressed as [13]:

$$H = \frac{\hbar\Omega_{\mu w}}{2} \sum_i \sigma_x^i - \frac{\hbar\delta_{\mu w}}{2} \sum_i \sigma_z^i + \sum_{i \neq j} \frac{C_3}{R_{ij}^3} (\sigma_+^i \sigma_-^j + \sigma_-^i \sigma_+^j) \quad (3.38)$$

where $\Omega_{\mu w}$ and $\delta_{\mu w}$ are the Rabi frequency and detuning of the microwave field. In this model, the first term represents the interaction of the spins with a transverse microwave field, inducing coherent oscillations between $|nS\rangle$ and $|nP\rangle$, analogous to

flipping between $|\downarrow\rangle$ and $|\uparrow\rangle$. The second term corresponds to an effective longitudinal magnetic field that detunes the two spin states, controlling their relative population. The third term describes the dipole-dipole interaction between atoms, resulting in a coherent exchange of their internal states. The dipole-dipole interaction decays as $1/R^3$, making it most significant for nearest-neighbours, while also allowing for next-nearest-neighbour interactions depending on the distance between the atoms. The competition between the exchange interaction and the external magnetic field terms can be adjusted by tuning the Rabi frequency $\Omega_{\mu w}$ and detuning $\delta_{\mu w}$, exploring different regimes where collective phenomena, such as quantum phase transitions, can be observed.

While both the Ising and XY spin models have been extensively explored, many important questions remain open, which can be effectively addressed using this platform. These include the impact of geometrical frustration, an exhaustive exploration of the system's phase diagram, understanding the dynamic response to sudden changes in the Hamiltonian's parameters, and investigating the influence of disorder and defects within the system. 3D spin models such as XXY [125] and XYZ [126, 127] have been explored, as well as the role of quantum gauge fields in a 2D ladder [128]. In this context, arrays of Rydberg atoms in optical tweezers enable extremely fine control of the array geometry and interaction strength, allowing for a precise study of these models. Additionally, the potential applications extend beyond many-body quantum simulations. It has been shown that several combinatorial problems can be mapped onto spin models [129], as discussed in the next subsection.

3.3.2 Optimization protocols and quantum annealing

The natural implementation of spin models in this platform makes it suitable for solving computationally complex problems. Indeed, many computational NP-complete and NP-hard problems have been shown to map onto a spin Hamiltonian [129]. Adiabatic quantum optimization (AQO) is a possible method to efficiently solve such problems. The basic concept behind AQO is as follows: suppose we have a quantum Hamiltonian H_P whose ground state encodes the solution to the problem, and another Hamiltonian H_0 whose ground state is trivial to prepare experimentally. We begin by preparing the system in the ground state of H_0 , and then adiabatically change the Hamiltonian to H_P over a time T according to the following interpolation:

$$H(t) = \left(1 - \frac{t}{T}\right) H_0 + \frac{t}{T} H_P, \quad (3.39)$$

If T is large enough, H_0 and H_P do not commute and the system remains in the ground state of $H(t)$ for all the times, as guaranteed by the adiabatic theorem of quantum mechanics [130]. Measuring the state of the system at time T gives the ground state of the target Hamiltonian, which corresponds to the solution of the problem. Once the computational problem has been mapped onto a spin Hamiltonian, implementing it on the experimental platform is relatively straightforward, as the main complexity lies in achieving the desired connectivity between the spins. This can be accomplished by adjusting the geometry of the array, the Rydberg interaction range, and possibly by introducing ancilla spins [131, 132, 133, 134]. The system can be initially prepared in a simple H_0 Hamiltonian, such as the paramagnetic configuration mentioned above,

and then evolved into the nontrivial H_P Hamiltonian by sweeping a system parameter, such as the detuning δ . The system will naturally evolve towards the final ground state, guided by the combination of the effective magnetic field and interactions. One limitation of this method is the time T required to maintain adiabaticity. As the system size N increases, the energy gap between the ground state and the excited states of $H(t)$ becomes exponentially small [129], meaning the time required to solve the problem can increase, making the process comparable to solving the problem on a classical computer. Furthermore, finite temperatures in the experiment can introduce fluctuations that might break the adiabatic evolution of the system.

To circumvent these limitations, experimental implementations often rely on quantum annealing algorithms, which are a finite-temperature generalization of AQO [129, 135]. Quantum annealing allows for faster evolution since it does not strictly require adiabatic conditions. However, this faster evolution often leads to finding a local minimum rather than the global minimum. Additionally, there are protocols designed to speed up the system evolution, referred to as *shortcuts to adiabaticity* [136], where the dynamics are deeply non-adiabatic but can still produce a solution close to the optimal one [137].

3.3.3 Quantum gates for quantum computing

Rydberg atom arrays also offer a powerful platform for digital quantum computing, by exploiting the strong, long-range Rydberg interaction. The Rydberg blockade mechanism can be leveraged to implement quantum gates, as it prevents multiple nearby atoms from being simultaneously excited, enabling precise control over qubit interactions. This approach allows for the creation of quantum gates in a flexible and scalable geometry, thus allowing for the implementation of large quantum registers [14, 138, 139, 140, 141]. Several different approaches have been proposed and realized experimentally, in platforms based on both alkali atoms [142, 143, 37, 36, 144, 87] and alkaline-earth atoms [45, 44, 145, 146, 46]. To build a universal quantum computer, the physical platform must satisfy several essential criteria. A well-known formulation of these key criteria take the name of *Di Vincenzo criteria* [147]. These include the ability to encode and scale quantum bits (qubits), initialize them in a known state, and maintain long coherence times to preserve quantum information during the computation. The platform must also support a universal set of quantum gates, allowing for any single- or multi-qubit operations, and the possibility of high-fidelity qubit measurements to read the output of the computation. Specifically, single-qubit gates and two-qubit entangling gates, such as the CNOT gate, form a universal set of quantum gates, as any multi-qubit operation can be decomposed into these two types of gates [148, 14, 139, 141].

Various approaches are used to encode qubits in two internal states of atoms, depending on the atomic species and the requirements of the experiment. Often, states that are isolated from the environment, such as hyperfine ground states in alkali atoms like Rubidium [142, 143, 36, 144] and Cesium [37], or fermionic Ytterbium [42, 44], are selected. For bosonic isotopes of Strontium and Ytterbium, which lack a hyperfine structure, qubits can be encoded in ground and clock states [45, 46, 47].

Single-qubit operations are performed by coherently driving transitions between the $|0\rangle$ and $|1\rangle$ states, to realize arbitrary rotations on the Bloch sphere representing

the qubit state. This can be realized by exploiting the optical clock transition if the qubit is encoded in the ground state and metastable clock state, or with a Raman transition if it is encoded in different hyperfine states. The system is scalable to hundreds or thousands of single atoms, as described in Subs. 3.1.2, and state readout is detailed in Chapter 4. To fully satisfy the Di Vincenzo criteria, a protocol for implementing two-qubit entangling gates is required to form, together with single-qubit operations, a universal set of quantum gates

Specifically, controlled-Z (CZ) gates can be realized using the Rydberg blockade mechanism [138, 142, 141], while the CNOT gate can be obtained by combining a CZ gate with single-qubit operations [148]. The principle involves utilizing the blockade effect in a logical operation involving both single-qubit operations and Rydberg excitation. Since the atoms can be excited only from $|0\rangle$ to $|r\rangle$, the phase acquired by a target atom will be different if the control atom is in $|1\rangle$ rather than in $|0\rangle$. By properly combining the laser pulses, it's possible to implement the CZ and CNOT gates, which take the following matrix form:

$$\text{CZ} = \begin{pmatrix} 1 & 0 & 0 & 0 \\ 0 & 1 & 0 & 0 \\ 0 & 0 & 1 & 0 \\ 0 & 0 & 0 & -1 \end{pmatrix} \quad \text{CNOT} = \begin{pmatrix} 1 & 0 & 0 & 0 \\ 0 & 1 & 0 & 0 \\ 0 & 0 & 0 & 1 \\ 0 & 0 & 1 & 0 \end{pmatrix}. \quad (3.40)$$

More advanced sequences have been developed to enhance the fidelity of single- and two-qubit operations. While these operations form a basis for any universal quantum gate, more efficient protocols may incorporate multi-qubit gates. These gates represent a natural extension of two-qubit gates, which can be achieved through the long-range interactions of Rydberg atoms [142, 139]. Additionally, computational complexity can be further increased by employing a multi-level computational basis in *qudits*. Such schemes have been proposed for fermionic ^{87}Sr [149, 150], which has a nuclear spin $I = 9/2$, offering 10 hyperfine ground states ($J = 0$) for encoding quantum information. By employing a deeper computational basis, more information can be stored within a single qudit, reducing the need to scale up the number of qubits.

Chapter 4

Site-resolved single-atom imaging

In this chapter we will discuss the techniques to detect single atoms trapped in optical tweezers via fluorescence imaging. So far, two different schemes have been demonstrated for strontium, one working on the blue $^1S_0 \rightarrow ^1P_1$ [39, 76, 41, 77] and one on the red $^1S_0 \rightarrow ^3P_1$ [43] transition. Fluorescence imaging is used in several platforms to detect single atoms [151, 152, 153, 23, 24, 154, 155, 156, 157]. We aim to achieve two key objectives with this imaging. First, detect with high precision the presence or absence of an atom. Second, the detection process has to be non-destructive, i.e. the detected atoms must not be expelled from the trap. We will quantify the level of confidence in achieving these two objectives with two figures of merit that will be described in the following: *detection fidelity* and *survival probability*. To detect atoms with high fidelity, a sufficient number of scattered photons have to be detected to distinguish the atomic signal from the background. During the scattering process, it is crucial to ensure that the atom does not end up in a dark state, where it can no longer scatter photons, and to prevent the atom from being expelled from the trap due to excessive heating. Ensuring a high survival probability is instead the key to create a large defect-free array of atoms.

We will first describe these two techniques, followed by a brief discussion of two potential new approaches that could enhance the established methods by reducing imaging time while maintaining the same level of fidelity.

4.1 Imaging using the blue transition

The first scheme, exploiting photon scattering from the broad $^1S_0 \rightarrow ^1P_1$ transition, has been implemented in different platforms with strontium [39, 76, 41, 77] and with ytterbium [42, 152] that has a similar level structure.

In this scheme the blue imaging light illuminates the atoms together with a red cooling light to ensure that the atoms do not escape the trap due to excessive heating induced by the energetic blue-photon scattering. The $^1S_0 \rightarrow ^1P_1$ transition is not

exactly a closed transition, the 1P_1 state having a small decay channel to 1D_2 , from which the metastable 3P_2 state is populated, as described in Subs. 1.3.2. A repumper laser at 707 nm removes the atoms from the 3P_2 dark state exciting them to the 3S_1 state, from which they can decay to all the three states in the 3P_J manifold. Then, another laser at 679 nm is necessary to remove atoms from the clock state and repump them into the imaging cycle. Indeed, the only state that gets populated due to the small decay channel from 1P_1 state is the 3P_1 state, from which the atoms spontaneously decay back to the ground state. In this way the cooling cycle is a closed loop, thus avoiding any infidelity in single atom detection due to dark states population. The repump transitions are MHz-broad transition, thus populating the 3P_1 state instantaneously if compared to the timescale set by the $^3P_1 \rightarrow ^1S_0$ decay rate. A schematic representation of the relevant levels and transition for this scheme is reported in Fig. 4.1

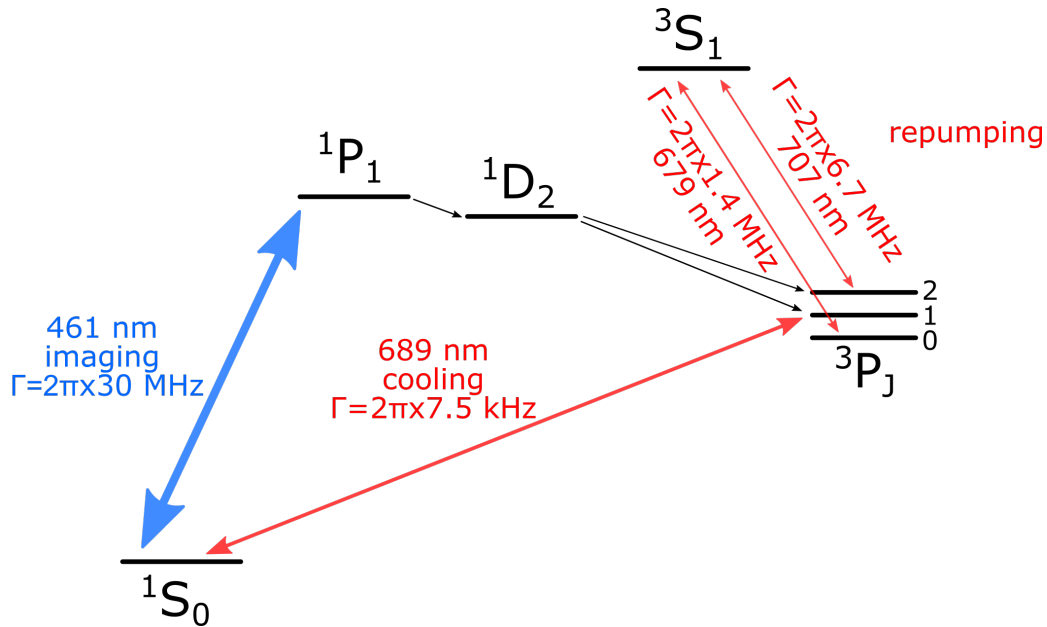


FIGURE 4.1: Energy levels involved in the blue imaging scheme. The atoms are detected by collecting the 461 nm photons scattered during the illumination with the blue imaging light. The atoms are heated during this process, so a cooling beam exploiting the narrow $^1S_0 \rightarrow ^3P_1$ transition keeps them close to the motional ground state of the trap. Repumpers are necessary to remove atoms that may decay to dark states in the 3P_J manifold via the small leakage channel of the 1P_1 state.

The imaging beam scattering rate can be tuned according to Eq. 2.2. While the maximum scattering rate is $R_{sc} = \Gamma/2$, it is convenient to work in a lower scattering rate regime to allow the cooling beam to compensate for the heating induced by blue photon scattering, which could cause atom loss and therefore a lower detection fidelity [39, 76, 41]. The maximum scattering rate of the blue transition is $R_{sc,max}(461 \text{ nm}) \simeq 95 \text{ MHz}$, while it is just $R_{sc,max}(689 \text{ nm}) \simeq 23 \text{ kHz}$ for the red transition. Therefore, to have an effective Sisyphus cooling on the red transition and keep the atoms in tweezers, the blue scattering rate is typically limited to $R_{sc} \sim 75 \text{ kHz}$ for trap depths on the order of $U_0 = 500 \mu\text{K}$ [39, 76, 41]. Moreover, since the red transition is

saturated in Sisyphus cooling (see Subs.2.4.3), the atom is shelved in the 3P_1 state for a significant fraction of the imaging time, limiting the time in which blue photons can be scattered. For this reason, it is possible to alternate many blue imaging and red cooling cycles to make the two processes independent, collecting all the blue photons that are scattered during multiple cycles. Additionally, unless the atoms are confined at a magic wavelength for the blue transition, the tweezer light causes a differential light shift on the imaging resonance. At 813.4 nm tweezer light the excited 1P_1 state is more tightly trapped than the ground state 1S_0 , thus the resonance is red detuned. The differential light shift is approximately -6.7 MHz for a trap depth of 200 μK , considering the polarizabilities of the 1S_0 and $^1P_1(|m_J| = 1)$ states in Tab. 2.1. The value is very similar even considering the $^1P_1(m_J = 0)$ state. It is useful to red-detune the imaging light so that the scattering rate is highest at the center of the trap, where the light shift is strongest, and decreases toward the edges of the tweezer. In this way, as the atom heats up and gains kinetic energy within the trap, the scattering rate naturally reduces, which helps in keeping the atom confined in the trap (and also facilitates the action of the cooling light).

Since the scattering rate can be adjusted by changing both the detuning and the laser intensity, a balance between these two factors must be found experimentally. If the detuning is too large, a higher laser intensity is needed to achieve a reasonable scattering rate, but this could lead to background photon scattering from the surfaces of the science cell, which may be captured by the objective and obscure the atom signal. If, instead, the intensity is very low, the detuning has to be reduced to increase the scattering rate. The closer the beam frequency is to the atomic resonance, the more sensitive the scattering rate is to small frequency variations. This is not a problem if a single imaging beam is used. However, if two counterpropagating beams are employed to balance the blue-photon recoil, their frequencies must be slightly different to avoid generating a standing wave on the atoms. In this case, it is convenient to maintain both frequencies away from the resonance such that the scattering rate for the two beams remains similar despite the slightly different frequency.

4.2 Imaging using the red transition

The second imaging scheme combines detection and cooling using a single laser beam addressing the $^1S_0 \rightarrow ^3P_1$ transition. As already demonstrated in tweezers platforms both with strontium [43], and ytterbium [40, 44], the photons re-emitted in the cooling cycle can be collected to detect the atoms. The advantage of such scheme with respect to the blue one is that it requires in principle just one imaging beam and the atom at the end of the sequence is still in the trap motional ground state as the cooling process was always on. Nonetheless, the blue scheme can achieve higher scattering rates than the red since the red transition is limited by the way narrower Γ . A sketch of the energy levels involved in this scheme is reported in Fig. 4.2. Unlike the blue scheme, the only mechanism through which the 3P_2 and 3P_0 dark states can be populated is via off-resonant scattering of the tweezer light at 813.4 nm [70, 43], which is suppressed for shallow tweezer traps. The lasers pumping the population out of the dark states are then not necessary. The two schemes also differ for the achievable optical resolution, since the diffraction limit is 1.5 larger at 689 nm with respect to 461 nm, and for the

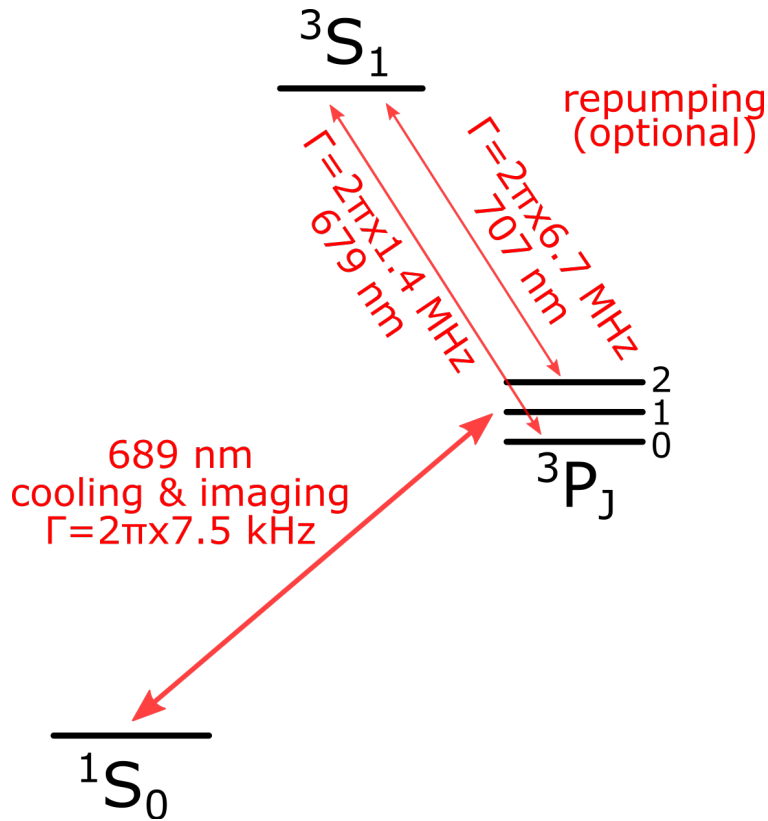


FIGURE 4.2: Energy levels involved in the red imaging scheme. In principle, a single red beam at 689 nm can be used for Sisyphus cooling of the atoms in tweezers, and the scattered photons can be collected to detect the single atoms. Repumpers are not explicitly required as the $3P_0$ and $3P_2$ states can only be populated via off-resonant scattering of tweezer light at 813.4 nm which is suppressed for low trap depths.

recoil energy of the photons, which is instead lower for the red photons, thus allowing for shallower traps without losing the atoms.

A single laser beam with a fixed direction and polarization can be used for cooling, imaging, and light-assisted collisions, as described in Ref. [43]. However, the optimal beam parameters, such as detuning and laser power, differ between cooling and imaging. Imaging requires the highest possible scattering rate, which does not match the optimal cooling conditions. Specifically, imaging performs best with light that is red-detuned by a few kHz and has a high saturation intensity, whereas optimal cooling requires a larger red detuning and lower saturation [43]. Two potential approaches to address this are either operating under the optimal imaging conditions while accepting suboptimal cooling or alternating between the two processes. In the latter case, the duty cycle can be fine-tuned experimentally, alternating long imaging periods (~ 10 ms) to short cooling intervals (~ 1.5 ms), as effective cooling can occur within a short timescale, for a total duration of approximately 100 ms [70, 43].

4.3 Atomic fluorescence collection

So far, we have described two different methods for inducing the emission of a fluorescence signal. In this section, we will focus on how to collect the scattered photons in order to detect the presence or absence of single atoms. This process has to be highly efficient, as every photon plays a crucial role in distinguishing the atom's signal from the background. To maximize the signal, every aspect of the detection system, from the radiation pattern to the imaging setup and camera, must be carefully optimized.

4.3.1 Dipole radiation

The polarization of the imaging beam plays an important role as it determines the radiation pattern of single atoms. If we imagine the atom as a classical dipole, its emission will be nonuniform, in particular the radiation will be maximal in a plane orthogonal to the dipole oscillation, which is set by the polarization of the imaging beam. The fluorescence radiation pattern of an atom decaying from an excited state with total angular momentum J_e to a ground state with J_g can be derived in a general case as in Ref. [66]. Both the fluorescence imaging schemes demonstrated so far involve the ground state with $J_g = 0$ and an excited state with $J_e = 1$ (1P_1 or 3P_1). This simplifies the general expression in two cases, when linearly or circularly polarized light is used, as derived in Ref. [69]:

$$\begin{aligned} D(\theta, \phi) &= \frac{3}{8\pi} \sin^2(\theta) \text{ [for } \pi \text{ polarized light]} \\ D(\theta, \phi) &= \frac{3}{16\pi} (1 + \cos^2(\theta)) \text{ [for } \sigma_{\pm} \text{ polarized light]} \end{aligned} \quad (4.1)$$

where θ is the angle from the quantization axis \hat{z} and ϕ is the azimuthal angle. The polarization should be chosen to maximize the radiation in the direction of the microscope objective. If π -polarized light is employed, the radiation is maximized at $\theta = 90^\circ$, while for σ -polarized light $\theta = 0^\circ$ is the optimal angle. In our case the convention about the cartesian reference axes is defined in Chapter 5. The objective axis is labeled as \hat{x} , the orthogonal axis in the horizontal plane is \hat{y} and the vertical axis is \hat{z} . The imaging beam propagates along \hat{z} and is linearly polarized along \hat{y} to maximize the fluorescence along the objective's axis \hat{x} . In this specific case, the collection efficiency C of the emitted fluorescence can be expressed in terms of the numerical aperture NA [69]:

$$C = \frac{1}{8} \left(4 + (NA^2 - 4) \sqrt{1 - NA^2} \right). \quad (4.2)$$

Plugging in the value of the numerical aperture for our objective $NA = 0.56$ at 461 nm (see Tab. 5.6), we get a maximum collection efficiency $C = 0.118$.

4.3.2 Imaging system and cameras

In order to detect single atoms, low-noise cameras are fundamental to clear out a signal of a few photons. There are two main types of cameras employed in single-atom detection, electron-multiplying charge-coupled device (EMCCD) [41, 22, 33, 35,

20, 156, 158, 159, 160] and quantitative complementary metal-oxide-semiconductor (qCMOS) [38, 161]. Although these are different technologies, as explained below, both are based on an array of pixels that will reproduce an image of the array of atoms. To do so, an imaging system is used to collect the fluorescence light emitted by the atoms and refocus it, through a microscope objective, onto the camera sensor. The atoms (approximated as point-like sources) are located in the focal plane of the objective, so their image is infinite conjugated. To focus the image on the camera sensor, another tube lens is placed at its focal distance away from the camera. Since the objective is infinitely conjugated for point-like sources, the objective and tube lens do not need to be in 4f configuration. Additional telescopes can be included to change the magnification of the images from one plane to the other. A typical choice is to project the signal of a single atom on a region corresponding to approximately one pixel in the camera plane, such that most of the photons are concentrated in one pixel thus helping the identification of an atom. Since different cameras (both EMCCDs and qCMOSs) have different pixel size, the magnification has to be adapted accordingly. Fig. 4.3 reports a sketch of the minimal setup for fluorescence detection. The imaging

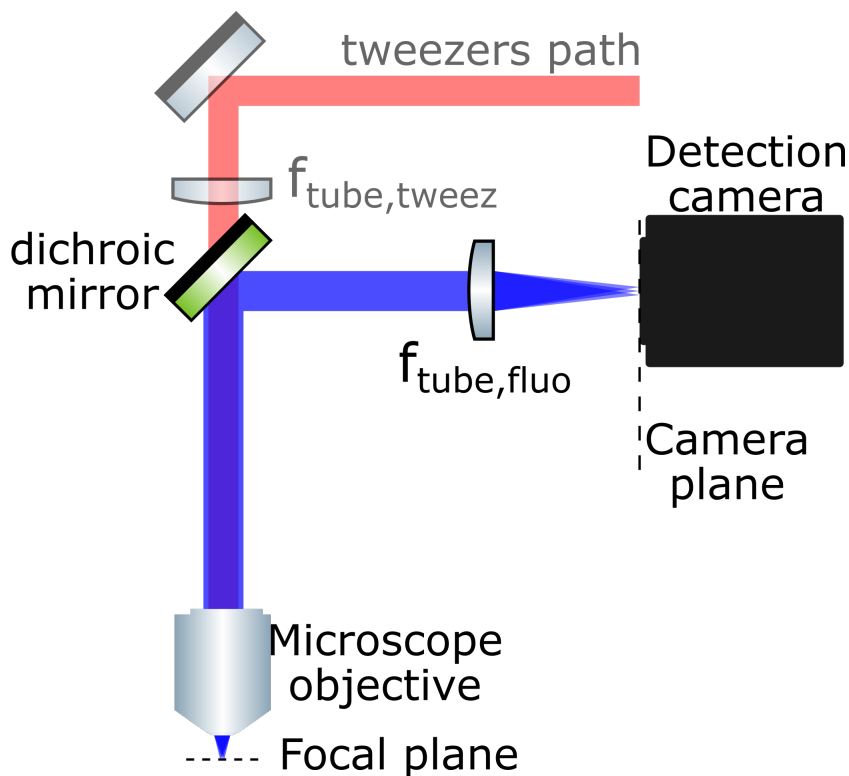


FIGURE 4.3: A single microscope objective is used to focus the tweezer light generating the array of micro traps and to collect the fluorescence imaging light. A dichroic mirror is used to combine the two paths. An imaging tube lens is used to image the focal plane of the objective to the plane of the camera sensor. The size of the fluorescence spots on the sensor is determined by the imaging system magnification, that may include an additional telescope.

path is separated from the tweezer path by a dichroic mirror in a section where the beams are collimated, located just behind the microscope objective. Similarly to what we discussed for the optical tweezers path in Subs. 3.1.1, it's fundamental to minimize

distortions of the fluorescence signal using aberration-corrected lenses. Moreover, the intense tweezer light can produce reflections on the science cell's surface, and even a good quality dichroic might not be enough to filter this background signal out. Bandpass filters can be added along the detection path to select just the light at the correct wavelength.

EMCCD cameras

A CCD sensor converts photons into electrons, or photoelectrons, to count them with a variable gain. In EMCCD cameras, an electron-multiplying (EM) gain is added before the readout register, so as to help in detecting small numbers of photons (see the manual of the EMCCD camera used in our lab in ref. [162]). The EM gain factor multiplies each photoelectron to many secondary electrons in order to overcome the noise electrons due to the analog electronics. During the readout of an image, the photoelectrons are shifted row by row to a shift register. Then, they are transferred into the gain register where they are amplified by an EM gain factor. However, not all the pixel behave the same from shot to shot, so we can expect a distribution in the amplification factor. More specifically, the probability distribution of the number x of secondary electrons produced amplifying n primary electrons is described by the Erlang distribution [158]:

$$P_n(x) = \frac{x^{n-1}e^{-x/g}}{g^n(n-1)!}\theta(x) \quad (4.3)$$

where g is the average EM gain and $\theta(x)$ is the Heaviside step function. For $n = 1$ this distribution is a simple exponential function. What we are interested in is whether the number of secondary photons is large enough to overcome the electronic noise. The overlap between the distribution for n and $n + 1$ initial photoelectrons can be calculated as in Ref. [69] as a function of the EM gain. It turns out that increasing the gain is beneficial to reduce the overlap only when distinguishing $n = 0$ and $n = 1$ cases, whereas for larger numbers of primary photoelectrons the overlap saturates to a constant value. Although Eq. 4.3 is not defined for $n = 0$, we may think of it as a delta function centered in $n = 0$ (intuitively, amplifying zero photoelectrons will always result in zero secondary electrons). While $n=1$ and $n=0$ can be safely distinguished provided that a large enough g to overcome electronic readout noise is used, one has to pay attention to the effect of noise or background electrons entering the EM amplification process and leading to false counts. These can be represented either by clock-induced charges produced during the register shift, or by background-light photons hitting the CCD sensor. This highlights the importance of minimizing background photons in the low-photon regime where we are operating, particularly by reducing unwanted scattered light at λ_{fluo} and filtering out scattered light at other wavelengths. Indeed, if the signal is just one photon that sums up to a background of many photons, the EM gain will not help in clearing out the signal.

qCMOS cameras

A different kind of camera capable of resolving a signal of very few photons is the quantitative CMOS. In our lab we employ the ORCA-Quest C15550-20UP from Hamamatsu (see technical notes in Ref. [163]). This camera has an extremely low readout

noise, thus allowing photon number resolution even in the multiple photons regime. The first difference is that CMOS cameras perform the readout pixel by pixel, whereas CCD cameras have a common readout amplifier at the end of the readout chain. Although each pixel will have a slightly different readout noise from shot to shot, processing the image in parallel allows for much faster readout. Therefore, the camera sensor can be extremely large: Hamamatsu ORCA-Quest qCMOS has a 4096×2304 pixels array while most of the EMCCD cameras have a 1024×1024 sensor. Furthermore, qCMOS cameras can achieve a high signal-to-noise ratio that enables photon counting without the multiplication gain that introduces excessive multiplication noise. The RMS readout noise is lower than 0.3 electron/pixel, making it possible to resolve the peaks corresponding to each photodetection outcome in the probability distribution with less than 5% probability of incorrect photon number classification. Typical EMCCD cameras can reach a readout noise of <0.1 electron/pixel with EM gain, which makes them more suitable for the detection of one photon on a zero photon background. The qCMOS camera is instead more flexible and can prove very useful in all the situations where the background is not exactly zero and a quantitative photon number resolution is necessary. We refer the reader to the manual [163] for a more detailed explanation of the qCMOS camera specifications.

4.3.3 Point-like source PSF

If we neglect the motion of the atom inside the tweezer, which is lower bounded by the characteristic length of the quantum harmonic oscillator, typically on the order of 50-100 nm, the atom can be treated as a point-like source, and the resolution of its image will be diffraction limited according to the imaging setup characteristics. The physics behind this process is the same as described in Subs. 3.1.1, and the corresponding diffraction-limited point spread function is described in Eq. 3.6. In the real case, the measured PSF will be the convolution of the diffraction-limit PSF and any additional aberrations introduced by the imaging system. This sets a lower bound to the minimum distance of two atoms to be distinguishable through the Rayleigh criterion introduced in Eq. 3.8. Additionally, the position of the atom will have some uncertainty due to its motion in the tweezer. Although the displacement of atoms in the vibrational ground state of the trap is much smaller than the diffraction limit, the motion of hot atoms in higher vibrational levels might be not negligible. Therefore, we will assume, conservatively, the maximum uncertainty in the position of the atom in the focal plane of the objective, which is given by the optical tweezer waist itself. This size is magnified by the detection setup depicted in Fig. 4.3 by a factor $M = \frac{f_{\text{fluo,tl}}}{f_{\text{EFL}}}$, where $f_{\text{fluo,tl}}$ is the focal length of the fluorescence tube lens and f_{EFL} is the effective focal length of the objective.

In our case we initially installed an EMCCD camera, Andor iXon Ultra 888, with 1024×1024 array size and $13 \mu\text{m}$ square pixel size. The magnification of the detection setup was determined by just one tube lens with focal length $f_{\text{fluo,tl}} = 500$ mm and the objective's $f_{\text{EFL}} = 24$ mm. That gave a magnification of roughly $20\times$ to spread the fluorescence signal over 1 pixel. Afterwards, we decided to replace the EMCCD camera with the qCMOS camera from Hamamatsu. This has a different square pixel size of $4.6 \mu\text{m}$ and therefore requires a smaller magnification to maintain the same proportions between the fluorescence PSF size and pixel size. A new tube lens with

$f_{\text{fluo,tl}} = 100$ mm was mounted collinear to the camera sensor on a threaded mount to position it with fine resolution and avoiding aberrations due to the off-axis propagation of the light. In terms of quantum efficiency (QE) the Andor iXon Ultra 888 guarantees a 88% QE at 461 nm ($> 90\%$ at 689 nm), while the Hamamatsu ORCA-Quest has 85% QE at 461 nm ($> 55\%$ at 689 nm).

4.3.4 Binary thresholding

The ultimate outcome of an image analysis is ideally a list of zeros and ones corresponding to either absence or presence of an atom in a particular site of the tweezer array. To be more precise, we should determine whether a particular atom is *visible* or not. To detect its presence we need to collect a sufficient number of photons to say that the signal corresponds to an atom and not to a spurious background signal. First of all, the centroid of each atom's PSF has to be determined. This can be done automatically by running many experiments and averaging several images to determine the position of all the centroids. For instance, the pixels with the highest counts can be taken as the centroid. A more accurate procedure could be fitting a 2D Gaussian profile to the measured PSF to account for the spread of the fluorescence signal over the neighboring pixels. A region of interest (ROI) can be drawn around each centroid. If the magnification is such that the expected PSF is on the order of the pixel size, a fair choice could be to sum the signal of a 3×3 ROI around the pixel corresponding to the centroid. An even further improvement could be to perform a weighted sum, giving more relevance to the pixels with higher counts. Indeed, pixels at the edge of the PSF will give a minor contribution to the signal and might only add noise to the signal if a normal sum is performed. The ROIs of different atoms have to be clearly separated to avoid cross-talks. Finally, to binarize the signals of a ROI, a threshold value must be set such that, if the sum (or weighted sum) of the counts within a specific ROI is larger than the threshold, then we automatically associate the presence of one atom to that tweezer site.

Fidelity

After a single-shot measurement, we obtain a matrix of ROI counts, one for each pixel, which is then compared to a binning threshold. Values above this threshold indicate the detection of an atom, while values below it are interpreted as the absence of atoms. The fidelity F reflects the likelihood that this assignment is correct. This probability depends on the underlying distribution governing the detection of a certain number of photons. The photons that are spontaneously emitted by a fluorescing atom are random and independent events. Therefore, the number of photons detected by an imaging system in a given time interval, the exposure time, follow a Poisson distribution [164], where the central parameter λ is the average number of scattered photons times the collection efficiency of the imaging system:

$$P_n(\lambda) = \frac{\lambda^n e^{-\lambda}}{n!}. \quad (4.4)$$

The photon count distribution is then the convolution of this Poisson distribution and the response function of the detector, i.e. the Erlang distribution for EMCCD

cameras described in Eq. 4.3. The electronics noise of the camera or thermal noise generate background counts in a stochastic process too, thus resulting in a Poisson distribution of background counts. In this case, the average value of the distribution is determined by the specific camera settings and exposure time. This behavior can be verified by collecting a large number of measurement outcomes and constructing a histogram of photon counts (or camera counts) versus occurrences. Repeating the measurement multiple times and/or accumulating data from all the sites in the tweezer array will produce a two-peaked distribution: one peak representing the background or noise counts from the empty sites, and another corresponding to the atomic signal from the occupied sites. An example of such a histogram is shown in Fig. 4.4, where two Poisson distributions with different λ values are simulated. The threshold value

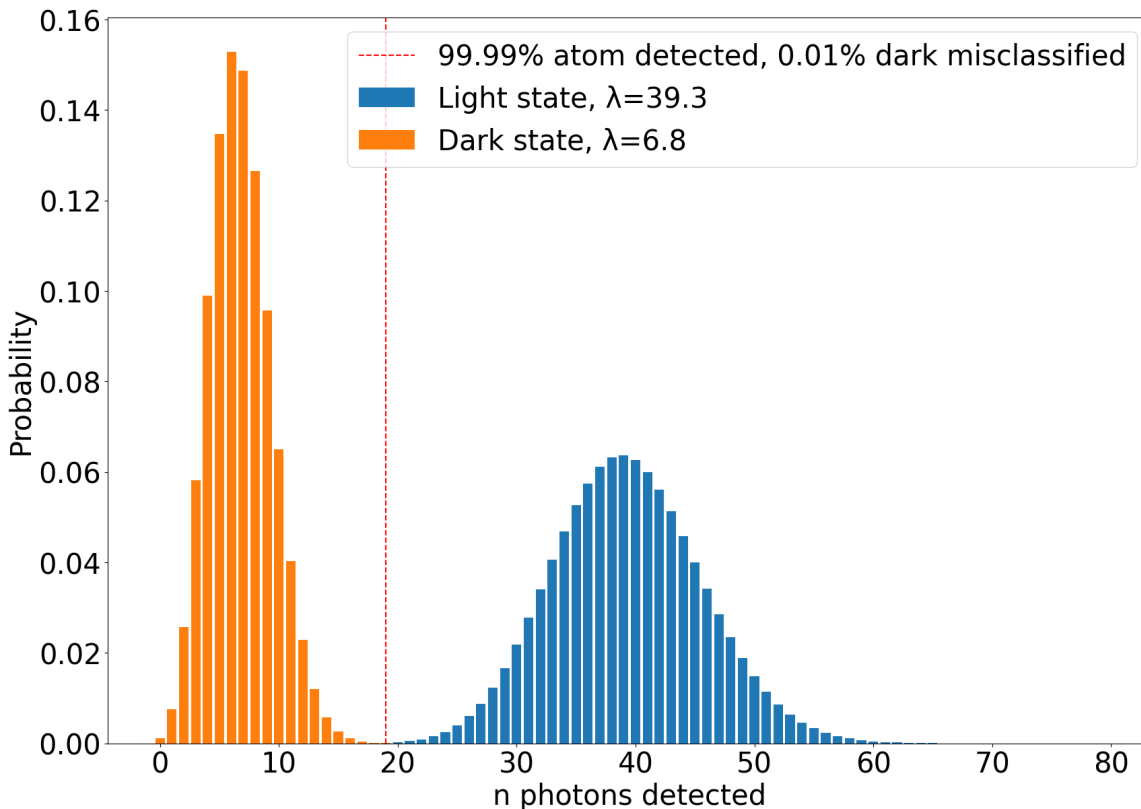


FIGURE 4.4: Simulated histogram for the number of detected photons versus occurrences. The orange histogram represents the distribution of background counts, whereas the blue histogram corresponds to the atomic signal. A threshold, depicted as a vertical dashed line, is set to the n -value that best separates the two distributions. Such histogram is obtained by the raw data distribution by subtracting the offset photon count common to all the pixels and converting the camera pixel counts back to detected photons. The fidelity can be extracted from this histogram by fitting a skewed Gaussian to the background peak and a Gaussian to the atom signal peak and defining the complementary quantity *infidelity* as the overlap between the two distributions.

plays a crucial role in determining the fidelity, as it defines whether the counts from a given histogram are correctly categorized. In Fig. 4.4, the background signal, labeled as the *Dark state*, follows a Poisson distribution with $\lambda_{\text{dark}} = 6.8$, while the atom fluorescence, labeled as the *Light state*, is centered at $\lambda_{\text{atom}} = 39.3$. With the threshold

set to 19, depicted by a vertical dashed line, the atom signal is correctly identified as the light state in 99.99% of cases, while the background signal is misclassified as the light state in 0.01% of the cases. Naturally, the further apart the two peaks are, the more effective the thresholding becomes. While the background peak is influenced by factors such as readout noise, background scattering, and other systematic effects during detection, the central value of the atomic signal peak is determined, for a given scattering rate and imaging duration, by the collection efficiency (Eq. 4.2), the camera's quantum efficiency (QE), and optical losses. Increasing either the scattering rate or the imaging duration would enhance the number of collected photons, resulting in better separation between the two peaks. However, this also brings drawbacks, such as reducing the atom survival rate and increasing the duration of the imaging sequence, impacting the overall experimental cycle.

To quantify the fidelity, one can calculate the overlap between the two distributions by fitting the two peaks with two Gaussians or a convolution between a Gaussian and a Poisson distribution [69]. Indeed, other noise sources, such as EMCCD multiplication noise, might modify the pure Poisson distribution [158]. Another experimental approach [165, 70], independent from the histogram fitting, relies on the comparison between two consecutive images without reloading atoms from the red MOT. In this case two types of errors can occur: an infidelity error when atoms are observed in the second image but not in the first, and a loss error when atoms are observed only in the first image.

Survival rate

Another key parameter in describing the imaging process is the survival probability. If the imaging fidelity were $F = 1$, we could directly estimate the survival probability by taking a second image and comparing it to the first: the fraction of atoms detected in both images would give the survival probability S . However, in real cases where $F < 1$, this approach is not entirely accurate, and a more refined model accounting for false positives and false negatives is needed [69]. Nonetheless, we will use this method as a reasonable first approximation for determining the survival probability.

4.4 Alternative imaging schemes

Another crucial aspect in engineering the imaging scheme is the duration of the detection process. Indeed, working with arrays of optical tweezers allows for a very short experimental cycle of hundreds of ms. Nevertheless, the detection of the atomic state takes a significant fraction of this time (tens of ms) to produce a reliable readout in terms of fidelity and survival probability. The hard limit that bounds the imaging time, as we said, is the limited NA of the detection objective, which can only collect a fraction of the emitted fluorescence, and the atoms have to scatter a lot of photons to collect enough to detect their presence. Reducing the readout time becomes even more important when mid-circuit measurements are required for error correction in quantum computation and simulation [166, 167], and metrology [168, 169, 170]. Ideally, one would like to sample the state of the system continuously in a nondestructive way, but this is incompatible with readout times of tens of ms or even more.

Several different approaches were developed to address this task for tweezers machines, falling within three main categories. The first one exploits a cavity that is strongly coupled with the atoms to enhance the fluorescence signal along the cavity axis [171, 172]. The second method relies on measuring the state of ancilla sites that are addressable without affecting the main system. This can be done by applying a site-selective light shift [43, 173], spatially separating a subarray of ancilla sites [38] and shelving the main sites in low-coupled states [174, 175]. The last one is based on preparing the state in a motional or state-sensitive shelved state [176, 177, 178, 179].

A full description of mid-circuit measurements is outside the scope of this thesis. Anyway, given the growing interest in this topic and the importance of performing fast, high-fidelity and survival readouts, we will present two possible improvements to the well-established techniques described above. The first one is based on a technical improvement: a camera with nearly zero readout noise allows for a decrease of the required average number of photons necessary to detect an atom. The second one is a modification of the red imaging scheme that could eventually increase the scattering rate of the bare red transition by dressing the 3P_1 state with the 3S_1 state.

Before explaining the following concepts, I would like to acknowledge the SrMic group at the University of Amsterdam for their valuable insights and contributions, which were fundamental in developing the ideas presented in this section. Particular thanks to Dr. Robert Spreuw, who carried out some of the simulations whose results are reported in Subs. 4.4.2

4.4.1 Fast imaging with an ultra-low noise camera

In this subsection we will outline a slightly different approach based on technical improvements of detection cameras. Indeed, if we look at a count histogram such as the one reported in Fig. 4.4, the dark count rate sets a lower limit to the threshold value. If the dark count rate were sufficiently low to push the background peak towards zero, detecting the presence of an atom would require far fewer photons. This is because the threshold for detection could be set lower, reducing the number of photons needed to distinguish signal from background noise. For a given scattering rate, this would result in a shorter imaging time, proportional to the average number of scattered photons.

Intensified camera A promising technical improvement in this sense is represented by a detector with a different nature from the ones introduced earlier in this chapter. In particular, this optical detector is based on a Tpx3Cam sensor combined with an optical intensifier. This is a hybrid CMOS chip, where a silicon optical sensor with high QE is bonded to a Timepix3 chip [180, 181, 182]. The sensor is composed of 256×256 pixels of $55 \mu\text{m}$ squared size, and each pixel has its own processing electronics to detect the collected charge. The electronic noise is roughly $100 e^-$, so a detection threshold is set to $\sim 600 e^-$ to detect only the signals that overcome that value. The fluorescence signal of single atoms is not intense enough to overcome this threshold by itself, so an image intensifier is placed before the camera to enhance the photon signal. This is done in a few steps: first a photocathode converts the impinging photons into electrons. These electrons are accelerated in a high voltage region and are multiplied using microchannel plates (MCP) with gain up to 10^6 . The

electrons are finally converted back to photons via a phosphore screen and detected on the silicon layer of the camera. The photons of the amplified stream, converted again to electrons for the pixel readout, are accumulated on a capacitor. Thanks to an internal clock, the Time of Arrival (ToA) of the signal is recorded and timestamped with a few ns resolution. Moreover, the capacitor is discharged at a constant rate until the charge falls below the threshold again. The Time over Threshold (ToT) registered and associated with the count “event” is recorded too. This information is proportional to the charge accumulated, and therefore to the initial photon number. Fig. 4.5 reports schematically the amplification and readout process. This *data-*

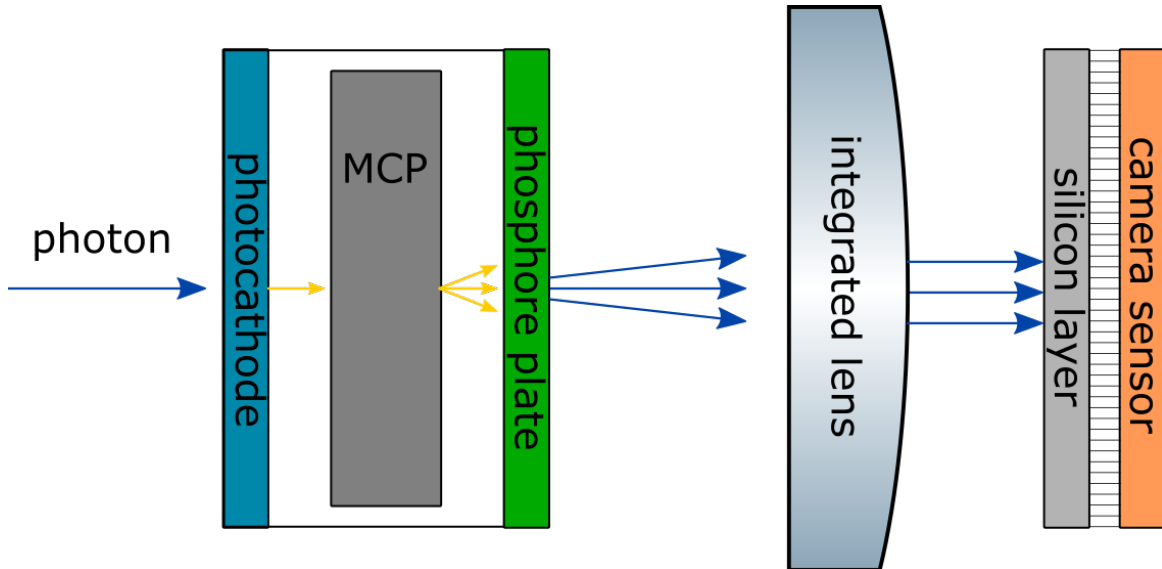


FIGURE 4.5: Sketch of the amplification and detection sequence using an image intensifier. An input photon (blue arrow) is converted into one electron with quantum efficiency of 50 % at best in the visible domain. An array of microchannel plates multiply the electrons by a gain factor, up to 10^6 . Although the charges are accelerated by a high electric potential, a small divergence in this phase limits the final resolution of the intensifier. The multiplied electrons are converted back to photons via a phosphore plate. An integrated lens compensates for the small divergence of the electrons (and consequently of the photons) and focuses the photons on a silicon layer with high QE. The silicon layer converts finally the photons into charges that are accumulated in the chip pixels for the readout.

driven readout approach, opposed to the usual *framed* imaging, where the signal is integrated in a time frame equal to the exposure time, provides a list of events, with information about the arrival time and the “intensity” of a signal via the ToT. An FPGA can process the parallel readout of all the pixels of the chip with tens of MHz rate. This approach is favorable in a low-light regime such as in fluorescence single-atom detection, and in cases where small portions of the chip are illuminated. The extreme temporal resolution might prove useful in other applications, such as photon heralding and coincidence measurements [183, 184]. In our case, the interesting time scale is the μs or tens of μs range, but the technology might be particularly appealing for the extremely low readout noise. Indeed, the electronic noise is mitigated by setting a minimum threshold to count a charge as a signal. The main source of noise

is the photocathode's dark count rate, which originates from thermionic emission at nonzero temperatures. This is often quantified as the Equivalent Background Input (EBI), which represents the amount of light that would produce the same photon flux as the dark count. EBI, typically measured in $\frac{\text{W}}{\text{cm}^2}$, can be converted into dark count rate, measured in $\frac{\text{photons}}{\text{s cm}^2}$, by considering the photon energy. Two additional limiting factors set by the intensifiers are the QE of the photocathode and the spatial resolution. Typical values can be found for example in Ref. [185]: the EBI is around $8 \times 10^{-15} \text{ W/cm}^2$ which is the equivalent of a dark count rate of $\sim 18.5 \times 10^3 \text{ Hz/cm}^2$ 461 nm photons, thus meaning a dark count rate of 0.5 Hz/pixel. The cathode QE is around 30-50 % in the visible 400-700 nm range. The resolution is limited to ($\sim 50 \text{ lp/mm}$), which gives, in terms of pixels, a resolution of ($\sim 2.75 \text{ lp/pixel}$). A first consideration regards the dark count rate of the intensifier: since this background source produces a constant flow of stray photons, we would benefit from a short imaging time during which only very few photons can hit the camera sensor. As shown later on in this subsection, the dark count rate per pixel can be negligible for a few μs exposure time, therefore we will consider here an imaging regime where atoms scatter photons on the blue transition in a saturated regime at a few MHz scattering rate.

In summary, the camera chip+intensifier is similar to an array of avalanche photodiodes (APD) with extreme time resolution. Indeed, the photons impinging on each pixel are amplified prior to the detection in order to magnify the signal. We will explore whether this approach, despite the limitations mentioned earlier, could offer improvements in fast fluorescence imaging. Here we report a semi-classical simulation of the photon scattering process using two counter-propagating beams that illuminate the atoms in the tweezers. To complete this study, an experimental characterization will be needed to benchmark its performance.

Simulation of the imaging performance To begin, we performed a 3D simulation of the photon scattering process within a confining potential, modeled by a Gaussian potential corresponding to the parameters of our optical tweezers. The scattering rate of the imaging light is determined by the saturation parameter s and the detuning Δ . With $s = 3$ and a no detuning to maximize the scattering rate, calculated from Eq. 2.2, we obtain $R_{sc} \simeq 2\pi \times 11.3 \text{ MHz}$. As mentioned in Sec. 4.1, the 1P_1 state is more tightly confined by the tweezer light at 813.4 nm compared to the ground state, resulting in a red-detuned resonance due to the light shift. Therefore, we consider the beam to be at the light-shifted resonance.

For the simulation, an effective tweezer potential is used, assuming that in a saturated regime ($s = 3$), the atom spends a significant fraction of its time in the 1P_1 state, where it experiences a potential with a different depth. The time-averaged potential is calculated by averaging the ground-state potential $U_{1S_0}(x, y, z)$ and the excited state potential $^1P_1(x, y, z)$, weighted by the probability p_e of finding the atom in the excited state:

$$U_{avg}(x, y, z) = U_{1S_0}(x, y, z) \cdot (1 - p_e) + U_{1P_1}(x, y, z) \cdot p_e, \quad p_e = \frac{1}{2} \frac{s}{s + 1}. \quad (4.5)$$

With a saturation parameter of 3, we find $p_e = 0.375$. Considering the polarizabilities of the 1S_0 and $^1P_1, m_J = 0$ states, which are 286 au and 708.4 au respectively, the

time-averaged potential is approximately 1.5 times deeper than the trapping potential of the ground state alone. In the simulation, we vary two parameters: the average number of photons scattered by the atom and the trap depth. The exposure time dt is determined by the ratio of the target average number of scattered photons to the scattering rate. The exposure time is divided into simulation steps, $dts = 1/R_{sc}$. At each step, the atom's position and velocity are updated based on two factors: photon absorption and spontaneous re-emission, and the restoring force from the Gaussian potential.

The tweezer axis is oriented along the z-axis. Photon absorption is modeled using two counter-propagating beams along the x-axis, along which the tweezer confinement is stronger being one of the two radial directions. The atom can randomly absorb a photon from either the positive or negative x-direction, resulting in a recoil velocity of $v_{rec} = \hbar k/m$ in that direction, where k is the wave number of 461 nm photons, and m is the mass of ^{88}Sr . Photon spontaneous emission occurs in any direction, introducing a velocity component v_{rec} in a random direction. The restoring force of the time-averaged Gaussian potential is calculated as the gradient of the effective potential. Dividing by the atom's mass, the resulting acceleration that influences both the atom's position and velocity for radial motion $r = (x, y)$ and axial motion z is expressed as:

$$\begin{aligned} a_r &= -\text{Exp} \left[-\frac{m\omega_r^2 r^2}{2U_{avg,0}} \right] \cdot \omega_r^2 r \\ a_z &= -\text{Exp} \left[-\frac{m\omega_z^2 z^2}{2U_{avg,0}} \right] \cdot \omega_z^2 z \end{aligned} \quad (4.6)$$

where $\omega_{r,z}$ are the trap frequencies that we derived in the harmonic oscillator approximation. At the end of the exposure time, on the order of a few μs , the spatial distribution of the scattered photons is visualized in a scatter map, as reported in Fig. 4.6. The scatter map is the result of 2500 identical repetitions of the simulation to obtain a probability distribution of the scattered photons. Fig. 4.6 is an example of the scatter map for a trap depth of 1.2 mK and 140 scattered photons per simulation. On the left side of the figure, the velocity along x is plotted versus the displacement on the x-axis, while on the right side, the x- and z-axis coordinates of the atom during the random walk are reported. Each repetition of the simulation determines a trajectory, where the vertices represent the emission of a photon that can change the propagation direction of the atom. The initial position and velocity are randomly chosen for each repetition of the simulation in a range between 0 and the RMS value determined using the trap parameters.

$$\begin{aligned} r_{RMS} &= \sqrt{\frac{\hbar}{2M\omega_r}}, & z_{RMS} &= \sqrt{\frac{\hbar}{2M\omega_z}}, \\ v_{r,RMS} &= \sqrt{\frac{\hbar\omega_r}{2M}}, & v_{z,RMS} &= \sqrt{\frac{\hbar\omega_z}{2M}}, \end{aligned} \quad (4.7)$$

where we have assumed that the atoms at the beginning of the imaging pulse occupy the ground-state vibrational level, and the harmonic oscillator approximation is valid to determine the starting conditions. Additionally, we compute the total energy (kinetic + potential) using the final positions and velocities. The atom is considered

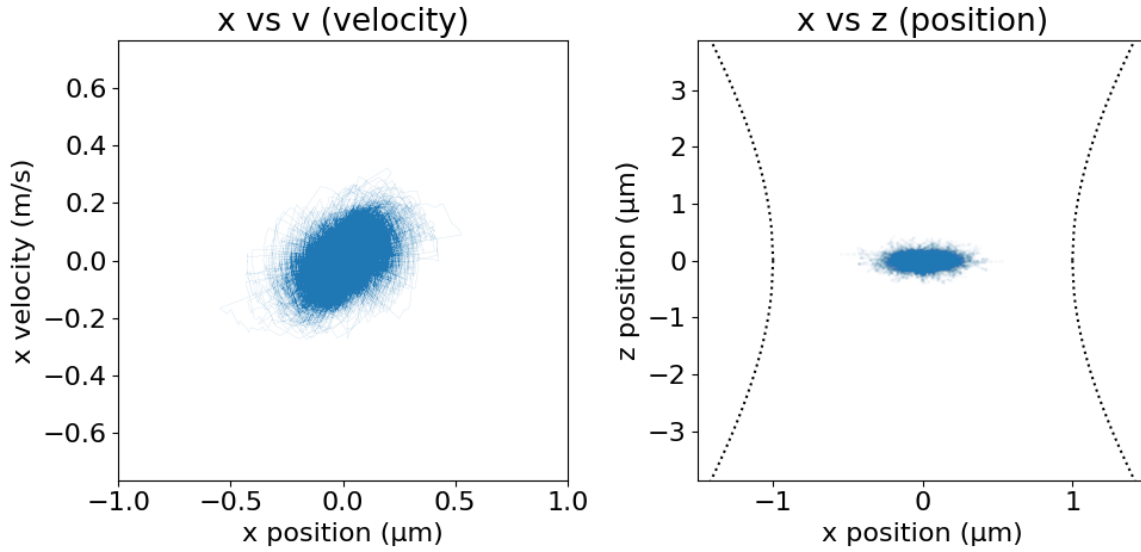


FIGURE 4.6: Example of a map of the scattered photons for a trap depth of 1.2 mK and 140 scattered photons. The results are accumulated for 2500 repetitions of the simulation. On the left, the velocity versus displacement along the x-axis, where the probe beam is aligned, are plotted. The spots seem to have a preferred orientation along a diagonal in the phase space. This is not surprising, as the atoms with large positive (negative) velocity will be displaced mostly towards positive (negative) values, particularly in this case where the dynamics is much faster than the trap frequencies and such correlations are not averaged by the effect of the oscillations within the trap. On the right plot, the displacement along the radial (x) and the axial (z) directions within the tweezer are displayed, with the dotted line representing the propagation profile of the tweezer (waist $w(z)$) as a guide for the eye.

lost after the imaging process if its total energy exceeds 0. By averaging the results over 2500 iterations of the same simulation for each parameter configuration, we can determine the survival probability.

Two separate studies were carried out. First, we set a fixed trap depth of 1 mK and calculated the survival probability using the method described above, along with an estimate of the detection fidelity. To determine the fidelity, we repeated a simulation similar to the one that generated the results shown in the histogram in Fig. 4.4. Both the background and signal peaks were assumed to follow a Poisson distribution, with the mean values λ derived as follows. The average number of detected photons for the signal is determined by the number of scattered photons multiplied by the collection efficiency. This includes the cone of light captured by the microscope objective with a numerical aperture (NA) of 0.56, the optical path's detection efficiency, and the intensifier's quantum efficiency. The geometric collection efficiency C is calculated using Eq. 4.2, while the detection efficiency η was set at 90% to account for potential losses on the optical surfaces. Regarding the QE of the intensifier, we refer to commercial products with the highest possible efficiency, such as the model V9501U-74 by Hamamatsu [185], with a QE of 50%.

The average number of counts for the background peak is determined by the specifications of the intensifier, as the photocathode is the main source of background

counts. Considering the same intensifier from Hamamatsu (V9501U-74), the equivalent background input (EBI) is 8.0×10^{-15} W/cm². By dividing this by the energy of a blue photon, we can estimate the background photon flux per unit area. From this, we calculate the background count rate per pixel. Due to the intrinsic behavior of intensifiers, which slightly spread the signal, the fluorescence from a single atom is not confined to the area on the chip strictly determined by the magnification of the detection optical system. Instead, it covers a slightly larger region. Even when magnifying the fluorescence image to concentrate the signal of the atom on a single pixel, we expect photons amplified by the intensifier to spread into neighboring pixels. Therefore, if we consider a 3x3 ROI around the central pixel to collect all the photons of the signal, the background contribution of all 9 pixels must be taken into account. The signal and background photon flux for a 3x3 ROI is then:

$$\begin{aligned}\phi_{sig} &= R_{sc} \cdot C \cdot \eta \cdot \text{QE} = 2\pi \times 340 \cdot 10^3 \frac{\text{ph}}{\text{s}} \\ \phi_{bg} &= \frac{\text{EBI}}{h\nu_{461}} \cdot A_{ROI} = 5.1 \frac{\text{ph}}{\text{s}}\end{aligned}\tag{4.8}$$

where we have used the C , η and QE parameters defined above, and the area of a ROI $A_{ROI} = 9 \cdot (55 \cdot 10^{-4} \text{ cm})^2$ is calculated considering the pixel size of the chip. The photon flux calculated in Eq. 4.8 can be multiplied for the exposure time to obtain λ_{sig} and λ_{bg} , which are then used to calculate the measurement fidelity.

By varying the expected number of scattered photons, we calculate both the survival probability for a fixed trap depth of 1 mK and the detection fidelity. The background peak is centered around λ_{bg} , which is a very small value for short exposure times of a few μs , as those we are considering in this approach. As a result, the probability of misclassifying a background count when setting the threshold at 1 count per ROI is less than 0.005% for all the cases considered in this study. The primary contribution to detection infidelity comes from the signal peak. If the exposure time is too short, with few scattered photons, there is a significant probability that the signal produces zero counts, leading to potential misclassification.

The survival probability and detection fidelity, as a function of the number of scattered photons, are shown in the left panel of Fig. 4.7. As expected, with a low number of scattered photons, the atom's survival is nearly perfect, but the detection fidelity decreases rapidly. On the other hand, when more photons are scattered, the detection fidelity approaches 100%, but the atoms are lost more frequently. An optimal balance is found around 140 scattered photons, where the survival probability reaches 99.92% and the fidelity is 99.94%. This corresponds to an exposure time of 2.0 μs , ensuring high-fidelity detection of a single atom while maintaining its survival. The second study focuses on the effect of the trapping potential. For a fixed number of scattered photons $N_{\text{scat}} = 140$, we vary the tweezer's trap depth. While the trap depth reported in the plot refers to the ground-state potential, the time-averaged potential in the simulation effectively results in a trap that is 1.5 times deeper. The results indicate that, for the fast imaging pulse described here, a deep tweezer potential is necessary to keep the atom trapped. Specifically, achieving a trap depth of 1.2 mK requires significant laser power, approximately 30 mW per tweezer with 1 μm waist.

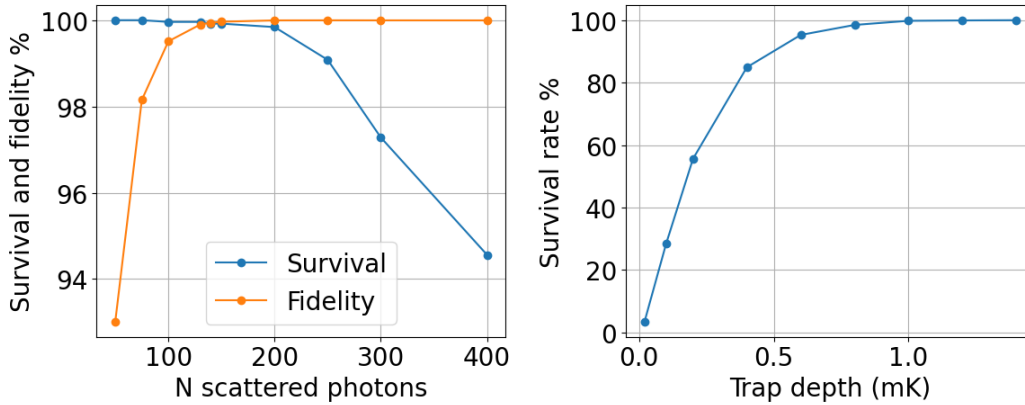


FIGURE 4.7: Survival probability and fidelity in a simulation with fixed trap depth of 1.2 mK. A scattering rate of $R_{sc} = 2\pi \times 11.2$ MHz is set by choosing a saturation parameter $s = 3$ and a detuning $\Delta = 0$. Changing the imaging time to vary the number of scattered photons, a nice experimental spot is found for $N_{scat} = 140$. In the right panel, the dependence on the trap depth for a fixed $N_{scat} = 140$ shows that a fairly deep trap (> 1 mK) is necessary to maintain a good survival probability.

Comments on the imaging technique

The imaging method outlined above seems to offer a fast and reliable procedure to detect single atoms. However, we haven't considered any cooling sequence, which is fundamental to operate the system in optimal conditions, especially during mid-circuit measurements where ideally many detection sequences are performed during an experimental cycle. Nevertheless, performing a fast imaging first and then, while the image is being processed, cool the atoms with a standard in-trap cooling sequence may offer an advantage with respect to the standard imaging techniques. An example of such approach was demonstrated experimentally in Ref. [159].

The method outlined here should also be validated by an experimental realization. As an additional note, in this work, we have treated the camera just like a standard detector with particularly low readout noise. However, two aspects related to its data-driven readout require further investigation. First, the chip has a readout rate that is limited by the electronics to $80 \cdot 10^6$ events per second, where each pixel trigger counts as an event. This could limit the maximum number of atoms that can be detected to a few hundred, as many events accumulate in a short period. It is crucial to ensure that the rate at which data are transmitted to the PC for analysis does not become a bottleneck in imaging. This factor can only be determined through experimental evaluation. The second key point is that the Timepix3 chip reads out events that can be aggregated into a single exposure during post-processing, allowing us to analyze a histogram of the counts, similar to standard detectors. However, the nanosecond time resolution of the camera may enable more efficient data analysis, potentially reducing the number of atoms needed for detection. For example, if the photon scattering from the signal has a characteristic temporal profile that distinguishes the time-of-arrival (ToA) or time-over-threshold (ToT) statistics from background photons, fewer photons may be required to confirm the presence of an atom.

Regarding the tweezer potential, we found that very deep traps are needed to

achieve a high atom survival probability. This could limit the scalability of the tweezer array due to constraints imposed by the total available laser power. A few potential solutions to address this limitation include introducing an additional pinning potential during the readout or using tweezers at a different wavelength with a smaller waist to create deeper traps. The use of auxiliary potentials during imaging has been demonstrated in previous works [49, 186, 77] with an overlapped optical lattice. Another common approach for Strontium involves using 515 nm tweezers [41, 39, 49, 186], which offer a smaller diffraction limit while maintaining high polarizability of the ground state [69]. This allows for deeper traps with the same laser power. A diffraction-limited 515 nm tweezer would require approximately 3.5 mW of power for a 1.2 mK deep trap, compared to 30 mW at 813 nm. Additionally, powerful laser systems are commercially available at this wavelength, allowing for scaling up the size of the tweezer arrays. However, since the 1P_1 state is anti-trapped in these tweezers, a more effective approach might be to release the atom into free space for fast imaging, then recapture it afterwards.

To simulate time-of-flight single atom fluorescence imaging, the contribution of the Gaussian potential can be removed from the simulation. In this case, the atom is released from the tweezer to scatter photons during a short TOF, equal to the exposure time, after which it is recaptured by the trap. If the atom's total energy, given by its kinetic energy and potential energy at the recapture position, is less than zero, it will be successfully recaptured. Similar to previous simulations, the average number of atoms recaptured over 2500 trials provides an estimate of the recapture probability.

In Fig. 4.8, the loss rate from the previous simulation ($1-P_{\text{survival}}$) is compared with the recapture loss ($1-P_{\text{recapture}}$) for both 813.4 nm tweezers (orange curve) and 515 nm tweezers (green curve) as a function of trap depth, in the left panel, and tweezer power, in the right panel. Recapturing atoms with both infrared and green tweezer requires nearly three times the trap depth. Looking at the corresponding power per tweezer, TOF imaging with green tweezers requires approximately 10 mW to have less than 0.1 % losses, compared to 30 mW power required for equivalent performances for in-tweezer imaging with 813 nm trapping light. It is important to note that TOF imaging requires particular care, as noted in Ref. [159], particularly in balancing the power of the two counter-propagating beams. Since there is no confining potential, alternating the beams to ensure the atom absorbs photons from opposite directions is key to keep it within the tweezer's capture range. The semiclassical simulation presented here is a simplified representation of TOF fluorescence imaging, and experimental validation is needed to verify this method.

4.4.2 Five-level imaging scheme

The second approach to potentially reduce the imaging time involves modifying the red imaging scheme. This scheme benefits from being compatible with shallow traps and, like in the red imaging sequence, the same 689 nm beam can be used during both imaging and cooling. However, a key limitation is the low achievable scattering rate, which is proportional to the linewidth of the $^1S_0 \rightarrow ^3P_1$ transition, with a maximum rate $R_{sc,max} = \frac{\Gamma_{3P_1}}{2} \simeq 2\pi \times 3.8$ kHz. To increase the scattering rate beyond this threshold and collect the necessary number of photons more quickly, one solution

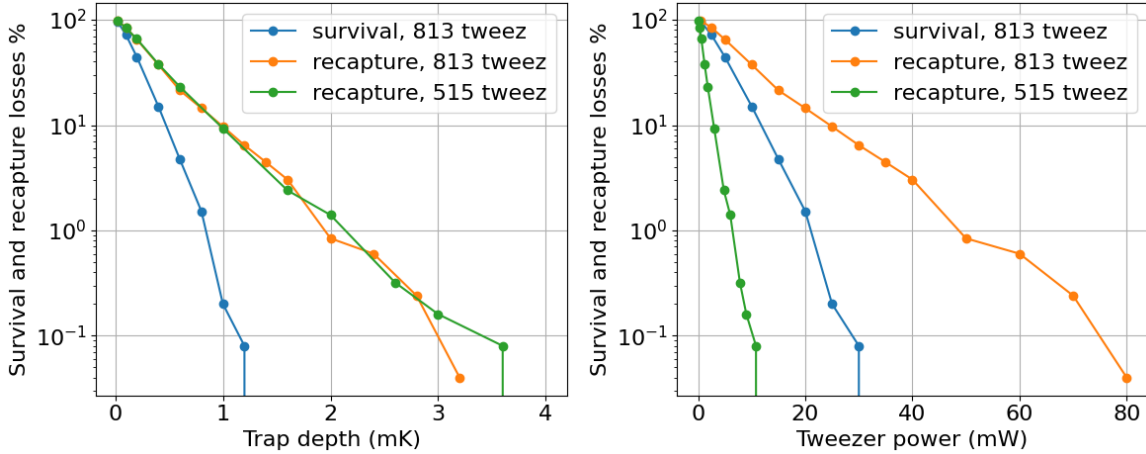


FIGURE 4.8: Comparison of the simulated fast fluorescence imaging performed in the tweezer (survival) or in TOF (recapture). The loss probability ($1-P_{\text{survival}}$ and $1-P_{\text{recapture}}$) is plotted in blue and orange/green, respectively. In the left panel, the loss probabilities are reported as a function of the trap depth, while in the right panel they are plotted as a function of the tweezer laser power. In terms of trap depth, the simulation shows an advantage of performing the imaging with the tweezer light always on, rather than trying to recapture the atom after a TOF imaging. The recapture loss is similar for both 813 nm and 515 nm tweezers, and a trap depth > 3 mW is required to have a loss probability below 0.1%. If we convert the horizontal scale to laser power per tweezer, green tweezers might offer an advantage as the power required to have a loss rate < 0.1 % is approximately 10 mW per tweezer, compared to 30 mW required to image in 813 nm tweezers.

could involve coupling the 3P_1 state to another state with a larger linewidth. Notably, the 3P_1 state is connected to the higher-lying $5s6s$ 3S_1 state via a transition at 688 nm with $\Gamma(^3P_1 \rightarrow ^3S_1) = 2\pi \times 4.3$ MHz. The relevant energy levels for this imaging scheme are shown in Fig. 4.9. Since the 3S_1 state can decay into both the 3P_0 and 3P_2 states, repumping is necessary to maintain the population in the imaging cycle. We will refer to this scheme as five-level imaging or *dressed-state imaging*, referring to the fact that an additional laser beam couples the upper level of the standard red imaging transition, effectively broadening its linewidth. The evolution of this five-level system was simulated by solving the Optical Bloch Equations [58], extracting the steady-state solution. We acknowledge Dr. Robert Spreuw for developing this simulation and the useful insights. The simulation models the system's evolution under a Hamiltonian that includes the atom-light interaction in the rotating-wave approximation, and the influence of a small external magnetic field to define a quantization axis. The magnetic field introduces Zeeman shifts that are proportional to the m_J values of the sublevels. In this case, we consider a small field along the z-axis to set the quantization axis.

The atom-light interaction is determined by the Rabi frequencies and detunings of each coupling laser. These detunings are referenced to the light-shifted transition resonance, which is affected by the scalar polarizability of each state in the tweezer light, as explained in Sec. 2.4. For simplicity, we neglect the vector and tensor polarizability terms that would induce differential light shifts across different m_J sublevels.

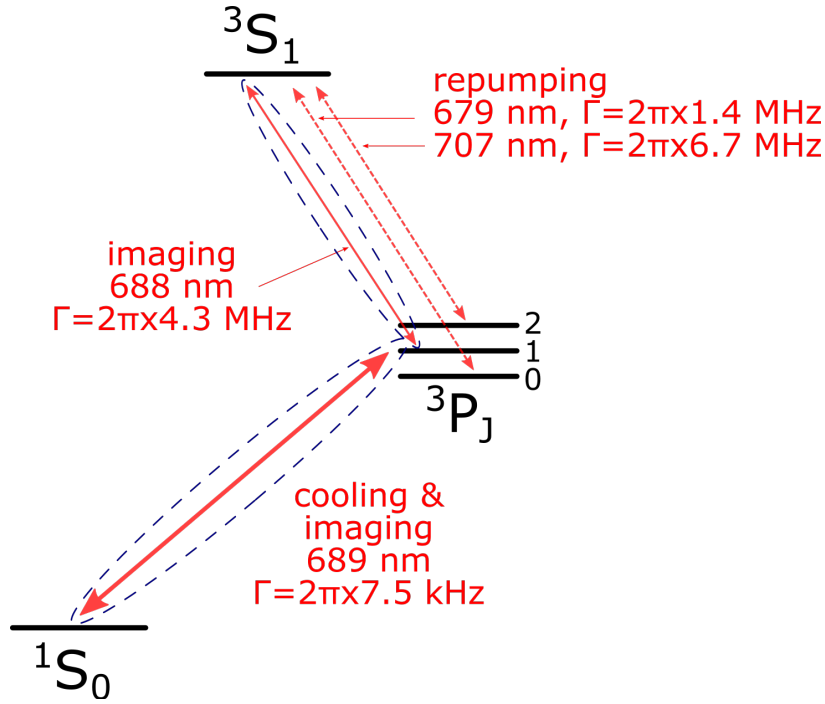


FIGURE 4.9: Possible implementation of a cooling and imaging scheme exploiting the transition from the $3P_1$ state to the $3S_1$ state at 688 nm to enhance the overall scattering rate. The idea is to red detune the 689 nm laser to produce a cooling effect during the scattering process, while exploiting the MHz linewidth upper transition to scatter photons to a faster rate.

The vector polarizability depends on $\cos(\theta)$, where θ is the angle between the quantization axis and the polarization of the light [66]. With a tweezer beam along the x-axis and linear polarization along y, the vector polarizability contribution vanishes. We also neglect the tensor polarizability, which becomes significant for states with high total angular momentum J .

The individual m_J states are treated separately, allowing us to assess the effects of different laser polarizations within the five-level system. The steady-state populations are used to calculate the combined scattering rate for photons at 689 nm and 688 nm:

$$R_{sc}(688 + 689) = P_{3S_1} \cdot \Gamma_{688} + P_{3P_1} \cdot \Gamma_{689} \quad (4.9)$$

where P_{3S_1} , P_{3P_1} are the steady state populations, and Γ_{688} , Γ_{689} indicate the linewidth of the transitions $3P_1 \rightarrow 3S_1$ and $1S_0 \rightarrow 3P_1$, respectively. To calculate $R_{sc}(688 + 689)$ the contribution of all the m_J were considered. Since photons at 688 nm and 689 nm are indistinguishable by typical optical filters, that are usually a few nm narrow, both contribute to atom detection. The combined scattering rate is compared to the maximum rate from saturating the 689 nm transition, and we tune the simulation parameters to maximize the scattering rate enhancement ζ .

$$\zeta = \frac{R_{sc}(688 + 689)}{R_{sc,max}(689)}. \quad (4.10)$$

TABLE 4.1: Initial parameters for the optimization of the scattering rate in the dressed-state imaging scheme.

Beam wavelength	Polarization	Rabi frequency	Detuning
689 nm	u_y	$2\pi \times 50$ kHz	$-2\pi \times 20$ kHz
679 nm	u_x	$2\pi \times 4$ MHz	$-2\pi \times 15$ kHz
688 nm	u_y	$2\pi \times 10$ MHz	$-2\pi \times 10$ MHz
707 nm	u_y	$2\pi \times 4$ MHz	$-2\pi \times 15$ kHz

We will also explore the possibility of adjusting the 689 nm laser Rabi frequency and detuning to achieve an effective Sisyphus cooling in the lower branch of the imaging cycle. To begin scanning the parameters, we set certain values based on physical considerations. The magnetic field direction, which sets the quantization axis, is along z , so circular polarization is required for the $^3P_2 \rightarrow ^3S_1$ transition to prevent dark states in the $|m_J| = 2$ sublevels. The 689 nm Rabi frequency and detuning are close to the optimal values for attractive Sisyphus cooling, as detailed in Ref. [43]. The beam's polarization is circular to address the $|m_J| = 1$ sublevels of the 3P_1 state, which have a higher scalar polarizability than the ground state, enabling attractive Sisyphus cooling, as described in Sec. 2.4. Moreover, since the role of the 679 nm and 707 nm repumpers is to remove atoms from states where they could accumulate, we started with nearly resonant beams (100 kHz detuning) and high Rabi frequencies. The 688 nm beam must also be in a saturated regime to significantly enhance the scattering rate. We initialized the polarizations, Rabi frequencies, and detunings as summarized in Tab. 4.1. Instead of using either σ_+ or σ_- polarizations, we employed linear polarizations orthogonal to the quantization axis (i.e., u_x and u_y), which correspond to combinations of circular polarizations in the spherical basis:

$$u_x = \frac{\sigma_+ + \sigma_-}{\sqrt{2}}, \quad u_y = \frac{\sigma_+ - \sigma_-}{\sqrt{2}}. \quad (4.11)$$

We began by scanning the Rabi frequency of both the repumpers, analysing the enhancement factor ζ in the scattering rate. The results are displayed in a 2D heatmap in Fig. 4.10, where we identified an optimal combination of parameters at $\Omega_{679} = \Omega_{707} = 2\pi \times 14$ MHz. With these optimized values, the enhancement factor reaches $\zeta = 73.7$, corresponding to a scattering rate of $R_{sc}(688 + 689) = 2\pi \times 225$ kHz. Next, we optimized the 688 nm beam's Rabi frequency and detuning simultaneously. As shown in Fig. 4.11, the highest ζ was obtained for $\Omega_{688} = \Delta_{688} = 2\pi \times 10$ MHz. These values match the initial parameters used during the previous optimization. This suggests that we may have found a local optimum by scanning parameter pairs separately. A more advanced optimization protocol working in the full parameter space could potentially lead to even better results.

In a standard imaging setup, approximately 40 photons need to be collected to detect the presence of a single atom with high fidelity. Given the solid angle collection efficiency $C = 0.118$, the detection efficiency $\eta = 0.9$, and the quantum efficiency $QE = 0.9$ (reasonable for EMCCD and qCMOS detectors), the total collection efficiency in our system is roughly 9.5%. Therefore, the atom must scatter an average

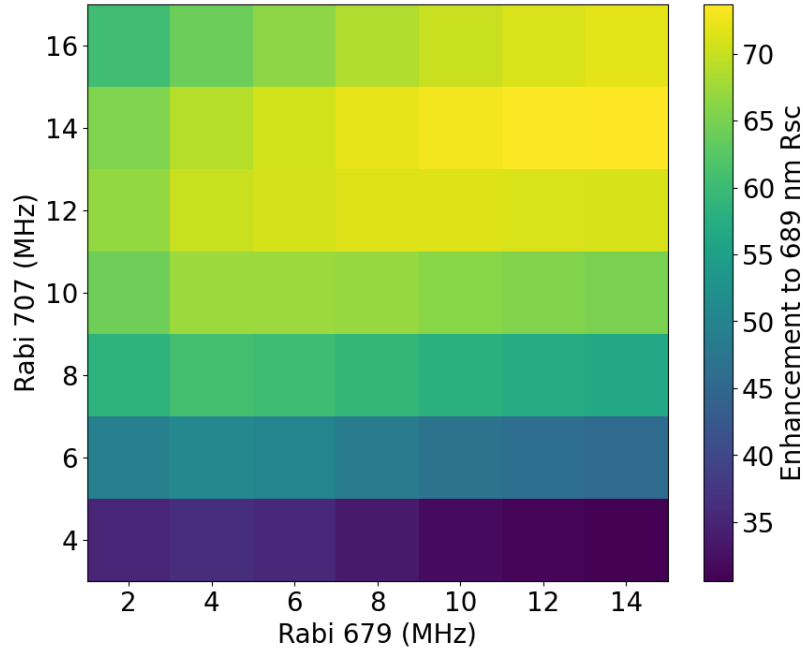


FIGURE 4.10: 2D heatmap showing the enhancement factor ζ scanning the Rabi frequency of 679 nm and 707 nm repumper lasers. The combination that maximizes the scattering rate is for $\Omega_{679} = \Omega_{707} = 2\pi \times 14$ MHz.

of 420 photons. With the enhanced scattering rate obtained in this simulation, this photon count is achieved in approximately $300 \mu\text{s}$. However, the scattering rate of the 3P_1 , $|m_J| = 1$ states, considering the relative steady state populations, is only $2\pi \times 1.2$ kHz. On average, only 2 out of 420 photons is scattered from these states. As a result, the cooling mechanism cannot work, because the scattering rate is so high that even with optimal Rabi frequency and detuning for 689 nm Sisyphus cooling, very few cycles occur during an imaging pulse. Therefore, the cooling cycle must be performed separately after the imaging pulse. Since we ruled out the possibility of an effective cooling during the imaging process, we can relax the constraints on the 689 nm beam and optimize its parameters too. As reported in the 2D heatmap in Fig. 4.12, the enhancement factor ζ is strongly dependent on the Rabi frequency but not significantly on the detuning. With a 2 mm beam waist and saturation intensity for the four transitions, we can achieve the target Rabi frequencies with only a few milliwatts of power. For the narrow 689 nm transition, using $70 \mu\text{W}$ yields a saturation parameter of 375 and $\Omega_{689} = 2\pi \times 100$ kHz. At this Rabi frequency, the scattering rate is enhanced by a factor of 90, leading to $R_{sc} = 2\pi \times 335$ kHz. At even higher Rabi frequencies, the ζ factor continues to increase, although it asymptotically saturates around 98 for $\Omega_{689} = 2\pi \times 500$ kHz. However, achieving such a large Rabi frequency on the narrow 689 nm transition requires a saturation parameter above 10^4 , so it is more reasonable to limit the scan range to the values shown in Fig. 4.12.

There are two additional factors to consider regarding the cooling and heating processes involved in the imaging cycle. First, we demonstrated that the scattering rates of the 689 nm and 688 nm photons can significantly exceed the saturated scattering rate of the bare 3P_1 state. However, due to the involvement of repumper branches,

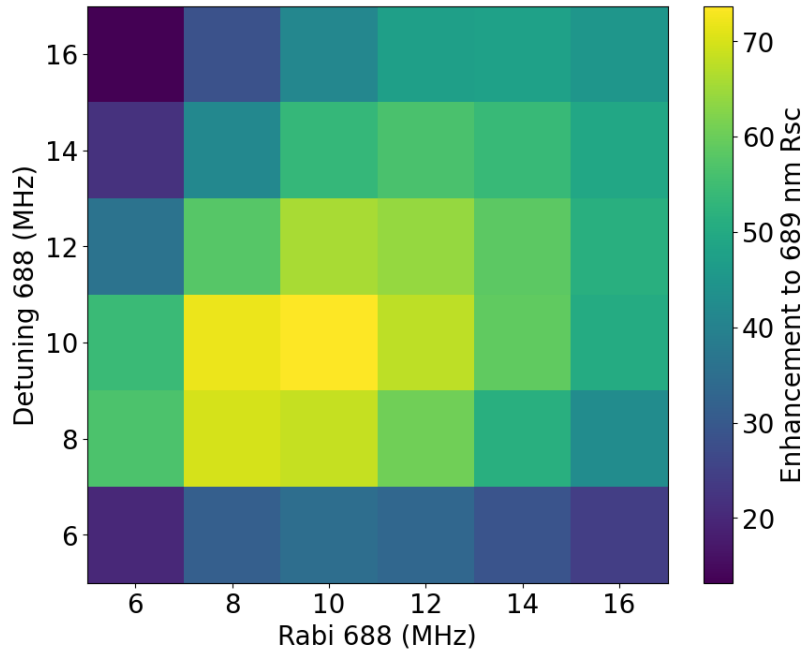


FIGURE 4.11: 2D heatmap showing the enhancement factor ζ scanning the Rabi frequency and detuning of the 688 nm laser. The combination that maximizes the scattering rate is for $\Omega_{688} = \Delta_{688} = 2\pi \times 10$ MHz.

TABLE 4.2: Optimized parameters for the scattering rate in the dressed-state imaging scheme.

Beam wavelength	Polarization	Rabi frequency	Detuning
689 nm	u_y	$2\pi \times 100$ kHz	$-2\pi \times 20$ kHz
679 nm	u_x	$2\pi \times 14$ MHz	$-2\pi \times 15$ kHz
688 nm	u_y	$2\pi \times 10$ MHz	$-2\pi \times 10$ MHz
707 nm	u_y	$2\pi \times 14$ MHz	$-2\pi \times 15$ kHz

the atom ends up scattering way more than 420 photons during the $200 \mu\text{s}$ imaging period. Specifically, the atom emits photons through spontaneous decay from the 3S_1 state to the 3P_J manifold, following the branching ratios, which can be calculated as $1/9$, $3/9$, and $5/9$ based on the Clebsch-Gordan coefficients. Experimentally measured decay rates for these transitions can be found in Refs. [52, 187]. For the optimized parameters, the scattering rates of the 707 nm and 679 nm photons are $R_{sc}(707) = 2\pi \times 515$ kHz and $R_{sc}(679) = 2\pi \times 116$ kHz, respectively. This means that, during the $200 \mu\text{s}$ exposure time, an average of 650 photons are scattered on the 707 nm transition and 146 photons on the 679 nm transition. In total, about 1,200 photons are scattered, potentially causing significant heating of the atoms, despite the fact that the recoil energy from these red photons is lower than that of 461 nm photons. It may be possible to detect the 707 nm photons, which are scattered at a higher rate, or to detect photons from all four wavelengths. However, this would require using optical filters, or combinations of filters, transmitting photons across a

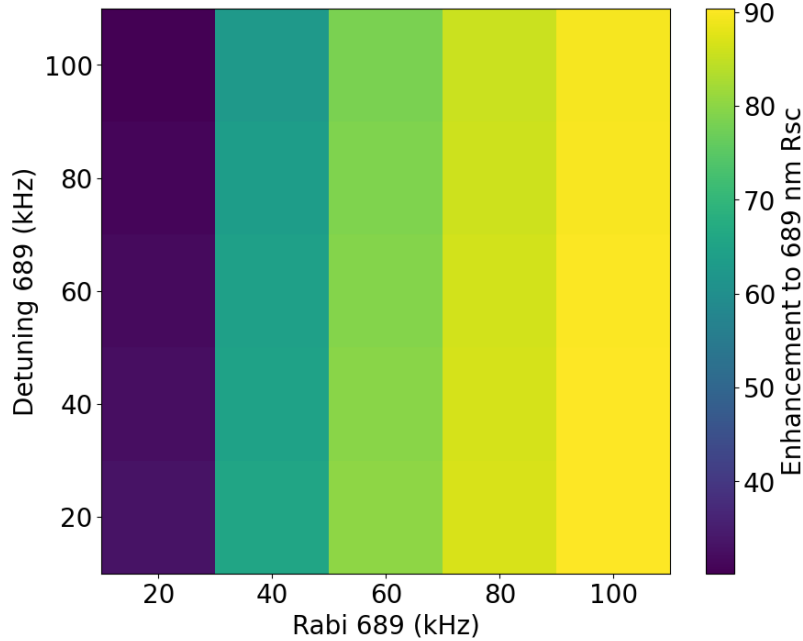


FIGURE 4.12: 2D heatmap showing the enhancement factor ζ scanning the Rabi frequency and detuning of the 689 nm laser. The enhancement factor strongly depends on the Rabi frequency, while not significantly on the detuning.

wide 30 nm range, covering from 679 nm to 707 nm, and having an optical system achromatic in this interval of wavelengths. This could reduce the detection efficiency by allowing more transmitted background photons. The second key factor concerns the negative polarizability of the 3S_1 state in 813.4 nm tweezers, which creates an anti-trapping potential. Although atoms in this state quickly decay into one of the 3P_J states and spend little time in the anti-trapping potential, this could still contribute to heating. Using the steady-state populations derived from simulations, an average polarizability can be calculated by multiplying the state-specific polarizabilities from Tab. 2.1 by their respective populations:

$$\alpha_{avg} = \sum_i p_i \cdot \alpha_i \quad (4.12)$$

Where the sum over i index includes all the m_J sublevels involved in the simulation, and p_i indicates the steady-state population of each substates with α_i being the corresponding polarizabilities. Using the optimized simulation values, the average polarizability is $\alpha_{avg} = 266$ au, which is 7% lower than that of the bare 1S_0 state. Thus, during the imaging cycle involving this five-level system, the atom is only slightly less trapped than it would be in the ground state alone, due to the small fraction of time spent in the anti-trapping 3S_1 state.

In summary, the simulations presented in this subsection propose an alternative fast imaging method for bosonic Strontium, increasing the scattering rate of the narrow $^1S_0 \rightarrow ^3P_1$ transition by addressing the 3S_1 state with additional laser beams. While the five-level system is complex to simulate, compare to what we did in the

previous subsection for a two-level system, these simulations indicate a promising enhancement in the scattering rate, which could be experimentally verified to determine its practical viability. Although direct cooling cannot be integrated into this imaging scheme due to the low scattering rate, it could be performed separately or by alternating imaging and cooling cycles, with the advantage of reducing the imaging time to a few hundred of microseconds. The atom experiences heating from scattering photons at four different wavelengths (679 nm, 688 nm, 689 nm, and 707 nm), which, compared to blue photons used in other imaging sequences, have the advantage of a lower recoil energy. However, this advantage may be lost when a large number of photons are scattered, especially if only a fraction of them are collected, which is the case if we collect just the 688 nm and 689 nm photons. One potential approach is to detect photons from all four wavelengths to avoid wasting any scattered photons, although this would likely increase background noise from stray photons. Additionally, since the 3S_1 state is anti-trapped in the 813 nm tweezers, this could also contribute to heating, even though the atom spends a very short time in this state during the imaging cycle. To evaluate its feasibility and assess its advantages and disadvantages with respect to a more standard blue imaging, this scheme has to be investigated experimentally.

Chapter 5

Experimental apparatus

The setup of this experiment is composed of three main elements. The main one is the vacuum system, which was designed essentially to meet two requirements: having a ultra-high-vacuum pressure inside the science chamber and maintaining the highest optical access as possible. The second element is a pair of high-magnetic-field coils that is necessary to perform the Magneto-Optical-Trap and produce a cloud of cold trapped atoms. This pair of coils is assembled with a set of compensation coils on the three axes to shield the atoms from external stray fields. The third element is the ensemble of all the laser setups that we need for trapping, cooling, manipulating and imaging the atoms.

These three elements are conveniently built on separate supports. This modularity is useful not only for a logical organization, but also simplifies the assembling of the different components as I will show in the next pages. A side view of the experimental setup in the main optical table is shown in Fig. 5.1 In this chapter I will describe how we designed the vacuum system to meet the requirements of the lowest possible ultra-high-vacuum pressure and a large optical access to move then to the assembling process. Next, the whole set of magnetic field control and compensation coils and its assembly will be addressed. To conclude, I will describe the optical setups that we designed to manipulate the atoms.

5.1 Overview of the experimental apparatus

The experimental optical table is occupied by two main breadboards, one for the vacuum system and one for the laser setups. The core of the experiment is the termination of the vacuum system, a rectangular glass cell where all the stages of the experiment take place, starting from the cooling and trapping to the excitation and detection of the atoms. The optical setup is designed in such a way that all the beams end up interacting with the atoms in this part of the vacuum system, taking advantage of the large optical access allowed by an all-transparent glass vacuum

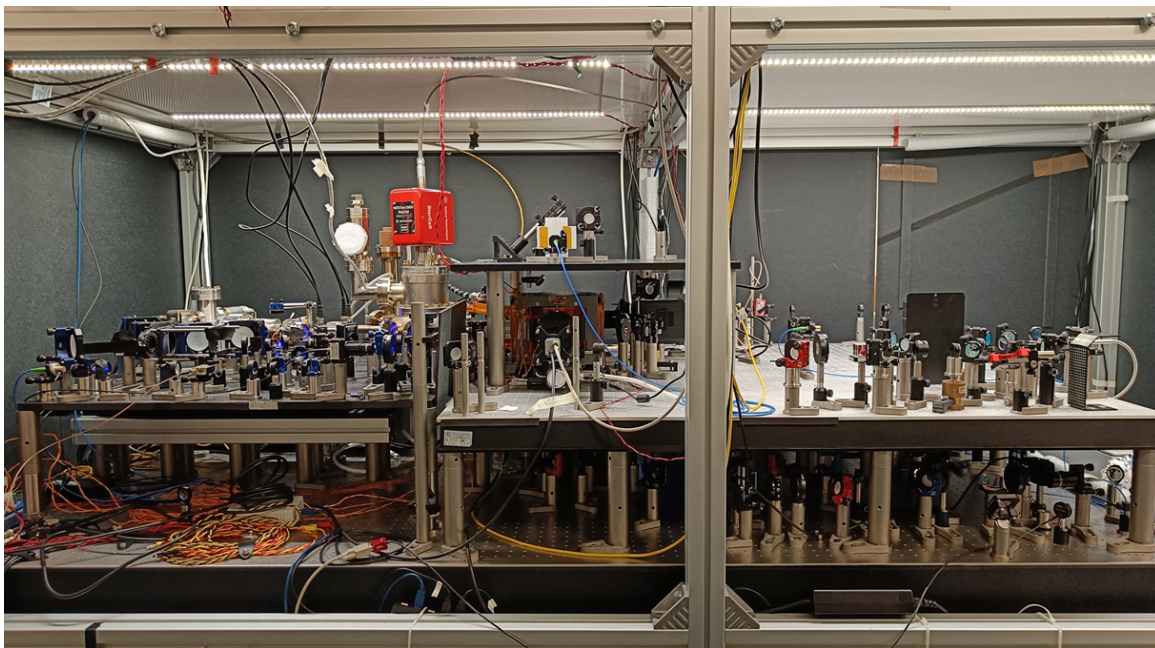


FIGURE 5.1: Side view of the main optical table. The vacuum system is on the left side, on a separate breadboard mounted on a translation stage. The main optical setups for trapping, manipulating and detecting the atoms are assembled in this optical table on three levels.

appendix. Around this glass cell, the magnetic field coils assembly is mounted to maintain a high control on the atomic sample. As we will show in the next pages, this assembly is the best compromise between keeping as much free space as possible for the laser beams and a high and uniform magnetic field on the atoms. The vacuum system assembled on its dedicated breadboard is shown in Fig. 5.2, while in the left bottom of the picture another non-anodized breadboard is partially visible. This second breadboard, that we will refer to as the horseshoe breadboard, is dedicated to the optics for the blue and red MOT, for the generation of optical tweezers arrays and the excitation to Rydberg states. The hole in the horseshoe breadboard leaves space to place the magnetic field coils assembly directly on the underlying optical table, decoupling in this way the vibrations produced by high-field coils turning on and off on the optical system.

The vacuum system breadboard is mounted on a high-load translation stage, model X-LRT0500AL-E08C-K from Zaber, which allows us to move independently the vacuum system away from the optics, like the microscope objectives and 3D MOT mirrors, and coils. This is beneficial both in the case that we need to operate on the vacuum system in the unlikely event of vacuum leaking or simply cleaning the glass cell surfaces, and for aligning the laser beams, checking the light's polarization or any other operation that can be carried out in an easier way without risking to damage the cell. Moreover, we took advantage of this possibility when we had to replace the temporary homemade coils with the custom water-cooled high-field coils. On the side of the atomic source, all the optics that are necessary to produce a slowed-down atomic beam are also mounted on the same moveable stage, in such a way that the vacuum system can be moved in and out without any misalignment.

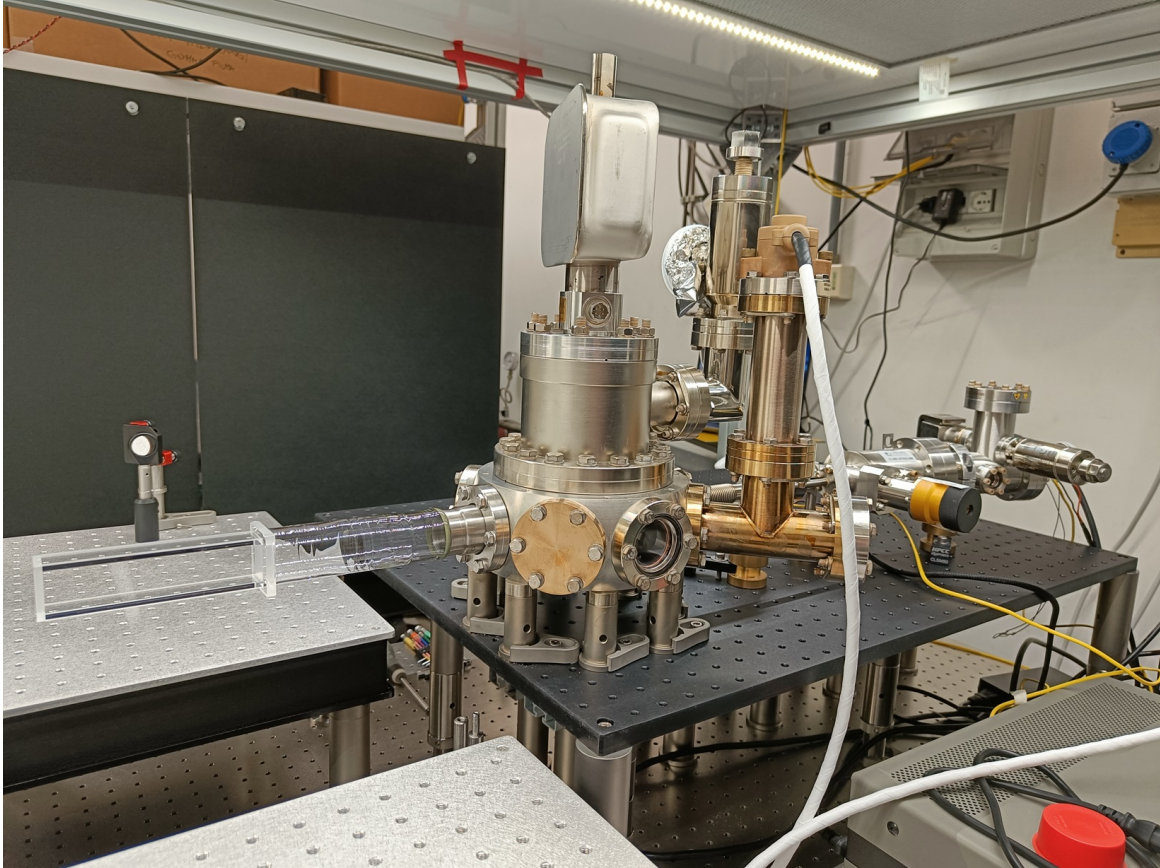


FIGURE 5.2: Vacuum system on the moveable breadboard.

The translation stage's travel range is 500 mm, allowing us to extract completely the glass cell from the coils assembly and the optics mounts. According to the datasheet, it guarantees a $125\ \mu\text{m}$ accuracy and $4\ \mu\text{m}$ repeatability. Moreover, we decided to position the overhanging breadboard to be in the correct position when the stage is at full range, to be sure that it can only be moved backwards without hitting any other component on the optical table. When the stage is in the steady-state position we secure this position by screwing six variable-height 1.5" posts under the vacuum system breadboard and disconnect the translation stage from its power supply to avoid unwanted movements of the whole breadboard. An advantage of this kind of assembly is that the position where the atoms are cooled and trapped is uniquely determined by the laser beams alignment on the horseshoe breadboard and by the relative position of the magnetic field coils used to produce the gradient, but it's not affected by the position of the vacuum system, whose role is to produce an atomic beam travelling across the whole length of the glass cell: as long as the translation stage moves the vacuum system along the glass cell's axis, the atoms could be trapped in any position of the glass cell, both in its center and at the edge. For this reason a $4\ \mu\text{m}$ error in the translation stage positioning, given its intrinsic repeatability, is completely negligible. Moreover, in the unfortunate case that the glass cell has a defect or gets scratched where the MOT beams hit the cell or where the optical tweezers beams are focused, we can always move the whole vacuum system a few millimeters apart.

5.2 Vacuum system

The vacuum system is composed of three main sections, as shown in Fig. 5.3, a commercial atomic source by AOSense, a pumping chamber and a full-glass science cell. The whole assembly is just 105 cm long from the oven to the end of the glass cell, mainly thanks to an optimized Zeeman slower stage that exploits a set of permanent magnets that are roughly 5 cm long, giving a huge reduction with respect to tens-of-centimeters-long Zeeman slower solenoids that are usually necessary in home-designed systems. The atomic source is connected to the pumping chamber via a differential pumping tube and a CF16 bellow that allows for the connection of the two rigid parts. On one of the sides of the octagonal pumping chamber we placed a tee-piece with a Bayard-Alpert gauge, while on top of it another tee-piece is connected to an ION-NEG pump and, by an elbow, to a valve where a turbo pump for initial rough pumping can be connected. Finally, the glass cell is attached to the pumping chamber on the opposite side of the connection bellow. The Ion-NEG pump is a NEX Torr D500 StarCell, with 500 l/s pumping speed for H_2 molecules, and the Bayard-Halpert Gauge (UHV-24P from Agilent) allows for measuring pressures as low as 5×10^{-12} Torr.

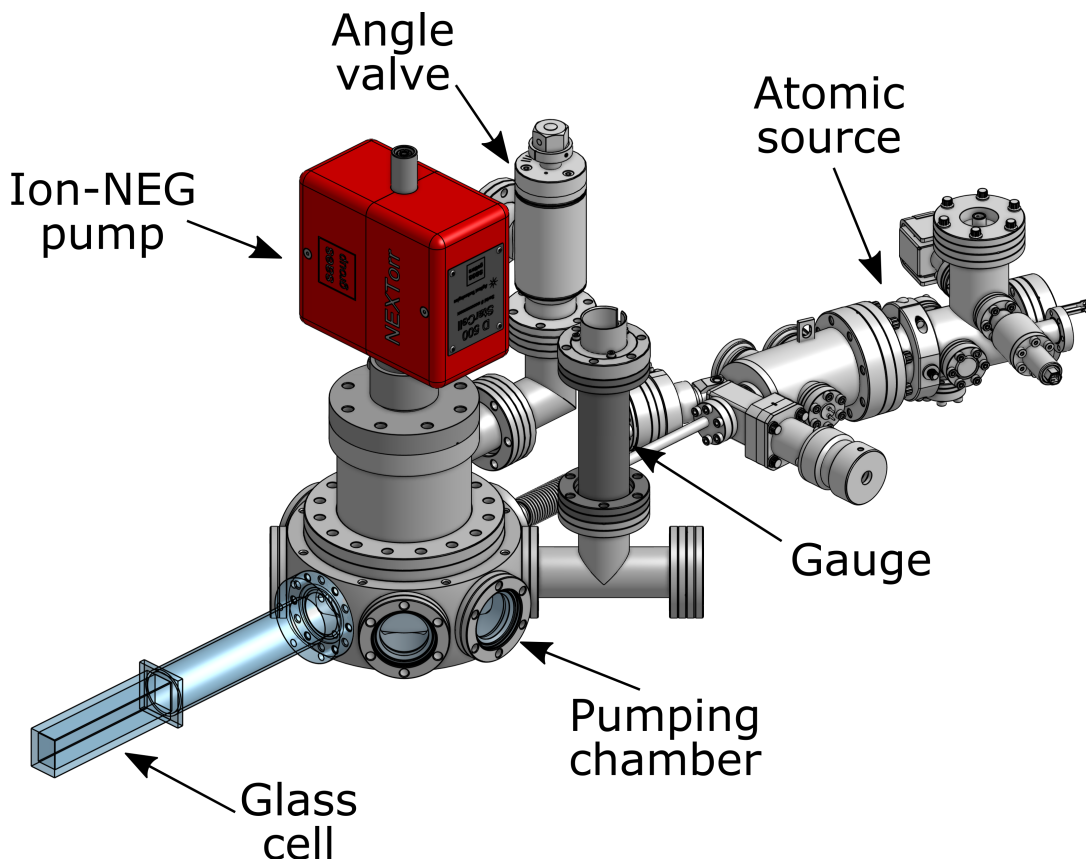


FIGURE 5.3: 3D render of the vacuum system showing the three main blocks: the atomic source, the pumping chamber and the glass cell.

5.2.1 Strontium atomic source

The atomic source employed in the experiment is an AOSense Sr Beam RevC, manufactured by AOSense. This commercial product comes as a complete vacuum subsystem including the oven, a set of permanent magnets for the Zeeman Slower, two viewports to optically deflect the cold atomic beam into an angled differential pumping tube and a small Ion pump. Before the differential pumping tube, an angle valve allows for sealing the atomic source and separating it from the rest of the vacuum system. We chose this commercial solution both to have a plug-and-play atomic source, saving months of work for the whole team, both for the compactness and design.

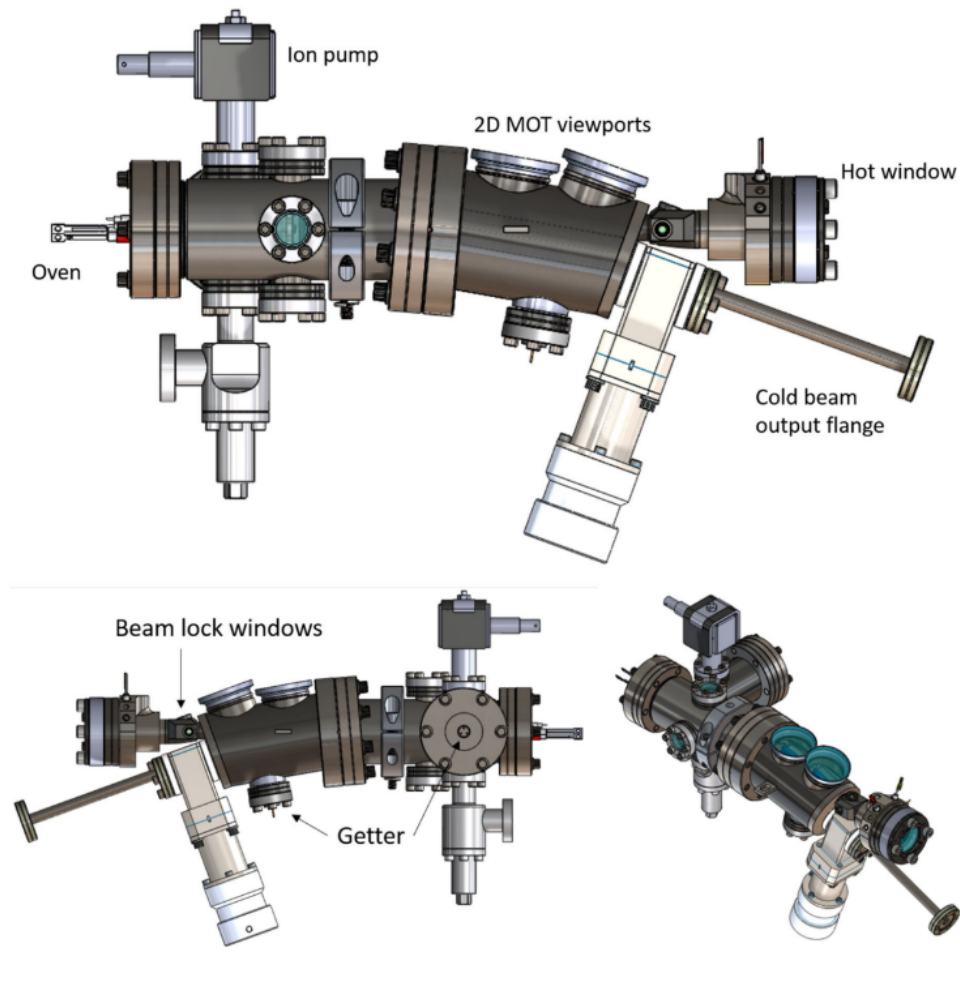


FIGURE 5.4: AOSense Sr beam atomic source.

In Fig. 5.4 a CAD model of the atomic source is reported. The oven can be connected to a power supply via two feedthroughs to heat up a resistive element and bring the Sr reservoir up to 480 °C. The atoms then fly through an array of microtubes that select a reduced range of transverse components in order to have a pre-collimated atomic beam. Three small viewports placed right after the oven can be used for spectroscopic measurements to characterize the atomic beam, taking care of the residual magnetic field produced by the permanent magnets that produce a Zeeman shift. The permanent magnets design is patented but we can see from the viewports that it consists of a 5 cm block between the first viewports and the

2D MOT viewports. A Zeeman Slower 461 nm laser beam coming through the Hot window, a Sapphire window kept at ~ 300 °C to avoid accumulating atoms on its surface, hits the counter-propagating atomic beam in the permanent magnets region, where the spatially variable magnetic field allows us to slow down the atoms enough to be deflected by the 2D MOT beams. These beams illuminate the atomic beam from the side, through the big 2D MOT viewports, and are retro-reflected by a set of in-vacuum optics. Such a combination can be optimized in terms of power balance and polarization in such a way that the atomic flux experiences both a transverse cooling effect, which collimates the atomic beam further, and a deflection. The deflection angle has to match the angle between the Zeeman slower axis and the angled differential pumping tube. This selects a class of velocities within the atomic velocity distribution that is slowed down enough by the Zeeman slower and deflected by the 2D MOT beams to go through the differential pumping tube. Such an optimization is not trivial, but the company gives a good initial guess in terms of Zeeman slower and 2D MOT beam shaping, powers, detunings and polarizations to get everything work together. During the first two years using this atomic source, we made a few optimizations around these values, especially when trying to maximize the number of atoms in the 3D MOT and minimizing its temperature, but the factory initial values were a good starting point.

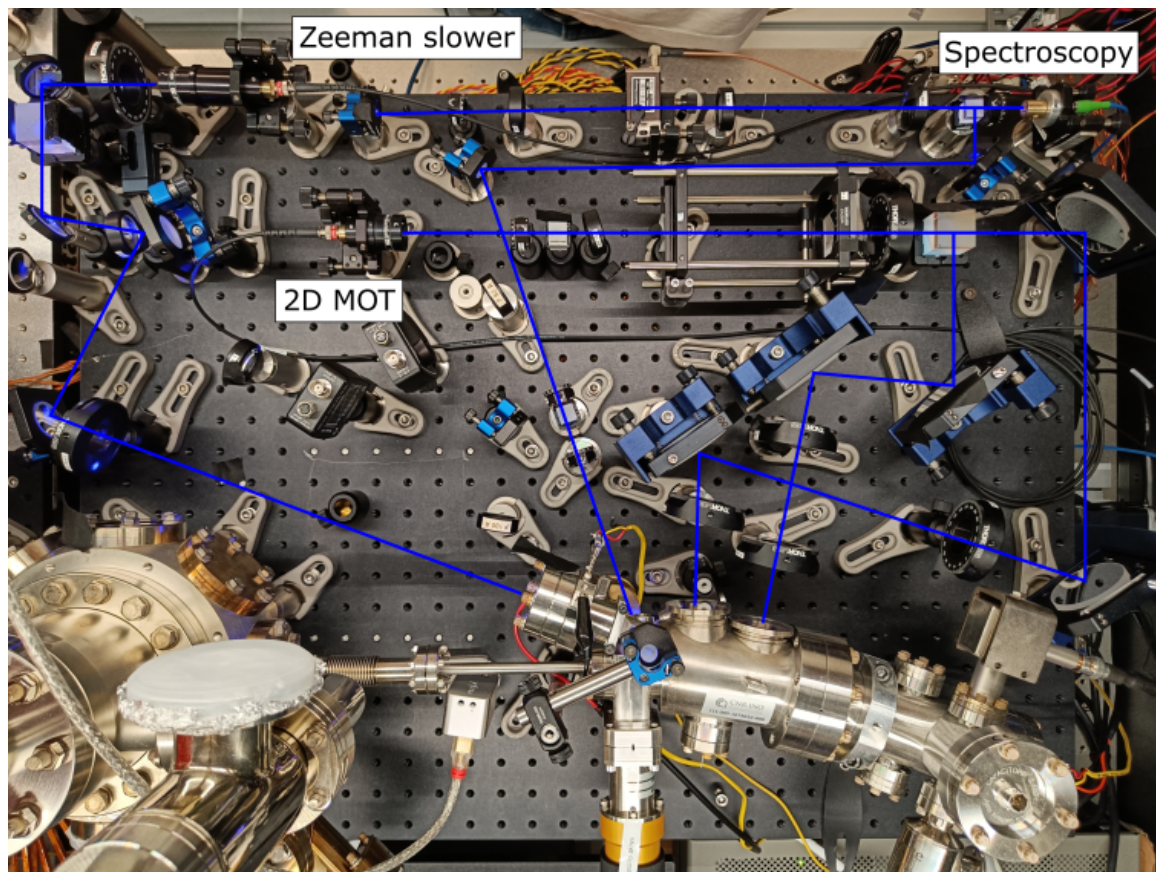


FIGURE 5.5: Zeeman slower, 2D MOT and spectroscopy optical setups.

Fig. 5.5 shows the optical setups for spectroscopy, Zeeman slower and 2D MOT. The spectroscopy beam is frequency tuned via a double-pass AOM that allows us to

TABLE 5.1: Optimized power, beam size and polarization for Zeeman slower and 2D MOT beams.

Beam	Waist	Power	Detuning	Polarization
Zeeman slower	8 mm (round)	50 mW	-580 MHz	σ^-
2D MOT (1)	25 mm x 5 mm	16 mW	-40 MHz	σ^+
2D MOT (2)	25 mm x 5 mm	8 mW	-40 MHz	σ^+

match the resonant frequency of the $^1S_0 \rightarrow ^1P_1$ 461 nm ^{88}Sr transition onto which the laser emission frequency is locked. The beam is aligned through a pair of tiny vertical viewports (called *Beam lock windows* in Fig. 5.4) to be orthogonal to the atomic beam. If the spectroscopy beam is perfectly orthogonal to the atoms' propagation direction, the resonance center frequency is the same as that of a steady atom, otherwise any nonzero velocity component induces a Doppler shift in this measurement. To minimize a possible Doppler shift, the beam was retro reflected in such a way that any Doppler shift component on the incoming beam is balanced by a Doppler shift of the opposite sign on the retro reflected beam. We aligned the incoming and the retroreflected beams in such a way that no Doppler shift was visible. By retro reflecting the spectroscopy beam we also double the absorptive signal on the resonance. Because of the large natural linewidth of the 461 nm transition ($2\pi \times 30$ MHz) and of the transverse interrogation scheme on a collimated atomic beam, no saturation dips are observed in the absorption spectrum, which shows up just as a single-maximum curve even in this retroreflected-beam configuration. The frequency of this beam is modulated at 250 kHz with an electronic component in the diode laser controller acting on the diode current, and the amplitude of the modulation can be tuned with a trimpot. The light is sent on a photodiode that is connected directly to the blue laser electronics that demodulates internally the signal to produce a dispersive error signal to lock the laser.

The Zeeman slower beam comes out of a Schäfter-Kirchhoff collimator (60FC-L-4-M50L-01) with a 8 mm waist that, according to AOSense, is the optimal value. The collimator's focal lens slightly focuses the beam inside the Zeeman slower branch of the atomic source, to maximize the slowing effect. Two 1" waveplates, $\lambda/2$ and $\lambda/4$, are placed in front of the Hot window aperture to set the correct Zeeman slower beam polarization.

The 2D MOT beams need more beam shaping since they need to have an elliptical shape with a 5:1 aspect ratio. A "parent" 2D MOT beam is shaped via a pair of cylindrical lenses to expand the horizontal direction, then it is split in two beams with a $\lambda/2$ waveplate and a PBS allowing us to tune the power balance. Each beam's polarization is then set through a pair of $\lambda/2$ and $\lambda/4$ waveplates. In Tab. 5.1 the optimized parameters for each beam are reported.

5.2.2 Pumping chamber and glass cell

The remaining part of the vacuum system is composed of two main parts: an octagonal custom pumping chamber and a glass cell. The octagonal chamber serves as an intermediate connection between the atomic source and the science chamber and is

TABLE 5.2: Common classification of vacuum regimes.

Pressure range	Pressure (Torr)
Low vacuum	$10^3 - 10^0$
Medium vacuum	$10^0 - 10^{-3}$
High vacuum	$10^{-3} - 10^{-7}$
Ultra high vacuum	$10^{-7} - 10^{-12}$

connected to all the devices that allow us to bring and keep the vacuum system down to ultra-high vacuum pressures (8×10^{-12} Torr base pressure during daily operation). As I will explain in the following subsections, the pumping operation requires different devices and technologies depending on the pressure regime that is considered. Vacuum regimes are commonly classified as reported in Tab. 5.2

The pressure of the residual gas in a vacuum chamber is often measured either in Torr or mbar (1 mbar = 1.33 Torr). Our goal, as explained in the following subsection, was to get to extreme ultra high vacuum to minimize the effects of the background gas that is detrimental to any experimental application. To do so, one has to start from atmospheric pressure and remove the gas from the system. In our case we used a Dry Scroll pump (Agilent IDP-7) that can reduce the pressure down to 10^{-1} Torr, while a Turbo Pump (Agilent TwisTorr 74 FS) is capable of pumping the pressure down to the 10^{-9} Torr level. These two devices are necessary to remove the main gas volume after the vacuum system is assembled but their use is not necessary (and could also be detrimental) in a continuous daily use. For this reason they are assembled together and connected to the vacuum system through a flexible bellow that is attached to an angle valve, which is closed as soon as the pumping procedure is finished. In the unlikely event of vacuum failure, the “pumping station” can be connected again to the angle valve, which is opened again to let the gas out of the system. In order to get from 10^{-9} Torr down to extreme ultra high vacuum pressure two additional technologies and devices are used. In particular, an Ion-NEG pump (NEXTorr D500 StarCell) is employed to remove as much background gas as possible and keep the pressure regime during the daily use. This element is mounted on a CF100 to CF63 flange adapter on top of the octagonal chamber. The last missing element is a Bayard-Halpernt Gauge (UHV-24P from Agilent) that allows for pressure readings between 10^{-3} and 5×10^{-12} Torr. All these elements are visible in Fig. 5.3.

Finally, the main part of the whole vacuum system is a glass science cell manufactured by JapanCell. This is a rectangular cell ($33 \text{ mm} \times 25 \text{ mm} \times 120 \text{ mm}$) with flat surfaces (flatness $\lambda/10$ as specified in the datasheet). The two $33 \text{ mm} \times 120 \text{ mm}$ surfaces are AR coated in the 460-815 nm range, specified for angle of incidence (AOI) of 0° , while all the other surfaces are uncoated. The optically usable part is connected with a glass tube to a glass-metal junction that is then attached to a CF40 flange of the octagonal chamber. This connection has a few degrees of tolerance on the rotation along the cell’s axis, and we used a horizontal beam as a reference to block it at the right angle. In particular, we aligned a 1-mm-waist blue beam with a pair of targets at fixed height and then slightly rotated the glass cell flange to overlap the reflections of the cell’s surfaces over the reference beam. This procedure was fundamental for

the next alignments, in particular of the microscope objectives, as mentioned in Subs. 5.5.2.

5.2.3 Outgassing in UHV systems and limit pressure

The vacuum system steady-state pressure is determined by the balance of the pumping rate of the ION+NEG pump and the outgassing rate of the vacuum components surfaces. Outgassing is a general process that can occur in different ways, both through diffusion from the bulk material or through desorption from the material's surface. The latter process, opposed to the adsorption mechanism, induces a gradual release of gas molecules. Whereas gas molecules (primarily water, hydrogen and nitrogen) are naturally adsorbed by a material's surface at room pressure and temperature, desorption can be induced by heating or changes in pressure. The desorption rate is specific for each gas molecule and type of surface. In particular, we are interested in the desorption rates of metal surfaces, which decline at a linear rate with time [188]:

$$Q_{des} = q_{des} \cdot A \cdot \frac{t_0}{t} \quad (5.1)$$

where q_{des} is the desorption rate per unit area, A is the surface area, t_0 is a time constant (typically around 1 h) and t is time. As mentioned above, outgassing can occur through diffusion of gas trapped in the bulk as well. This is extremely important for steel objects, which trap hydrogen atoms in the material during the manufacturing process. Even if the pumping system is efficient enough to continuously remove all the molecules that desorb from the surface, the "bulk reservoir" of atomic and molecular gas will continue to diffuse towards the surface and desorb inducing a constant background gas source. The global outgassing process is rather complex, but under vacuum conditions it's reasonable to assume [189, 188, 190] that the gas desorbed from the surface can be pumped out efficiently and the diffusion from the bulk, rather than desorption from the surface, is the limiting factor in the time needed to reach UHV pressures and the asymptotic pressure value. In this regime, the outgassing rate is exponential with a time constant [189]:

$$t_d = \frac{d^2}{\pi^2 D(T)} \quad (5.2)$$

where d is the thickness of the material. The diffusion rate $D(T)$ is given by $D(T) = D_0 e^{-E_D/k_B T}$ where E_D is an activation energy. Analyzing the latter equation, it's easy to note that if the activation energy is very low then the gas species will diffuse quickly, even at room temperature, without requiring any heating. In the opposite case, if E_D is very high, it will not cause a significant contribution to the baseline pressure as the diffusion will be very slow. All the activation energies in between can be troublesome as those gases will diffuse quickly but not quick enough to remove all the gas from the bulk in a short time. In this case, a thermal activation of the process is required, and this is exactly what the bakeout process is used for. Bringing the material to a higher temperature accelerates the outgassing process by orders of magnitude and typically allows to take the vacuum system down to UHV pressure within a couple of weeks instead of years. The thermal dependence of the outgas rate explains why some groups started to build cryogenic setups where the whole vacuum system, or the

most critical parts of it, is held inside a cryostat maintaining a temperature of a few K. The result is a background pressure as low as 10^{-12} Torr or even lower [191, 192].

Vacuum lifetime, meaning the lifetime of an atom in an optical tweezer without any external laser or EM field excitation, is typically on the order of tens of seconds for a UHV pressure around 10^{-11} Torr. This lifetime can become a limiting factor as the array of optical tweezers is scaled up to thousands of sites, since this increases a lot the time required for the rearrangement of the atoms. Scaling the system size up to thousands of atoms is an important challenge for quantum simulation and computing, but this requires a very low baseline pressure to maintain a high survival rate of the whole array. If τ_{vac} is the lifetime of a single atom, the lifetime of an N -atom array, defined as the average time after which one atom is lost from an array of N atoms, is $\tau_N = \tau_{vac}/N$. Moreover, the larger N , the longer it takes to sort the atoms in a defect-free configuration (see Subs. 3.1.3). The N -scaling of the reordering time depends on the algorithm used to perform it, but a lower bound can be set as in Ref. [191]. Considering a constant time to acquire the image of the trap occupations, analyse it and compute the moves, and that at least $N/2$ atoms on average will not be in the target position, the time to sort a N -atoms array is $t_N = t_{analysis} + t_{move} * N/2$. Typical numbers for $t_{analysis}$ and t_{move} are 50 ms and 1 ms, respectively. Fig. 5.6, adapted from Ref. [191], shows the assembly time compared to the array lifetime for a standard vacuum setup ($\tau_{vac} = 19.8(7)$ s) and cryogenic setup ($\tau_{vac} = 500$ s). The assembly time of the array rapidly overcomes the lifetime of the standard setup for increasing N . The two curves cross at $N \sim 150$, where the time to prepare the array (150 ms) equals the vacuum lifetime. For even larger arrays ($N = 1000$) the assembly time (500 ms) is much larger than the array lifetime (10 ms), meaning that it is impossible to prepare defect-free arrays when scaling up the number of sites. On the other hand, a cryogenic system ensures a much larger vacuum lifetime, relaxing the constraints on the total assembly time and thus on the size of the array N .

Building a cryogenic setup can increase the vacuum lifetime by two orders of magnitude, but it makes the setup much more complicated as the whole setup have to be enclosed in a cryostat. On the other hand, many groups have demonstrated the realization of hundreds or even thousands of atoms in arrays of tweezers with standard UHV setups [33, 35, 38]. For this reason, we decided to build a standard UHV setup, as compact as possible to minimize the outgassing contribution to the baseline pressure in order to get to a pressure as low as few parts in 10^{-12} Torr.

5.2.4 Assembling and bakeout

We assembled the vacuum system starting from the central part. First we fastened all the connections to the octagonal chamber, including five viewports, an adapter for the CF16 bellow, a tee mount with a viewport and the gauge, and the custom tee that serves as CF100 to CF63 adapter on top of it, with an elbow connecting to the valve for a rough pumping. A temporary blank flange was placed on the aperture where the glass cell was going to be connected to. Finally, we placed the ION+NEG pump and removed the magnet cage for the bakeout and connected the scroll and turbo pumps to the angle valve. In this first assembly we excluded the glass cell because it is the most fragile part and, although it is rated up to 250 °C (fused silica), we didn't want to take any risk of damaging it. The other part of the vacuum system, the atomic source from

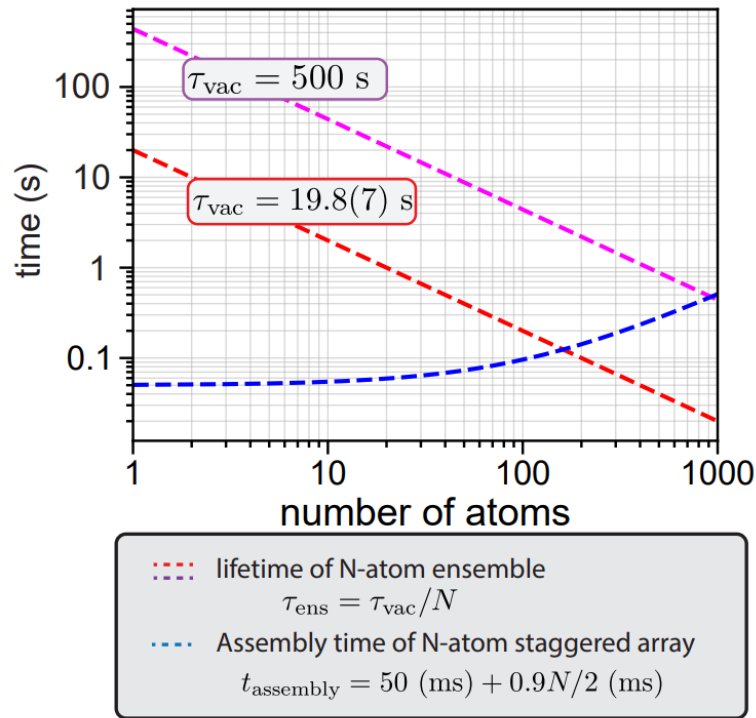


FIGURE 5.6: Vacuum lifetime and reordering time for a N-atoms array. Image adapted from [191]

AOSense, was already pre-baked and had no need for an additional bakeout. We then covered the whole apparatus with aluminum foils to better distribute the heat and wrapped it with four different heating tapes with different lengths in order to cover the whole surface and heat it as uniformly as possible. Having a few different heating tapes, each of them controlled by a separate variac (or autotransformer) allowed us to minimize the gradients across the surfaces. All the steel components are made of SAE 316 stainless steel and can easily overcome 900 °C with no damage. The ION+NEG pump is rated for 250 °C, while the Bayard-Alpert gauge and the viewports are both rated for 400 °C. As mentioned above, the higher the bakeout temperature, the faster the outgassing takes place. We chose a safe target temperature for each component, according to the rating, that guaranteed a reasonably fast desorption of the gas, and monitored the temperatures with thermocouples rated up to 600 °C that were placed all around the apparatus. In particular, we brought the bottom of the octagonal chamber and the viewports to 320 °C, the gauge and angle valve to 330 °C and the ION pump to 230 °C. We ensured that the spatial gradient across the setup was not too big by keeping the custom tee to an intermediate temperature around 270 °C.

Vacuum failure

After four days of bakeout, during which we were increasing gently the voltage on each variac to keep the thermal stress as small as possible, we finally reached the target temperatures mentioned above. One hour after the last adjustment of the variac current the temperatures were almost settled down, when we noticed that the

turbo pump started operating at its peak power of 75 W, instead of the 5 W that it maintained previously, and the vacuum pressure began to increase rapidly from approximately 5×10^{-8} Torr towards 10^{-5} Torr. The pressure was monitored by three different devices: the Bayard-Alpert gauge inside the apparatus, a cold cathode Pirani gauge (PKR 251 by Pfeiffer) and a Residual Gas Analyser (RGA200 by SRS). The Pirani gauge and the RGA were both connected through a tee mount to the turbo pump block. After eight minutes we measured a sudden bump in the temperature reading at the upper part of the custom tee of approximately 30 °C in just a couple of minutes. We decided to stop the bakeout, turning off the turbo pump to prevent damage from the increased pressure, and starting the cooling down process by reducing the heating stripes voltages. As for heating up, even in the cooling down process we tried to decrease the temperature by roughly 1°C/min and that took us the whole day and part of the day after. The following day we finished to cool down the apparatus and removed the aluminum wrapping. We noticed one damaged viewport whose brazing was completely melted, located to the right of the CF16 bellow, as can be seen Fig. 5.7. Remarkably, this viewport is the only damaged one, even though all the viewports were treated and heated in the exact same way (measured peak of 315 °C, occurred during the sudden temperature bump), and largely below the 400 °C temperature limit the viewports were rated for.

With a very large probability, the brazing melting at this viewport produced a sudden and large leak in the system that caused the vacuum failure. The most critical consequence of such failure is that the sudden hot air flux interacted with the NEG element of the StarCell pump, which is very sensitive to oxygen in the high-temperature regime, and started a destructive chemical reaction during which the getter material of the pump violently burned out (the Venting instructions in the NEX Torr StarCell manual warn about this process, as we found out discussing with the manufacturer). The results of such event are evident in Fig. 5.8, showing a large amount of ashes lying on the vacuum system lower baseplate, coming from the burnt components of the StarCell pump.

As we found out after a deep investigation, the viewport that caused the vacuum failure was not defected, but it was a completely different product that was unfortunately delivered with the other viewports. Among the other a Kodial viewports with Kovar brazing rated for 400 °C, we received two fused-silica viewports rated for 250 °C, packaged in the same box labeled as Kodial, one of which was mounted on the setup. This viewport failed when the bakeout temperature reached 310 °C. Fig. 5.9 reports the pressure readings of some notable gases (H₂, N₂, O₂ and water from the most abundant to the least abundant) registered with the RGA. A very narrow peak at the end corresponds to the moment when the window vacuum seal failed at 17:32 of 20/12/2022. No data is available after this event as the RGA switched to protection mode.

This unpredictable failure was really detrimental for our experiment since the pump was broken and all the internal surfaces of all the vacuum components were covered by the dust produced during this chemical reaction: we found this dust even in the angle valve and in the bellow that connects it to the turbo pump, which is the most far-away part in this apparatus. We agreed with the manufacturer of our vacuum components for an in-factory cleaning of all the custom components that would have required a too long remanufacturing time, and replacement of all the

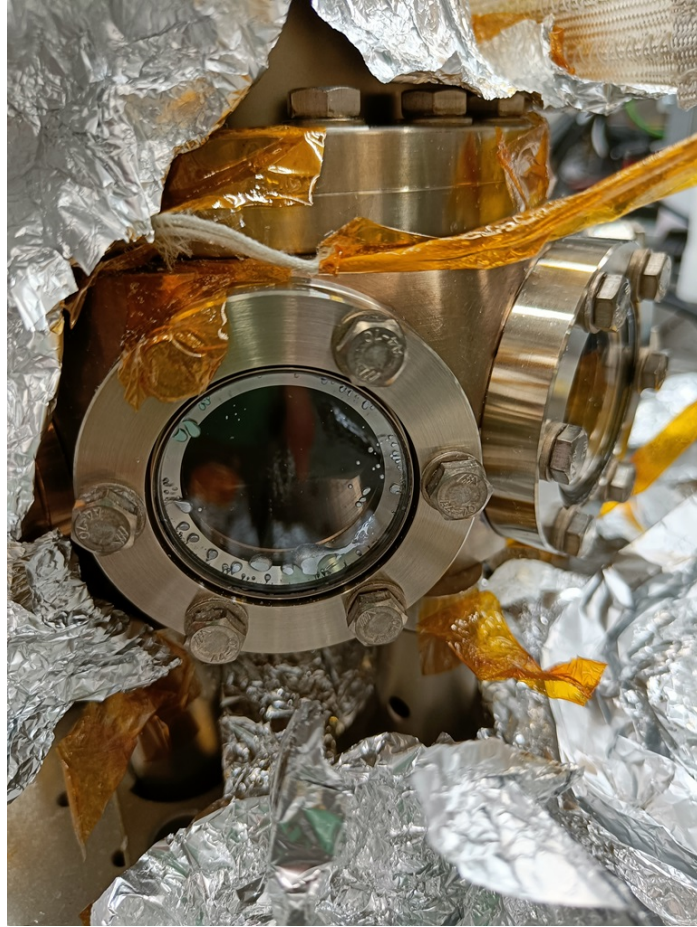


FIGURE 5.7: The brazing of this viewport melted and caused the vacuum failure. As we discovered later, this viewport was of the wrong type and rated only up to 250 °C, and it failed when the chamber reached 310 °C.

in-stock components such as the viewports, flanges, bellows, tees and angle valve. The two big custom components, the octagonal chamber and the tee adapter, were further treated with a vacuum firing, which is a pre-bakeout technique that consists in heating these components up to 900 °C in an in-vacuum oven. The glass cell and atomic source, that we smartly excluded from the first bakeout assembly, were luckily unaffected. Since the delivery of all the components took 3.5 months to complete, in the meantime we proceeded with a slow and controlled pre-bakeout of the glass cell. To better distribute the heat on the fused silica surfaces, the glass cell was mounted on a tee connected to a Bayard-Alpert gauge and to the turbo pump through a bellow, and it was covered with a copper cylindrical tube. The tube was wrapped in aluminum foils and then the heating stripes were distributed above. We brought the cell to 160 °C (measured on two thermocouples placed in two different spots on the cell's surface) and baked it for two weeks. In the first days of April 2023 we received back all the components and started again the assembly.



FIGURE 5.8: The sudden flow of hot air at 300 °C started a chemical reaction with the getter material (primarily zirconium) of the StarCell pump, inducing its complete burning out within a couple of minutes. The dust completely covered the bottom of the pumping chamber and contaminated most of the connections.

Second assembly and bakeout

The second assembly was rather fast as we already had experience from the first time. We assembled again the whole bulk excluding the glass cell and not connecting it to the atomic source. This assembly was then baked for three weeks following the same guidelines as the first time. After this period, we cooled the system down and activated the ION+NEG pump for the first time. The ION pump needs to be switched on and off for a couple of times before the NEG activation, because this helps removing the first layer of gas impurities from the electrodes surfaces. The NEG element was then activated by heating it under vacuum with a heating component included in the pump, enabling the full pumping capability of the getter. We increased the temperature of the getter, measured by an internal sensor, up to 550 °C in two hours and then let it cool down. It's important to activate these elements as long as the system is connected to the turbo pump, which can efficiently pump the activation product gases out of the system. Indeed, we measured a pressure increase while activating these elements. Finally, we closed the angle valve and disconnected the turbo pump. Then, we moved the system in its final position, on top of the movable breadboard that stands on the big translation stage, and connected it to the atomic source and ultimately to the glass cell. At that point, we reconnected again the turbo pump and gently opened the valve that isolated the atomic source in order to evacuate again the whole system. It is important to note that every time that we needed to fasten a new connection we had to first vent the system and let a small air flow penetrate the system to restore the atmospheric pressure inside the apparatus. If the flow is slow enough it should

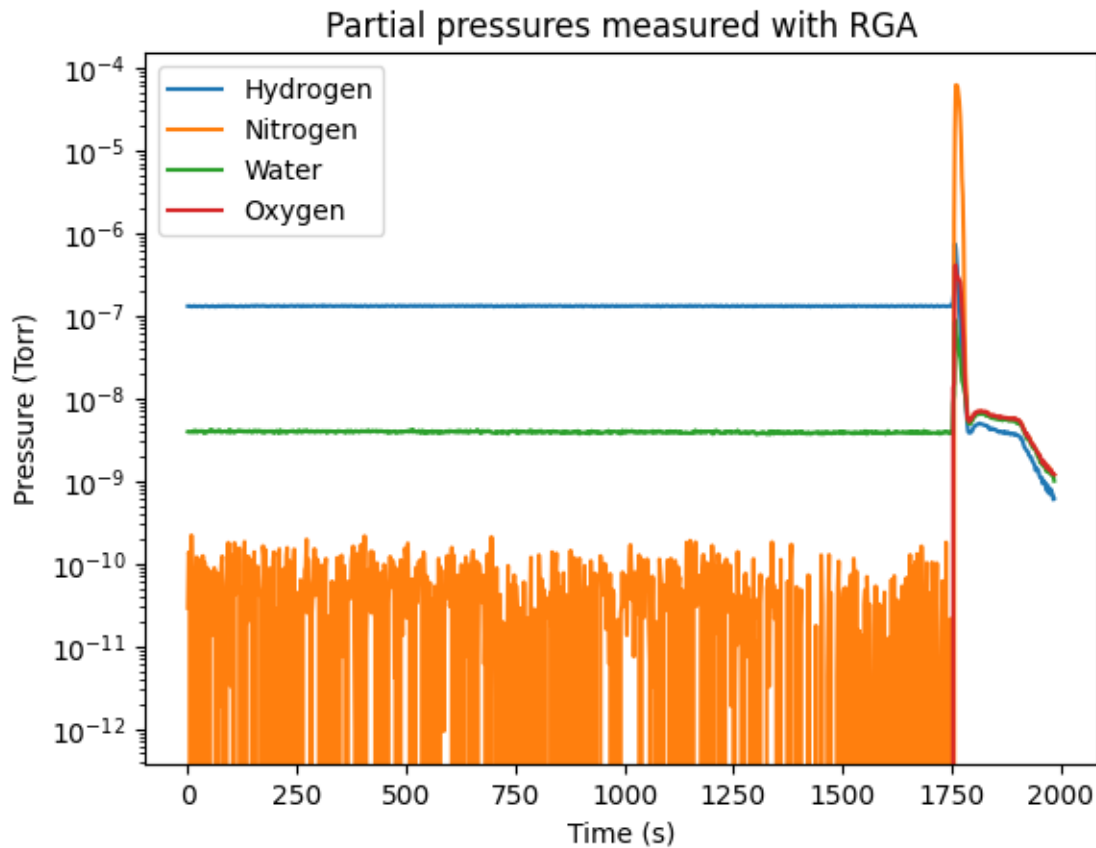


FIGURE 5.9: Partial pressure measurements with a residual gas analyser. All the partial pressures increased by three orders of magnitude within a few seconds.

not contaminate the surfaces and a full additional bakeout is not necessary.

With the glass cell finally installed, we proceeded to the last bakeout of the glass cell only at 160 °C for six days, while monitoring the system's temperature to avoid big thermal gradients. The angle valve for rough pumping was closed and the turbo pump disconnected, and the only pumping element was the ION+NEG pump. When the cell got back to room temperature we measured a pressure of 1.1×10^{-11} Torr, and it decreased further and further as the system settled down in the following months. Right now our baseline pressure is about 7×10^{-12} Torr with the atomic source oven at 300 °C, a temperature for which the atomic flux is almost negligible.

5.2.5 Tips and tricks for the vacuum system

There are a few tips that should be considered when building a new vacuum system that help in getting extreme UHV pressures even with a non-cryogenic setup. First of all, the size of the system matters, as having the system as small as possible reduces the surface from which the gas is desorbed. Moreover, the main pumping element, the ION+NEG pump, should be placed in a position where the conductance of the steel element is not limiting the pumping speed of the pump. In our case, the CF63 custom tee's height is roughly the same as the in-vacuum StarCell pump element, that is then hanging just above the CF100 pumping chamber and can efficiently remove the gas

from there. Line of sights are very important as well: all the pumping elements should not be placed in direct line of sight with the science cell, because they could sputter impurities, especially during the first activation, that might deposit on the science cell surfaces [193]. For this reason the StarCell pump and the angle valve where the turbo pump is connected are placed after angled elements. Even the Bayard-Alpert gauge, which works with two filaments that are heated up to measure the pressure, had to be activated to degas impurities from the filaments. We decided then to put it in a tee to avoid sputtering gas to the pumping chamber or the glass cell. This position also has a similar conductance as the glass cell, and this should give, according to our simulation, a pressure reading that is quite close to what could be measured in the glass cell (where we actually want to know the pressure value). As mentioned above, both the gauges and the pumps have to be activated and sputter impurities from the surfaces, especially during the first activation. We noticed on both the elements that the pressure increase as a consequence of the switching on and off reduced a lot after the third activation. Last but not least, having additional viewports in an apparatus like this where all the science happens in a glass cell may be useful to have an extra line of sight on the atomic sample (to do spectroscopy, transverse cooling etc), but it is indeed one of the biggest weaknesses of a vacuum system, as we dramatically experienced. In the second assembly, after the vacuum failure, we replaced two of the six viewports on the octagonal pumping chamber with blank flanges in order to keep some optical access but minimize the weakness points.

5.3 Main Magnetic field coils

Magnetic field control is fundamental in several aspects of atomic physics experiments. Although the bosonic ^{88}Sr isotope has zero nuclear magnetic dipole moment and the ground state is insensitive to magnetic fields, controlling the magnetic field is key for trapping the atoms in the Magneto Optical Trap (MOT), moving the position of the red MOT, exciting the atoms to the clock state and tuning the polarizabilities. In particular, we designed a pair of high-field coils and a set of six compensation coils that fulfilled the following requirements:

1. Capability to produce a gradient > 50 G/cm in all the directions in anti-Helmholtz¹ configuration to generate the MOTs.
2. Capability to produce a magnetic field > 900 G in one direction to excite the bosonic isotopes on the doubly forbidden clock transition.
3. Form factor maximizing the optical access to the glass cell.
4. Possibility to produce a magnetic field of a few G in all three directions with an independent set of coils, to compensate for stray external fields and tune the position of the red MOT.

¹Helmholtz and anti-Helmholtz configurations refer to a specific configuration of a pair of round coils with radius d placed at distance d , such that the field contributions proportional to d^2 (Helmholtz) and d^3 (anti-Helmholtz) are zeroed, respectively. Here we will refer to these configurations in a more general way, referring to equal currents flowing in the same direction in the first case, and equal currents flowing in opposite direction in the second.

5. Uniformity across a typical tweezer array size (hundreds of μm).
6. Efficient thermal dissipation to minimize electric heating of the coils, which could be harmful to the delicate optical alignments around the cell and could cause air turbulence affecting the imaging quality.

These requirements are further elaborated in the following subsections. We chose to design a pair of hollow-core copper wires coils, that we called “high field coils”, to produce both a high quadrupole field for the MOTs and a large unidirectional field to excite the atoms to the clock state. Up to now these coils were only used in anti-Helmholtz configuration to produce the quadrupole field, but we designed, together with the LENS electronic workshop, an H-bridge-like circuit to quickly switch the coils connection from Helmholtz to anti-Helmholtz, which will be tested and installed in the next months. Another set of three pairs of coils, which are referred to as the “compensation coils” serves as magnetic-field compensation of the background fields and to offset the position of the red MOT. The two sets of coils are mounted together on an independent structure placed on the optical table and surround the glass cell. The convention that we use about reference axes is the following: the long direction of the glass cell is the y axis, the orthogonal axis in the plane is the x axis or objective axis (since it is the direction along which the microscope objectives are mounted) and the vertical axis is the z axis.

5.3.1 Motivation and requirements

A large magnetic field gradient is necessary to trap the atoms in the MOT, since the restoring force towards the center of the trap is an interplay between laser power and polarization and the magnetic field spatial profile. The requirements are more strict for the blue MOT than the red, as explained in the following paragraph. On the other hand, since ^{88}Sr (with all the other bosonic isotopes of Strontium) has zero nuclear spin, there is no hyperfine mixing of the 3P_J manifold levels, and therefore the clock transition has exactly zero line width. An external magnetic field can open this channel by mixing the manifold levels through the Zeeman effect. The Rabi frequency of this transition is proportional to the external magnetic field, so it is beneficial to have the largest B field possible.

B field for magneto-optical traps

Recalling the description of Magneto-Optical traps in Subs. 2.3.3, a combination of counter-propagating crossed laser beams and a magnetic field quadrupole can produce an effective restoring force for the atoms towards the center of the trap. The role of the magnetic field is to induce an imbalance in the scattering rate and therefore in the radiation forces that push the atoms from either side. Eq. 2.24, which describes the force applied to the atoms, can be rewritten in a more general vectorial form [58]:

$$\begin{aligned} \mathbf{F}_{\text{MOT}} &= -\alpha \mathbf{v} - \frac{\alpha g \mu_B}{\hbar k} \mathbf{r} \nabla \|\mathbf{B}\|, \\ \alpha &= 4\hbar k^2 \frac{I}{I_{\text{sat}}} \frac{-2\Delta/\Gamma}{[1 + (2\Delta/\Gamma)^2]^2}, \end{aligned} \tag{5.3}$$

where \mathbf{r} is the position of the atom with respect to the center of the trap, α is the molasses friction constant, $g = g_F$ is the Landé factor of the excited state, μ_B is the Bohr magneton, $k = \frac{2\pi}{\lambda}$ is the wave vector of the transition, Δ is the detuning and $\nabla\|\mathbf{B}\|$ is the gradient of the magnetic field. The second term of the equation contains both a dependence on the magnetic field gradient and on the linewidth of the transition, therefore an optimal value of the magnetic field gradient can be found to maximize the number of atoms or cool the atoms efficiently as close as possible to the Doppler limit $T_D = \frac{\hbar\Gamma}{2k_B}$. In this balancing process, the linewidth of the transitions is fixed, whereas the detuning of the MOT beams and the gradient can be adjusted. Typical values of magnetic field gradients for both the blue and red mot can be found in literature. The blue MOT requires a gradient of around 50 G/cm, while the red a gradient of around 1 G/cm [194, 69, 70, 92].

A naive explanation of why the red MOT is realized with a smaller gradient is the following. The atoms have already been cooled down to a few mK during the blue MOT stage and their velocity is reduced by a factor of 500 with respect to the hot atoms exiting the oven. The size of the MOT is linked to the magnetic field gradient and can be estimated by assuming a classical harmonic oscillator motion. To have a significant force at the points where motion reverses (where the Doppler shift is zero), the Zeeman shift $\Delta\nu = m_J g_J \mu_B B / \hbar$ must match the laser detuning magnitude, ensuring a resonant interaction area. The trapping volume can be thought as an ellipsoid around the trap center (the gradient is not constant along the three axes due to Maxwell's equations) where the interaction is resonant with the atomic transition, and this occurs at different distances according to the magnetic field gradient. The vertical radius of such ellipsoid along the z axis, for instance, will be $z_E = \hbar\Delta / (m_J g_J \mu_B \partial B / \partial z)$. As described in Subs. 2.3.3, the detuning must be the same order of magnitude of the linewidth of the transition Γ to minimize the MOT Doppler temperature. In the red MOT case, for which the linewidth is $\Gamma = 2\pi \times 7.5$ kHz, we can consider a detuning of 20 kHz, which results in a typical radius of ~ 150 μm for a gradient of 1 G/cm. The ellipsoid radius would be just 3 μm for a gradient of 50 G/cm. This would cause a sub-efficient loading of the atoms because of a small overlap with the blue MOT, which has a typical diameter of 1-2 mm. Moreover, confining the atoms in such small volume would increase the density of the cloud, which results in detrimental collisional processes that cause atom losses. It is therefore convenient to use a lower gradient to trap a higher number of atoms. Anyway, the detuning and the gradient have to be adjusted experimentally to give the best MOT in terms of either temperature, number of atoms or density. As we have understood, in order to operate the blue MOT we need magnetic field gradients of the order of 50 G/cm, that must be then decreased rapidly to a much lower value to operate the red MOT. We produce these gradients with a pair of water-cooled coils in anti-Helmholtz configuration, as described in the following subsection.

Excitation to the clock state

One of the most appealing features of employing two-electron atoms is the presence of ultra-narrow transitions and long-lived metastable states like the 3P_0 and 3P_2 states. The 3P_0 state, often referred to as the clock state, is insensitive to magnetic fields and has an extremely narrow linewidth. This happens because the transition from the ground to the clock state is doubly forbidden by selection rules. First of all, it

does not conserve the total spin S , since it is connecting an $S = 0$ (singlet) state to an $S = 1$ (triplet) state. Moreover, a $J = 0$ to $J' = 0$ transition is further forbidden by selection rules. Both S and J are exact quantum numbers for the clock state: indeed, the spin-orbit mixing of singlet and triplet states leading to intercombination transitions here does not apply, since the spin-orbit interaction alone can mix only states with the same J , so it does not affect the 3P_0 state. So, in the absence of other mechanisms leading to higher-order level mixing (as it happens with the hyperfine interaction in fermionic Sr isotopes), the ${}^1S_0 \rightarrow {}^3P_0$ transition in bosonic Sr isotopes is completely forbidden to all orders in the multipole expansion [195].

The transition from the ground state $|1\rangle$ to the clock state $|2\rangle$ can still be driven, by applying a magnetic field that mixes the clock state with a small component of the 3P_1 state with $J=1$ [196]. The field \mathbf{B} couples $|2\rangle$ to $|3\rangle$ (3P_1 state) with matrix element $\hbar\Omega_B = \langle 2|\hat{\mu} \cdot \mathbf{B}|3\rangle$, where $\hat{\mu}$ is the magnetic-dipole operator. Following first-order perturbation theory in a small coupling regime $|\Omega_B/\Delta_{32}| \ll 1$, where Δ_{32} is the energy difference between the two levels, the state $|2\rangle$ is admixed to a small component of $|3\rangle$:

$$|2'\rangle = |2\rangle + \frac{\Omega_B}{\Delta_{32}}|3\rangle \quad (5.4)$$

The transition $|1\rangle \rightarrow |2'\rangle$ is then partially allowed, using the 3P_1 state as a bridge. If we now consider an optical field \mathbf{E} at frequency ω , the Rabi frequency of the clock transition can be derived:

$$\Omega_{12} = \langle 2'|\hat{d} \cdot \mathbf{E}|1\rangle / \hbar = \frac{\Omega_L\Omega_B}{\Delta_{32}}, \quad \Omega_L = \langle 3|\hat{d} \cdot \mathbf{E}|1\rangle / \hbar \quad (5.5)$$

where \hat{d} is the electric-dipole operator and $\Delta_{32} = 2\pi \times 5.6$ THz is the energy difference between $|3\rangle$ and $|2\rangle$ states. The linewidth of this transition is broadened both via power broadening of the optical field, and by to the magnetic field, and it is proportional to the natural linewidth of the 3P_1 state Γ_{3P_1} :

$$\Gamma_{12} \sim \Gamma_{3P_1} \frac{\Omega_L^2/4 + \Omega_B^2}{\Delta_{32}^2} \quad (5.6)$$

The equations above can be further simplified if we consider the vector nature of the applied magnetic field and take the \mathbf{B} direction as quantization axis. The simplified expressions for the linewidth of the clock transition in bosonic Strontium become (see [69] for further details):

$$\Gamma_{12}(B) = \Gamma_{3P_1} \frac{\mu_C^2 B^2}{\hbar^2 \Delta_{32}^2}, \quad (5.7)$$

$$\mu_C \equiv \sqrt{\frac{2}{3}} (g_L - g_S) \mu_B$$

where $g_L \sim 1$ and $g_S \sim 2$. The linewidth, for which just the contribution of the magnetic field was taken into account, is proportional to the B field squared. With a field of 900 G, that we can generate with our coils, the linewidth becomes roughly $2\pi \times 0.3$ mHz. This is still a very small value (it is approx. 10^{18} times smaller than the transition frequency), but being nonzero opens up the possibility of coherent driving

the transition with Rabi frequency

$$\Omega_{12}(B) = \frac{\mu_C B}{\hbar \Delta_{32}} \sqrt{\frac{3\Gamma_{3P_1} \lambda^3 I}{4\pi^2 \hbar c}} (\hat{\epsilon} \cdot \hat{B}), \quad (5.8)$$

which is proportional to the B field and to the square root of the intensity of the drive laser field. As discussed extensively in Refs. [196, 69], broadening the clock linewidth with a magnetic field implies a few systematic shifts and effects that could ruin the precision of an optical atomic clock. Nevertheless, for us the main goal is to be able to drive the atoms to the clock state with a high Rabi frequency, for example to encode in that state one of the states of the qubit base. Differently from optical clock experiments, in which the frequency precision and accuracy is of utmost importance and the smallest possible linewidth is favorable, for these applications it is important to have a high Rabi frequency, both to reduce the time required to coherently excite the atoms and to have a broader linewidth. Working with a broader linewidth allows to relax the tight constraints for the frequency stabilization of the laser driving the clock transition. Indeed, the achievable Rabi frequency with the parameters used in Subs. 3.2.2 is $2\pi \times 8$ kHz, compatible with the values obtained in Refs. [69, 92]. Since the scaling is favorable for the B field rather than the intensity of the beam, we decided to design our set of water-cooled coils to be able to reach more than 900 G field in Helmholtz configuration. The coil configuration can be switched from Helmholtz to anti-Helmholtz with a circuit that is described later in this section.

5.3.2 High field coils

The high field coils were manufactured by Oswald Elektromotoren GmbH. Each coil is made of 7x6 windings of insulated hollow-core copper wire that has a square section with 4 mm side and an inner circular core with 2.5 mm diameter, and the wire is insulated by a 0.3 mm thick Kapton layer. A render of the CAD file of one of the two identical rhomboidal coils is shown in Fig. 5.10. The coils have two plaquettes for the connection to the power supply, one input and one output (3). Two cables are connected there with lug connectors, and all the windings are connected in series. The cooling circuit is instead split into three blocks of two layers each, as explained in the following paragraphs. We have three pairs of water inputs and outputs (2), one for each block of 7x2 windings. Since the conductor is not a unique hollow core wire, the electrical connection between layers had to be done by soldering a wire from one layer to another, with the soldering performed in a straight part outside the windings (4). The whole coils core is immersed in an epoxy resin cage (1). The resin part has four holes to hold the coils in an assembly together with the compensation coils, as shown in Subs. 5.4.1. The coils are spaced by 51 mm, mainly limited by the size of the objectives that have an outer diameter of 44 mm, leaving a 3.5 mm clearance on both sides.

The magnetic field achievable with this pair of coils was simulated on COMSOL Multiphysics, comparing three different shapes: a rhomboidal shape like this, a circular and an oval. Keeping constant the internal size along the cell's long direction (long axis of the rhomboid in Fig. 5.10) to maintain a good optical access through the coils, we realized that this shape resulted in a higher and more uniform magnetic field for the same current when the current circulates in both the coils with the same

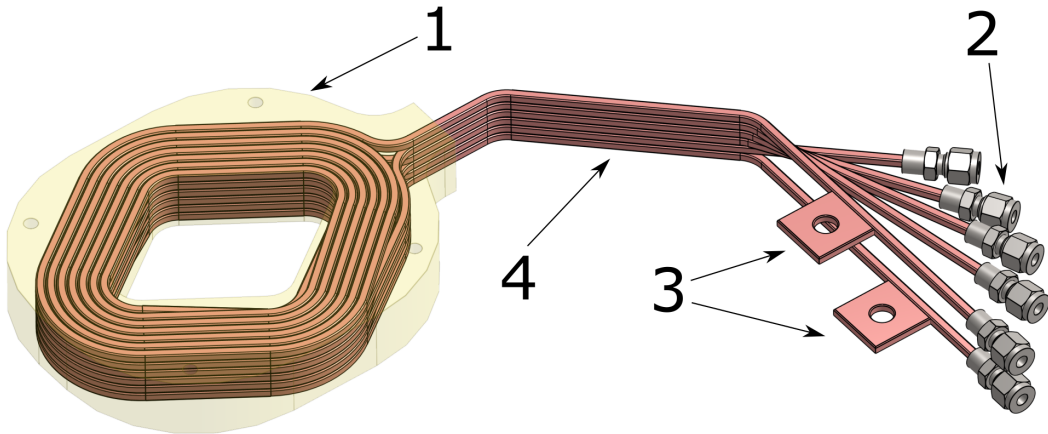


FIGURE 5.10: Three pairs of layers of windings are embedded in an epoxy resin structure (1) that serves as mounting structure too. The water Swagelok inlets and outlets (2) and the electrical connection plates (3) are visible. A straight section of the coils is necessary to make internal electric connections between layers (4). The rhomboidal shape is the one that leaves most of the optical access clear while guaranteeing high and uniform fields (in Helmholtz configuration) and gradients (in anti-Helmholtz configuration) at the center of the glass cell.

TABLE 5.3: B field homogeneity for a separation of $500 \mu\text{m}$ from the field center.

	x-axis	y-axis	z-axis
$\frac{\Delta B}{B}(500\mu\text{m})$	2×10^{-5}	2×10^{-5}	4×10^{-5}
$\frac{\Delta B}{B}(100\mu\text{m})$	1×10^{-5}	1×10^{-5}	1×10^{-5}

direction (Helmholtz-like configuration). According to our simulations, we can generate a field larger than 900 G at the center of the pair of coils placed 51 mm far apart with a current of 190 A. Such field should allow us to drive the clock transition with a Rabi frequency $\Omega \sim 2\pi \times 10$ kHz by considering a beam with intensity $I = 10^3 \frac{W}{\text{cm}^2}$ in Eq. 5.5. The field value is uniform around the center, ensuring a homogeneity in addressing atoms that are trapped in tweezers far away from each other. The typical size of an array of optical tweezers is a few hundreds of μm : the fractional uniformity of the field is reported in Tab. 5.3 for distances of $\pm 500\mu\text{m}$ and $\pm 100\mu\text{m}$ from the field center. Given this fractional uniformity, we are confident that the dephasing effect of magnetic field inhomogeneity on atoms driven to the clock transition across a typical array size is negligible (the Rabi frequency of the clock excitation scales linearly with the magnetic field, so we expect the same fractional homogeneity for it). This is valid as long as the tweezer array is formed around the central position of the coils, which is absolutely non trivial as discussed in Chapter 7.

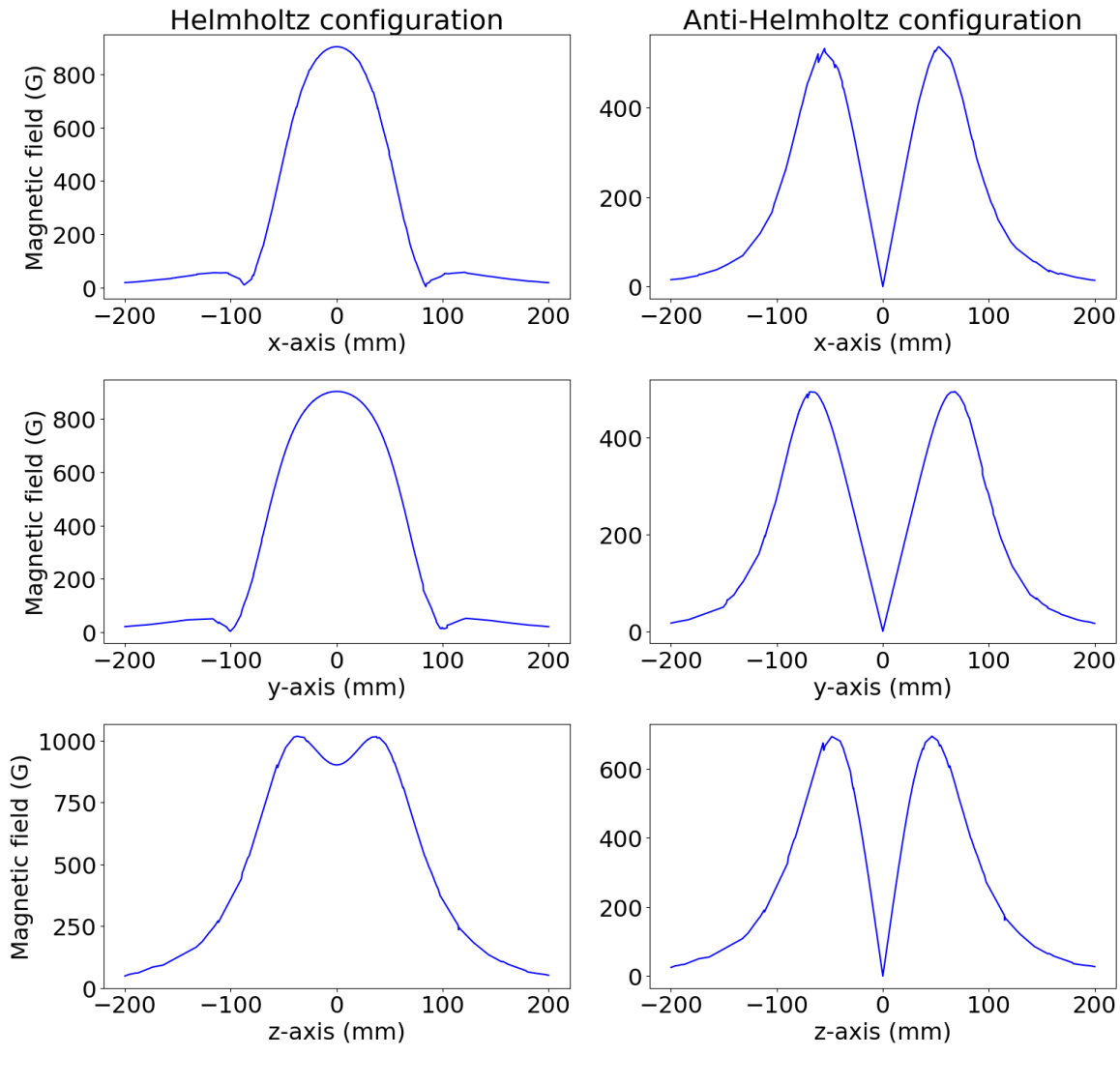


FIGURE 5.11: Absolute value of the magnetic field profile along three orthogonal axes for the coils in Helmholtz (left column) and anti-Helmholtz (right column) configuration and a current of 190 A.

The same simulation was carried out driving the coils in anti-Helmholtz configuration, where the current is circulating in opposite directions. The coils don't have a cylindrical symmetry, so the quadrupole-field gradient is different in the three directions, as shown in the second column in Fig. 5.11. The simulated slopes along the three axes for a current of 190 A are $125 \frac{\text{G}}{\text{cm}}$, $90 \frac{\text{G}}{\text{cm}}$ and $200 \frac{\text{G}}{\text{cm}}$ for x, y, z axes, respectively. Since the magnetic field produced by a coil is linear with the current (Biot-Savart's law), the coils can be operated at half the current, around 100 A, to still have more than $50 \frac{\text{G}}{\text{cm}}$ gradient in the weakest direction.

The maximum voltage drop, for a current of 190 A, is about 11 V on a 60 m Ω resistance of the coils series. The power dissipation is 2.2 kW, so we decided to use a 6 kW power supply delivering a maximum of 200 A, 30 V from Delta Elektronika (SM30-200). It is clear that such a system cannot dissipate heat in air and a water-cooling circuit is necessary. The simulations were carried out in COMSOL with the Magnetic

Fields interface and AC/DC module, that solves Ampere's law for the magnetic vector potential. The full description of the simulations and results can be found in Ref. [197].

When we received the coils from the company, we tested them in both Helmholtz and anti-Helmholtz configurations to compare the real case with the simulations. First of all, the linear dependence of the magnetic field on the current was tested, as shown in Fig. 5.12 for the Helmholtz configuration. The slope of the linear fit is $5.2 \frac{\text{G}}{\text{A}}$, showing that we can get up to 1000 G at the maximum current of the power supply (200 A). Once we confirmed the linear dependence of the B field on the current, we

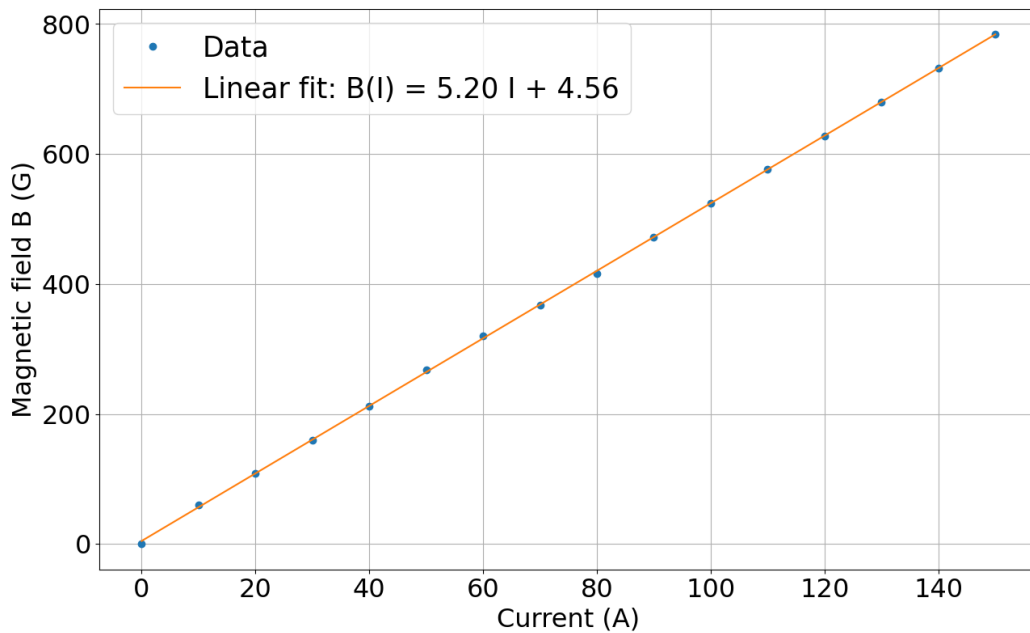


FIGURE 5.12: Measured linear response of the coils, producing a magnetic field B proportional to the driving current I in Helmholtz configuration. The slope is 5.2 G/A , allowing us to reach a 1000 G field at the maximum current provided by the power supply.

decided to test the spatial dependency along the x axis at 100 A current. In Fig. 5.13, the measured magnetic field is compared to the simulated values, where the latter ones were re-scaled to correspond to a current of 100 A. Also in this case we observe that the coils perform slightly better than what we estimated, and the spatial behavior is similar. The anti-Helmholtz configuration was tested as well with a current of 100 A. Also in this case we confirmed that the gradient that can be achieved with the coils is slightly higher than what the simulations suggested. The simulated and measured results for the magnetic field in Helmholtz and anti-Helmholtz configurations are reported in Tab. 5.4. All the data are rescaled to correspond to a current of 190 A, which is a safe workable value close to the maximum current that the power supply can provide.

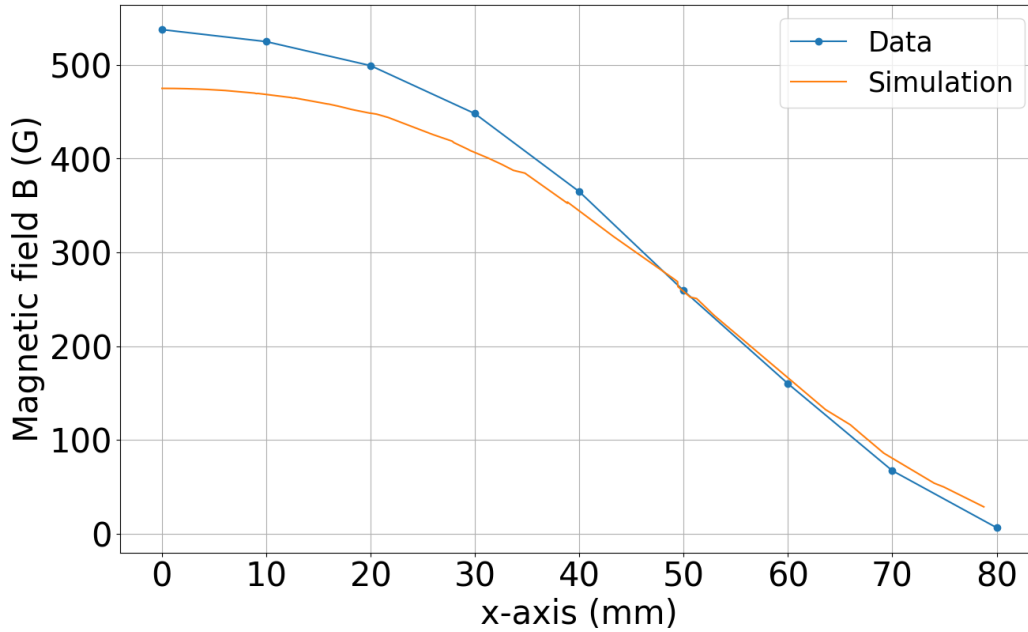


FIGURE 5.13: Spatial B field profile along the x-axis for a current of 100 A and the coils connected in Helmholtz configuration. The x-coordinate measures the distance from the coils axis. The data (blue) overcome the simulation results (yellow), meaning that the coils over-perform what we expected from our simulations.

TABLE 5.4: B field amplitude and gradients comparing the simulations and measurements.

	Sim. value	Meas. value
B field (Helmholtz)	902 G	988 G
x-axis B gradient (anti-Helmholtz)	125 G/cm	128 G/cm
y-axis B gradient (anti-Helmholtz)	90 G/cm	96 G/cm
z-axis B gradient (anti-Helmholtz)	200 G/cm	211 G/cm

Water cooling circuit

The water cooling circuit is composed of a chiller P30300 manufactured by Techno-trans systems GmbH and a set of pipes and connectors that allow us to send a water flow through the hollow core wires of the coils. The chiller is capable of dissipating 3 kW of power through a water-to-water cooling circuit. The resistance of the two coils in series, based on the length of the conductor, cross section and copper resistivity, is about 60 m Ω . When we connected them to the power supply with 20 m long cables with 50 mm² section, the voltage-current curve of the power supply gives us the total resistance of the circuit. The measured resistance of the two coils is 75.7 m Ω , compatible with the estimate for the bare coils (considering a minor contribution from the contacts). The total power that the cooling circuit has to dissipate at 190 A current in continuous mode is $P = I^2 R = 2.7$ kW, of which about 2.2 kW are dissipated inside the coils bulk. As mentioned above, the cooling circuit inside the coils is divided into

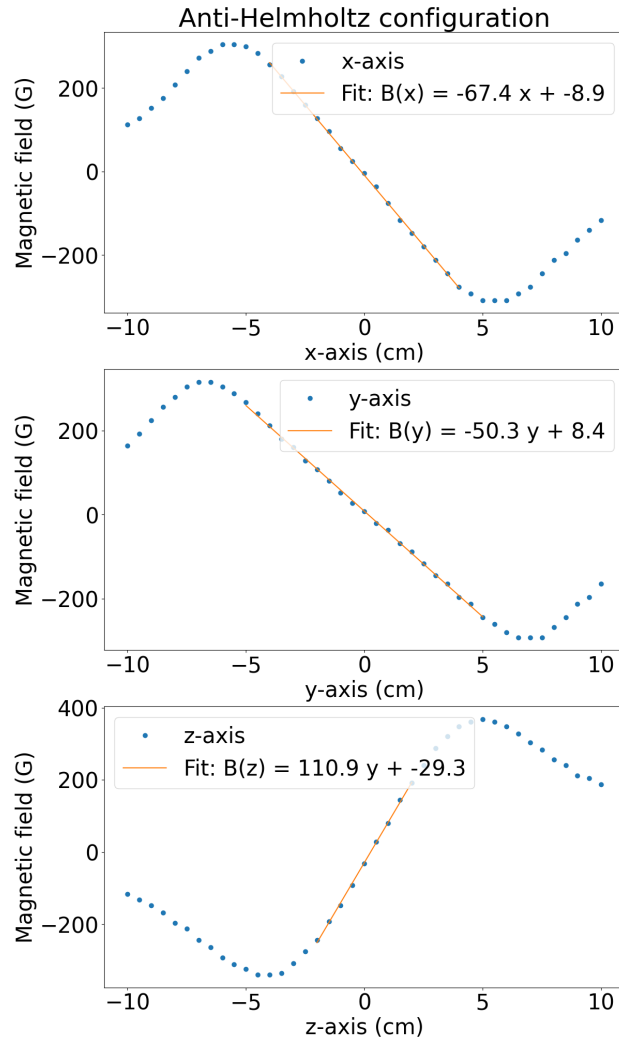


FIGURE 5.14: Spatial B field profile measured around the $B=0$ position along the three axes, for the coils in anti-Helmholtz configuration and a current of 100 A. The fitted slope of the linear part of the quadrupole field is $67.4 \frac{\text{G}}{\text{cm}}$, $50.3 \frac{\text{G}}{\text{cm}}$ and $110.9 \frac{\text{G}}{\text{cm}}$ for x , y and z directions.

three blocks for each coil, so that the six blocks can be cooled in parallel. Similarly to electric circuits, operating a water flow in parallel instead of in series reduces the pressure drop (analogous of the voltage drop) whilst increasing the water flow rate (analogous of the electric current). Based on a simulation carried out with COMSOL Multiphysics software, connecting the circuit in series would have meant having a very small flow rate but with a pressure drop along the circuit that is incompatible with commercial chillers. When our circuit is split in parallel elements, the system can be cooled with a water flow of $6 \times 0.7 \text{ l/min} = 4.2 \text{ l/min}$. Each layer of 7 windings is around 3 m long, and the simulations, extensively reported in Ref. [197], suggest that the water flowing in each block of 2×7 windings will have a temperature increase of $8.4 \text{ }^\circ\text{C}$ and a pressure drop of 2.2 bar. What actually happens is that the chiller adapts the water flow to keep the water chilled as long as it doesn't overcome the maximum operating pressure, which is 4 bar for the chiller that we employ. That implies that

the chiller will typically operate at a higher pressure than what we simulated and it will keep the temperature increase even lower. In everyday use, we experienced that, if the coils are operated at 100 A, which is enough to produce a blue MOT, the dissipation is reduced to 750 W on the whole circuit, and the temperature increases by less than 3 °C in continuous operation relative to ambient temperature when the coils are off. We still haven't employed the coils in Helmholtz configuration for the clock excitation, for which the coils will be driven at maximum current to produce the highest Rabi frequency possible and therefore dissipate 2.7 kW. Nevertheless, the clock excitation is a pulse with a short duration, on the order of 10 ms or less, which implies a very small impact in the duty cycle of an experiment, which is typically on the order of hundreds of ms. In other words, the instantaneously dissipated power is high, but the time available for cooling is way longer than the laser pulse during which the coils are on at full current.

Electric circuit

The electrical connection of the windings is in series: each 2x7 windings block is soldered to the following one as depicted in Fig. 5.10, and the output of one coil is connected to the input of the other one. The two plaquettes are connected to the input and output of the power supply with a 20 m long and 50 mm² section cable rated for high voltage and current. We chose this conductor because its resistance is low (0.386 Ω/km) and only gives a minor contribution to the resistance of the whole circuit. The current power supply is providing a maximum of 200 A and 30 V, which is suitable for our applications where a total resistance of the circuit of 75.7 mΩ produces a voltage drop of about 15 V when employing the maximum current. The measured time constant of the circuit, which defines the time necessary to turn off the coils depending on the inductance of the system L and resistance R , is $\tau = L/R$. During the tests the two coils were connected to the power supply with short cables, and we measured $\tau \simeq 9.9$ ms for $R = 60$ mΩ (negligible contribution of the cables), which gives an indirect estimate of the coils inductance $L \simeq 750$ μH. This time constant is too long for many applications, where ideally the coils are switched off instantaneously or in a much shorter timescale. This intrinsic physical limit given by the Faraday's Law can be overcome by introducing a circuit in series with the conductor that dissipates the energy stored in the coils much faster than the coils themselves.

The circuit currently used to switch off the coils is shown in Fig. 5.15. In this circuit, the inductor ($L1$) and the resistor ($R1$) represent the pair of coils. When the power supply is active and the Insulated-Gate Bipolar Transistor (IGBT) is closed (switched on), current flows clockwise through the inductor and $R1$, storing energy in the form of a magnetic field in the inductor. Since the resistance of $R2$ is much greater than that of $R1$ ($R2 \gg R1$), almost no current flows through $R2$ at this stage. The IGBT plays a critical role in controlling the flow of current by rapidly switching the circuit. When the IGBT opens (switches off), the current flow to the IGBT loop is interrupted, and the energy stored in the inductor must be released. Since the current cannot flow through the IGBT, a sudden high voltage is generated by Faraday's law and applied to the in-series varistor. A varistor is a variable resistor with a strongly nonlinear voltage-current curve, and its resistance is almost zero when a high voltage is applied. These electronic components are used to protect sensitive components, such as the IGBT and the power supply, during transient phases where a sudden high

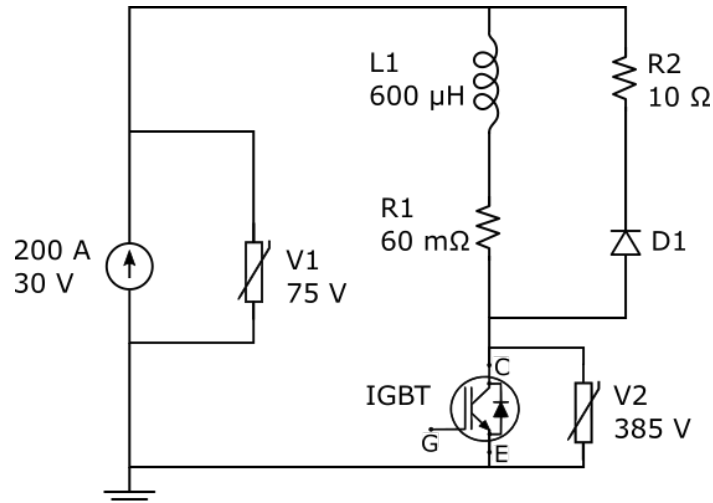


FIGURE 5.15: Schematic circuit for fast switch off of the coils. The current generator supplies the coils, represented by the inductance $L1$ and resistance $R1$. To control the current flow, an IGBT which is activated with a control voltage is connected in series. When the IGBT is closed, the current flows through the coils only. By switching the control voltage to open the IGBT, the current starts to flow through $R2$ too, thus introducing a higher resistance to speed up the circuit discharge.

voltage might damage them. The current is then redirected through the diode ($D1$). This creates a counterclockwise current in the $R1$ - $L1$ - $R2$ loop, allowing the stored energy to be dissipated through the load resistor $R2$. The diode ensures that the current flows in the proper direction during this phase.

To summarize, the key concept here is that the inductor stores energy in its magnetic field when the IGBT is on, and this energy is released to the circuit (through $R2$) when the IGBT is off. The rapid switching of the IGBT allows control over how much energy is transferred and when, while the diode ensures that the energy stored in the magnetic field is dissipated properly when the circuit is switched off.

This is a temporary design that allows us to switch off the coils very quickly, as the time constant of the circuit during the discharge is $\tau_d = \frac{L1}{R1+R2} \simeq 60 \mu s$. Anyway, the measured switching-off time is approximately $300 \mu s$ probably limited by other transient effects. The ability to switch-off the magnetic field in a few hundred microseconds is a key to pass from the blue MOT stage to the red MOT, as well as during the imaging, that could be Zeeman shifted by residual magnetic fields. A final design of this circuit has been designed together with the LENS electronic workshop and it will be assembled and implemented soon. This new circuit will not only allow for a fast switching off of the current, but also for switching the coils configuration between Helmholtz and anti-Helmholtz. The latter task is accompanied by similar problems, as we would like to change the circulation of the current in one of the coils abruptly, not being limited by the inductance of the system. To do so, we designed a H-bridge-like circuit, which uses four IGBTs to fully control the current flow in the two coils. A simplified schematic of the final circuit is shown in Fig. 5.16. This circuit shows the two coils, each of them schematized as a series of an ideal inductor and resistor and labeled as 1 and 2. Similarly to the previous circuit, two resistance in parallel ($R3$ and $R4$) allow for dissipating the energy stored in the coils faster than the

coils alone. The four IGBTs are labeled referring to Helmholtz (H), anti-Helmholtz (AH), High voltage (HI) and Low voltage (LO). By selectively activating the IGBTs in pairs, the current flowing in coil 2 can be inverted. When HHI and HLO are switched on, the current flows from left to right in both the coils (Helmholtz configuration). When AHHI and AHLO are switched on, instead, the current flows in the opposite direction through coil 2 (anti-Helmholtz configuration).

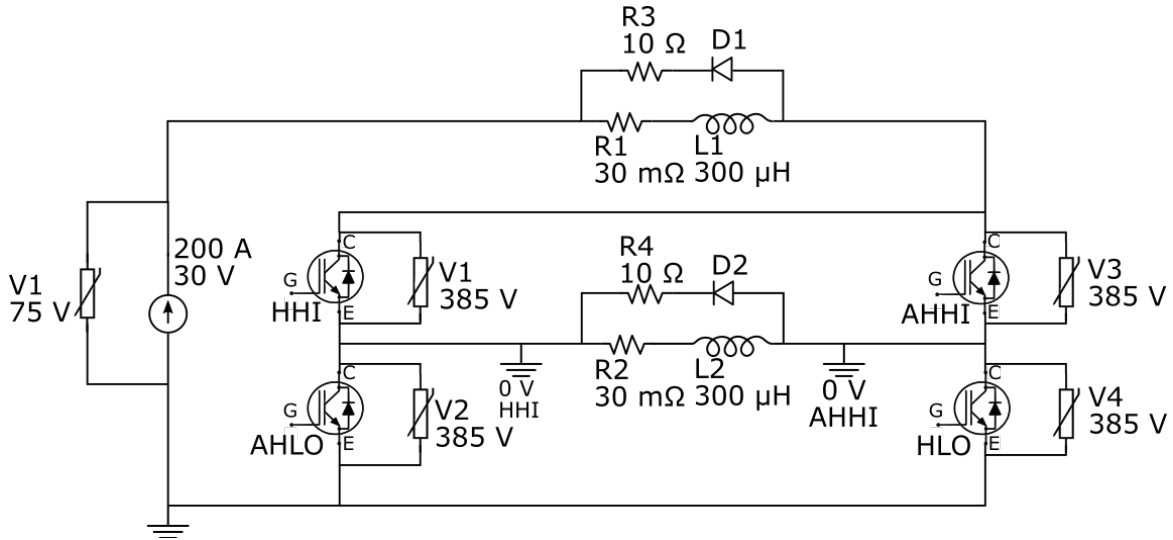


FIGURE 5.16: Sketch of half of the H-bridge circuit to control the high-field coils. The basic idea is to use separate IGBTs to selectively control the flow through the two coils. When the high-side IGBT (HHI) is closed and the low-side IGBT (HHLO) is open, the current flows through both L1 and L2, which represent the two coils separately, in the same direction. If instead HHI is open and HHLO is closed, the current will flow in opposite direction through the coils. This allows to switch from Helmholtz to anti-Helmholtz configuration, still enabling a fast switching off of the coils that is achieved by opening both the HHI and HHLO.

5.4 Stray fields compensation coils

A set of three pairs of low-field coils is used to compensate for stray magnetic fields, as well as for applying a controlled external field that can be used to tune the position of the red MOT and set a quantization axis. All the coils were manually wound with a Kapton isolated single conductor wire on a 3D-printed support that is used to assemble the coils orthogonally. Each pair of coils points along one orthogonal axis in the lab frame defined above. Once again, the x axis is the horizontal direction along the objectives axis, the y axis is in the horizontal plane along the glass cell's axis and the z axis is vertical. The main properties measured for these coils are reported in Tab. 5.5. The x axis coils have a rectangular shape with inner side lengths of 166 mm \times 138 mm and are separated by 138 mm. The y axis coils also have rectangular shape, with inner side lengths of 144 mm \times 138 mm and are separated by 192 mm. The z axis coils have instead an elliptical shape with inner full major axis of 138 mm and inner full minor axis of 98 mm, and are separated by 138 mm. The three

TABLE 5.5: Main properties of the set of compensation coils.

Property	X coils	Y coils	Z coils
Resistance (R)	2.5 Ω	1.8 Ω	2.1 Ω
Time constant (τ)	12.8 ms	11.56 ms	14.35 ms
Number of turns	100	70	120
Nearest separation	138 mm	192 mm	138 mm
Helmholtz field	5.0 G/A	4.2 G/A	7.0 G/A

pairs of compensation coils are connected each to an independent low-noise power supply (Delta Elektronika ES 015-10) that can deliver up to 15 V 10 A. The current flows in the same direction in both the coils of each pair to have them in Helmholtz configuration, producing an offset of a few G at the center of the assembly. The measured time constant of the pair of coils connected to the power supply is on the order of 15 ms. The power supply gives a non-negligible contribution to the time constant, as the switching time reported in the datasheet is of a few ms.

After characterizing the zeroing of external magnetic fields at the center of the assembly with a magnetic field probe (Stefan Mayer Instruments FCL 100, 0.5 mG/V sensitivity and 2.5 V range), the current flowing through the coils can be tuned to apply an arbitrary field to the atoms. This is particularly important to tune the red MOT position, which is very sensitive even to magnetic fields below 1 G. Indeed, the MOT is centered in the zero-field position, so applying an external bias field along three orthogonal axes independently can shift the position of the zero field in any position. The gradient determines the sensitivity to magnetic fields offsets. If a uniform offset field δB is applied along a direction with gradient b , the zero field position moves by $\delta x = \delta B/b$. Typical gradients for the red MOT are on the order of $b \sim 1$ G/cm in the weakest direction, so the zero field position, and therefore the position of the red MOT, can be moved by 5 mm by applying an offset field of 0.5 G along that axis. Being able to move the red MOT around the zero field position is fundamental to overlap it to the tweezer array, as explained in Chapter 7. The drawback of such high sensitivity to very small fields is that the position of the MOT can jitter if the applied field is not stable, and for this reason employing low noise power supplies is key. The blue MOT, opposed to the red, is trapped with a gradient 50 times higher and is less sensitive to magnetic-field offsets.

5.4.1 Supportive structure

The main high-field coils and the low-field compensation coils are assembled together in a structure that uses the 3D-printed pieces where the wire is wound. The assembly is shown in Fig. 5.17. The low-field coils along x (1), y (2) and z (3) are wound before assembling the structure and give support to the high-field coils (4), which are kept 51 mm apart through four cylindrical spacers (5). The z compensation coils supports are then secured on four variable height pillars that sustain the whole structure around the glass cell and allow for a fine tuning of the height of the assembly.

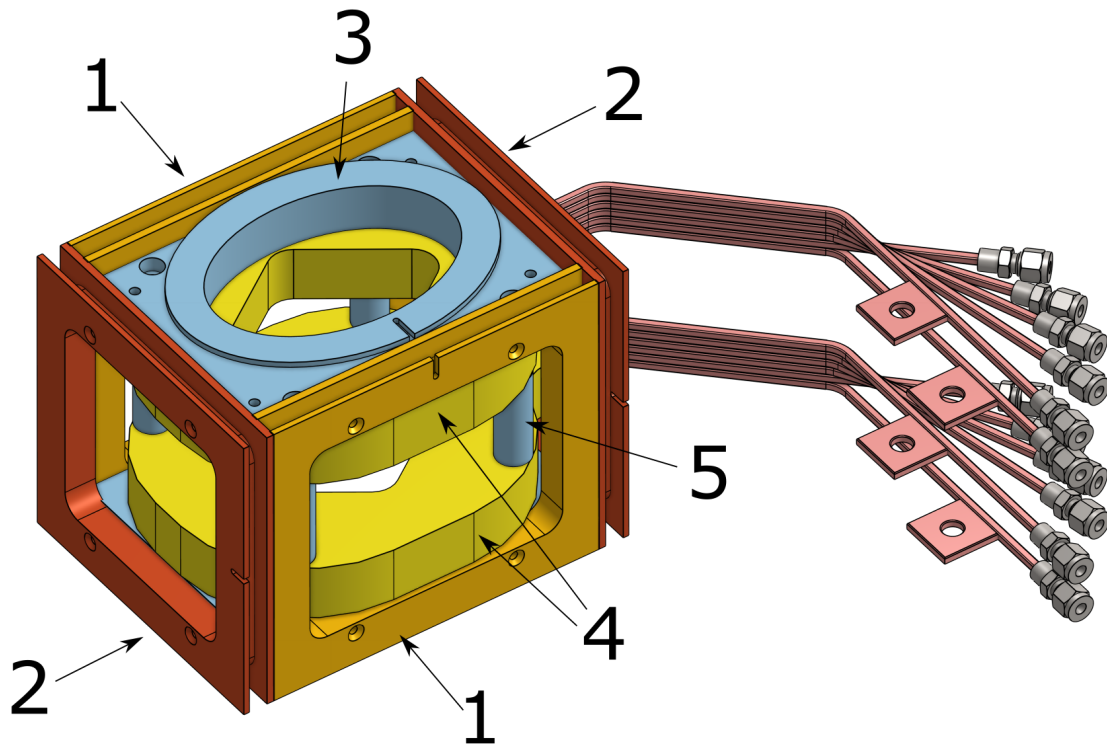


FIGURE 5.17: Assembly of the high-field coils and low-field compensation coils.

5.5 Microscope objective

The high-numerical-aperture microscope objective ($NA = 0.55$) used in this experiment is a custom product manufactured by Special Optics. Its role is to generate the optical tweezer array by focusing the tweezer-trapping laser light at 813.4 nm and to collect the fluorescence of the single atoms. The imaging technique that we perform is fluorescence imaging and it can be performed both on the $^1S_0 \rightarrow ^1P_1$ and on the $^1S_0 \rightarrow ^3P_1$ transitions, as discussed in Chapter 3 via fluorescence imaging. Moreover, in future developments of the experiment we might want to address individual sites of the tweezer array with the clock transition at 698 nm. The objective is therefore optimized for all these wavelengths, at 461 nm, 689 nm, 698 nm and 813 nm. In particular, it is designed to work in the diffraction limited regime for 461 nm, 698 nm and 813 nm, with no focal shift between 461 nm and 813 nm. It has a focal shift of $\sim 4\mu\text{m}$ between the tweezer light and 689 nm light. The working distance is 14 mm and it is compensated for the 3.5 mm thickness of the fused-silica science cell. The measured transmission is 92.6 %, 94.8 % and 96.6 % at 461 nm, 689 nm and 813 nm, respectively. The objective is assembled in an Ultem housing, blackened both inside and outside to minimize reflections. This material is a thermoplastic polymer with high dielectric strengths, which is very suitable for operating in an environment surrounded by hundreds of G magnetic fields. We purchased two identical objectives, both to have a spare copy in case the first one is damaged, both to use the second one for imaging the tweezer array directly to minimize aberrations and non-uniformities

TABLE 5.6: Specifications of the high-NA microscope objectives.

Property	Value
NA	0.56 @461 nm, 0.55 @813 nm
EFL	24 mm @461 nm, 24.5 mm @813 nm
Aperture	27 mm
FOV	0.36 mm @813 nm, 0.24 mm @461 nm, 0.25 @689 nm
WD	9 mm vacuum + 3.5 mm fused silica + 1.5 mm air
Diffraction limited	@461 nm and 813 nm
Transmission	92.6 % @461 nm, 94.8 % @689 nm, 96.6 % @813 nm

across the array. Indeed, the second objective is placed on the opposite side of the science cell to recollect the transmitted optical tweezers light. In the future, we plan to use the two objectives at the same time to double the fluorescence light collected by doubling the solid angle of photon collection. The specifications of the microscope objectives are reported in Tab. 5.6.

5.5.1 5-axes control

The microscope objective is mounted in an assembly that allows for 5-axes control, which is placed horizontally on the main breadboard on the optical table. A high-load pitch and yaw platform (PY004/M from Thorlabs) enables the tip and tilt control of the assembly. On top of that, a linear translation stage (L-509.44AD00 manufactured by PI) and a two-axes translating lens mount (CXY2 from Thorlabs) control the position of the objective along three orthogonal directions. In particular, the linear stage from PI moves the objective along the x axis in our cartesian axes convention, bringing the objective inside the magnetic field assembly. It has a 102 mm travel range, which is enough to extract completely the objective from the assembly. The objective assembly has enough degrees of freedom to align the objective orthogonal to the glass cell and with its axis centered on the center of the quadrupole field of the coils, where the blue and red MOT are formed and where we want to project the array of optical tweezers. Fig. 5.18 shows a front view of the objective in the coils assembly as seen from the opposite side of the science cell.

5.5.2 Alignment procedure

To align the objective centered on the MOTs and orthogonal to the science cell, we used a 2-mm-waist reference blue beam. This beam is aligned on the opposite side of the glass cell with a pair of mirrors, with two constraints: hitting the red MOT and being orthogonal to the glass cell's surface. As for the first constraint, we performed a blue fluorescence imaging of the red MOT, collecting the light with a small imaging system on an off-axis angle. By maximizing the fluorescence signal we optimized the alignment of the beam over the MOT. To orient the beam orthogonal to the science cell's surfaces we observed the reflection of different interfaces, overlapping them to the input beam by beam walking on the pair of mirrors. Moreover, we improved this method by looking at the interference between reflections on different interfaces of the

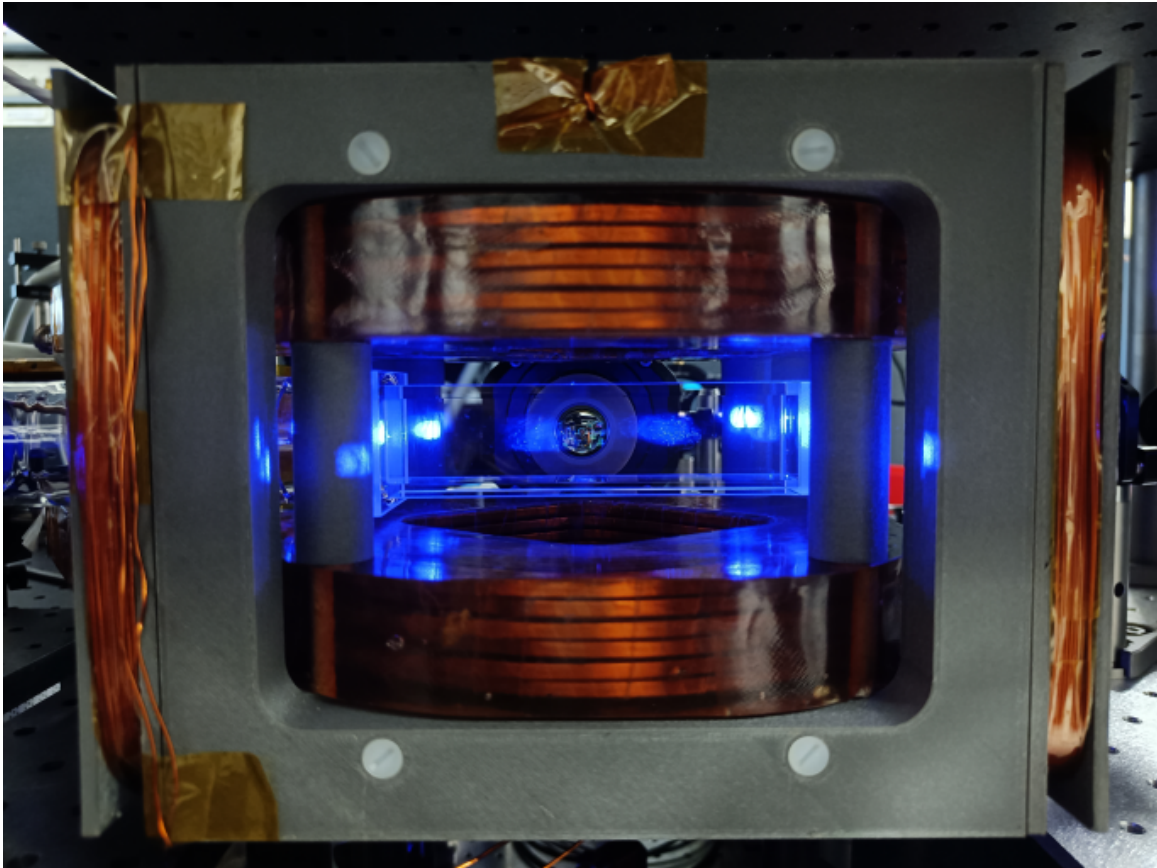


FIGURE 5.18: Front view of the microscope objective at its final position, surrounded by the coils assembly.

cell. These reflections are separated and picked up from the input beam by placing a half waveplate, a PBS and a quarter waveplate on the path, in such a way that the reflections from the cell get reflected by the PBS when they pass there on the way back. The interference pattern, observed on a camera, shows in general horizontal and vertical fringes that are generated by the non-orthogonality of the input beam. Beam walking the beam position and angle, the spacing between the fringes becomes larger and larger the closer one gets to 90° angle with respect to the surface. After iterating the two alignments (on the MOT and orthogonal to the cell) we got to convergence. This beam defines an optimal axis to align the microscope objective.

Ideally, the outer surface of the microscope objective is a flat surface that can be used, similarly to the alignment of the reference blue beam, to orient the objective. Unfortunately, the surface of our objective is concave and cannot be used for this purpose. We then proceeded to the alignment of the 5-axes control assembly without the objective, replacing it with a mirror mounted in the same threading. Overlapping again the reflection to the input beam we could set the right pitch and yaw angles, then we placed a pinhole to ensure the y-z alignment on the CXY2 mount. The only missing degree of freedom was the x axis, that was optimized directly on the fluorescence of the red MOT imaged through the objective itself. Since the linear translation stage has a step size of 1 nm and repeatability of 200 nm, we could move the objective back

and forth sampling the red MOT in different planes². When the sampled focal plane is well centered on the MOT, we could see the highest fluorescence signal, while at its edges the signal gradually falls. We determined the “edge focal planes” as those for which the fluorescence signal amplitude was half of the maximum, and used the corresponding positions of the translation stage to estimate the plane corresponding to the center of the red MOT, which corresponded to the position where we got the highest fluorescence. The reference blue beam was used to have a coarse alignment of the tweezer light too, ensuring that we were orienting it along the objective’s axis. Although the alignment optimization had to be done on the atoms signal, with this procedure we already got a coarse alignment close to optimal.

5.6 Laser systems

In this section the laser setups employed in the experiment are described. Right now, we have a blue laser, addressing the $^1S_0 \rightarrow ^1P_1$ transition at 461 nm, a red laser for the $^1S_0 \rightarrow ^3P_1$ transition at 689 nm, a tweezers laser for far-detuned dipole trapping at 813 nm and an UV laser to excite the atoms to Rydberg states, tunable from 316 nm to 319 nm. We will soon receive two lasers at 679 nm and 707 nm to repump the atoms from the 3P_0 and 3P_2 states and close the 461 nm transition by emptying the dark states (see the Subs. 1.3.2). In the near future, a laser addressing the clock transition will be purchased too.

5.6.1 Blue laser

The blue laser is an Injection-Locked Amplifier (ILA) diode-laser system manufactured by MOGLabs. The seed laser diode is a Nichia NDB4916T laser diode, tunable from 450 to 465 nm, producing a maximum of 250mW in ECDL configuration. A part of the power is used to inject the ILA diode, approximately 30 mW, while the remaining 200 mW are available through an aperture in the chassis. The seed diode is driven at a current around 290 mA, while the ILA, driven at 700 mA, outputs more than 650 mW laser power. A schematic of the optomechanic setup for the blue laser is reported in Fig. 5.19, with two outputs: the residual seed laser power output (ECDL seed) and the ILA output (ILA). Both the branches require a beam shaping to have a round gaussian profile with $w \simeq 1$ mm. On the seed side we have a branch going to a wavelength meter (WS8-10 by HighFinesse with 10 MHz absolute accuracy), which reads the bare emission frequency of the diode. Then, a branch goes on the main optical table to perform spectroscopy on the AOSense atomic source and get a locking signal. The last branch on the seed side is used for the 2D MOT beams described in Subs. 5.2.1, outputting around 30 mW out of the optical fiber on the experiment table.

To lock the laser on the atomic transition we exploit the ECDL controller to introduce a modulation at 250 kHz on the current and apply a linear voltage ramp on the EC piezo to scan the resonance. The spectroscopy signal is measured by a balanced photodiode and sent back to the ECDL driver that demodulates it and

²A microscope objective has a depth of field $DOF \simeq \frac{\lambda\sqrt{n^2-NA^2}}{NA^2}$, where n is the refractive index of the medium. The DOF for 461 nm light and $NA = 0.56$ is approximately 1.2 μm .

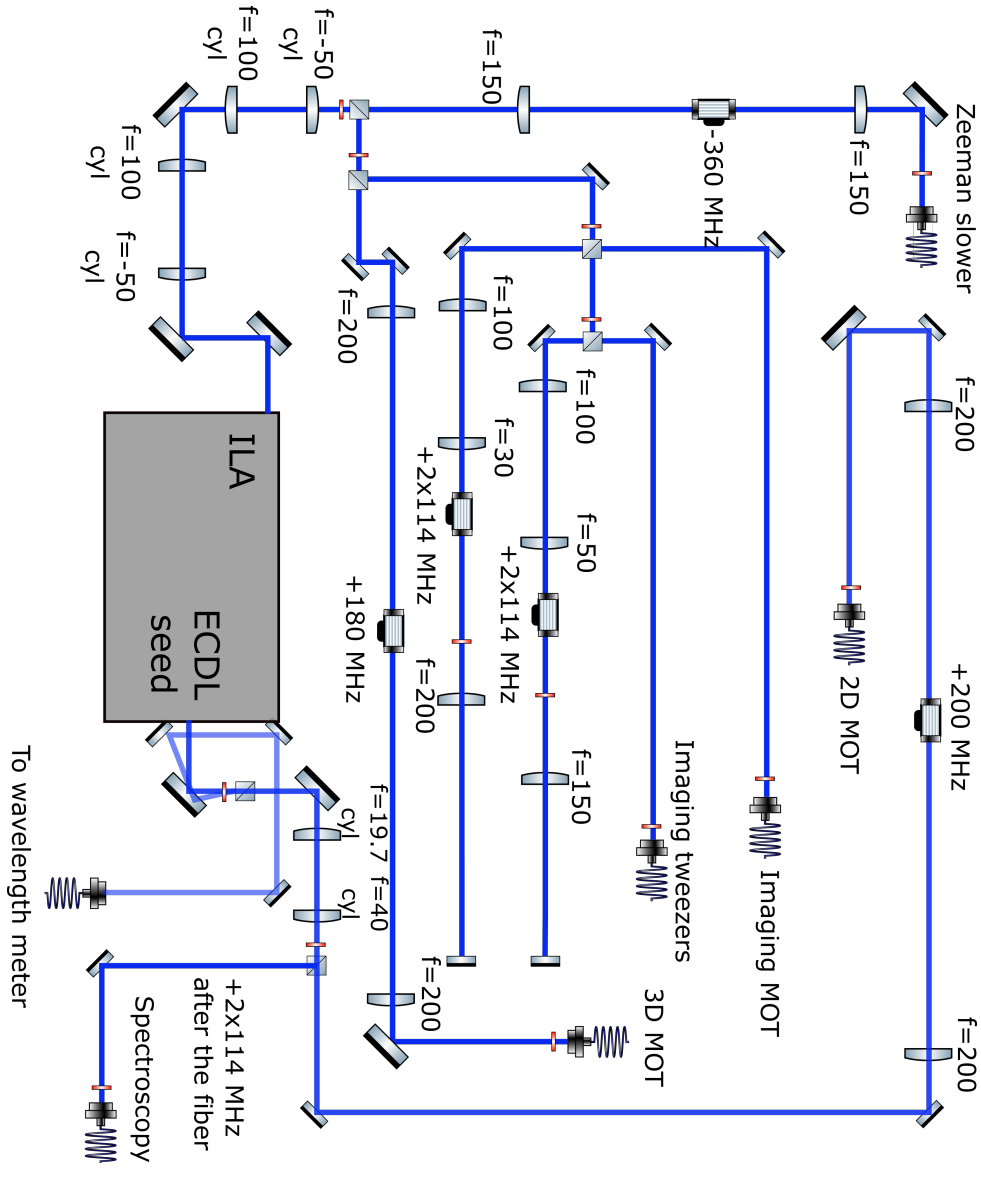


FIGURE 5.19: Schematic layout of the optomechanic setup for the 461 nm laser.

outputs a dispersive error signal. Again, a built-in PID locks the emission frequency to the error signal provided by the spectroscopy, acting on the diode current and on the piezo voltage. The PID gains can be adjusted from the front panel.

On the slave branch we have most of the power going to the Zeeman slower branch and to the 3D MOT, around 60 mW and 20 mW out of the optical fibers on the main optical table side, respectively. Two other branches are used for a resonant absorption imaging beam, which is used to image the blue and red MOTs in time-of-flight, and a “tweezers-imaging beam” which is used to image in fluorescence the atoms in optical tweezers and is red detuned to compensate for the light shift induced by tweezer light. The power of the two imaging beams output on the main optical table side is around 0.5 mW each.

Since the Zeeman slower beam requires high laser power with a large detuning (-580 MHz), we have to minimize the losses of the AOM frequency shifts. We decided

to lock the laser at a frequency roughly 230 MHz below the resonance, using then a single-pass 350 MHz AOM (3350-199 by G&H) to match the frequency gap and detune the Zeeman slower beam 580 MHz below the resonance (using the -1 diffracted order). This solution avoids employing a double-pass AOM (less efficiency) and AOMs working in higher frequency domain. The spectroscopy and the two imaging branches have a double-pass AOM centered at 110 MHz (3110-120 by G&H), while the 2D MOT and 3D MOT use a single-pass 200 MHz AOM (3200-121 by G&H). All these AOMs work with the +1 diffracted order. The specific frequency values driving the AOMs are reported in Fig. 5.19.

5.6.2 Red laser

The red laser is a Titanium:Sapphire (Ti:Sa) laser from MSquared (SolsTis with Equinox pump laser). The pump laser outputs up to 18 W at 532 nm and injects a Ti:Sa crystal that emits in the red and NIR range. The frequency is selected and filtered by a few elements inside the cavity, such as birefringent filters and etalon filters. We are currently using the pump laser at 13.5 W, which produce around 300 mW of red light at 689 nm. This is more than enough to lock the laser on an ULE cavity, perform the red MOT, in-tweezer Sisyphus cooling and monitor the frequency on a wavelength meter. For the excitation to the Rydberg states instead, as discussed in Subs. 3.2.1, a high power is required to have a good Rabi coupling, and therefore we will exploit the whole power available with this laser (up to 800 mW with maximum pump power). The laser setup presented in Fig. 5.20 is composed of a branch for the cavity lock, one for the 3D MOT beam, one for the Sisyphus cooling and one for the 2-photons Rydberg excitation scheme. Finally, one last branch goes to the wavelength meter to monitor the frequency. The 3D MOT, Sisyphus and cavity lock branches use a double-pass AOM at 80 MHz (3080-125 by G&H) while the Rydberg branch has a single-pass AOM at 350 MHz (3350-199 by G&H). The wavelength branch is not frequency shifted, like in the blue setup.

Frequency locking to ULE cavity

The frequency locking of this laser is realized by using a notched ULE cavity manufactured by Stable Laser Systems. The cavity length is $L=100$ mm and it is coated for high reflectivity at 633 nm, 689 nm and 698 nm. This allows us to lock the red laser, the clock laser and the Rydberg laser to the same high-finesse cavity ($F = 265.000$). The Rydberg light is produced by two consecutive SHG cavities, and the wavelength of the intermediate step is around 633 nm. Extending the high-reflectivity range of the cavity to this value was relatively easy for the company, thus allowing us to have a stable reference for the Rydberg laser too. The cavity is in a vacuum housing held at a pressure of 1×10^{-7} Torr. Two layers of in-vacuum thermal shielding, with a thermal time constant >30 h, ensure very high control on the cavity temperature to operate in the specific zero-expansion regime of the optical cavity, which is 37.63°C in our case.

The laser frequency is stabilized with the Pound-Drever-Hall (PDH) locking technique [198], which uses the optical-cavity length as a frequency reference. When laser light is coupled to a cavity, the intensity of the light reflected from the cavity input mirror shows a reduction (a dip in the intensity signal) when the light is resonant with one

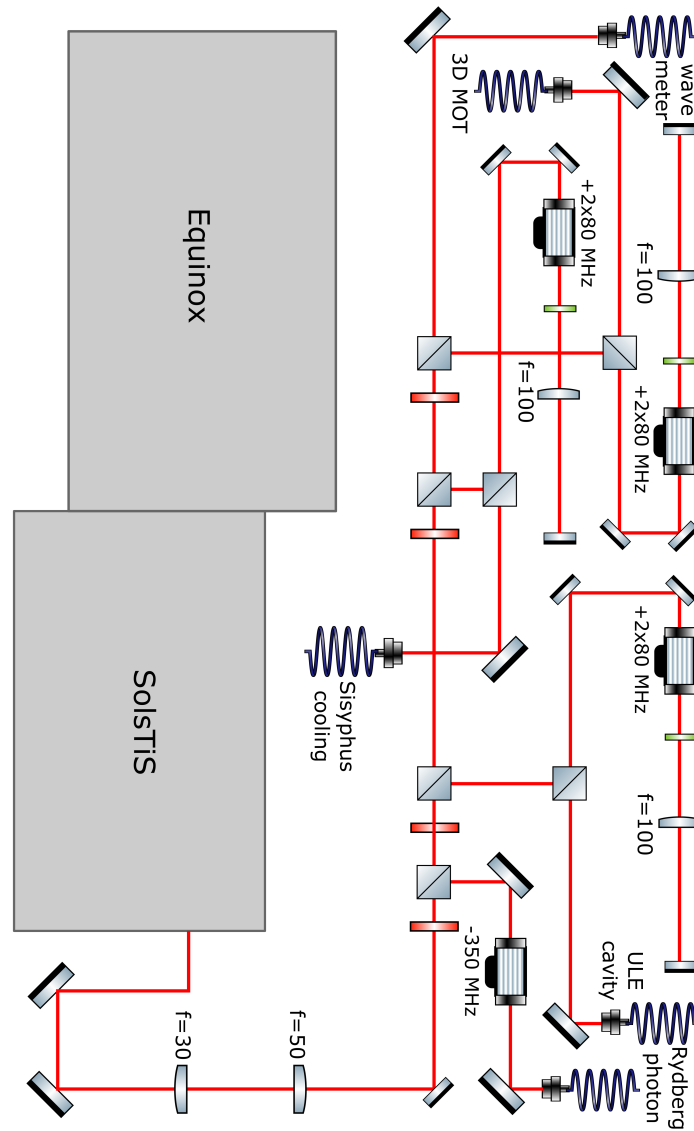


FIGURE 5.20: Schematic layout of the optomechanic setup for the 689 nm laser.

of the cavity modes. The resonance condition happens whenever the laser frequency is an integer multiple of the cavity free spectral range, i.e. $f = n\Delta\nu_{fsr} \equiv nc/2L$, where c is the speed of light and L the cavity length. In order to get a dispersive signal for locking the laser frequency on a cavity mode, in the PDH technique the light coupled to the cavity is phase-modulated: the spectrum of phase-modulated laser light has a carrier and two sidebands, spaced in frequency by an amount Δf which equals the frequency of the phase modulation. The reflected light has then three dips, corresponding to the carrier and sidebands. If the carrier is exactly at the resonant frequency f , it is partially transmitted and partially reflected but with no phase shift. The sidebands are instead reflected with a nonzero phase shift. The interference between the carrier and sidebands generates a signal that is sensitive to this phase difference and depends on the laser-cavity detuning. After mixing the intensity signal detected by a photodiode with a local oscillator signal at the same frequency as the

modulation, an electronic dispersive signal is obtained. The strength of this method is that, by looking at the phase shift, we can tell from the sign of the error signal if the frequency of the laser is becoming larger or smaller than the resonance. The error signal is then controlled by a PID module and sent to two actuators in the laser cavity, which can modify the emitted frequency according to the feedback. Specifically, we act on a pair of piezoelectric actuators mounted on a mirror that modify the cavity length and therefore the emitted frequency. The “slow piezo” has a ± 15 GHz range and 1.5 GHz/V sensitivity, with a flat response from dc to 50 Hz. The “fast piezo” has instead a ± 40 MHz range with 4 MHz/V sensitivity, with a flat response from dc to 100 kHz.

In our case, the light going to the cavity is phase-modulated at 8 MHz in a fibered electro-optical modulator (EOM) PM705b by Jenoptik. The amplitude of the modulation and of the local oscillator signal that we use to demodulate are optimized to maximize the signal of the sidebands. Moreover, we do not lock the laser with the carrier and sidebands directly, but we create two additional offset sidebands, each of them serving as an additional carrier with two PDH sidebands each, as shown in Fig. 5.21. This offset is introduced by mixing the phase modulation with an additional

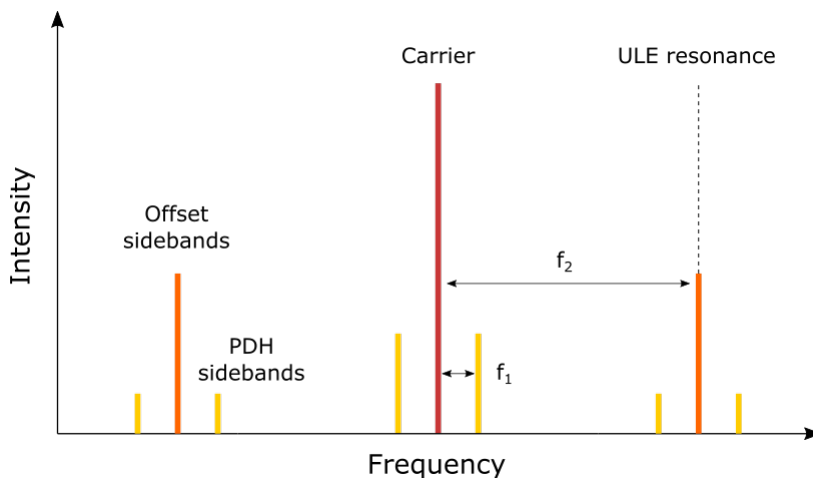


FIGURE 5.21: A fiber-coupled electro-optic modulator (EOM) is used to generate dual sidebands on a laser for Pound-Drever-Hall (PDH) locking with a frequency offset. High-frequency sidebands ($f_2 \simeq 643$ MHz in orange) are produced to act as carriers for lower-frequency PDH sidebands ($f_1 = 8$ MHz, shown in yellow). One of these high-frequency sidebands is locked to the resonant mode of an ULE cavity, stabilizing the laser’s carrier frequency (red) and keeping it close to the atomic resonance. The frequency can be adjusted to fine-tune the laser’s detuning relative to the atomic transition.

sinusoidal modulation at 643 MHz, generated by a Marconi 2019A signal generator. The two modulations are mixed through a power combiner and then sent to the EOM. This offset is necessary to compensate for the frequency difference between the cavity TEM00 mode, that we use as a reference, and the atomic resonance. Since the free spectral range of the cavity is 1.5 GHz, the closest TEM00 mode could be at most 750 MHz away from the resonance. The advantage of an offset PDH locking is that the offset is just used to create a new frequency triplet with carrier and sidebands,

around one of which the laser is locked with a standard PDH locking with low frequency modulation <50 MHz (see Ref. [199] for a detailed description of PDH offset lock).

We measured the frequency noise spectrum of the laser connected to the PID loop for frequency stabilization. Characterizing the frequency noise spectrum of the PDH

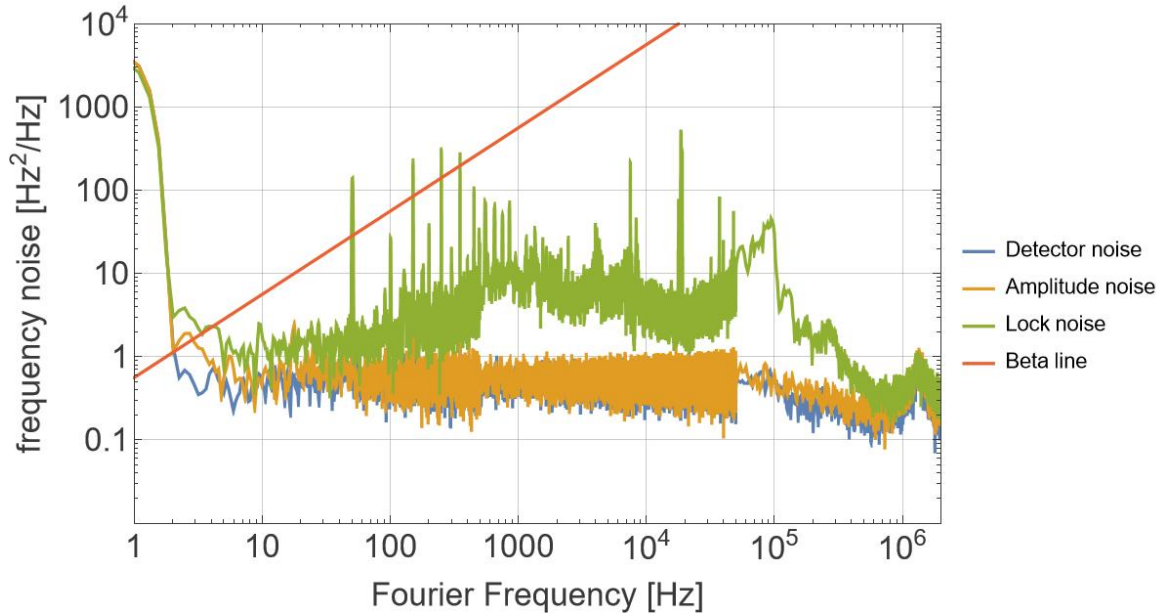


FIGURE 5.22: Frequency noise spectrum of the locked red laser. This spectrum is compared to the electronic noise and the amplitude noise of the circuit (see main text). The *Beta Line* [200] defines the noise level above which the frequency noise of the locked laser contributes to the laser linewidth.

error signal is important, as a dispersive error signal like this converts frequency fluctuations in amplitude fluctuations. Fig. 5.22 presents the frequency noise spectra of the electronic circuit, the amplitude noise, and the noise spectrum of the locked laser. The electronic noise sets the lower limit imposed by the photodiode and electronic circuit alone, while the amplitude noise accounts for the additional contribution from off-resonant laser light (not carrying information on the lock) reflected onto the photodiode. The amplitude noise may be larger than the electronic noise if laser intensity influences the noise spectrum. Ideally, minimal power should be used to avoid any additional contribution to the noise spectrum. The noise spectrum of the locked laser is measured after locking the laser to the cavity resonance of the TEM00 mode. The Beta Line [200] defines the noise level above which the frequency noise spectrum contributes to the laser linewidth. In our case, the lock noise spectrum remains below the Beta Line for frequency components above 500 Hz, which can be taken as an estimate for the linewidth of the locked laser. This level of noise is sufficient for the current setup, as the laser addresses a 7.5 kHz linewidth. However, for narrower transitions, such as the clock transition in Strontium, an improved lock circuit is needed to further reduce low-frequency noise. Indeed, the low-frequency part of the noise spectrum is already close to the limit of the electronic noise, which establishes a lower bound for the achievable noise level.

5.6.3 Tweezers laser

The laser used to generate tweezer light at 813.4 nm is a Matisse by Sirah, a Ti:Sa laser which is pumped by up to 25 W of green light at 532 nm produced by Millennia EV25S (Spectra-Physics Inc.). We can get up to 6.5 W of IR power that are fiber-coupled in a high-power photonic crystal fiber (LMA-PM-10 by NKT Photonics) that brings the tweezer light to the main optical table. Before the fiber, an AOM is used to control the power and can act as a fast switch. On the main optical table, the setup is divided into two main paths, one for the static array of optical tweezers, generated by a spatial light modulator (SLM), and one for a pair of crossed AODs, which can be used both for the reordering process and for the generation of simple rectangular-based arrays. The first version of the tweezer setup, including only the AOD branch, is reported in Fig. 7.1. This setup, which was used for the first characterization of the optical tweezers, was improved to the final design which includes the SLM, reported in Fig. 3.3.

5.6.4 UV laser

Our source of UV light for the Rydberg excitation is an IR laser whose frequency is quadruplicated through a custom system made by two SHG cavities in cascade. The source laser is a VECSEL laser from Vexlum, model VALO SF, which is tunable within the 1266 nm to 1276 nm range. The wavelength tunability range reduces by a factor of 2 after every SHG cavity, since the frequency is doubled and the wavelength is a half. Therefore, the laser light out of the quadruplication module can be tuned between 316.5 and 319 nm. This allows us to cover the energy gap between the 3P_0 and 3P_1 states, making both the excitation schemes described in Subs. 3.2.1 addressable. The quadruplication module (FHG) is manufactured by Leos S.r.l. and it exploits the Hänsch-Couillaud locking technique to keep the SHG cavities resonant with the laser frequency [201]. Between the first and second SHG modules, a small amount of power at around 633 nm is picked off the chassis and can be used to stabilize the frequency of the laser to the ULE cavity. Overall, the VECSEL laser emits around 1.1 W of IR power and we get around 250 mW of UV power out of the FHG cavity. Since the optics for UV photons have typically a few percent of losses on each optical element, we designed the optical path with the least number of optics. Moreover, this reduces the chance of scattering of highly energetic photons that can be hazardous for the scientists as well as detrimental for the experiment, even if well shielded. For this reason, the VECSEL laser and the FHG cavity are placed on the main optical table, to avoid both long optical paths and the use of optical fibers. An AOM will be used as a switch and to tune the laser power of the beam, which will be then elevated to the main optical breadboard level with a periscope and then aligned orthogonally to the glass cell's front surface. On this path, the beam will be shaped to produce a light sheet on the atoms to maximize the intensity, and it will be combined to the 689 nm light for the two-photon excitation scheme.

5.7 Control system

In this section we will briefly introduce the control system framework. The entire experimental cycle is managed using the Labscript-suite, a relatively new open-source framework developed specifically for atomic-physics experiments. However, its flexibility makes it suitable for a wide range of laboratory applications. Written in Python, Labscript requires a properly configured Python environment on the computers where it runs. In principle, Labscript cycles can be run simultaneously on different interconnected computers (via a local network), with each one performing a specific task, such as executing experimental shot routines or analyzing data, through dedicated apps. This setup would benefit for distributed computational load across multiple CPUs, preventing a single workstation from becoming overwhelmed. However, we are currently running everything on a single central computer. Labscript-suite consists of four main apps (GUIs), each with a distinct function:

- **BLACS:** This app monitors the status of connected devices, adjusts their output, and executes the experimental routine. Essentially, BLACS handles device control and routine execution.
- **RUNMANAGER:** This is where the Python routine code is converted into an HD5 shot database and sent to BLACS for execution, or to Visualmanager for sequence visualization. It also allows you to group *global* values, enabling direct control of experimental parameters from the GUI without editing the Python code. Runmanager is responsible for parameter control and routine preparation.
- **VISUALMANAGER:** This app displays the output values of all devices throughout the experiment timeline. It is a quick and effective way to verify if the code is functioning as expected. Visualmanager is used for shot visualization.
- **LYSE:** After shots are executed by BLACS, LYSE processes the data for analysis. Two types of analysis can be performed: single-shot or multi-shot, making LYSE essential for both single- and multi-shot runs, analysing automatically parameter scans and optimization sequences.

To add a new device in the Labscript-controlled experimental setup, it is sufficient to install the appropriate Labscript driver and initialize the new device in a Python file called the *connection_table*, which lists all the connected devices. Once the connection table is ready, BLACS will read the updated table and make a new list of connected devices. After this implementation, the devices can be controlled directly through BLACS, with no need to launch any other device-control software. When controlling a device manually through BLACS, the software operates in *manual mode*. However, when running an experimental routine, BLACS switches to *buffered mode*, controlling the devices according to the Runmanager routine.

Labscript is a flexible framework that allows one to define sequences using any logical structure in Python. Every action in the routine must be referenced to a timeline, which begins with the *start(t=0)* command and ends with the *stop(t = t_f)* command. No actions are allowed after the *stop* command. For this reason, it is important to define a master clock device that establishes Labscript's timing. All

the other devices, if sequence-timed, are triggered by the master device, typically a fast-triggering TTL device. This hierarchy must be strictly followed, with only one master device allowed. Some devices are already supported by Labscript developers (e.g., Pulseblaster, IMAQ cameras, etc.), while others have been implemented by users over the years. GitHub or the Google Group Labscript online community are regularly updated by other Labscript users.

Chapter 6

Production of a two-stage Magneto-Optical Trap

In this chapter, we present the results about the creation of a two-stage Magneto-Optical Trap for ^{88}Sr . We begin by detailing the optical configurations used for the 3D blue and red MOT setup. Following this, the blue MOT is analysed in terms of some key parameters such as atom number, density and temperature. In the following section we move to the red MOT, reporting our approach to get to a single-frequency narrow-linewidth MOT. This includes a crucial intermediate step, which we refer to as *Multi-frequency red MOT* or *Broadband red MOT*. Finally, we conclude with a characterization of the single-frequency red MOT, evaluating atom number, density and temperature.

6.1 Blue and red optical setups

The optical setups for the blue and red 3D MOT are assembled directly on the main optical table, below the main *horseshoe* breadboard described in Sec. 5.1. A sketch of the optics layout is shown in Fig. 6.1.

Both the blue and red 3D MOT are generated via three pairs of retro-reflected beams. We decided to use this configuration to simplify the optical setup and save half of the laser power with respect to a setup with six independent laser beams. The three branches are obtained by splitting a single laser beam with $\lambda/2$ waveplates and PBSs, in such a way that we have just a single optical fiber on the table. In this way we can control easily the power stability of the laser light and the fiber coupling by monitoring just two optical fibers, one for the blue light and one for the red light. The fibers are polarization-maintaining and we have optimized their alignment by checking the polarization stability with a polarization analyser SK010PA by S&K. Any residual polarization fluctuation is then converted into a power fluctuation by placing a $\lambda/2$ waveplate and a PBS after each fiber. Then, a beam sampler picks-off a fraction of the

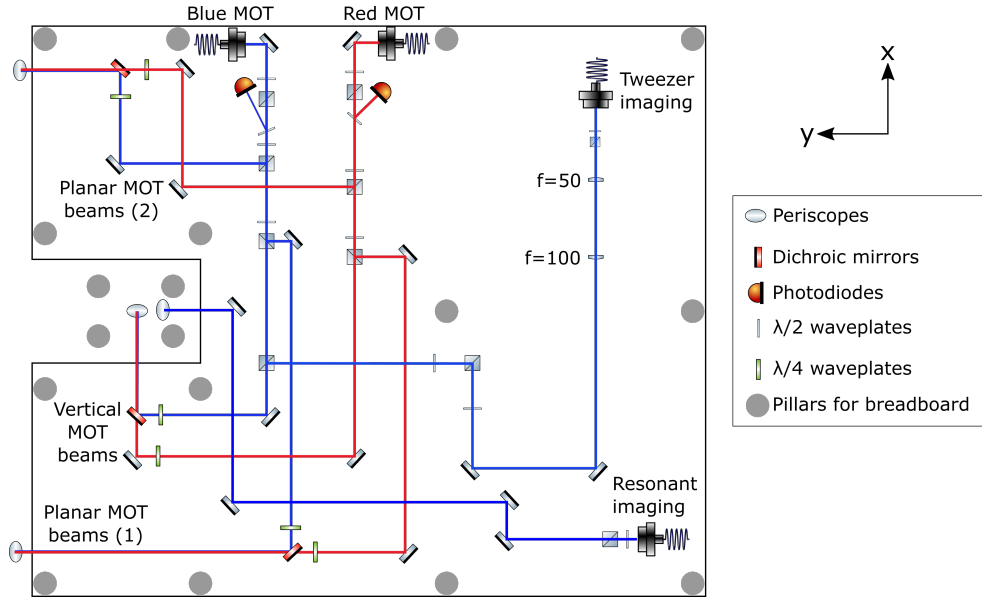


FIGURE 6.1: Layout of the optical setups for blue and red 3D MOT, and two imaging beams. The MOT beams are all coming from a single optical fiber, both for the blue and the red setups. This allows us to pick-off a fraction of the laser light on a photodiode for monitoring and stabilizing the power via a feedback loop. Each beam is split in three branches with $\lambda/2$ waveplates and PBSs and three dichroic mirrors are used to overlap the blue and red paths. The setup is mounted on the optical table, below the main breadboard where the tweezers and detection optics are mounted. The pillars holding this breadboard, reported as gray circles, limit the optical access in this plane. The three combined blue-red branches are sent vertically via periscopes: the central one addresses the vertical direction and is retro-reflected by a mirror placed on an additional breadboard above the glass cell (not shown in this picture, see Fig. 6.2(a)). The other two branches account for the confinement of the atoms in the plane: a periscope brings the laser lights on the main breadboard, from which they are directed to the glass cell and are then retroreflected by two pairs of mirrors (not shown here). Two blue imaging beams are integrated in the optical setup: one for resonant imaging, typically for detecting the blue and red MOT, and a tweezers imaging which is detuned to account for the differential light shift induced by the optical tweezers on the blue transition.

light which is directed on a photodiode, thus allowing us to monitor the power level. In this way, power stabilization can be implemented in a feedback loop using the AOMs on the lasers optical table as actuators. It is sufficient to connect the output of the photodiode to a PID controller and set a constant reference value. The PID output will feed the AOM RF driver with a voltage that modifies the RF power output, which in turn affects the laser power deflected by the AOM. A configuration with six independent beam, on the other hand, would have allowed for a higher flexibility, i.e. a fine balancing of the counter-propagating beams, which cannot be controlled in the retro-reflected configuration. The retro-reflected horizontal beams, in particular, experience 16 % losses due to the high incidence angle on the glass cell surfaces. We compensate for this imbalance by refocusing the reflected beams with a long focal distance lens ($f = 2500$ mm) on both the horizontal paths, placed in front of the retro-reflecting mirror. The beam passes through the lens twice, slightly reducing the

beam waist at the MOT position to obtain the same intensity of the incoming beam.

After separating three branches on both the blue and red paths, these are combined in pairs with dichroic mirrors that transmit the red light and reflect the blue. Before the dichroic mirrors, $\lambda/4$ waveplates select the proper circular polarization for the 3D MOT on each beam. One of the branches propagates vertically through the glass cell and is re-collected on an additional small breadboard that is mounted above the horseshoe breadboard, where blue and red light are separated again with a dichroic mirror and retro-reflected after passing through two $\lambda/4$ waveplates, as shown in Fig. 6.2(a). Two other branches are raised to the horseshoe breadboard level via two

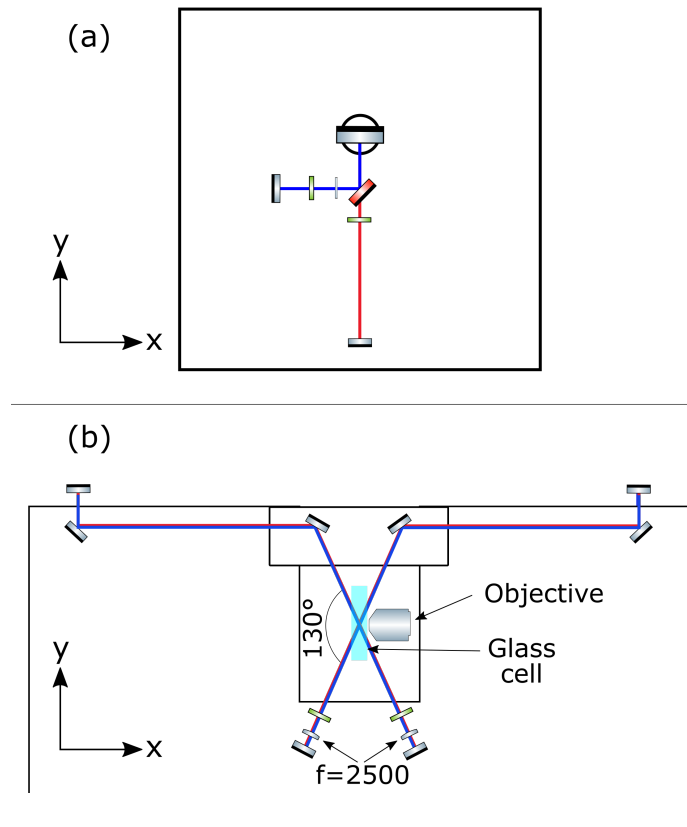


FIGURE 6.2: (a) A breadboard with a 2.5" hole is mounted above the horseshoe breadboard. The top mirror of a periscope collects the 3D MOT vertical beams, which are separated again with a dichroic mirror. Blue and red lights are separately retro-reflected, and their polarization is rotated with $\lambda/4$ waveplates to have opposite polarization with respect to the incoming beams. The blue beam also benefits from a $\lambda/2$ waveplate to finely adjust the polarization. (b) The two horizontal branches of the 3D MOT are aligned on the intermediate horseshoe breadboard. Instead of crossing at a 90° angle, because of the size of the microscope objectives the beams are angled at 130° . Two achromatic $\lambda/4$ waveplates rotate the polarization of both blue and red light with the same angle, before a mirror retro-reflects the beams. The glass cell is represented by the light blue rectangle as a guide for the eye. Only the relevant part of the horseshoe breadboard is shown in this sketch.

periscopes at the corners of the breadboard, then they propagate horizontally at this level. The beams cross the vertical beam at the center of the glass cell and are then retro-reflected by two mirrors. As shown in Fig. 6.2(b), they remain overlapped after

exiting the cell, and a achromatic $\lambda/4$ waveplate is used to rotate the polarization of both the blue and red beams. Because of the space occupied by the microscope objectives, we had to angle the horizontal beams at 130° , as indicated in figure. The 3D printed structure for the compensation coils, described in Subs. 5.4.1 was designed taking this constraint into account as well. The small upper-level breadboard, shown in Fig. 6.2(a), can be used to align other beams exploiting the optical access from above. For instance, the resonant imaging beam that we use for absorption imaging of the blue and red MOT is directed onto the atoms with a periscope at a small angle with respect to the vertical direction and is collected with an imaging setup mounted upside down at the bottom of this breadboard.

The resonant imaging, blue and red 3D MOT beams all have a waist of $w_0 = 8$ mm out of the fiber collimator and no further beam shaping is performed. The tweezers imaging instead, has a beam waist of $w_0 = 1$ mm and is expanded by a factor of 2 with a telescope.

6.2 Blue MOT, imaging and characterization

To generate our blue MOT, we decided to optimize all parameters, including intensity, detuning, and loading time, while operating the oven at 420°C . The oven temperature, indeed, modifies the atom flux in terms of both velocity distribution and integrated value. Zeeman Slower and 2D MOT play a role too, since they determine which classes of velocity are selected, as described in Subs. 5.2.1. Moreover, the blue transition suffers from a small decay channel from the $5s5p^1P_1$ state to the $5s4d^1D_2$ state, as anticipated in Subs. 1.3.2. This loss channel leads a fraction of the atoms to populate dark states 3P_2 and 3P_0 , so that the MOT loading curve reaches a steady state with a smaller number of atoms. Although repumpers that empty the dark states increase the number of atoms by more than an order of magnitude [202, 203, 204], a blue MOT with millions of atoms can be produced even without repumpers. All measurements and characterization reported below were performed without repumpers. When the repumper lasers will be implemented, the atom number will improve by a factor of 10 or more.

The blue MOT is imaged using absorption imaging, with the *Resonant imaging* beam shown in Fig. 6.1. As the beam passes through the atomic cloud, part of it is absorbed, creating a shadow in the beam profile. The beam is captured by a camera (Basler Ace acA4024-29um from Edmund Optics), which records a sequence of three images: the *atoms* image, the *beam* image and the *background* image. These three images are essential for a quantitative analysis of the atomic cloud. Intuitively, by dividing the *atoms* image by the *beam* image we isolate the contribution of the atoms. However, as we will explore later, a more detailed analysis that includes a background subtraction enables a more precise measurement of important quantities, such as the number of atoms and the density of the cloud.

This set of three images is acquired at the end of each experimental sequence. Initially, the atoms image is taken with the atom cloud absorbing part of the imaging beam light. The absorption cross section is determined by [205, 61]

$$\sigma(\Delta, s) = \frac{3\lambda^2}{2\pi} \left(\frac{1}{1 + (2\Delta/\Gamma)^2} \right) \left(\frac{1}{1 + s} \right) \quad (6.1)$$

where Δ is the detuning, s is the saturation parameter, λ is the wavelength and Γ is the linewidth of the electronic transition. The transmitted intensity is given by the Beer-Lambert law [206]:

$$I_t(x, y) = I_0(x, y)e^{-\sigma\tilde{n}(x, y)} \quad (6.2)$$

where $\tilde{n}(x, y) = \int n(x, y, z)dz$ is the atomic density integrated along the propagation direction of the beam z , (x, y) are the coordinates on the imaging camera sensor and $I_0(x, y)$ is the intensity of the Gaussian probe beam. Note that the product $\sigma\tilde{n}(x, y)$ is a quantity known as Optical Density, or OD. We can solve for the integrated density of the MOT cloud:

$$\tilde{n}(x, y) = -\frac{1}{\sigma} \log \left(\frac{I_t(x, y)}{I_0(x, y)} \right). \quad (6.3)$$

In principle, measuring the transmitted intensity $I_t(x, y)$ in presence of the atoms (atoms image) and the profile of the probe beam $I_0(x, y)$ after the MOT is released (beam image) is enough to determine the density of the atomic cloud. A final *background* image is acquired after switching off the imaging beam, and this is subtracted from both the intensity profiles. Considering the finite size of the sensor pixels, we can discretize Eq. 6.3 for the (i, j) pixel, subtracting the background B_{ij} from the signal S_{ij} (corresponding to $I_t(x, y)$) and the probe P_{ij} (corresponding to $I_0(x, y)$):

$$\tilde{n}_{ij} = -\frac{A}{\sigma} \log \left(\frac{S_{ij} - B_{ij}}{P_{ij} - B_{ij}} \right) \quad (6.4)$$

where A is the pixel area, including the magnification factor of the imaging system. A 2D Gaussian profile is fitted to the resulting profile:

$$\tilde{n}(x_i, y_j) = b + a \exp \left[- \left(\frac{(x_i - x_0)^2}{2\sigma_x^2} + \frac{(y_j - y_0)^2}{2\sigma_y^2} \right) \right] \quad (6.5)$$

where the fit parameters are a global residual offset b , the amplitude a and the size and center coordinates of the cloud σ_x , σ_y , x_0 and y_0 .

6.2.1 Number of atoms and temperature

The number of atoms can be estimated in two different ways, either using the fit parameters to calculate the integral of the Gaussian profile:

$$N_{\text{atoms}}^{(fit)} = \frac{a}{\sigma(\Delta)} 2\pi\sigma_x\sigma_y A, \quad (6.6)$$

Or summing the contributions of all the pixels in Eq. 6.4:

$$N_{\text{atoms}}^{(px)} = -\frac{A}{\sigma(\Delta)} \sum_{i, j} \log \left(\frac{S_{i, j} - B_{i, j}}{P_{i, j} - B_{i, j}} \right). \quad (6.7)$$

The two values are always in good agreement, but we tend to use the first one because it is less sensitive to shot-to-shot fluctuations in the offset background b ¹. An example

¹A background offset can occur due to shot-to-shot fluctuations in the probe beam intensity, which can have slightly different power in the atoms and probe images. This can be compensated for

of an absorption imaging analysis is shown in Fig. 6.3. The fitted 2D Gaussian profile

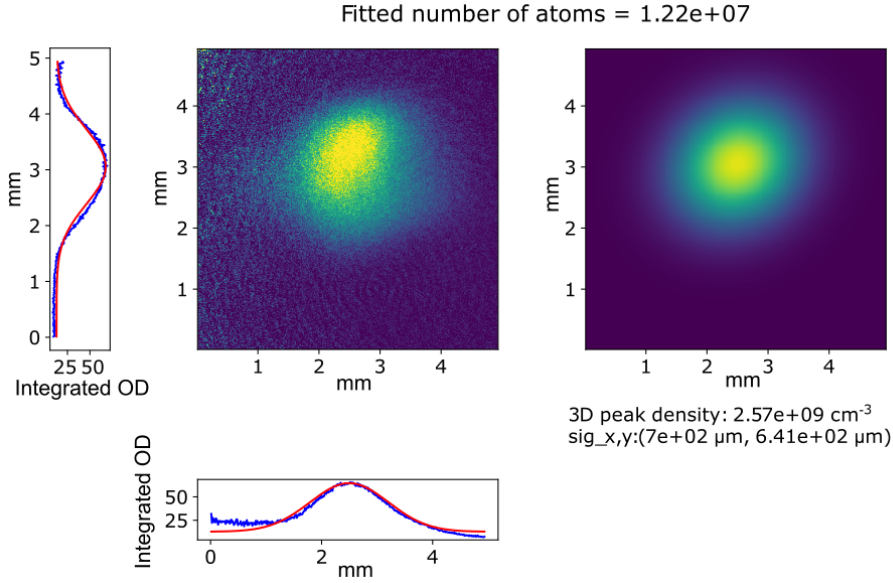


FIGURE 6.3: Example of an absorption imaging analysis of a blue MOT, as from a screenshot of our imaging analysis software. The original absorption image (left) and the fitted 2D Gaussian profile (right) are shown next to each other. To the left and below the absorption image, the linear plot of the measured (blue) and fitted (red) integrated density along the x and y axis are reported, respectively. Below the fitted profile, the relevant outcomes of the analysis are reported, such as the atom peak density, the size of the cloud (converted to μm). Above the images, we report the number of atoms estimated via Gaussian integration.

(right) is plotted next to the absorption image derived according to Eq. 6.4 (right). We plot in the same image the key parameters of the MOT, such as the atom number, the peak density and the size of the cloud.

All the absorption images that we record are performed in time-of-flight (TOF) measurements, during which the atomic cloud is left to expand freely in absence of magnetic and laser fields, just falling under the effect of gravity. Indeed, switching the magnetic field and the MOT beams off eliminates unwanted Zeeman shifts and light shifts which could affect the absorption cross section. If we just want to measure the number of atoms and density we just wait for the coils to turn off completely, which occurs in roughly $300 \mu\text{s}$, and take the shots. If we let the cloud expand for a set of different TOF values, we can measure how the size increases as a function of time and relate the expansion speed to the temperature of the cloud. Since we are far away from the quantum degeneracy regime, the velocity of the atoms in the MOT is described by a Maxwell-Boltzmann distribution [53], leading to a density at time of flight t [205]:

$$\tilde{n}(x, y, t) \propto \exp \left[-\frac{(x - x_0)^2}{2\sigma_x^2(t)} - \frac{(y - y_0)^2}{2\sigma_y^2(t)} \right], \quad \sigma_i^2(t) = \sigma_{0i}^2 + \sigma_v^2 t^2 \quad (6.8)$$

calculating an intensity-correction factor by comparing the integrated signal in an area of the probe beam where the atoms are not present.

where $\sigma_v^2 = \frac{k_B T}{M}$. The size of the cloud along the two axes $\sigma_i(t)$, grows with respect to the $t = 0$ value σ_{0i} with a thermal contribution proportional to σ_v . By measuring $\sigma_x(t)$ and $\sigma_y(t)$ at different TOF values, we can extract a value for $\sigma_{v_x}^2$ and $\sigma_{v_y}^2$ independently. We experimentally verify that $\sigma_{v_x}^2 = \sigma_{v_y}^2$ within experimental uncertainties and we can extract the best determination of the temperature value from $\sigma_{avg}^2 = (\sigma_{v_x}^2 + \sigma_{v_y}^2) / 2$. Fitting the expression for $\sigma_{avg}(t)$ to the experimental data, as in Fig. 6.4, we obtain

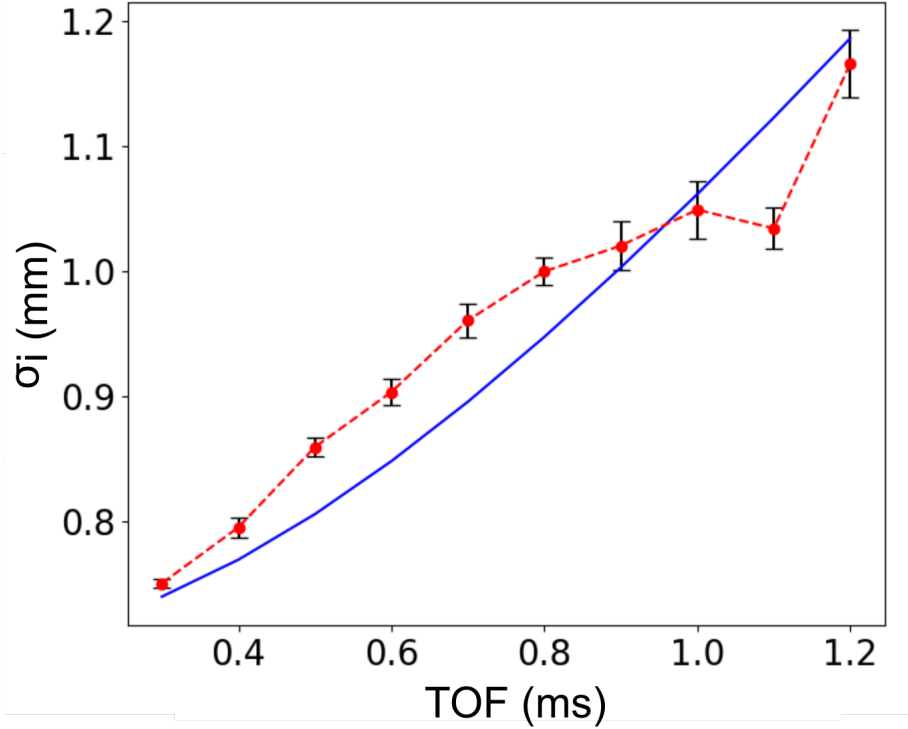


FIGURE 6.4: TOF measurement of the average cloud size for the blue MOT. Looking at the expansion we can extract an average temperature of the atoms of 6.8 mK. The blue line corresponds to the best fit with the function $\sigma_i(t) = \sqrt{\sigma_{0i}^2 + \sigma_v^2 t^2}$.

a temperature of 6.8 mK for the blue MOT.

The blue MOT is optimized by scanning individually the key parameters: quadrupole gradient, 3D MOT beams power and detuning, but also 2D MOT and Zeeman slower powers and detunings. In general, we aim to maximize the total number and density of the MOT for each scan. Some parameters are correlated, like the laser power and frequency of each beam, so we performed a 2D scan of such parameters, as shown in Figs. 6.5 and 6.6 for the 2D MOT and blue 3D MOT beams, respectively. The power of the lasers are scanned by tuning the RF power that drives the AOMs. Although the laser power in the diffracted order does not scale linearly with the RF power, we can easily calibrate and convert the values and report the scan in terms of a relevant physical property, the saturation parameter of the laser beam, considering that the saturation intensity for the $^1S_0 \rightarrow ^1P_1$ transition at 461 nm is $I_{\text{sat}} \simeq 42.6 \frac{\text{mW}}{\text{cm}^2}$. The AOM frequencies are instead referred to the spectroscopy frequency to calculate the corresponding detunings, which are reported as multiples (or fractions) of the linewidth Γ_{1P_1} . As a result of this optimization we found that the optimal 2D MOT

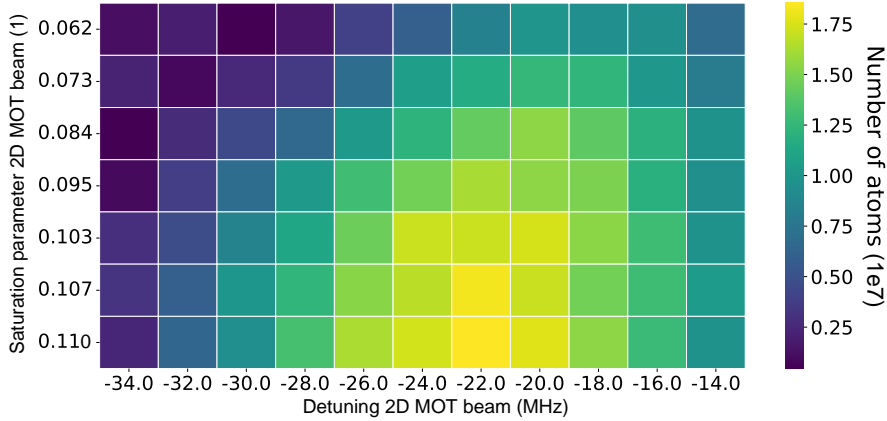


FIGURE 6.5: 2D MOT power and frequency optimization to maximize the number of atoms in the blue MOT. The RF power driving the AOM that provides for the proper frequency shift on the 2D MOT branch is tuned to change the laser power on the diffracted order. This parameter is scanned together with the AOM frequency. We report the number of atoms as a function of the corresponding saturation parameter for the 2D MOT beam (1) and the detuning from the free space resonance. The other 2D MOT beam has half the power and half the saturation parameter. The colorbar to the right indicates the number of atoms in the blue MOT in the heatmap. The best value is found for a detuning of $\Delta/(2\pi) = -22$ MHz and saturation parameter $s = 0.11$ on the first and $s = 0.055$ on the second 2D MOT beams. Although this plot shows that the number of atoms might be higher for an even higher laser power, we are limited by the current laser system.

power is 9.4 mW ($s = 0.11$) and 4.7 mW ($s = 0.055$) for the two separate beams, with corresponding detuning of $-0.7 \Gamma_{1P_1} = -2\pi \times 22$ MHz (see Fig. 6.5). The 3D MOT optimal power is 4.3 mW for each beam ($s = 0.1$) and the optimal detuning is instead $-2 \Gamma_{1P_1} = -2\pi \times 60$ MHz compared to the atomic resonance (see Fig. 6.6). In both the cases the heatmaps show that we could benefit from a higher laser power, although we are limited by the current laser system. The optimal parameters for the blue MOT are reported in Tab. 6.1. The magnetic field gradient was optimized as well, to have the best compromise between atom number and density. The final value that we chose, as reported in Sec. 5.3, is $50 \frac{\text{G}}{\text{cm}}$.

6.3 Red MOT

Loading atoms from the blue MOT to a single-frequency red MOT presents challenges due to the narrow linewidth of the red transition, which is 4000 times smaller than that of the blue. This large difference leads to two significant effects considering Eq. 2.24: the restoring force on the atoms is much weaker, and the atoms can only scatter photons within a small region before the Zeeman and Doppler shifts move the red transition out of resonance. To address this, an intermediate step is needed between the two MOT stages, where multiple frequency components are introduced into the red 3D MOT light. Two approaches have been demonstrated for ^{88}Sr . The first is the

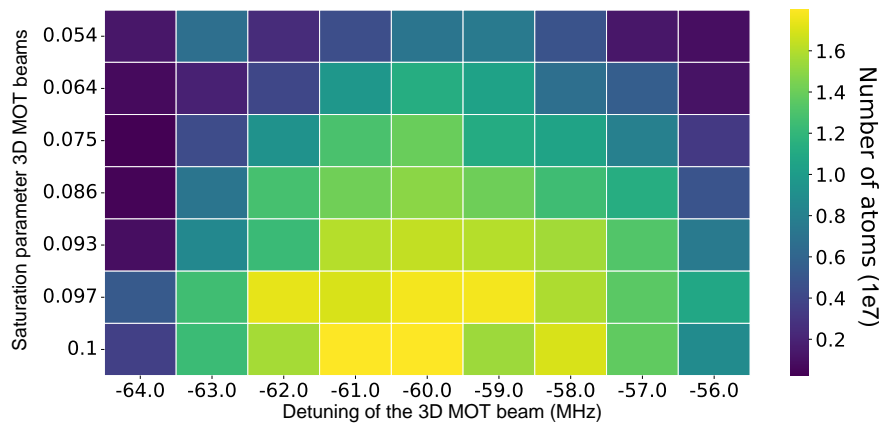


FIGURE 6.6: 3D MOT power and frequency optimization to maximize the number of atoms in the blue MOT. The RF power driving the AOM that provides for the proper frequency shift on the 3D MOT branch is tuned to change the laser power on the diffracted order. This parameter is scanned together with the AOM frequency. The scan parameters are converted to physically relevant parameters, the saturation parameter for each of the 3D MOT beams and the detuning with respect to the free space resonance. The number of atoms in the blue MOT is reported in a heatmap together with the colorscale on the right. The best value is found for a detuning $\Delta/(2\pi) = 169$ MHz and saturation parameter $s = 0.1$. Also in this case, the limited amount of power doesn't allow us to explore the power range further. However, for the 3D MOT beams we might consider slightly reducing the beam waist to increase the intensity on the atoms.

broadband red MOT or *multifrequency red MOT*, which involves modulating the laser to generate a frequency comb [207, 208, 43]. The second is the *SWAP* (Sawtooth-Wave Adiabatic-Passage) red MOT [209, 210, 211, 212], which uses a frequency chirp from red-detuned to blue-detuned light, ensuring that all atoms become resonant and scatter the MOT light at some point during the periodic scan.

In our experimental sequence we exploit the broadband (BB) red MOT approach, which is described in detail in the next subsection. After this step, the atoms are cold enough to be loaded into a single-frequency red MOT, which ultimately gives the highest density and lower temperature, as described in the following subsection.

6.3.1 Multi-frequency MOT

To create a multi-frequency laser beam, we modulate the RF signal driving the AOM that we use to fine-tune the frequency of the red 3D MOT beam. The RF signal is generated by a Siglent SDG6022X Arbitrary Waveform Generator (AWG) which produces a carrier frequency modulated sinusoidally at 30 kHz, deviating by ± 2.4 MHz from the carrier. The Fourier transform of this time-modulated signal results in a frequency comb approximately 4.8 MHz wide, with 30 kHz spacing between components. Among the available modulation options, sinusoidal modulation provides the fastest amplitude roll-off for frequency components outside the modulation range. Fig. 6.7 illustrates the spectrum of an RF signal at a central frequency of 75 MHz, with a

TABLE 6.1: Optimal parameters for the blue MOT

Beam	Power	s parameter	Detuning $\Delta/(2\pi)$ (Γ units)
Zeeman slower	40 mW	0.93	-580 MHz (-19 Γ)
2D MOT (1)	9.4 mW	0.11	-22 MHz (-0.7 Γ)
2D MOT (2)	4.7 mW	0.055	-22 MHz (-0.7 Γ)
3D MOT	4.3 mW	0.1	-60 MHz (-2 Γ)
Res. imaging	0.12 mW	0.003	0 MHz (0 Γ)
Tweezer imaging	0.2 mW	0.07	-40 MHz (-1.3 Γ)

modulation depth of ± 2 MHz and a modulation frequency of 30 kHz, comparing sinusoidal and triangular wave modulation. The measurement was performed with a Signal Hound SA44B spectrum analyser. While both types of modulation introduce

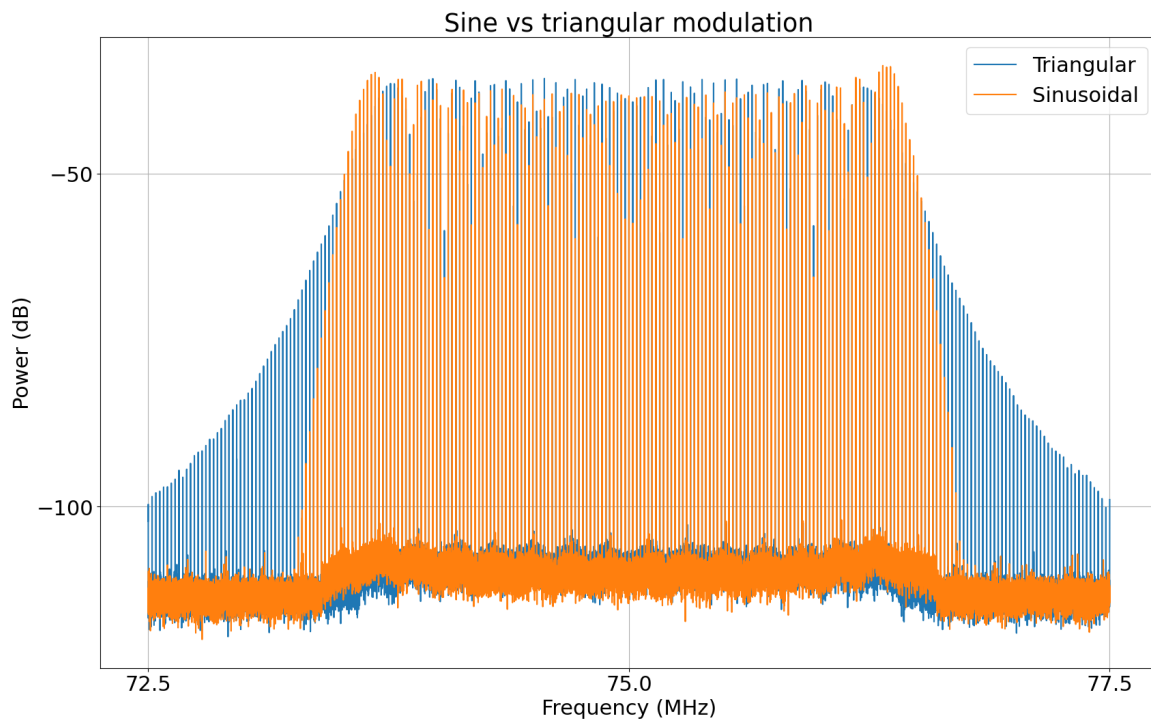


FIGURE 6.7: Frequency spectrum of the RF signal used to generate the multi-tone laser beam for the multifrequency red MOT. Equal modulation depth and modulation frequency give a different amplitude roll off of the frequency components beyond the modulation range for triangular (blue) and sinusoidal (orange) modulations.

some frequency components beyond the desired range, the amplitude falls off more rapidly with sinusoidal modulation. This is critical because the comb of red-detuned frequency components should stop as close as possible to the atomic transition resonance. If the roll-off is too slow, significant amplitude components may fall in the blue-detuned region, potentially causing heating of the atoms rather than cooling.

Since the AOM is operated in a double-pass configuration, this modulation results in an effective frequency comb that is 9.6 MHz wide in the laser light. To verify this,

we measured the beat signal of the modulated light with an unmodulated beam. The central frequency of the comb is around 75 MHz, which, in double-pass, shifts the laser frequency by 150 MHz. The unmodulated light is shifted by 80 MHz using a single-pass AOM, leading to a beat signal centered near 70 MHz. This approach eliminates DC and 50 Hz noise, which would have interfered if we had measured the beat note between two beams with identical central frequencies. The beat note spectrum shown in Fig. 6.8 was recorded using a spectrum analyser. The top image shows the full

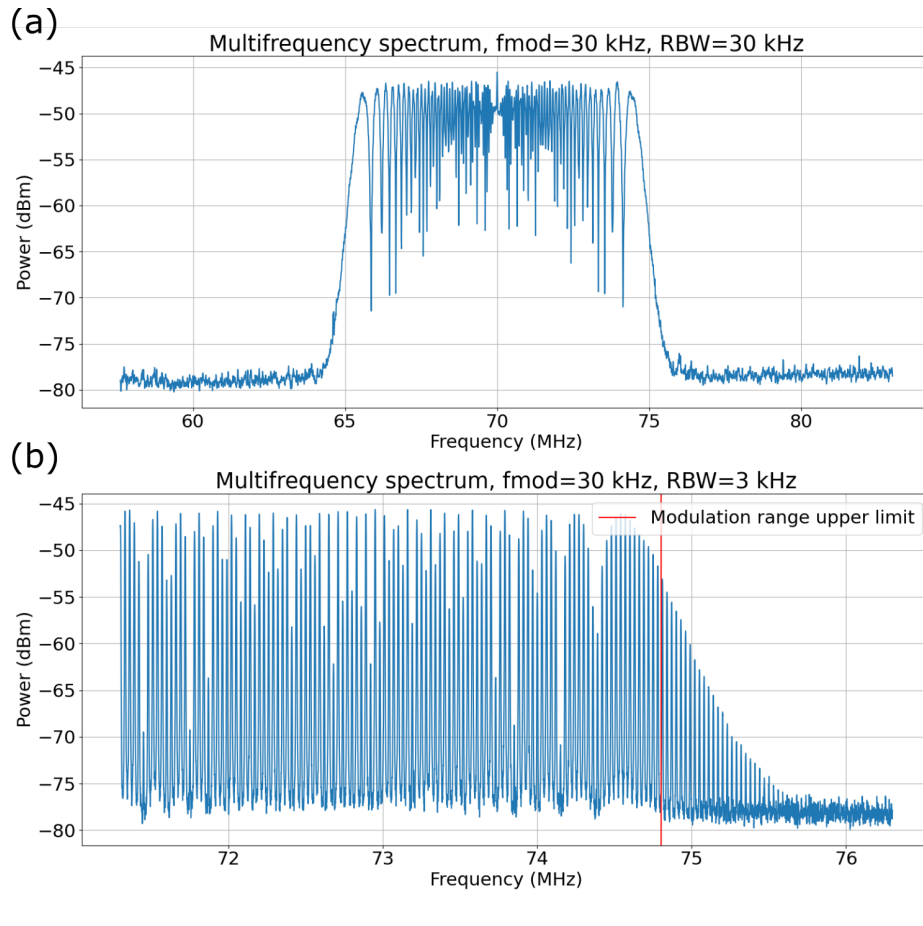


FIGURE 6.8: Beat signal between the light, modulated with a double-pass AOM at 30 kHz and span 2.4 MHz, and a reference unmodulated beam, measured on a photodiode. The top frame (a) shows the spectrum of the full modulation range, which covers roughly 9.6 MHz. The large scan range allowed for a minimum resolution bandwidth of 30 kHz. The lower frame (b) shows the detail of the frequency components with a finer resolution bandwidth of 3 kHz. The red vertical line corresponds to the upper limit of the modulation range. Above this threshold, the amplitude of the additional frequency components becomes rapidly negligible.

modulation range, covering almost 10 MHz. Due to the limited resolution bandwidth (RBW) of 30 kHz available for a 30 MHz scan range, the details of the frequency components are not visible. In the lower image we focus on the higher frequency edge, where a RBW of 3 kHz allows us to resolve the frequency components evenly spaced by 30 kHz. A red line corresponds to the upper edge of the modulation range. We can reasonably consider this frequency value as a threshold above which the additional frequency tones can be neglected. Indeed, the amplitude of those tones is more than

10 dBm lower than the main frequency components, giving a factor of 10 in the power amplitude. Ideally, the frequency components of the comb should be all red-detuned, extending from right below the $^1S_0 \rightarrow ^3P_1$ resonance (a few $\Gamma_{^3P_1}$ red-detuned) on the upper side towards lower frequencies with higher detuning on the lower side. In practice, the upper frequency limit of the comb needs to be adjusted to precisely find the optimal detuning. A wider frequency comb range improves the capture efficiency from the blue MOT. However, the lower frequency limit is more flexible and can be tuned to further optimize capture efficiency. In our setup, since we use a basic AWG to generate the multitone signal, we can only adjust the central frequency and frequency span, which together set the upper and lower frequency limits. As a result, any change to the frequency span requires to adjust the central frequency accordingly.

Immediately after transferring the atoms from the blue to the red MOT, all frequency tones interact with the atoms and the cooling process begins. As the atoms cool down, their Doppler shift decreases, causing the more red-detuned frequencies to become ineffective because they no longer interact with the atoms. Ideally, one would reduce the number of frequency tones and lower the power of each component to further cool the atoms, transitioning to a single-frequency configuration. However, in our setup, this is not possible because the AWG cannot be programmed remotely, and we cannot independently control the upper and lower frequency limits during the experiment. Nevertheless, as we will demonstrate later, it is still possible to load atoms into a single-frequency red MOT without modifying the broadband frequency comb by saturating the linewidth of the single-frequency transition.

The total power in each 3D MOT beam is 4 mW, which are divided into 320 frequency components. Therefore, given a beam waist of 8 mm and the saturation intensity of the red transition of $3 \mu\text{W}/\text{cm}^2$, each component has a saturation parameter of $s \simeq 4.2$ and a saturated linewidth of $\Gamma_s = 2\pi \times 17 \text{ kHz}$.

Regarding the quadrupole magnetic field, it is necessary to rapidly reduce the gradient from 50 G/cm, which is required for the blue MOT, to just a few G/cm. As discussed in Sec. 5.3, a lower gradient is essential for trapping atoms in a MOT using the red transition. We investigated two possible methods: either by suddenly adjusting the control voltage of the coils' power supply or by turning the coils off and then back on at the desired final value. In the first method, the coils response time to the current variation is limited by their time constant, which we measured to be approximately $\tau \simeq 9.9 \text{ ms}$. As confirmed experimentally through current flow measurements with a current probe (Danisense DS400UB-10V), the coils take 8 ms to adjust from the initial 100 A current to the final 4 A current. This approach offers a gradual current change, but its drawback is the transition from high gradients (with a small capture region) to low gradients, reaching only a few G/cm after several milliseconds. The second approach that we implemented involves turning off the coils at the end of the blue MOT sequence, along with the blue 3D MOT beams, and then turning them back on at the target current value. This method takes advantage of the fast switch-off circuit described in Subs. 5.3.2, allowing the coils to discharge in less than 300 μs . Once discharged, we can apply the new current value to the coils. However, when controlling the power supply as a current source, we observed a significant overshoot using the current probe, nearly double the target current, before it stabilized after a few oscillations, which occur on a milliseconds timescale. To mitigate this, we added an additional control to limit the maximum voltage provided

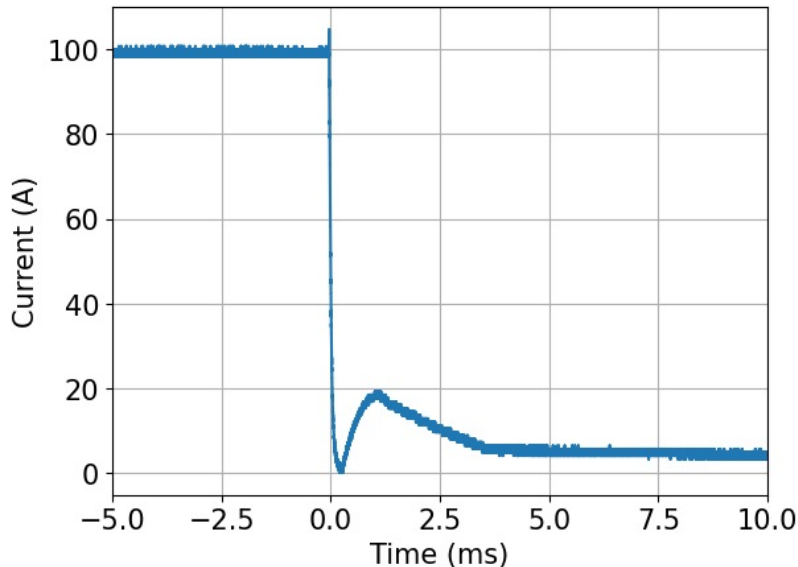


FIGURE 6.9: Current flowing in the high-field coils measured with a current probe during the transient between the blue and red broadband MOT. The power supply is controlled with two control input voltages, one for the maximum output current and one for the maximum output voltage. This interplay minimizes the overshooting effect. The steady state current value corresponds to a gradient of 2 G/cm.

by the power supply, which can be independently adjusted. During the transient, the competition between the voltage and current outputs produces a damped oscillation, reducing the overshoot effect. Fig. 6.9 shows the current flowing in the coils during the transient, measured with the current probe. Moreover, the atoms remain in free fall for just a few hundred microseconds before the gradient begins to increase, allowing for a gradual recapture of the atoms. As the gradient rises from 0 to 2 G/cm, it naturally compresses the atom cloud, since the interaction region becomes smaller as the gradient strengthens. We tested a few final gradient values and ultimately selected 2 G/cm. Given that the time to reach the target value remains roughly constant, the coils achieve a gradient of 1 G/cm, commonly used for the red MOT in strontium, at half the rise time. This gradient maximized the number of trapped atoms. Lower gradients slightly reduce the density, while higher gradients can increase it.

We characterized the loading time of the red MOT as a function of the multifrequency red MOT density, observing experimentally that the atoms are compressed by the comb of red frequencies in hundreds of ms. In Fig. 6.10 a characterization of the loading time relative to the single-frequency red MOT is reported, instead of the multifrequency red MOT. Indeed, after achieving the SF red MOT, we decided to optimize many of the multifrequency red MOT parameters such that the number of atoms and density in the SF red MOT are maximized, rather than trying to optimize each step of the MOT independently. We observe that the MOT density saturates after 250 ms. In the normal experimental sequence we load the multifrequency red MOT for 300 ms. An absorption image of the broadband red MOT is shown in Fig. 6.14(b). The temperature of the red MOT during the BB stage was measured in a TOF sequence, similar to Fig. 6.4, obtaining $T_{BBred} = 21 \mu\text{K}$.

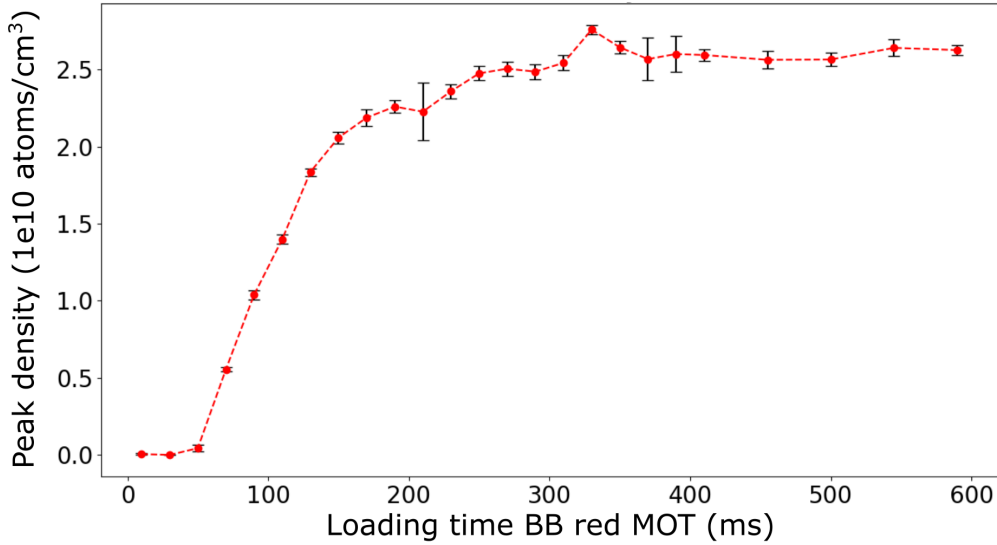


FIGURE 6.10: Number of atoms in the broadband red MOT as a function of the loading time. A stable saturated value is obtained after 250 ms.

Red transition spectroscopy and shielding-enhanced blue MOT

As mentioned earlier, trapping atoms in the red multifrequency MOT requires precisely tuning the resonant frequency and setting the upper frequency limit of the comb to a few tens of kHz on the red-detuned side. To achieve this, we exploited the *Shielding* effect outlined in Refs. [213, 214]. This technique involves resonantly driving the red $^1S_0 \rightarrow ^3P_1$ transition during the blue MOT loading phase. In a highly saturated regime, the 689 nm light maintains the atoms in the 3P_1 state for half of the time. This effect, together with the fact that the blue transition is lossy without repumpers (as discussed in Subs. 1.3.2), reduces the loss rate by a factor of 2. In the absence of additional repumper lasers, when atomic densities are low ($n < 10^{10} \text{ cm}^{-3}$), one-body losses become the dominant factor limiting the number of atoms that can be trapped. In this case, the loading process follows the rate equation described in Ref. [213]:

$$\frac{dN(t)}{dt} = L - \gamma N(t) \quad (6.9)$$

where $N(t)$ is the number of atoms in the blue MOT at time t , L is the loading rate and γ is the one-body loss rate. Because of the shielding effect described before, in the presence of a resonant, intense red beam, the one-body loss rate gets a factor of 2 smaller, resulting in doubled atom number. In addition to increasing the number of atoms in the blue MOT, this effect can be used to obtain an initial estimate of the frequency of the red transition. This measurement provides a rough experimental determination of the resonant frequency of the $^1S_0 \rightarrow ^3P_1$ transition, but it suffers from systematic effects as the resonance is light-shifted due to the blue light that remains on during the blue MOT loading. For this spectroscopic measurement, we used a test beam with 689 nm light directed along the y-axis (the long axis of the glass cell)

with circular polarization. The shielding feature is broadened due to the saturated red linewidth, so we began with a saturation parameter of $s = 10^4$ and gradually reduced the power to more accurately identify the resonance position. Additionally,

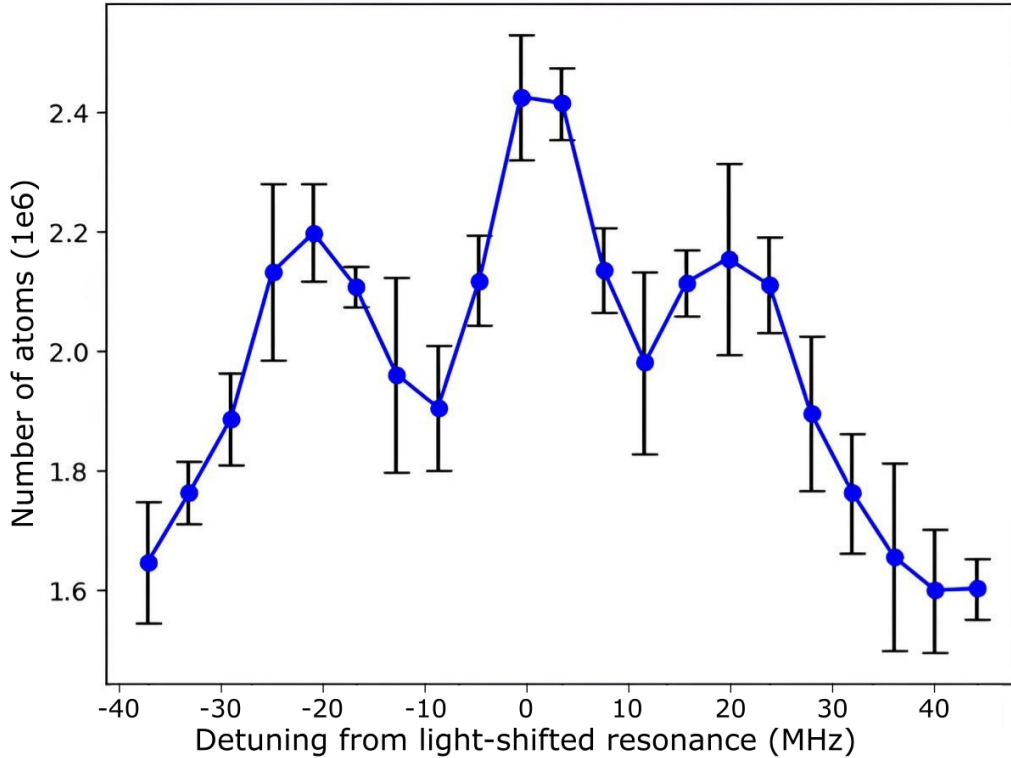


FIGURE 6.11: Enhanced number of atoms obtained via 689 nm light resonant driving during the blue MOT loading. The beam is circularly polarized and has a saturation parameter of $s = 10^4$. The three visible peaks can be attributed to the different m_J states that are Zeeman shifted by a different amount. By lowering the saturation parameter, the feature becomes narrower, thus allowing for a more precise estimate of the resonance. Note that the x-axis in the plot reports the frequency set on a double-pass AOM, thus the feature is actually twice as big. The baseline number of atoms that we measured in absence of shielding is visible at the edge of this feature, at approximately 1.6×10^6 atoms.

this feature displays three peaks, corresponding to $m_J = \pm 1$ at the sides and $m_J = 0$ in the center, which become resonant at different Zeeman shifts, as illustrated in Fig. 6.11. Even though the transition is driven with σ polarized light, a peak corresponding to $m_J = 0$ appears because of the not well-defined quantization axis at the center of the quadrupole field [213]. The side peaks, corresponding to the σ_{\pm} transitions to the $|m_J| = 1$ Zeeman-shifted sublevels of the 3P_1 state, indicate the presence of a residual magnetic field at the position where the blue MOT is formed that result in a Zeeman shift of approximately 20 MHz. This observation suggests that the MOT may not be precisely centered at the zero of the quadrupole magnetic field, likely due to an imbalance in the power of the MOT beams within the plane. This imbalance is probably caused by power losses on the surfaces of the glass cell, as

discussed previously. By reducing s to 10^3 we observed that the feature narrows down around the magnetically insensitive $m_J = 0$ peak, which then provides a better reference for the atomic resonance. We estimated the contribution of the blue light shift (approx. 5 MHz for our standard MOT operational parameters) by measuring the atom enhancement at different blue 3D MOT power levels, giving us a reliable initial estimate for the resonance. Indeed, when we finally tried to transfer atoms from the blue to the broadband red MOT, we found the optimal frequency within 2 MHz from the initial guess.

Although the red multifrequency 3D MOT beams are red detuned with respect to the free space resonance, we still observe a 1.5x increase in the number of atoms in the blue MOT when the red light is turned on during the blue MOT loading.

6.3.2 Single-frequency MOT

The final stage of the red MOT is the single-frequency (SF) red MOT. Ideally, we would gradually decrease the span of the BB frequency comb, transitioning from hundreds of saturated frequency components to a single narrow line to get a denser and colder atomic cloud. However, after the 250 ms red BB MOT loading, only a

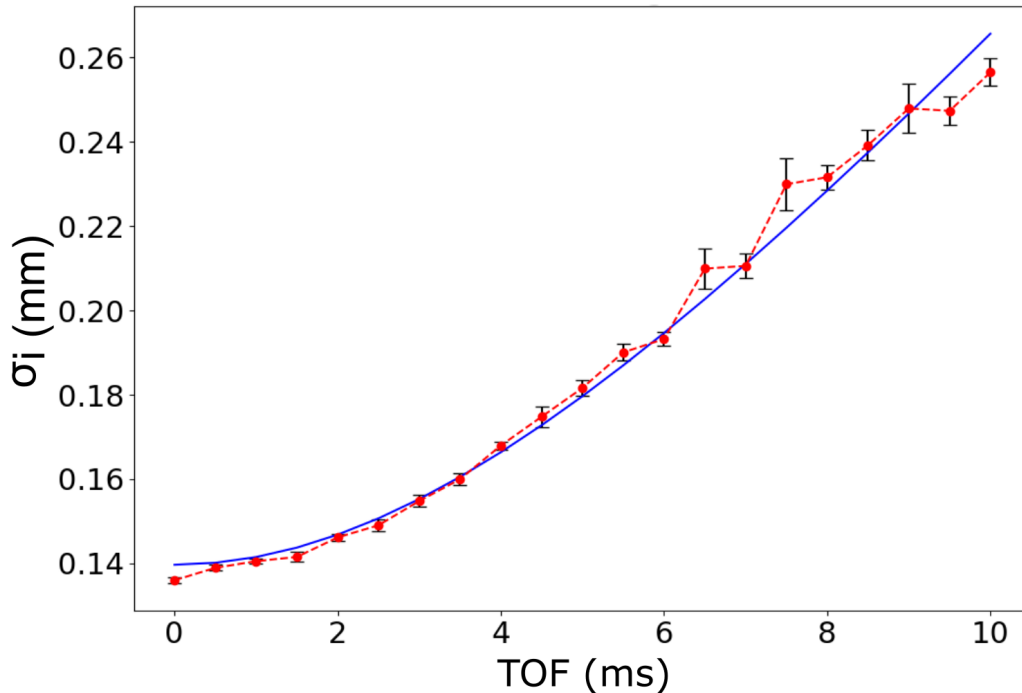


FIGURE 6.12: Fit of the single-frequency red MOT size expanding in TOF to determine a cloud's temperature of $5.4 \mu\text{K}$. The blue curve represents the best fit parameters for the function $\sigma_i(t) = \sqrt{\sigma_0^2 + \sigma_v^2 t^2}$.

few frequency tones will still be interacting with the atoms, while the far-off detuned components will not play any role anymore. Then, our approach consists in switching from the multifrequency laser light to a single-frequency saturated line suddenly. This

is also easier from the experimental side, as the AWG we are currently operating does not support fast reconfiguring of the output spectrum. We can transfer more than 80% of the atoms from the BB to the SF red MOT using a single frequency component with $s = 200$, which results in a saturated linewidth of $\Gamma_s = 2\pi \times 105$ kHz. This broadening allows us to cover the gap between a broad multifrequency comb and a single frequency beam. The temperature of the single-frequency red MOT was measured by analysing the TOF expansion of the cloud. As shown in Fig. 6.12. The Doppler temperature achievable for the saturated linewidth is $2.4 \mu\text{K}$ and we measured a temperature of $5.4 \mu\text{K}$.

Following the calculations carried out in Subs. 3.1.3 about the number of atoms that are instantaneously in the capture volume of one tweezer, a key parameter is the atomic density. Indeed, to have a high chance of loading atoms in optical tweezers, the density has to overcome $n = 3 \times 10^{10} \text{ cm}^{-3}$. This value is only reached in the single-frequency red MOT, while the blue MOT and the BB red MOT have a density which is too low to load atoms in tweezers. A scan of the red SF laser power and frequency, like the one reported in Fig. 6.13, is performed daily to maximize the density of the cloud and have an efficient loading of the optical tweezers. The optimal combination of parameters is a saturation parameter $s \simeq 200$ and detuning $\Delta/(2\pi) = -100$ kHz. This frequency gap is covered by the saturated linewidth Γ_s . Even working with a

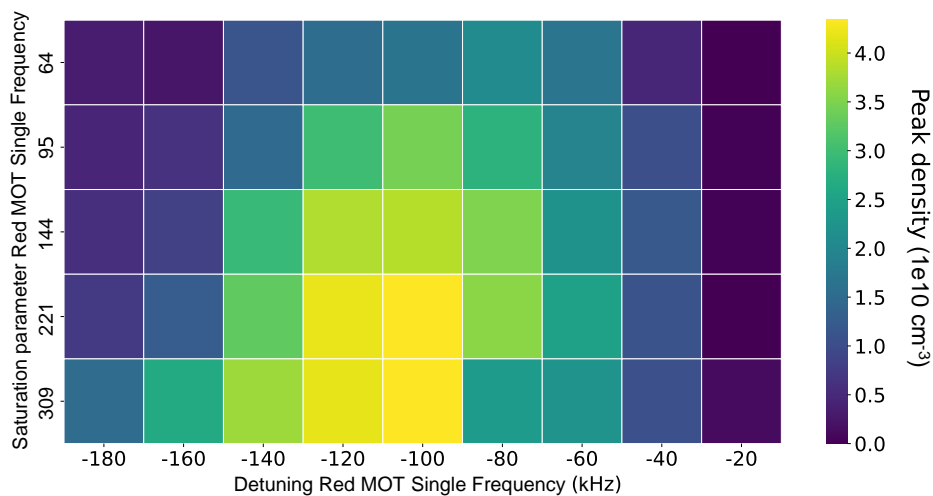


FIGURE 6.13: Optimization of the red single-frequency 3D MOT beam by scanning the power and frequency of the RF signal driving the corresponding AOM. This optimization is particularly important as we need a high atomic density to load them in optical tweezers efficiently. The peak density obtained by the absorption imaging is reported in the colorscale to the right of the heatmap, as a function of the saturation parameter and detuning from the free-space resonance.

single-frequency red beam in a saturated regime (the maximum density value in Fig. 6.13 is obtained for a saturation parameter of $s \simeq 200$), the frequency value has to be very precise. Since we estimated that the ULE cavity drifts of approximately 12 kHz per day, this optimization is required every couple of days to maintain a high density. The ULE cavity can be calibrated with red spectroscopy and, since the drift is linear,

we can compensate for it with a feed forward on the offset frequency applied to the fibered EOM that is used in the lock scheme. A similar approach will be necessary to use this cavity as a reference for the clock laser.

In the SF red MOT we usually achieve more than 500 k atoms with a density $n \simeq 4 \times 10^{10} \text{ cm}^{-3}$. In Fig. 6.14 an absorption image of the blue, red BB and red SF MOTs are reported, showing the different size and density, reported on the color scale as optical density.

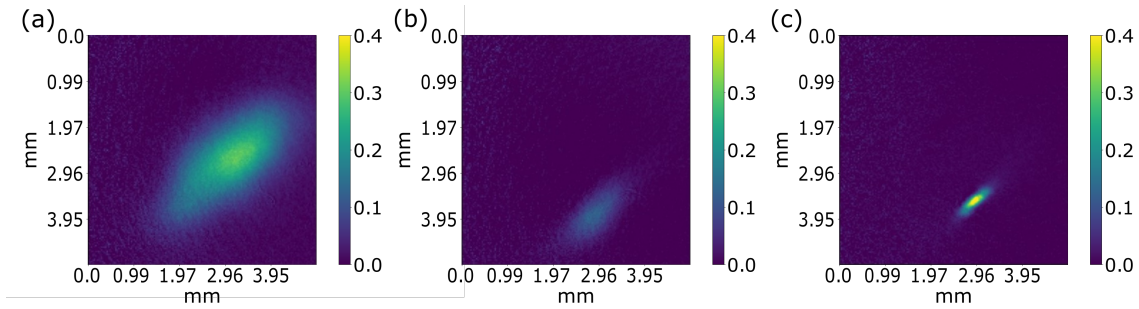


FIGURE 6.14: (a) Absorption image of the blue MOT. (b) Absorption image of the broadband (BB) red MOT. (c) Absorption image of the single-frequency (SF) red MOT. The three MOTs are squeezed along the z axis because of the stronger magnetic field gradient along that direction. Since the imaging plane is tilted with respect to the cartesian reference axes, the z axis projection appears tilted in the absorption images.

Chapter 7

Loading atoms in an array of optical tweezers

In this final chapter, we will cover the remaining steps necessary to create an array of single atoms trapped in optical tweezers. First, we will provide an overview of the experimental setup and the alignment process for the optical tweezers. Next, we will outline the method used to overlap the red MOT with the optical tweezers, followed by the presentation of fluorescence images showing atoms successfully loaded into the tweezers. Finally, we will describe the approach for implementing Sisyphus cooling within the tweezers and inducing pairwise light-assisted collisions. The characterization of the first fluorescence signal of atoms in optical tweezers described in this chapter was carried out with a temporary optical setup for the tweezer array. The setup, sketched in Fig. 7.1, employs two crossed AODs to generate a rectangular-based static 2D pattern. This allows us to load atoms in optical tweezers, although the setup lacks the flexibility of an SLM-generated pattern. During this period, the SLM has been characterized to implement it at a later stage in the final setup.

7.1 Alignment of the optical tweezers

To efficiently trap atoms from the red MOT into the optical tweezers, it is crucial to overlap the array of optical tweezers and the red MOT. In Sec. 5.5 we outlined the procedure for aligning the microscope objective with the MOT, using a reference blue beam orthogonal to the glass cell. This ensures that the objective is both orthogonal to the cell and properly centered on the MOT. The microscope objective mount, which provides independent 5-axes control, is adjusted to satisfy two criteria: first, the reference blue beam must pass through the center of the mount; second, when a mirror is fixed to the mount with the surface parallel to the mount plane, the reference beam should reflect exactly along its incoming path. Once the objective is placed at the correct focal distance, it is geometrically aligned in such a way that the red MOT,

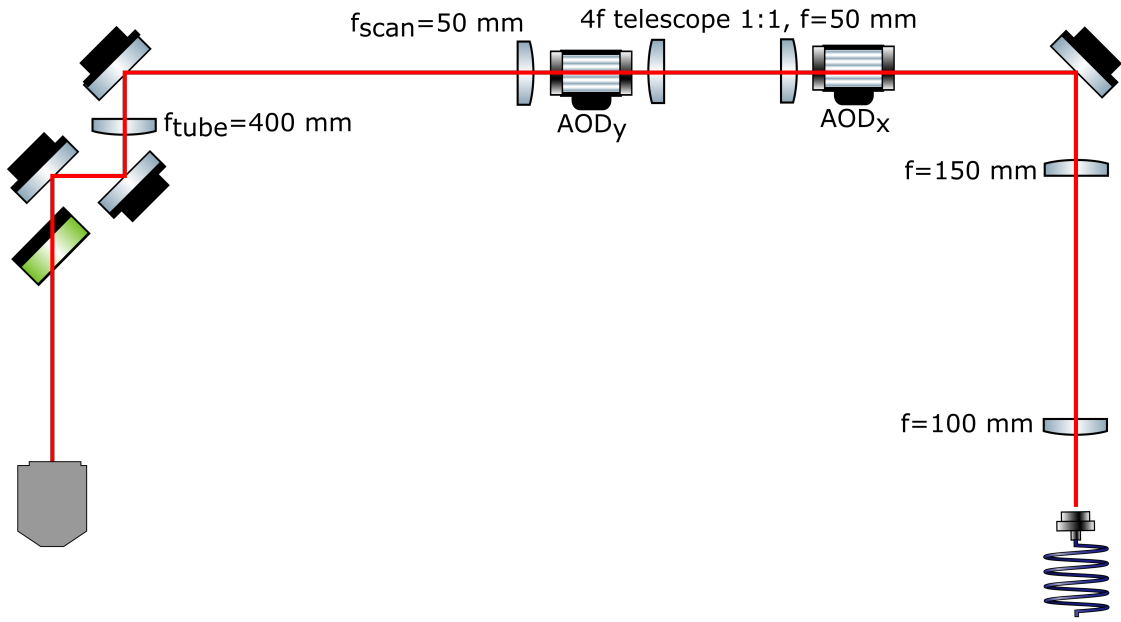


FIGURE 7.1: Tweezer setup used during the initial characterization loading atoms in optical tweezers. The array of optical tweezers is generated by a pair of crossed AODs.

when imaged through the objective itself, is formed in the center, or very close to, of the objective's field of view (FOV), where we can achieve diffraction-limited resolution. However, this does not guarantee that the optical tweezers will be precisely focused on the red MOT, as this depends on how the incoming laser beam impinges on the back focal plane aperture.

The initial coarse alignment of the optical tweezer light was performed by aligning the laser beam to overlap with the reference blue beam. To achieve this, the microscope objective was temporarily replaced with a beam target, coaxial with the 5-axis mount, allowing us to coarsely center the beam to the microscope objective. Once this was done, the microscope objective was reinstalled, focusing the tweezer light roughly at the 14 mm working distance, accounting for 3.5 mm of in-glass propagation, which the objective is compensated for. To verify the correct projection of the optical tweezers, we positioned a service objective, identical to the other one, on the opposite side of the glass cell with a simple imaging system and a camera (Basler Ace acA4024-29um from Edmund Optics) to detect the optical tweezer array. The service objective, mounted on a similar 5-axis assembly, was aligned with the same method as the science objective, again making use of the reference blue beam to place it orthogonal to the glass cell (and thus to the other objective). The imaging system magnifies the tweezers by 8X and projects them onto the camera. When the service objective is placed at the working distance from the plane where the tweezers are focused by the main objective, the tweezers, with a waist of $w_0 = 1 \mu\text{m}$, appear on the service camera as spots with an expanded waist of $w'_0 = 8 \mu\text{m}$. Given that the camera has a pixel size of $1.85 \mu\text{m}$, each tweezer is spread over several pixels, thus allowing for a detailed detection of the spot. This detection system allows us to evaluate the presence of aberrations in the system, which we can minimize by fine-tuning the alignment of

the tweezer beam injected through the main microscope objective. Fig. 7.2 shows an

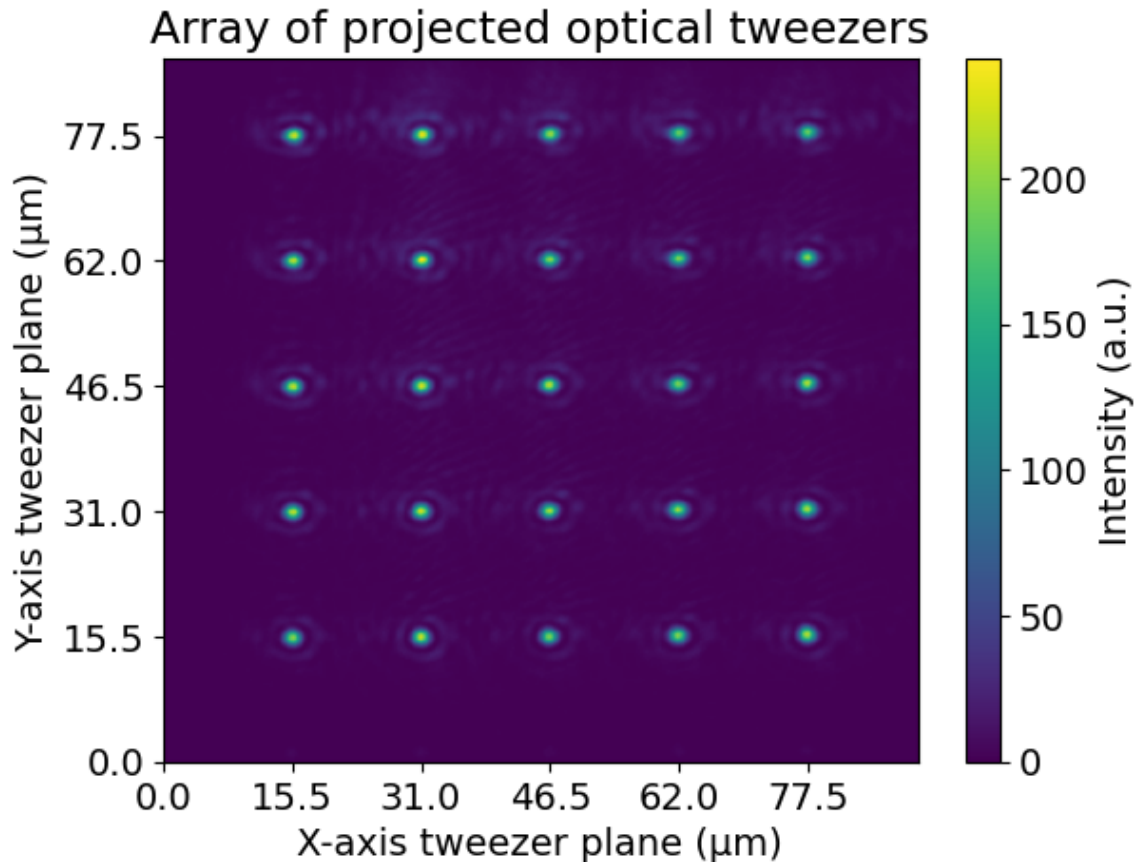


FIGURE 7.2: Array of 5x5 tweezers generated by a pair of crossed AODs. The array is generated by sending a multitone RF signal on each AOD, and the relative balance of RF powers is adjusted to compensate for the efficiency curve of each AOD. The array is imaged through the service objective, mounted on the opposite side of the glass cell.

example of a 5x5 array of optical tweezers, imaged through a camera mounted after the service objective imaging system. It is important to note that this imaging system could also introduce aberrations if the two objectives are not aligned correctly and are not at the proper distances, so we take particular care to ensure they are parallel and coaxial. To confirm that the service objective is actually coaxial with the main one, we can move the service objective out of focus with the translation stage controlling the axial position. If it moves coaxially, the tweezer spot will expand according to Gaussian beam propagation, on a length scale set by the Rayleigh distance z_R introduced in Eq. 2.31, while remaining in the same position. Any transverse motion of the spot image during the axial motion could signal a misalignment of the two axes, which can then be corrected. This observation is key for overlapping the red MOT to the tweezers, as discussed in the next section.

7.2 Overlap the red MOT and the tweezer array

Overlapping the optical tweezer array with the red MOT is essential to ensure a proper population of all the tweezers, in particular when working with large arrays. The size of the tweezers array can extend to a few hundreds μm , which is comparable to the red MOT, for which we measured a cloud diameter of approximately $400 \mu\text{m}$. A straightforward approach to achieve this overlap might be to align the tweezer light through the objective so that the microtraps are focused directly at the MOT position. However, as noted in the previous section, these micro traps are extremely sensitive to alignment and aberrations. Ideally, the tweezer light should be injected coaxially through the objective to be focused within the objective's FOV, which spans only a few hundreds μm . Therefore, a more effective method is to move the red MOT to overlap with the tweezer array. This can be done by applying a bias magnetic field along the three cartesian axes using the compensation coils described in Sec. 5.4. In particular, the red MOT can be smoothly shifted by several hundred μm from its original position by applying a ramp on the compensation coils voltage [69, 70].

With the coarse geometric alignment outlined above, we expect the objective to project the optical tweezers near the center of its diffraction limited field-of-view. Additionally, since it was aligned with the red MOT fluorescence, the MOT should also be close to the center of the FOV. Therefore, applying a small bias field along the three axes should allow for the overlap of the red MOT with the tweezers. The bias field shifts the center of the quadrupole magnetic field by an amount δx , which depends on the bias field strength δB and the gradient b , as described in Sec. 5.4. Our red MOT is trapped with a 2 G/cm gradient in the weak direction, thus we can move it by $500 \mu\text{m}$ with a 100 mG bias field. In the more strongly confined direction, with a gradient of roughly 4 G/cm , this shift is about half as large (or a bias field twice as big is necessary). However, determining the precise set of compensation coil bias fields required to overlap the red MOT with the tweezers is not straightforward.

The strategy that we initially explored involved observing both the red MOT fluorescence and the tweezer light on the same camera to determine their relative position. Specifically, we overlapped a blue beam with the tweezer light before the microscope objective, such that a single blue tweezer was focused at the same position of the 813.4 nm tweezer. The objective is optimized for both wavelengths, with a minimal focal shift of less than $4 \mu\text{m}$ between them. The blue light was focused directly on the atomic beam flux in the glass cell, in absence of magnetic fields and additional laser beams. The large atomic flux on an extended volume can scatter a high number of photons in the whole blue tweezer profile.

To image this fluorescence, we placed a camera below the glass cell, observing the blue tweezer at a 90 degree angle to determine exactly the position of its focus. The same camera could also detect the fluorescence of the red MOT, which was shifted with the bias fields to overlap to the blue tweezer, and therefore to the 813.4 nm tweezer, as the two optical paths were geometrically aligned. However, the imaging system of this camera only sampled a 2D plane, meaning that one direction still needed to be optimized to fully overlap the MOT to the tweezers. Although this method eliminated many degrees of freedom in the relative alignment of the red MOT and the tweezers, it was not precise enough to achieve proper overlap and detect the fluorescence signal of atoms trapped in the tweezers.

We adopted a different approach to observe the relative distance between the tweezers and the red MOT, exploiting the service objective aligned on the opposite side of the glass cell. This imaging system allowed us to directly compare the positions of the projected tweezer array and the red MOT fluorescence. Although the previous alignment method was giving what we believed was a reliable overlap, the service objective camera revealed that the red MOT fluorescence was nearly $400 \mu\text{m}$ away from the tweezer array in the horizontal plane. We attributed this discrepancy to the challenges in overlapping the 461 nm and 813.4 nm tweezers and trying to infer the infrared tweezer position by observing an effect of the blue one. By detecting the infrared tweezers directly with this new method, we eliminated uncertainties associated with this additional step.

While this approach allows for overlapping the red MOT and the tweezers in a 2D plane, we could further refine the alignment by moving the service objective slightly back and forth from the tweezer's focal plane. This enabled us to observe both the red MOT fluorescence and an out-of-focus image of the tweezers. Since the two remained aligned even in out-of-focus positions, we confirmed that we had achieved a good overlap.

As a result, we were able to observe an initial fluorescence signal from atoms loaded into the optical tweezer array. Further fine-tuning of the overlap, along with other critical experimental parameters, was based on the fluorescence signal of the atoms collected during the imaging process described in the next section. Additionally, when the SLM pattern will be implemented to generate the final setup, we will be able to address non-uniformity in trap depth across the array as well as to correct for aberrations in the microtraps. Both these effects can modify the fluorescence from trap to trap, thus the fluorescence signal from different sites of the array can be compared to make it as uniform as possible.

7.3 Fluorescence imaging of atoms in tweezers

The first fluorescence signal of multiple atoms in optical tweezers was measured with a setup like the one depicted in Fig. 7.3(a). The atoms scatter blue light from a 461 nm beam entering the bottom of the glass cell, along z-axis, with linearly polarized light along the y-axis. The microscope objective is oriented along the x-axis to maximize the collection efficiency, as described in Subs. 4.3.1. The quantization axis is set along the y-axis by applying a bias field with the compensation coils along that direction. Fig. 7.3(b) reports the experimental sequence in a block scheme, reporting the duration of each step in ms. The imaging beam illuminates the atoms in the tweezers along a radial direction to minimize the recoil, since it is not retroreflected. It cannot be oriented along the axial tweezer direction as that axis is occupied by the two objectives. Moreover, in this case we would not only collect the fluorescence light, but also the probe beam light. The saturation parameter of the beam is $s \simeq 0.007$ and the frequency is red detuned by $2\pi \times 10 \text{ MHz}$ with respect to the light-shifted resonance. The differential light shift induced by the tweezers on the imaging transition is approximately $-2\pi \times 6.5 \text{ MHz}$ for $200 \mu\text{K}$ deep tweezers, according to the polarizability data reported in Tab. 2.1.

The corresponding expected scattering rate is $R_{sc} = 2\pi \times 25 \text{ kHz}$. The polarization of the imaging beam was optimized by maximizing the fluorescence signal of the

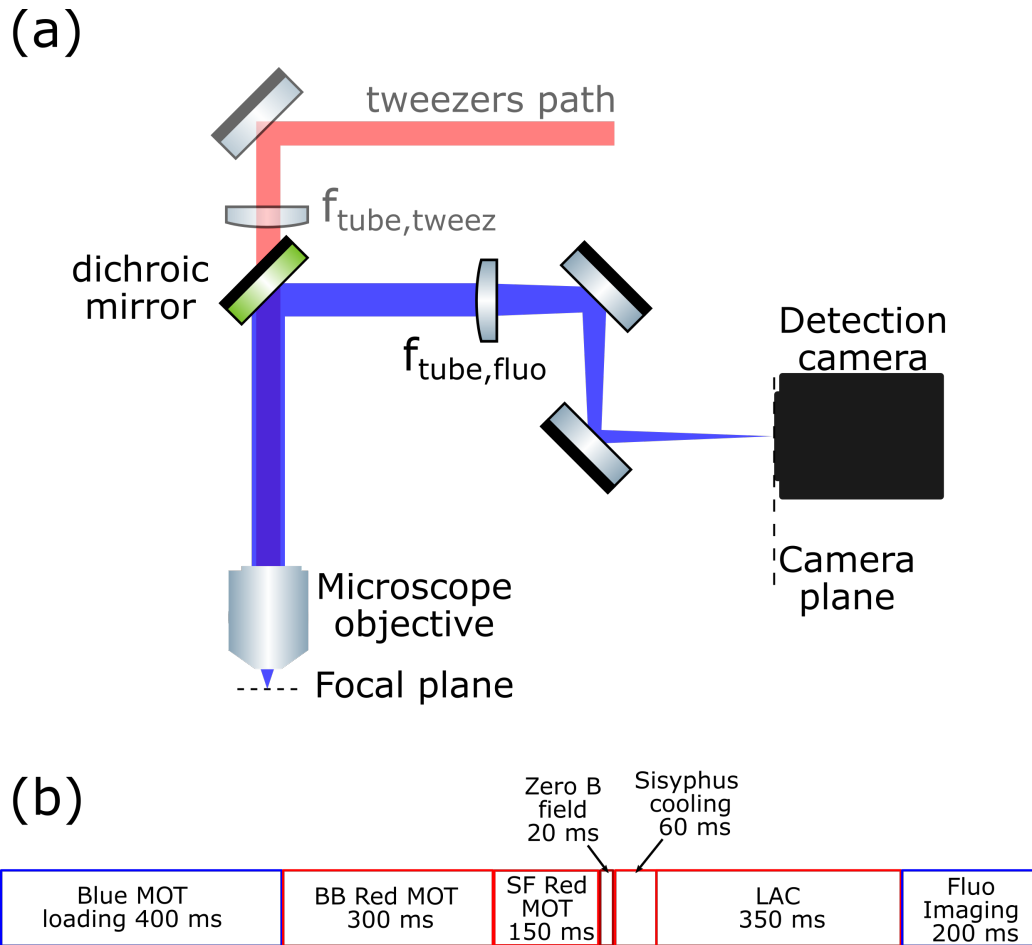


FIGURE 7.3: (a) Imaging setup used during the initial characterization of atom loading in optical tweezers. The site-resolved fluorescence at 461 nm is collected by the microscope objective and separated from the 813.4 nm trapping light with a dichroic mirror. A tube-lens on the detection path is placed at focal distance from the camera to focus the image of the array of atoms on the camera sensor. (b) Block scheme of the experimental sequence, starting from the two-stage MOT to tweezer array loading, Sisyphus cooling, LAC and fluorescence imaging.

atoms, for which we expect to collect approximately 10% of the scattered photons. The fluorescence light scattered by the atoms rapidly saturates while increasing the imaging time, as a consequence of the heating induced by the imaging light in the absence of cooling. Then, we worked on a sequence to implement Sisyphus cooling on many atoms, before inducing the light-assisted collisions.

Fig. 7.4(a) shows the fluorescence signal of multiple atoms in each optical tweezer as they are loaded from the red MOT. For comparison, Fig. 7.4(b) reports the signal of a few atoms (compatible with single-atom occupancy) obtained after the cooling and light-assisted collisions described in the following sections. Fig. 7.4(b) is averaged over 10 measurements to highlight the signal of a few photons per site. The red frames indicate the three 7x7 ROIs over which the photon signal is integrated.

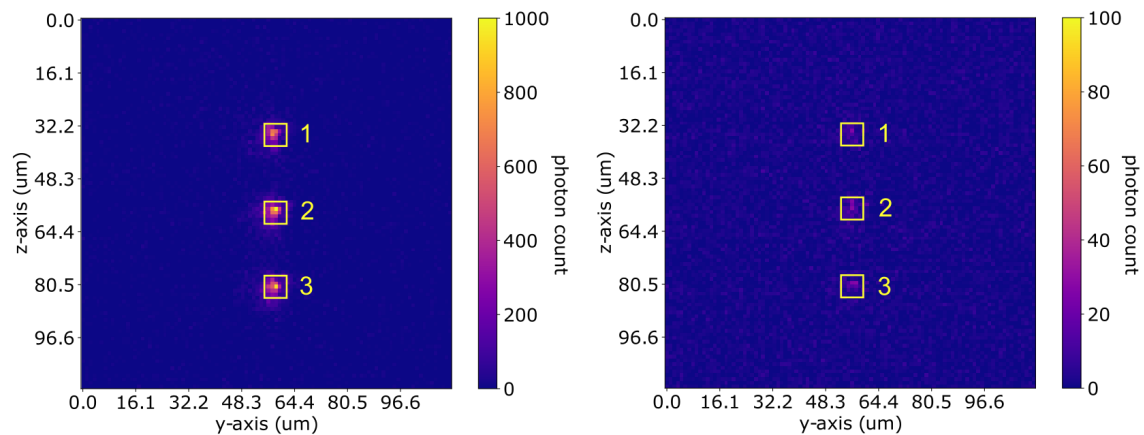


FIGURE 7.4: (a) Fluorescence signal of multiple atoms in each optical tweezer. To analyse the photons scattered by the atoms in each tweezer, the signal is integrated over a 7×7 Region Of Interest (ROI) for each micro trap. (b) Before the fluorescence imaging sequence, light-assisted collisions are induced to reduce the number of atoms towards binary occupation (zero or one atom). The image is averaged over 10 experiments to highlight the weak fluorescence, which is compatible with a single-atom, or a few atoms, occupancy. Note that the colorbars cover different ranges as the fluorescence signal of the reduced number of atoms, after the light-assisted collisions, is an order of magnitude lower.

7.4 Cooling and light-assisted collisions

In our 813 nm tweezers setup, which produces non-magic traps for the $^1S_0 \rightarrow ^3P_1$ cooling transition, the Sisyphus cooling scheme can be simply implemented with a single beam, as explained in Subs. 2.4.3. Moreover, we can use the same beam to induce pairwise losses via light-assisted collisions (LAC). This beam is aligned over the atoms along the z axis, with a small tilt with respect to the MOT beams and the imaging beam. The polarization is set to circular to address the transition towards a sublevel of the 3P_1 state with $m_J = 1$ or $m_J = -1$, thus performing an attractive Sisyphus cooling (see Subs. 2.4.3). To find the optimal frequency and power to cool the atoms, we scanned the frequency of the beam observing the atomic fluorescence from three identical tweezers positioned on a 1D line. The fluorescence signal is quantified by summing over 7×7 square ROIs centered on each tweezer. An example of such scan is reported in Fig. 7.5. An increased fluorescence centered around $\Delta = -2\pi \times 0.4$ MHz is a clear signal of effective cooling, as the atoms are prepared in a lower vibrational level in the tweezers and can scatter a higher number of photons before being lost. Comparing different tweezers allows us to evaluate the uniformity of the array, since power imbalances would cause differential light shifts in the array, which would result in cooling and LAC occurring at different detunings. In this case, we balanced the power on the three tweezers by acting on the frequency tones that are sent via the AWG to the AOD that generates the linear array of tweezers until we saw the cooling feature occurring at the same frequency for all the tweezers. Comparing the signal of the three different tweezers, we chose a detuning of $\Delta = -2\pi \times 0.4$ MHz for the cooling beam (see Fig. 7.5). The cooling sequence is performed right after loading atoms from

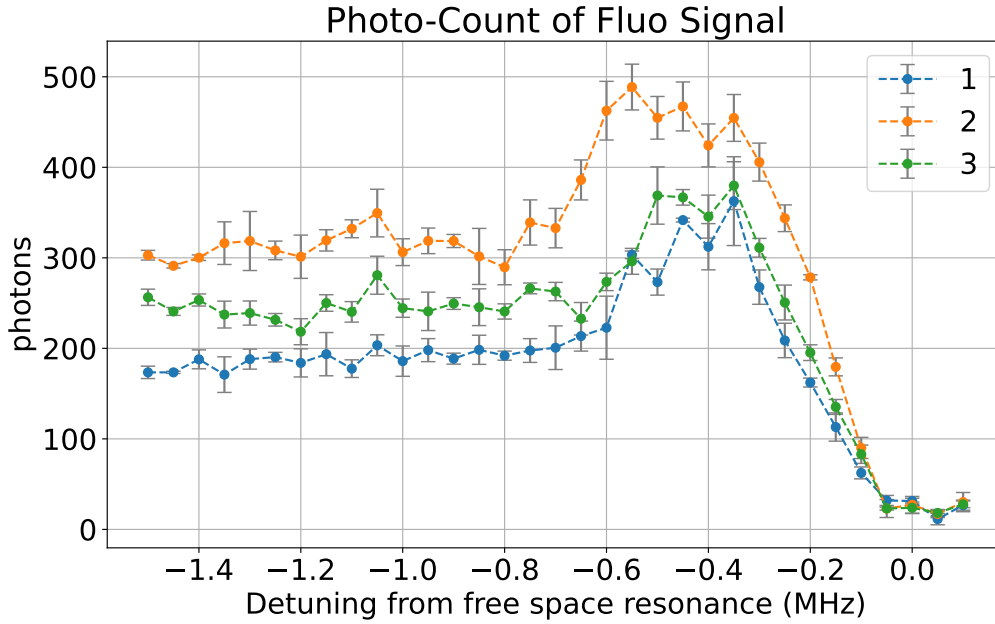


FIGURE 7.5: Scan of the Sisyphus cooling beam frequency at fixed intensity of $1500 I_{sat}$. Three tweezers with the same trap depth on a 1D line are compared. In this phase, cooling is performed only before the fluorescence imaging to prepare the atoms in the lower vibrational states of the traps. This allows for scattering almost $1.5\times$ the photons, thus increasing the fluorescence. A broad loss feature around the free space resonance is caused by the presence of many hot atoms in each tweezer, eventually occupying the high-lying levels for which the differential light shift is close to zero. We attribute the peak of photon counts centered around $\Delta = -2\pi \times 0.4$ MHz to an effective cooling, allowing us to prepare atoms in a lower vibrational level on average. This enables a higher number of blue-photon scattering cycles before the atoms are lost.

the red MOT in the tweezers, with a beam intensity of $1500 I_{sat}$ illuminating the atoms for 5 ms. This provides an optimal situation for imaging multiple atoms, as they are cooled close to the vibrational ground state before the fluorescence imaging. Cooling during fluorescence imaging is not included at this stage. It is convenient to cool the atoms before inducing LAC to obtain a binary occupation of the array, because the optimal LAC frequency can be optimized more easily if all the atoms are in, or near, the vibrational ground state of the trap, and the differential light shift is the same for all atoms.

The optimization of LAC frequency follows a similar procedure. The same beam that we use for cooling is tuned to a different power and frequency after the cooling sequence. In Fig. 7.6 the frequency scan of LAC frequency is reported. The intensity of this beam is $7500 I_{sat}$. We observe two dips, one around $\Delta = -2\pi \times 0.5$ MHz and one around the resonance. We attributed the first to the effect of LAC, reducing the number of atoms and therefore the fluorescence. The second one is compatible with losses induced by resonantly illuminating the atoms with an intense beam. Between the two peaks, the fluorescence slightly rises again in correspondance of $\Delta = -2\pi \times 0.3$ MHz, which is close to the frequency that we selected for cooling, possibly indicating a good configuration for cooling. After fixing the LAC detuning at a value of $\Delta =$

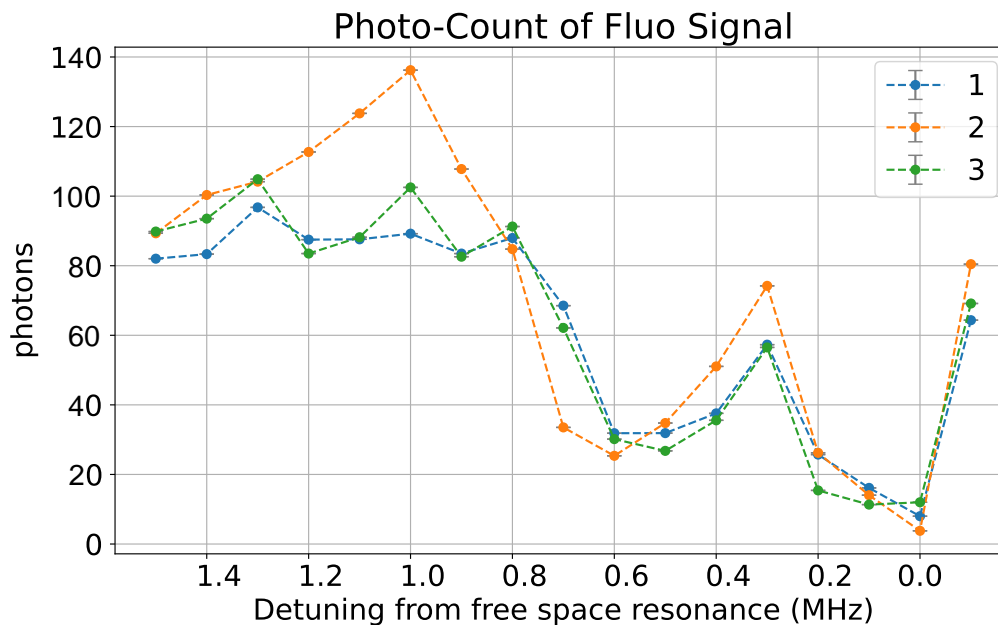


FIGURE 7.6: Scan of the light-assisted collisions beam frequency at fixed intensity of $7500 I_{sat}$. After the cooling sequence is performed, the same laser beam is tuned to a different power and frequency to induce LAC. We observe a clear reduction in the fluorescence from each tweezer for a detuning between $\Delta = -2\pi \times 0.5$ MHz and $\Delta = -2\pi \times 0.6$ MHz.

$-2\pi \times 0.5$ MHz we tried to observe the signal of single atoms.

Note that the features that indicate cooling or LAC are a few tens of kHz broad, therefore it is beneficial to optimize them quite often (basically every morning) to compensate for a possible drift of the reference ULE cavity, which could cause a drift of the laser frequency of the same order of magnitude.

7.5 Towards single atoms in optical tweezers

To observe a single atom with high fidelity via fluorescence imaging we need to collect approximately 40 photons on the detector (see Subs. 4.3.4). The scattering rate for the blue imaging beam that we employ ($s \simeq 0.05$, $\Delta = -2\pi \times 20$ MHz) is $R_{sc} \simeq 2\pi \times 25$ kHz. The estimated collection efficiency of the objective and detection setup is around 10%, so each atom should scatter around 400 photons during an imaging sequence. During an imaging time of 5 ms we expect each atom to scatter 800 photons, which are in principle enough to distinguish its presence from the background noise. In Fig. 7.7 the count histogram for atoms in the three tweezers is reported. The signal of the three tweezers is obtained by integrating over a 7×7 ROI and it is compared to an identical ROI placed in a region distant from the tweezers. The imaging time is 2 ms and the estimated scattering rate is $R_{sc} \simeq 2\pi \times 25$ kHz. The three tweezers show a similar behavior, although no bimodal distribution is visible yet. In particular, a 7×7 background ROI is traced on an area of the camera sensor outside of the array, to evaluate the background signal. This is a good estimate for the "zero atom" peak

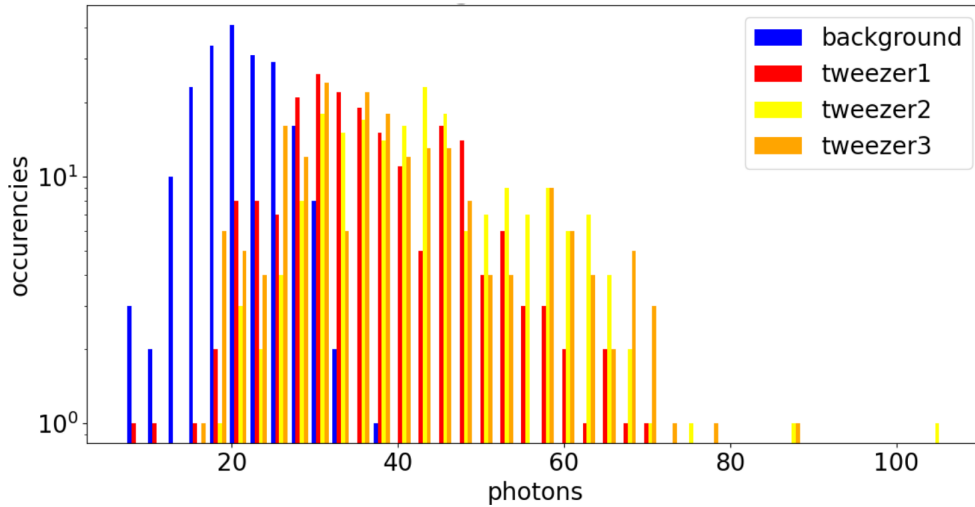


FIGURE 7.7: Measured count histogram for single-atom fluorescence in three different tweezers. The pixel counts are converted to photons with the conversion factor provided in the camera manual (Hamamatsu ORCA-Quest qCMOS). We still cannot distinguish a bimodal distribution, which would allow us to distinguish the background signal (zero atoms) from the occupation signal (one atom). The main motivation is that we could not implement an effective cooling sequence during the blue fluorescence imaging yet, and the single atoms can only scatter a few photons before being lost.

of the bimodal distribution that we expect to observe in the tweezer ROIs. The tweezer ROIs present a broader distribution, indicating that photons scattered from one or very few atoms are collected in this regions. The small offset between the background ROI and tweezer ROIs might be caused by stray photons, like reflected tweezer light at 813 nm that is not perfectly blocked by the dichroic mirror and the two bandpass filters. However, observing a broad distribution indicates that we are collecting fluorescence signal from the atoms, although we cannot accumulate enough photons to distinguish the two peaks.

In order to increase the fluorescence signal, we tried to implement Sisyphus cooling during the fluorescence imaging, by alternating 1 ms of imaging with 2 ms of cooling. By using the same cooling frequency that we found during the measurement reported in Fig. 7.5, we did not observe any improvement in the fluorescence yet. These are preliminary results that will be extended and explored carefully in order to realize imaging and keeping the atoms cold during the fluorescence is indeed crucial because it allows for a repeated imaging sequence without losing the atom and collecting a much better signal-to-noise ratio.

We recorded a fluorescence image of the fluorescence signal after LAC, as reported in Fig. 7.8, averaged over 10 repetitions. In this way we could see the three tweezers all occupied, on average. This kind of measurement allowed us to finely tune the position of the tube lens on the tweezer path to match the focal plane of the tweezers path with the focal plane of the detection path (see Subs. 5.5.2). While in single-shot measurements we see a weak fluorescence appearing randomly in one or two of the tweezers, which would be compatible with a binary occupation of the array after

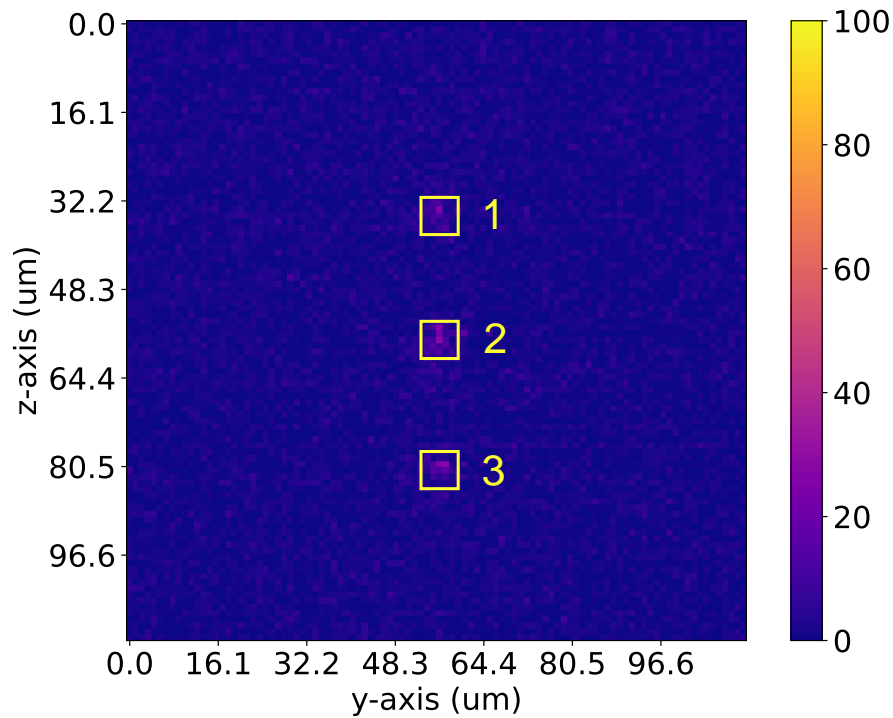


FIGURE 7.8: Reduced number of atom averaged fluorescence. After inducing losses via LAC, we observe the fluorescence of a reduced number of atoms, compatible with single atom occupancy, in three tweezers. In single-shot experiments we observe fluorescence randomly from half the traps, which is a good indication of binary occupation but not enough to prove it. By averaging over 10 shots, we can see the mediated signal on all the tweezers.

LAC, on an averaged image we can observe all the traps occupied. This signal is concentrated over a few pixels, but still too low to clearly determine, on a single-shot basis, the presence or absence of single atoms. An efficient Sisyphus cooling alternated with the fluorescence imaging will help to increase the signal.

Conclusions and outlook

Quantum simulation using Rydberg atoms in optical tweezer arrays has demonstrated remarkable versatility in many different experimental platforms worldwide. The platform's flexibility enables individual control over quantum objects and scalability to thousands of single atoms, paving the way towards applications in quantum simulation, information and computing.

In this work, I report the construction and development of a next-generation optical-tweezers platform based on two-electron strontium atoms. My contributions included the assembly of most components of the experimental apparatus, including the vacuum system and the optical setups for lasers, which I also designed. I simulated and designed the optimal geometry for a system of custom coils for magnetic field control. These coils, by being water cooled, allowed us to run continuously the experiment with high stability, addressing the heat management limitations of the previous handmade coils.

In our custom rectangular quartz science cell, all the trapping and manipulation of the atomic sample takes place. We successfully demonstrated cooling and trapping in a two-wavelength magneto-optical trap (MOT), leveraging the broad-linewidth 461 nm transition to cool atoms to approximately 8 mK. From there, atoms are transferred to a multifrequency red MOT using the narrow 689 nm transition, to bridge between the blue MOT and a single-frequency red MOT. By optimizing the transition to a single-frequency red MOT, we achieved temperatures of about 5 μ K and densities reaching $n \sim 4 \times 10^{10}$ atoms/cm³ that are necessary for subsequently loading into optical tweezers.

I also contributed to developing and designing the optical setups to generate the optical tweezer array and to implement single-atom fluorescence imaging for detection. We explored fundamental concepts of Rydberg atoms and their interactions, giving an overview of the research areas in quantum science that we plan to investigate with this platform. Additionally, I presented and analysed two possible new fluorescence imaging schemes through theoretical and semi-classical simulations to reduce single-atom readout time.

Preliminary experimental results show successful trapping of several atoms in a small array of optical tweezers, generated through a setup using crossed AODs that

are capable of producing a two-dimensional rectangular array. For imaging, a high-numerical-aperture microscope objective designed to be diffraction-limited at both 813 nm and 461 nm allows for efficient fluorescence detection. The initial results include fluorescence signals that are compatible with expected single-atom signatures, which can be further refined for high-fidelity detection by accumulating a higher number of photons per atom and demonstrating a binomial distribution.

Future developments aim to achieve high-fidelity preparation of single atoms in defect-free arrays. We will develop an algorithm for optimal atom sorting and update the optical setup to include a spatial light modulator (SLM) for realizing versatile static trap geometries. Additionally, a UV laser system for Rydberg state excitation will be aligned, enabling controlled long-range interactions between atoms at different sites. With single-atom excitation and inter-atomic interaction fully characterized, initial quantum simulation experiments will be performed to investigate the 1D Ising spin model, progressing later to more complex 1D-2D schemes, like Heisenberg XXZ [125] and XYZ [126] spin models with nearest neighbor and beyond nearest neighbor interactions and complex topology, that will fully realize the platform's quantum simulation potential.

Bibliography

- [1] R. P. Feynman. “Simulating Physics with Computers”. *International Journal of Theoretical Physics* 21, 1982, pp. 467–488.
- [2] I. M. Georgescu et al. “Quantum simulation”. *Rev. Mod. Phys.* 86, 2014, pp. 153–185.
- [3] E. Altman et al. “Quantum Simulators: Architectures and Opportunities”. *PRX Quantum* 2, 2021, p. 017003.
- [4] I. Bloch. “Ultracold quantum gases in optical lattices”. *Nature Physics* 1, 2005, pp. 23–30.
- [5] C. Gross and I. Bloch. “Quantum simulations with ultracold atoms in optical lattices”. *Science* 357, 2017, pp. 995–1001.
- [6] J. I. Cirac and P. Zoller. “Quantum Computations with Cold Trapped Ions”. *Phys. Rev. Lett.* 74, 1995, pp. 4091–4094.
- [7] R. Blatt and C. Roos. “Quantum Simulations with Trapped Ions”. *Nature Physics* 8, 2012, pp. 277–284.
- [8] M. Greiner et al. “Quantum phase transition from a superfluid to a Mott insulator in a gas of ultracold atoms”. *Nature* 415, 2002, pp. 39–44.
- [9] G. Roati et al. “Anderson localization of a non-interacting Bose–Einstein condensate”. *Nature* 453, 2008, pp. 895–898.
- [10] J. K. Chin et al. “Evidence for superfluidity of ultracold fermions in an optical lattice”. *Nature* 443, 2006, pp. 961–964.
- [11] J. W. Britton et al. “Engineered two-dimensional Ising interactions in a trapped-ion quantum simulator with hundreds of spins”. *Nature* 484, 2012, pp. 489–492.
- [12] J. Zhang et al. “Observation of a many-body dynamical phase transition with a 53-qubit quantum simulator”. *Nature* 551, 2017, pp. 601–604.
- [13] A. Browaeys and T. Lahaye. “Many-body physics with individually controlled Rydberg atoms”. *Nature Physics* 16, 2020, pp. 132–142.
- [14] M. Morgado and S. Whitlock. “Quantum simulation and computing with Rydberg-interacting qubits”. *AVS Quantum Science* 3, 2021.

-
- [15] A. Kaufman and K.-K. Ni. “Quantum science with optical tweezer arrays of ultracold atoms and molecules”. *Nature* **17**, 2021, pp. 1324–1333.
- [16] A. Ashkin. “Optical trapping and manipulation of neutral particles using lasers”. *Proceedings of the National Academy of Sciences* **94**, 1997, pp. 4853–4860.
- [17] A. Ashkin and J. M. Dziedzic. “Optical Trapping and Manipulation of Viruses and Bacteria”. *Science* **235**, 1987, pp. 1517–1520.
- [18] S. Chu et al. “Experimental Observation of Optically Trapped Atoms”. *Phys. Rev. Lett.* **57**, 1986, pp. 314–317.
- [19] N. Schlosser et al. “Sub-poissonian loading of single atoms in a microscopic dipole trap”. *Nature* **411**, 2001, pp. 1024–1027.
- [20] F. Nogrette et al. “Single-Atom Trapping in Holographic 2D Arrays of Microtraps with Arbitrary Geometries”. *Phys. Rev. X* **4**, 2014, p. 021034.
- [21] D. Barredo et al. “An atom-by-atom assembler of defect-free arbitrary two-dimensional atomic arrays”. *Science* **354**, 2016, pp. 1021–1023.
- [22] M. Endres et al. “Atom-by-atom assembly of defect-free one-dimensional cold atom arrays”. *Science* **354**, 2016, pp. 1024–1027.
- [23] W. S. Bakr et al. “A quantum gas microscope for detecting single atoms in a Hubbard-regime optical lattice”. *Nature* **462**, 2009, pp. 74–77.
- [24] J. Sherson et al. “Single-Atom Resolved Fluorescence Imaging of an Atomic Mott Insulator”. *Nature* **467**, 2010, pp. 68–72.
- [25] M. Endres et al. “Observation of Correlated Particle-Hole Pairs and String Order in Low-Dimensional Mott Insulators”. *Science* **334**, 2011, pp. 200–203.
- [26] M. F. Parsons et al. “Site-Resolved Imaging of Fermionic Lithium-6 in an Optical Lattice”. *Physical Review Letters* **114**, 2015.
- [27] A. Mazurenko et al. “A cold-atom Fermi–Hubbard antiferromagnet”. *Nature* **545**, 2017, pp. 462–466.
- [28] D. Jaksch et al. “Fast Quantum Gates for Neutral Atoms”. *Phys. Rev. Lett.* **85**, 2000, pp. 2208–2211.
- [29] M. D. Lukin et al. “Dipole Blockade and Quantum Information Processing in Mesoscopic Atomic Ensembles”. *Phys. Rev. Lett.* **87**, 2001, p. 037901.
- [30] A. Gaëtan et al. “Observation of collective excitation of two individual atoms in the Rydberg blockade regime”. *Nature Physics* **5**, 2009, pp. 115–118.
- [31] E. Urban et al. “Observation of Rydberg blockade between two atoms”. *Nature Physics* **5**, 2009, pp. 110–114.
- [32] T. Wilk et al. “Entanglement of Two Individual Neutral Atoms Using Rydberg Blockade”. *Phys. Rev. Lett.* **104**, 2010, p. 010502.
- [33] S. Ebadi et al. “Quantum phases of matter on a 256-atom programmable quantum simulator”. *Nature* **595**, 2021, pp. 227–232.
- [34] P. Scholl et al. “Quantum simulation of 2D antiferromagnets with hundreds of Rydberg atoms”. *Nature* **595**, 2021, pp. 233–238.

- [35] K.-N. Schymik et al. “In situ equalization of single-atom loading in large-scale optical tweezer arrays”. *Phys. Rev. A* **106**, 2022, p. 022611.
- [36] D. Bluvstein et al. “A quantum processor based on coherent transport of entangled atom arrays”. *Nature* **604**, 2022, pp. 451–456.
- [37] T. M. Graham et al. “Multi-qubit entanglement and algorithms on a neutral-atom quantum computer”. *Nature* **604**, 2022, pp. 457–462.
- [38] H. J. Manetsch et al. *A tweezer array with 6100 highly coherent atomic qubits* 2024.
- [39] A. Cooper et al. “Alkaline-Earth Atoms in Optical Tweezers”. *Phys. Rev. X* **8**, 2018, p. 041055.
- [40] S. Saskin et al. “Narrow-Line Cooling and Imaging of Ytterbium Atoms in an Optical Tweezer Array”. *Phys. Rev. Lett.* **122**, 2019, p. 143002.
- [41] M. A. Norcia et al. “Microscopic Control and Detection of Ultracold Strontium in Optical-Tweezer Arrays”. *Phys. Rev. X* **8**, 2018, p. 041054.
- [42] A. Jenkins et al. “Ytterbium Nuclear-Spin Qubits in an Optical Tweezer Array”. *Phys. Rev. X* **12**, 2022, p. 021027.
- [43] A. Urech et al. “Narrow-line imaging of single strontium atoms in shallow optical tweezers”. *Phys. Rev. Res.* **4**, 2022, p. 023245.
- [44] S. Ma et al. “Universal Gate Operations on Nuclear Spin Qubits in an Optical Tweezer Array of ^{171}Yb Atoms”. *Phys. Rev. X* **12**, 2022, p. 021028.
- [45] I. S. Madjarov et al. “High-fidelity entanglement and detection of alkaline-earth Rydberg atoms”. *Nature Physics* **16**, 2020, pp. 857–861.
- [46] M. Mohan et al. “Robust control and optimal Rydberg states for neutral atom two-qubit gates”. *Phys. Rev. Res.* **5**, 2023, p. 033052.
- [47] N. Schine et al. “Long-lived Bell states in an array of optical clock qubits”. *Nature Physics* **18**, 2022, pp. 1067–1073.
- [48] I. S. Madjarov et al. “An Atomic-Array Optical Clock with Single-Atom Read-out”. *Phys. Rev. X* **9**, 2019, p. 041052.
- [49] A. W. Young et al. “Half-minute-scale atomic coherence and high relative stability in a tweezer clock”. *Nature* **588**, 2020, pp. 408–413.
- [50] J. T. Wilson et al. “Trapping Alkaline Earth Rydberg Atoms Optical Tweezer Arrays”. *Phys. Rev. Lett.* **128**, 2022, p. 033201.
- [51] M. Yasuda et al. “Photoassociation spectroscopy of ^{88}Sr : Reconstruction of the wave function near the last node”. *Phys. Rev. A* **73**, 2006, p. 011403.
- [52] J. E. Sansonetti and G. Nave. “Wavelengths, Transition Probabilities, and Energy Levels for the Spectrum of Neutral Strontium (SrI)”. *Journal of Physical and Chemical Reference Data* **39**, 2010, p. 033103.
- [53] H. Metcalf and P. Van der Straten. *Laser Cooling and Trapping*. 1999.
- [54] C. Cohen-Tannoudji et al. *Quantum mechanics; 1st ed.* 1977.
- [55] M. Inguscio and L. Fallani. *Atomic Physics: Precise Measurements and Ultra-cold Matter*. 2013.

- [56] O. Onishchenko. “Ultracold atomic gases of strontium: production and narrow-line spectroscopy”. PhD thesis. Universiteit van Amsterdam, 2020.
- [57] J. Sakurai and J. Napolitano. *Modern Quantum Mechanics*. 2017.
- [58] C. Foot. *Atomic Physics*. 2004.
- [59] W. D. Phillips and H. Metcalf. “Laser Deceleration of an Atomic Beam”. *Phys. Rev. Lett.* **48**, 1982, pp. 596–599.
- [60] E. L. Raab et al. “Trapping of Neutral Sodium Atoms with Radiation Pressure”. *Phys. Rev. Lett.* **59**, 1987, pp. 2631–2634.
- [61] G. Pagano. “Raffreddamento e Intrappolamento di atomi di Itterbio”. MA thesis. Università la Sapienza, 2011.
- [62] A. Ashkin. “Trapping of Atoms by Resonance Radiation Pressure”. *Phys. Rev. Lett.* **40**, 1978, pp. 729–732.
- [63] S. H. Autler and C. H. Townes. “Stark Effect in Rapidly Varying Fields”. *Phys. Rev.* **100**, 1955, pp. 703–722.
- [64] R. Grimm et al. “Optical Dipole Traps for Neutral Atoms”. Vol. 42. *Advances In Atomic, Molecular, and Optical Physics*. Academic Press, 2000, pp. 95–170.
- [65] S. Chu et al. “Experimental Observation of Optically Trapped Atoms”. *Phys. Rev. Lett.* **57**, 1986, pp. 314–317.
- [66] D. Steck. *Quantum and Atom Optics (revision 0.16.1, 16 June 2024)*. 2024.
- [67] M. M. Boyd. “High Precision Spectroscopy of Strontium in an Optical Lattice: Towards a New Standard for Frequency and Time”. PhD thesis. University of Washington, 2002.
- [68] I. H. Deutsch and P. S. Jessen. “Quantum-state control in optical lattices”. *Phys. Rev. A* **57**, 1998, pp. 1972–1986.
- [69] I. S. Madjarov. “Entangling, controlling, and detecting individual strontium atoms in optical tweezer arrays”. PhD thesis. California Institute Of Technology, 2021.
- [70] A. A. Urech. “Single strontium atoms in optical tweezers”. PhD thesis. Universiteit van Amsterdam, 2023.
- [71] G. Morigi et al. “Laser cooling of two trapped ions: Sideband cooling beyond the Lamb-Dicke limit”. *Phys. Rev. A* **59**, 1999, pp. 3797–3808.
- [72] S. E. Hamann et al. “Resolved-Sideband Raman Cooling to the Ground State of an Optical Lattice”. *Phys. Rev. Lett.* **80**, 1998, pp. 4149–4152.
- [73] H. Perrin et al. “Sideband cooling of neutral atoms in a far-detuned optical lattice”. *Europhysics Letters* **42**, 1998, p. 395.
- [74] J. D. Teufel et al. “Sideband cooling of micromechanical motion to the quantum ground state”. *Nature* **475**, 2011, pp. 359–363.
- [75] A. M. Kaufman et al. “Cooling a Single Atom in an Optical Tweezer to Its Quantum Ground State”. *Phys. Rev. X* **2**, 2012, p. 041014.
- [76] J. P. Covey et al. “2000-Times Repeated Imaging of Strontium Atoms in Clock-Magic Tweezer Arrays”. *Phys. Rev. Lett.* **122**, 2019, p. 173201.

- [77] R. Tao et al. “High-Fidelity Detection of Large-Scale Atom Arrays in an Optical Lattice”. *Physical Review Letters* 133, 2024.
- [78] C.-C. Chen et al. “Sisyphus optical lattice decelerator”. *Phys. Rev. A* 100, 2019, p. 023401.
- [79] S. Buob et al. “A Strontium Quantum-Gas Microscope”. *PRX Quantum* 5, 2024, p. 020316.
- [80] V. V. Ivanov and S. Gupta. “Laser-driven Sisyphus cooling in an optical dipole trap”. *Phys. Rev. A* 84, 2011, p. 063417.
- [81] H. Kogelnik and T. Li. “Laser Beams and Resonators”. *Appl. Opt.* 5, 1966, pp. 1550–1567.
- [82] I. H. A. Knottnerus. “Tweezer machine for Sr atoms using a homebuilt microscope objective from commercial lenses”. MA thesis. University of Amsterdam, 2018.
- [83] E. Hecht. *Optics*. 2017.
- [84] A. Goutzoulis. *Design and Fabrication of Acousto-Optic Devices*. 2021.
- [85] L. Guariento. “Development of Optical Tweezer techniques with Acousto Optic Deflectors for atomic quantum simulators.” MA thesis. University of Florence, 2021.
- [86] M. Born and E. Wolf. *Principles of Optics: Electromagnetic Theory of Propagation, Interference and Diffraction of Light (7th Edition)*. 1999.
- [87] D. Bluvstein et al. “Logical quantum processor based on reconfigurable atom arrays”. *Nature* 626, 2023, pp. 58–65.
- [88] J. Hennebichler. “Towards the creation of a two-dimensional optical tweezer array using a liquid crystal spatial light modulator”. MA thesis. University of Innsbruck, 2023.
- [89] D. Kim et al. “Large-scale uniform optical focus array generation with a phase spatial light modulator”. *Optics Letters* 44, 2019, p. 3178.
- [90] Y. Wu et al. “Adaptive weighted Gerchberg-Saxton algorithm for generation of phase-only hologram with artifacts suppression”. *Opt. Express* 29, 2021, pp. 1412–1427.
- [91] D. M. Stamper-Kurn et al. “Reversible Formation of a Bose-Einstein Condensate”. *Phys. Rev. Lett.* 81, 1998, pp. 2194–2197.
- [92] A. W. Young. “Programmable arrays of alkaline earth atoms: qubits, clocks, and the Bose-Hubbard model”. PhD thesis. University of Colorado, 2023.
- [93] T. Grünzweig et al. “Near-deterministic preparation of a single atom in an optical microtrap”. *Nature Physics* 6, 2011.
- [94] B. J. Lester et al. “Rapid Production of Uniformly Filled Arrays of Neutral Atoms”. *Phys. Rev. Lett.* 115, 2015, p. 073003.
- [95] M. O. Brown et al. “Gray-Molasses Optical-Tweezer Loading: Controlling Collisions for Scaling Atom-Array Assembly”. *Phys. Rev. X* 9, 2019, p. 011057.

- [96] N. Schlosser et al. “Collisional Blockade in Microscopic Optical Dipole Traps”. *Phys. Rev. Lett.* **89**, 2002, p. 023005.
- [97] T. Zelevinsky et al. “Narrow Line Photoassociation in an Optical Lattice”. *Phys. Rev. Lett.* **96**, 2006, p. 203201.
- [98] J. Ang’ong’a et al. “Gray molasses cooling of ^{39}K atoms in optical tweezers”. *Phys. Rev. Res.* **4**, 2022, p. 013240.
- [99] A. L. Shaw et al. “Dark-State Enhanced Loading of an Optical Tweezer Array”. *Phys. Rev. Lett.* **130**, 2023, p. 193402.
- [100] R. El Sabeih et al. “Efficient algorithms to solve atom reconfiguration problems. II. Assignment-rerouting-ordering algorithm”. *Phys. Rev. A* **108**, 2023, p. 023108.
- [101] G. Pichard et al. “Rearrangement of individual atoms in a 2000-site optical-tweezer array at cryogenic temperatures”. *Phys. Rev. Appl.* **22**, 2024, p. 024073.
- [102] H. Kim et al. “Gerchberg-Saxton algorithm for fast and efficient atom rearrangement in optical tweezer traps”. *Opt. Express* **27**, 2019, pp. 2184–2196.
- [103] T. F. Gallagher. *Rydberg Atoms*. 1994.
- [104] J. Lim et al. “Review of cold Rydberg atoms and their applications”. *Journal of the Korean Physical Society* **63**, 2013, pp. 867–876.
- [105] N. Šibalić et al. *Rydberg Physics*. 2018.
- [106] A. Reinhard et al. “Level shifts of rubidium Rydberg states due to binary interactions”. *Phys. Rev. A* **75**, 2007, p. 032712.
- [107] L. Béguin et al. “Direct Measurement of the van der Waals Interaction between Two Rydberg Atoms”. *Phys. Rev. Lett.* **110**, 2013, p. 263201.
- [108] H. Levine et al. “High-Fidelity Control and Entanglement of Rydberg-Atom Qubits”. *Phys. Rev. Lett.* **121**, 2018, p. 123603.
- [109] S. Ye et al. “Production of very-high- n strontium Rydberg atoms”. *Phys. Rev. A* **88**, 2013, p. 043430.
- [110] L. Couturier et al. “Measurement of the strontium triplet Rydberg series by depletion spectroscopy of ultracold atoms”. *Phys. Rev. A* **99**, 2019, p. 022503.
- [111] R. Ding et al. “Spectroscopy of ^{87}Sr triplet Rydberg states”. *Phys. Rev. A* **98**, 2018, p. 042505.
- [112] C. L. Vaillant et al. “Long-range Rydberg–Rydberg interactions in calcium, strontium and ytterbium”. *Journal of Physics B: Atomic, Molecular and Optical Physics* **45**, 2012, p. 135004.
- [113] R. A. Brienza et al. “Microwave spectroscopy of low- l singlet strontium Rydberg states at intermediate n , $50 \lesssim n \lesssim 70$ ”. *Phys. Rev. A* **108**, 2023, p. 022815.
- [114] C. S. Adams et al. “Rydberg atom quantum technologies”. *Journal of Physics B: Atomic, Molecular and Optical Physics* **53**, 2019, p. 012002.
- [115] P. Schauss. “Quantum simulation of transverse Ising models with Rydberg atoms”. *Quantum Science and Technology* **3**, 2018, p. 023001.

- [116] H. Labuhn et al. “Tunable two-dimensional arrays of single Rydberg atoms for realizing quantum Ising models”. *Nature* **534**, 2016, pp. 667–670.
- [117] H. Bernien et al. “Probing many-body dynamics on a 51-atom quantum simulator”. *Nature* **551**, 2017, pp. 579–584.
- [118] V. Lienhard et al. “Observing the Space- and Time-Dependent Growth of Correlations in Dynamically Tuned Synthetic Ising Models with Antiferromagnetic Interactions”. *Phys. Rev. X* **8**, 2018, p. 021070.
- [119] A. Keesling et al. “Quantum Kibble–Zurek mechanism and critical dynamics on a programmable Rydberg simulator”. *Nature* **568**, 2019, pp. 207–211.
- [120] S. de Léséleuc et al. “Observation of a symmetry-protected topological phase of interacting bosons with Rydberg atoms”. *Science* **365**, 2019, pp. 775–780.
- [121] V. Lienhard et al. “Realization of a Density-Dependent Peierls Phase in a Synthetic, Spin-Orbit Coupled Rydberg System”. *Phys. Rev. X* **10**, 2020, p. 021031.
- [122] G. Semeghini et al. “Probing topological spin liquids on a programmable quantum simulator”. *Science* **374**, 2021, pp. 1242–1247.
- [123] S. Blundell. *Magnetism in Condensed Matter*. 2001.
- [124] P. M. Chaikin and T. C. Lubensky. *Principles of Condensed Matter Physics*. 1995.
- [125] P. Scholl et al. “Microwave Engineering of Programmable XXZ Hamiltonians in Arrays of Rydberg Atoms”. *PRX Quantum* **3**, 2022, p. 020303.
- [126] L.-M. Steinert et al. “Spatially Tunable Spin Interactions in Neutral Atom Arrays”. *Physical Review Letters* **130**, 2023.
- [127] S. Geier et al. “Floquet Hamiltonian engineering of an isolated many-body spin system”. *Science* **374**, 2021, pp. 1149–1152.
- [128] S. Ohler et al. “Self-generated quantum gauge fields in arrays of Rydberg atoms”. *New Journal of Physics* **24**, 2022, p. 023017.
- [129] A. Lucas. “Ising formulations of many NP problems”. *Frontiers in Physics* **2**, 2014.
- [130] J. Roland and N. J. Cerf. “Quantum search by local adiabatic evolution”. *Physical Review A* **65**, 2002.
- [131] H. Pichler et al. *Quantum Optimization for Maximum Independent Set Using Rydberg Atom Arrays* 2018.
- [132] S. Ebadi et al. “Quantum optimization of maximum independent set using Rydberg atom arrays”. *Science* **376**, 2022, pp. 1209–1215.
- [133] M.-T. Nguyen et al. “Quantum Optimization with Arbitrary Connectivity Using Rydberg Atom Arrays”. *PRX Quantum* **4**, 2023, p. 010316.
- [134] L. Zhou et al. “Quantum Approximate Optimization Algorithm: Performance, Mechanism, and Implementation on Near-Term Devices”. *Phys. Rev. X* **10**, 2020, p. 021067.
- [135] S. Kirkpatrick et al. “Optimization by Simulated Annealing”. *Science (New York, N.Y.)* **220**, 1983, pp. 671–80.

- [136] A. Lukin et al. *Quantum quench dynamics as a shortcut to adiabaticity* 2024.
- [137] D. Guéry-Odelin et al. “Shortcuts to adiabaticity: Concepts, methods, and applications”. *Rev. Mod. Phys.* 91, 2019, p. 045001.
- [138] M. Saffman et al. “Quantum information with Rydberg atoms”. *Rev. Mod. Phys.* 82, 2010, pp. 2313–2363.
- [139] M. Saffman. “Quantum computing with atomic qubits and Rydberg interactions: progress and challenges”. *Journal of Physics B: Atomic, Molecular and Optical Physics* 49, 2016, p. 202001.
- [140] L. Henriët et al. “Quantum computing with neutral atoms”. *Quantum* 4, 2020, p. 327.
- [141] F. Cesa and H. Pichler. “Universal Quantum Computation in Globally Driven Rydberg Atom Arrays”. *Phys. Rev. Lett.* 131, 2023, p. 170601.
- [142] H. Levine et al. “Parallel Implementation of High-Fidelity Multiqubit Gates with Neutral Atoms”. *Phys. Rev. Lett.* 123, 2019, p. 170503.
- [143] I. Cong et al. “Hardware-Efficient, Fault-Tolerant Quantum Computation with Rydberg Atoms”. *Phys. Rev. X* 12, 2022, p. 021049.
- [144] S. J. Evered et al. “High-fidelity parallel entangling gates on a neutral-atom quantum computer”. *Nature* 622, 2023, pp. 268–272.
- [145] S. R. Cohen and J. D. Thompson. “Quantum Computing with Circular Rydberg Atoms”. *PRX Quantum* 2, 2021, p. 030322.
- [146] S. Jandura et al. “Optimizing Rydberg Gates for Logical-Qubit Performance”. *PRX Quantum* 4, 2023, p. 020336.
- [147] D. P. DiVincenzo. “The Physical Implementation of Quantum Computation”. *Fortschritte der Physik* 48, 2000, pp. 771–783.
- [148] M. A. Nielsen and I. L. Chuang. *Quantum Computation and Quantum Information*. 2010.
- [149] J. R. Weggemans et al. “Solving correlation clustering with QAOA and a Rydberg qudit system: a full-stack approach”. *Quantum* 6, 2022, p. 687.
- [150] S. Omanakuttan et al. “Qudit Entanglers Using Quantum Optimal Control”. *PRX Quantum* 4, 2023.
- [151] M. Miranda et al. “Site-resolved imaging of ytterbium atoms in a two-dimensional optical lattice”. *Phys. Rev. A* 91, 2015, p. 063414.
- [152] R. Yamamoto et al. “An ytterbium quantum gas microscope with narrow-line laser cooling”. *New Journal of Physics* 18, 2016, p. 023016.
- [153] D. S. W. Karl D. Nelson Xiao Li. “Imaging single atoms in a three-dimensional array”. English (US). *Nature Physics* 3, 2007, pp. 556–560.
- [154] L. W. Cheuk et al. “Quantum-Gas Microscope for Fermionic Atoms”. *Phys. Rev. Lett.* 114, 2015, p. 193001.
- [155] M. F. Parsons et al. “Site-Resolved Imaging of Fermionic ${}^6\text{Li}$ in an Optical Lattice”. *Phys. Rev. Lett.* 114, 2015, p. 213002.

- [156] E. Haller et al. “Single-atom imaging of fermions in a quantum-gas microscope”. *Nature Physics* **11**, 2015, pp. 738–742.
- [157] G. J. A. Edge et al. “Imaging and addressing of individual fermionic atoms in an optical lattice”. *Phys. Rev. A* **92**, 2015, p. 063406.
- [158] A. Bergschneider et al. “Spin-resolved single-atom imaging of ${}^6\text{Li}$ in free space”. *Phys. Rev. A* **97**, 2018, p. 063613.
- [159] L. Su et al. *Fast single atom imaging in optical lattice arrays* 2024.
- [160] D. S. Grün et al. *Optical Tweezer Arrays of Erbium Atoms* 2024.
- [161] D. Petrosyan et al. *Fast measurements and multiqubit gates in dual species atomic arrays* 2024.
- [162] Andor. *iXon Ultra & Life 888*. Available at https://andor.oxinst.com/downloads/uploads/Hardware_Guide_iXon_Ultra_Life_888.pdf. Sept. 2023.
- [163] Hamamatsu. *ORCA-Quest Technical note*. Available at https://www.hamamatsu.com/content/dam/hamamatsu-photonics/sites/documents/99_SALES_LIBRARY/sys/SCAS0154E_C15550-20UP_tec.pdf. May 2022.
- [164] H. Arnoldus and G. Nienhuis. “Photon Statistics of Fluorescence Radiation”. *Optica Acta: International Journal of Optics* **33**, 1986, pp. 691–702.
- [165] N. C. Jackson et al. “Number-resolved imaging of ${}^{88}\text{Sr}$ atoms in a long working distance optical tweezer”. *SciPost Phys.* **8**, 2020, p. 038.
- [166] P. W. Shor. “Scheme for reducing decoherence in quantum computer memory”. *Phys. Rev. A* **52**, 1995, R2493–R2496.
- [167] A. M. Steane. “Error Correcting Codes in Quantum Theory”. *Phys. Rev. Lett.* **77**, 1996, pp. 793–797.
- [168] E. M. Kessler et al. “Quantum Error Correction for Metrology”. *Phys. Rev. Lett.* **112**, 2014, p. 150802.
- [169] W. Dür et al. “Improved Quantum Metrology Using Quantum Error Correction”. *Phys. Rev. Lett.* **112**, 2014, p. 080801.
- [170] S. Zhou and L. Jiang. “Optimal approximate quantum error correction for quantum metrology”. *Phys. Rev. Res.* **2**, 2020, p. 013235.
- [171] E. Deist et al. “Mid-Circuit Cavity Measurement in a Neutral Atom Array”. *Phys. Rev. Lett.* **129**, 2022, p. 203602.
- [172] M. A. Norcia et al. “Iterative Assembly of ${}^{171}\text{Yb}$ Atom Arrays with Cavity-Enhanced Optical Lattices”. *PRX Quantum* **5**, 2024, p. 030316.
- [173] M. A. Norcia et al. “Midcircuit Qubit Measurement and Rearrangement in a ${}^{171}\text{Yb}$ Atomic Array”. *Phys. Rev. X* **13**, 2023, p. 041034.
- [174] T. M. Graham et al. “Midcircuit Measurements on a Single-Species Neutral Alkali Atom Quantum Processor”. *Phys. Rev. X* **13**, 2023, p. 041051.
- [175] R. Finkelstein et al. *Universal quantum operations and ancilla-based readout for tweezer clocks* 2024.

- [176] J. W. Lis et al. “Midcircuit Operations Using the omg Architecture in Neutral Atom Arrays”. *Phys. Rev. X* 13, 2023, p. 041035.
- [177] S. Ma et al. “High-fidelity gates and mid-circuit erasure conversion in an atomic qubit”. *Nature* 622, 2023, pp. 279–284.
- [178] A. L. Shaw et al. *Erasure-cooling, control, and hyper-entanglement of motion in optical tweezers* 2024.
- [179] A. L. Shaw. “Learning, Verifying, and Erasing Errors on a Chaotic and Highly Entangled Programmable Quantum Simulator.” PhD thesis. California Institute of Technology., 2024.
- [180] M. Fisher-Levine and A. Nomerotski. “TimepixCam: a fast optical imager with time-stamping”. *Journal of Instrumentation* 11, 2016, p. C03016.
- [181] A. Zhao et al. “Coincidence velocity map imaging using Tpx3Cam, a time stamping optical camera with 1.5 ns timing resolution”. *Review of Scientific Instruments* 88, 2017.
- [182] A. Nomerotski. “Imaging and time stamping of photons with nanosecond resolution in Timepix based optical cameras”. *Nuclear Instruments and Methods in Physics Research Section A: Accelerators, Spectrometers, Detectors and Associated Equipment* 937, 2019, pp. 26–30.
- [183] A. Nomerotski et al. “Intensified Tpx3Cam, a fast data-driven optical camera with nanosecond timing resolution for single photon detection in quantum applications”. *Journal of Instrumentation* 18, 2023, p. C01023.
- [184] A. Nomerotski et al. “Counting of Hong-Ou-Mandel Bunched Optical Photons Using a Fast Pixel Camera”. *Sensors* 20, 2020.
- [185] Hamamatsu. *Image Intensifiers*. Available at https://www.hamamatsu.com/content/dam/hamamatsu-photonics/sites/documents/99_SALES_LIBRARY/etd/II_TII0007E.pdf. May 2020.
- [186] A. W. Young et al. “Tweezer-programmable 2D quantum walks in a Hubbard-regime lattice”. *Science* 377, 2022, pp. 885–889.
- [187] H. G. C. Werij et al. “Oscillator strengths and radiative branching ratios in atomic Sr”. *Phys. Rev. A* 46, 1992, pp. 1248–1260.
- [188] Pfeiffer. *The Vacuum Technology Book*. 2013.
- [189] J. A. Fedchak et al. “Vacuum furnace for degassing stainless-steel vacuum components”. *Journal of Vacuum Science & Technology A* 36, 2018, p. 023201.
- [190] B. Ferrario and A. Calcatelli. *Introduzione alla tecnologia del vuoto*. 1999.
- [191] K.-N. Schymik. “Scaling-up the Tweezer Platform-Trapping Arrays of Single Atoms in a Cryogenic Environment”. PhD thesis. Université Paris-Saclay, Institut d’Optique Graduate School, 2022.
- [192] K.-N. Schymik et al. “Single Atoms with 6000-Second Trapping Lifetimes in Optical-Tweezer Arrays at Cryogenic Temperatures”. *Physical Review Applied* 16, 2021.
- [193] G. Colzi. “A new apparatus to simulate fundamental interactions with ultracold atoms”. PhD thesis. Università degli Studi di Trento, 2018.

- [194] S. Stellmer. “Degenerate quantum gases of strontium”. PhD thesis. University of Innsbruck, Institute for Quantum Optics and Quantum Information, 2013.
- [195] R. Santra et al. “Properties of metastable alkaline-earth-metal atoms calculated using an accurate effective core potential”. *Physical Review A* **69**, 2004.
- [196] A. Taichenachev et al. “Magnetic Field-Induced Spectroscopy of Forbidden Optical Transitions with Application to Lattice-Based Optical Atomic Clocks”. *Physical Review Letters* **96**, 2006.
- [197] V. Giardini. “Development of a novel platform for quantum simulation with Sr Rydberg atoms”. MA thesis. University of Florence, LENS, 2022.
- [198] R. Drever et al. “Laser Phase and Frequency Stabilization Using an Optical Resonator”. *Appl. Phys. B* **31**, 1983, pp. 97–105.
- [199] F. Scazza. “Probing SU(N)-symmetric orbital interactions with ytterbium Fermi gases in optical lattices”. PhD thesis. LMU München, 2015.
- [200] G. D. Domenico et al. “Simple approach to the relation between laser frequency noise and laser line shape”. *Appl. Opt.* **49**, 2010, pp. 4801–4807.
- [201] T. Hansch and B. Couillaud. “Laser frequency stabilization by polarization spectroscopy of a reflecting reference cavity”. *Optics Communications* **35**, 1980, pp. 441–444.
- [202] W. Shaokai et al. “Cooling and Trapping 88Sr Atoms with 461 nm Laser”. *Chinese Physics Letters* **26**, 2009, p. 093202.
- [203] K. Patel et al. *Spectroscopy of the $5s5p\ ^3P_0 \rightarrow 5s5d\ ^3D_1$ transition of strontium using laser cooled atoms* 2023.
- [204] K. Wen et al. *Apparatus for producing single strontium atoms in an optical tweezer array* 2024.
- [205] A. Yamaguchi. “Metastable State of Ultracold and Quantum Degenerate Ytterbium Atoms: High-Resolution Spectroscopy and Cold Collisions”. PhD thesis. Kyoto University, 2008.
- [206] K. Hueck et al. “Calibrating high intensity absorption imaging of ultracold atoms”. *Opt. Express* **25**, 2017, pp. 8670–8679.
- [207] N. Poli et al. “A transportable strontium optical lattice clock”. *Applied Physics B* **117**, 2014, pp. 1107–1116.
- [208] H. Katori et al. “Magneto-Optical Trapping and Cooling of Strontium Atoms down to the Photon Recoil Temperature”. *Phys. Rev. Lett.* **82**, 1999, pp. 1116–1119.
- [209] M. A. Norcia et al. “Narrow-line laser cooling by adiabatic transfer”. *New Journal of Physics* **20**, 2018, p. 023021.
- [210] J. P. Bartolotta et al. “Laser cooling by sawtooth-wave adiabatic passage”. *Phys. Rev. A* **98**, 2018, p. 023404.
- [211] S. Snigirev et al. “Fast and dense magneto-optical traps for strontium”. *Phys. Rev. A* **99**, 2019, p. 063421.
- [212] A. Sitaram. “Experiments with ultracold strontium in compact grating Magneto-Optical Trap geometries”. PhD thesis. University of Maryland, 2022.

- [213] J. Höschele et al. “Atom-Number Enhancement by Shielding Atoms From Losses in Strontium Magneto-Optical Traps”. *Phys. Rev. Appl.* **19**, 2023, p. 064011.
- [214] J. Höschele. “A strontium quantum gas microscope”. PhD thesis. ICFO, 2024.